NASA Technical Paper 3151

AVSCOM Technical Report 91-A-003

November 1991

NACA 0015 Wing Pressure and Trailing Vortex Measurements

K. W. McAlister
and R. K. Takahashi

US ARMY AVIATION SYSTEMS COMMAND
AVIATION R&T ACTIVITY

NASA

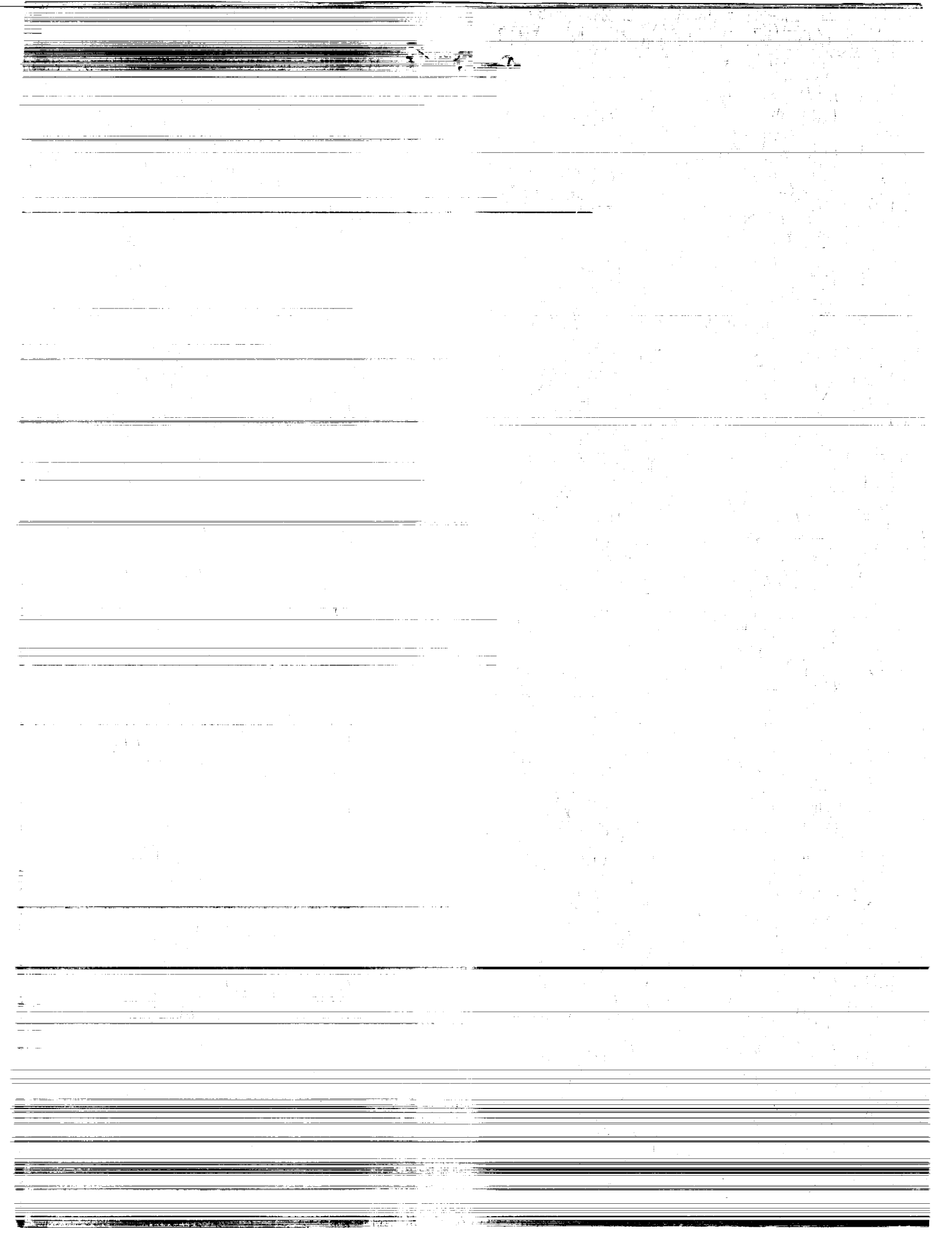

ERRATA

NASA Technical Paper 3151
AVSCOM Technical Report 91-A-003

NACA 0015 WING PRESSURE AND TRAILING VORTEX MEASUREMENTS

K. W. McAlister and R. K. Takahashi

November 1991

Pages 89-90: Figure 39 is out of sequence. It should come after Figure 38 (page 93).

Issued 11-26-91

NASA Technical Paper 3151

AVSCOM Technical Report 91-A-003

1991

NACA 0015 Wing Pressure and Trailing Vortex Measurements

K. W. McAlister
and R. K. Takahashi
Aeroflightdynamics Directorate
USAARTA-AVSCOM
Ames Research Center
Moffett Field, California

National Aeronautics and Space Administration
Office of Management
Scientific and Technical Information Program

CONTENTS

Page

NOMENCLATURE v

SUMMARY 1

INTRODUCTION 1

TEST DESCRIPTION 3
- Facility and Model 3
- Pressure Measurements 3
- Velocity Measurements 4
- Vortex Locator 4
- Data Acquisition 4

RESULTS AND DISCUSSION 5
- Surface Pressure 5
- Wing Circulation 8
- Trailing Vortex 9

CONCLUDING REMARKS 13

APPENDIX—WALL CORRECTIONS 15
- Solid and Wake Blockage 15
- 2D Blockage Factor 16
- 3D Blockage Factor 17
- 2D Lift Interference 17
- 3D Lift Interference 18

REFERENCES 20

TABLES 22

FIGURES 28

NOMENCLATURE

A_a	cross-sectional area of airfoil (perpendicular to wing span)
A_p	planform area of wing (cs for rectangular wing)
A_t	cross-sectional area of tunnel (bh for rectangular tunnel)
AR	Aspect ratio, $2s/c$
b	test-section breadth parallel to airfoil span (double, if half-span model)
c	airfoil chord
C_c	chord force coefficient, chord force/A_pq$_\infty$
C_d	drag coefficient, drag/$A_p q_\infty$
C_l	lift coefficient, lift/$A_p q_\infty$
C_m	moment coefficient, moment/$cA_p q_\infty$
C_n	normal force coefficient, normal force/$A_p q_\infty$
C_p	pressure coefficient, $(p - p_\infty)/q_\infty$
d	distance from airfoil to nearest wall
e	ratio of ellipse chord to ellipse chord plus fin
F	function defined by equations (A-26)
h	test-section height (perpendicular to airfoil span)
k	function of fitting ellipse, defined by equation (3)
M	Mach number
p	static pressure
q_∞	dynamic pressure, $\frac{1}{2}\rho V_\infty^2$
r	ratio of nose radius to airfoil chord
Re	Reynolds number, cV_∞/ν
s	airfoil span (half-span, if mounted on wall)
S_1	function defined by equations (A-26)
t	airfoil thickness
v	velocity along airfoil surface
V_x	velocity in free-stream direction
V_z	velocity in vertical direction
V_∞	free-stream velocity
w	test-section width parallel to airfoil span
x	coordinate in free-stream direction
$\overline{x}$	coordinate along airfoil chord
y	coordinate along test-section width parallel to airfoil span
z	coordinate along test-section height
$\overline{z}$	coordinate normal to airfoil chord
α	airfoil angle of attack
β	compressibility factor, $\left(1 - M_{\infty u}^2\right)^{1/2}$
Γ	circulation
δ	offset correction to solid blockage, defined by equation (A-14)
δ_E	mean lift interference parameter for elliptic spanwise loading
δ_o	upwash interference at a lifting line
δ_1	upwash interference associated with streamline curvature due to finite chord
Δ	corrected – uncorrected value
ϵ	blockage factor
η	solid blockage due to angle of incidence, defined by equation (A-15)
λ	test-section shape parameter, defined by equations (A-18) and (A-19)
μ	function of fitting ellipse, defined by equation (4)
ν	fluid kinematic viscosity
ξ	nh/b
ρ	fluid density
τ	quantity appearing in equation (2), $\sqrt{2re}$
σ	span ratio, $\frac{\pi^2}{48}(\frac{c}{h})^2$
χ	span ratio, $2s/b$

Subscripts

∞	free-stream value
u	uncorrected value
b	blockage-corrected value
sc	streamline-curvature-corrected value
0	value of quantity at zero lift

SUMMARY

A NACA 0015 semispan wing was placed in a low-speed wind tunnel, and measurements were made of the pressure on the upper and lower surface of the wing and of the velocity across the vortex trailing downstream from the tip of the wing. Pressure data were obtained for both 2D and 3D configurations. These data feature a detailed comparison between wing tips with square and round lateral edges. A two-component laser velocimeter was used to measure velocity profiles across the vortex at numerous stations behind the wing and for various combinations of conditions. These conditions include three aspect ratios, three chord lengths, a square- and a round-lateral tip, presence or absence of a boundary-layer trip, and three image plane positions located opposite the wing tip. Both pressure and velocity measurements were made for angles of attack of $4^\circ \leq \alpha \leq 12^\circ$ and for Reynolds numbers of $1 \times 10^6 \leq Re \leq 3 \times 10^6$.

The addition of a round-lateral edge to the wing tip was found to eliminate the secondary vortex near the wing tip, but had little effect on the downstream characteristics of the trailing vortex. The increase in wing lift near the tip because of the presence of the trailing vortex was evident in the surface pressure, but was not captured by circulation-box measurements. The circumferential velocity within the vortex was found to reach free-stream values and produce core rotational speeds as high as 44,000 rpm. The streamwise velocity within the viscous wake that is shed from the wing was observed to form islands of peak velocity in the spiraling sheet that feeds into the trailing vortex. Near the wing, the trailing vortex is asymmetric and contains definite zones where the streamwise velocity both exceeds and falls behind the free-stream value. When referenced to the free-stream velocity, the maximum vertical velocity of the vortex is directly dependent on α and is independent of Re.

INTRODUCTION

The trailing vortex from a rotor blade can be a major source of noise and vibration as it interacts with the other blades of a rotor system (refs. 1 and 2). To study these blade–vortex interactions, experiments are commonly attempted in ground facilities on geometrically and aerodynamically "similar" models, with the notion that the test results can be applied to the full-scale rotor environment when the governing dimensionless scaling groups are held constant. However, since the details of the vortex formation and maturation process are not well understood, there is some uncertainty about how to formulate the relationships between various physical quantities (ref. 3). Part of the difficulty in formulating good theoretical models stems from the scarcity of reliable and complete experimental data that might offer guidance and validation opportunities to the computational physicist (refs. 4–6). Fortunately, there is some evidence that the structure of a trailing vortex from a fixed wing is essentially the same as that from a rotor (ref. 7). Furthermore, it has been reported that centrifugal effects have little influence on the path of the tip vortex from a rotor (ref. 8). These findings offer support for examining trailing vortices in relatively simple fixed-wing experiments.

Trailing vortices owe their origin to viscosity and the boundary layers that develop on lifting surfaces. The pressure differential that exists between the lower and upper surface of a wing drives a portion of the vorticity-laden fluid in the boundary layer around the tip and toward the upper surface (suction side) of the wing. Streaklines on the upper surface and near the leading edge will therefore show the flow near the tip to be moving in an inboard direction. The boundary-layer vorticity (called bound vorticity), which was initially oriented parallel to the span of the wing, is redirected and reorganized as the fluid undergoes a highly 3D deformation and mixing at the tip. Before the fluid near the tip reaches the trailing edge of the wing, a prevailing vortex emerges (although secondary ones may also exist) that has separated slightly from the surface (thus becoming a free vortex) and has a downstream orientation; this is called the trailing vortex. The surface streaklines near the trailing edge will be driven in an outboard direction under the action of the vortex. This vortex also causes the pressure to be reduced on the surface of the wing beneath it and is therefore responsible for an increase in lift in this region. If the path of the vortex were to be extrapolated back toward the surface of the wing, it would appear to originate from a location around midchord at low α and move progressively toward the leading edge as α increased (ref. 9).

As the trailing vortex passes off the surface and enters into the wake, it may already be carrying about half of the wing circulation (ref. 10). The remainder of the vorticity generated on the wing is contained in

the viscous wake that is shed along the entire trailing edge. The vorticity near the wing tip enters the innermost part of the trailing vortex, while vorticity shed at increasing distances from the tip appears in the vortex at increasing radial distances from the center (ref. 11). The difference between the component of velocity in the streamwise direction and the free-stream velocity tends to reach a maximum (either an excess or a deficit) at the center of the vortex, the likelihood of a deficit condition increasing with decreasing lift-to-drag ratio (ref. 12). The angle at which the viscous wake is shed from the wing is equal to the aerodynamic angle of attack (ref. 13). This wake forms a continuous sheet which is attached to and is rapidly drawn toward the trailing vortex along a helical contour. Details of the roll up and the maximum circumferential velocity in the vortex at different positions downstream of the wing greatly depend on the specific loading distribution that exists along the wing span (refs. 14–17). Assuming there are no other, competing, vortices in the flow, it is often assumed that the trailing vortex eventually captures all of the vorticity from the wing (ref. 18 reports that 90% of the measurable circulation in the wake is contained within the trailing vortex by $x/c = 1$). As the trailing vortex moves downstream, the path of the vortex moves inboard about 5% to 10% of the wing span (ref. 13). Trailing vortices are known to persist for many spanlengths behind the wing. This longevity, which is significant compared to swirling flows (perhaps 100 times longer for a vortex), is attributed to the rapid decay of turbulence and a corresponding decrease in eddy diffusion within the vortex (ref. 19).

Although trailing vortices have been studied for many years, and certain general characteristics are well known, there are a variety of different accounts that have been given for the details of their formation and downstream development as well as the parameters on which they scale. For example, in descriptions of where tip vortices originate, it has been reported that they sometimes develop at the tip (when α and Re are high) and sometimes develop farther inboard (ref. 20). It has also been reported that two tip vortices can occur simultaneously, one forming at the front corner of a wing from flow along the pressure side and the other forming farther inboard from flow along the suction side, both with the same apex (ref. 21). Another example deals with the characteristic length on which the core size scales. Some investigators have claimed that the correct scaling length is the boundary-layer thickness on the pressure side of the wing, but others disagree (ref. 22). The more popular lengths that appear in the literature are the wing span (refs. 17 and 23), the wing chord (refs. 24 and 25), and the product of the wing chord and the lift coefficient (ref. 3). Another issue is the total circulation that is contained in a trailing vortex from a wing. Whereas many investigators have assumed that the total circulation is equal to the midspan value (refs. 17, 26, and 27), others have claimed that the circulation is not necessarily equal to the midspan value (ref. 22), or that it is somewhat less than the theoretical value because of dissipation (ref. 20), or that it is equal to half (or nearly half) of the midspan value (refs. 14, 20, 28, and 29). Although other examples of controversy can be found in the literature (such as how to define the Reynolds number, or whether it is even an important parameter, and how to describe the shape of the circumferential velocity profile outside the core), it is already sufficiently evident that there is much more to learn about trailing vortices.

In the present study, a NACA 0015 wing was placed in a steady stream so that measurements could be made of the pressure on the upper and lower surface of the wing and of the velocity across the vortex trailing downstream from the tip of the wing. Pressure data, obtained for both 2D and 3D configurations, feature a detailed comparison between wing tips with square and round lateral edges. A two-component laser velocimeter was used to measure velocity profiles across the vortex at numerous stations behind the wing and for various combinations of conditions. These conditions include three aspect ratios, three chord lengths, a square- and a round-lateral tip, presence or absence of a boundary-layer trip, and three image plane positions located opposite the wing tip. Both pressure and velocity measurements were made for angles of attack of $4^\circ \leq \alpha \leq 12^\circ$ and for Reynolds numbers of $1 \times 10^6 \leq Re \leq 3 \times 10^6$.

Because of the relative size of the supporting endplate (which also served as a splitter plate), both pressure and velocity data were affected to some extent by the flow confinement imposed by the wind-tunnel walls. This is not of any concern as long as comparisons are made between cases within this experiment. For interpretation of these results in the light of other experimental data, or comparison with numerical calculations that are performed in free air, wall corrections are recommended. Since the available methods for determining wall corrections are not exact, the data are

presented as measured, without introducing any questionable (and irreversible) alterations. Should circumstances warrant an attempt to make wall corrections, the procedures for both 2D and 3D cases are presented in the appendix.

TEST DESCRIPTION

Facility and Model

The experiment was conducted in the NASA Ames 7- by 10-Foot Subsonic Wind Tunnel No. 2 under the authority of the U.S. Army Aeroflightdynamics Directorate. This is a closed-circuit atmospheric tunnel with a maximum speed of 375 fps. The free-stream velocity in the tunnel was measured by a pitot-static probe located at the center of the entrance to the test section. The free-stream temperature was measured with a thermistor located in the aft portion of the test section.

All of the wing configurations studied were rectangular and had a constant and untwisted NACA 0015 profile along the entire span. The lateral edge of each wing tip was machined to a flat or square face, but could be made round by the addition of an end cap (fig. 1). All wing elements were made from black anodized aluminum. Three wings were made with the same aspect ratio, $AR = 6.6$, but with chord lengths of 12.0, 16.2 and 20.4 in. (fig. 2). The aspect ratio is defined in terms of the distance between wing tips, even though only half a wing physically existed in this experiment. Only the largest wing was instrumented for surface pressure measurements. Two spanwise extensions (each 9 in. in length) were made for the smallest wing to enable aspect ratios of 8.1 and 9.6 to be studied.

The wings were mounted on a splitter plate (a supporting endplate extending from floor to ceiling) that was positioned 1 ft away from the side wall of the tunnel (fig. 3). This wing support, which was used to test all wings, could be rolled along a track to place the wing at any streamwise position in the test section. The endplate was 2.5 in. thick and 48 in. wide in the streamwise direction (formed on a 2-in. thick aluminum core) to which was attached a 4-in. elliptical fairing along the leading edge and a 7-in. elliptical fairing along the trailing edge. An image endplate (with a wood core) of the same shape as the support endplate was installed at positions opposite to the wing tip during special studies.

In all cases, the angle of attack was set by rotating the wing about its quarter-chord axis. The quarter-chord axis of the wings passed through the support endplate at a point 23 in. from the leading edge of the elliptical fairing (back 39% of the total endplate width). The relative sizes of the various wings and extensions are indicated in a plan view of the test section shown in figure 4.

Positioning the image endplate against the tip of the largest wing prevented the formation of the trailing vortex, so that 2D pressure measurements could be obtained (fig. 5(a)). Without the image endplate, the tip of this wing was 1.9 c from the opposte test-section wall. To ascertain the effect of the image vortex on the trailing vortex from the large wing, the image endplate was placed at two specific distances away from the tip of the small wing. These two positions of the endplate relative to the small wing corresponded to integer multiples (1 or 2 times, and 3 times when completely removed) of the distance of the large wing from the test-section wall (fig. 5(b)).

Pressure Measurements

Wing pressures were measured at 320 stations on the largest model (c = 1.70 ft), over an area favoring the leading edge and the tip of the wing. The matrix of coordinates included 14 span locations and 18 chord locations (fig. 6). Tubes were routed from each measurement location to a place outside the test section where they were connected to 12 scanivalves. Each scanivalve contained a 5-psi differential-pressure transducer and was arranged so that one side could be selectively exposed to any one of 24 ports. One particular port on each scanivalve was reserved for calibrations. The opposite side of each transducer was vented to ambient conditions in the control room. Since only a portion of the wing could be surveyed for any given set of port assignments, tubes were selected depending on whether emphasis was to be on full-span characteristics or on obtaining a higher resolution over the outer portion of the wing. The pressure transducers were calibrated over a range of -4 psi $< p <$ $+1$ psi at a 0.1-psi interval. As these calibration pressures were applied to the transducers, they were simultaneously measured and digitized by a calibrated pressure analyzer.

Velocity Measurements

Two components of velocity (oriented normal to the span of the wing) were measured with a two-color laser-velocimeter (LV) system (fig. 7). An Argon-ion laser was used with an etalon and a multiline mirror to emit a predominately blue (4880-Å) and green (5145-Å) beam. The purpose of the etalon was to increase the coherence length, to narrow the lasing bandwidth, and to reduce mode hopping. After separating the colors with a dispersion prism, the blue and green beams were split into a four-beam matrix and directed into a 3.75× beam expander. The set of four parallel beams exited from the beam expander at a diametral spacing of 131 mm and then entered a traversing apparatus that consisted of two 200-mm mirrors and one 2286-mm focusing lens. A computer-controlled traverse device was used to move the focusing lens (and thus the measuring volume) over a 500- by 500-mm area. The measurement-volume fringe spacings were determined (from calibration) to be 8.90 μm in the horizontal direction (blue beams) and 8.98 μm in the vertical direction (green beams). The diameter of both measurement volumes, based on an e^{-2} intensity fall-off of a Gaussian beam, was calculated to be 0.3 mm, and the length was similarly calculated to be 10 mm. One beam of each color was frequency shifted using an acousto-optic device (Bragg cell) in order to determine the direction of flow.

A portion of the window in the near wall of the test section was removed to provide a direct viewing path into the wind tunnel. The clear opening eliminated the possibility of window reflections as a source of noise in the signals. Airflow through the opening was minimal since the pressures in the test section and the control room are nearly equal during steady tunnel operation. The backscattered light was collected through the sending optics, color-separated using dichroic mirrors, and focused onto photomultiplier tubes. The amplified signals from the photomultipliers were down-mixed and then routed into signal processors (counters), which filtered and again amplified the signals and timed the Doppler cycles.

The tunnel was seeded with a liquid consisting of 1 part glycerin to 3 parts water, by volume. The liquid was atomized with a commercial seeder (which produced particles about 1–3 μm in diameter) and three oil misters (which produced particles estimated to be less than 5 μm). All four seeding devices were placed in the settling chamber and allowed to continuously replenish the atomized mixture that was being carried by the flow around the entire circuit of the closed-loop tunnel. Seeding in this fashion provided a measurement rate of about 150 samples/sec over most of the flow. However, tunnel operation during August resulted in a free-stream temperature increase from 65 °F in the early morning to about 105 °F by noon. These higher temperatures accelerated the evaporation of water from the particles, reducing their size to below what could be detected and causing the measurement rate to fall significantly. This obstacle was overcome by shifting the hours of tunnel operation to earlier in the day.

Vortex Locator

Vortex meander is a familiar phenomenon in trailing-vortex experiments, and has led to numerous rapid-scan techniques for measuring the velocity profile (refs. 23 and 30). The approach taken in this experiment was to detect the passage of the vortex across a given location and thereby establish a conditional sampling criterion that could be imposed during the analysis phase. A vortex meter, consisting of a feathered cruciform structure mounted on a bearing and attached to a Hall-effect transducer (fig. 8), was mounted on the survey apparatus and used to locate the center of the trailing vortex and to track its meandering behavior. The rotational action of the vortex on the vanes of the meter produced a sinusoidal voltage output from the transducer. The frequency of this signal increased as the meter approached the center of the vortex; therefore this was an effective method for statistically locating the y and z coordinates of the trailing vortex at any location downstream of the wing. Signal frequency was converted into dc voltage and was recorded along with all data related to the trailing vortex. Although the tunnel was operating under steady conditions, a sufficient level of disturbance may have existed in the flow to account for the meandering path of the vortex (refs. 19 and 30). The vortex was observed to move laterally to a new location about once per second, with an amplitude that increased with increasing distance downstream of the wing tip.

Data Acquisition

Two computers were used to carry out the various censoring, managing, and numerical computing

tasks of this experiment. A PC was used for control and data acquisition (HP CPU and multiplexer) and a large mainframe computer (VAX-785) was used for data reduction, archiving, and graphical display functions (fig. 9). Two input lines were used for the VAX: one for general communication and graphics, the other for data transfer. This division of tasks between the two classes of computers (the PC and the mainframe) allowed the smaller computer to function as a "manager"—to reset switches and reposition devices in preparation for new data while a file that was recently transferred to the larger computer was being converted into engineering units, statistically analyzed, and returned to a separate monitor. Information was also displayed concerning various test parameters, warnings about specific anomalies and numerous automatic decisions that were made by each computer or processor.

After setting the airfoil angle of attack and the tunnel free-stream velocity, the scanivalves were indexed to record the upper- and lower-surface pressures. Selected ports were monitored to make certain that equilibrium had been reached before any data were taken after indexing the scanivalves to a new position. Once the full set of data was accumulated (this took about 30 min), the pressures were reduced to coefficient form so that the chordwise distributions of pressure and the spanwise distribution of lift could be displayed.

LV measurements were obtained either along a contour around the wing at various span locations or across the trailing vortex at various streamwise locations. The measurement grid (fig. 10) was located in a space-fixed coordinate system with the origin at the trailing edge of the wing tip ($y = 0, z = 0$) when the wing was at zero angle of attack. The contour around the wing was composed of 40 discrete points to form a "circulation box" that was aligned with the free-stream velocity (fig. 11). The trailing vortex was normally surveyed at 41 points along a straight horizontal line (parallel to the airfoil span) across the core of the vortex or at 160 points over an area normal to the free-stream direction (fig. 12). The matrix of coordinates to be surveyed was centered around the vortex core (which was usually inboard from the wing tip and below the pitch axis) and therefore appears offset from the coordinate reference ($y = 0, z = 0$). In all cases, the survey coordinates were placed in a file and the computer was given the task of automatically positioning the probe volume and acquiring the data. After collecting a total of (typically) 1000 validated samples at a given location, the computer would signal the traverse controller to move to the next point of measurement. Following a wait of 2 sec to allow any traverse vibrations to damp out, the computer would begin accepting data again.

Specifying the actual coordinates at which the trailing vortex was to be surveyed required that the center of the vortex be known. The center of the vortex was found by first positioning the vortex meter in the approximately correct location indicated by the response of the cruciform. The computer would then reposition the meter over a predetermined number of intervals in the y and z directions (centered around the assumed location of the vortex) and then display the matrix of responses. This procedure was found to be effective in locating the statistical center of the vortex. Based on this value for the vortex center, a new matrix of coordinates was generated.

Because several hours might be required to complete an LV survey of an extensive matrix of positions, the manager computer was programmed to announce the completion of various tasks by means of unique audible signals. This allowed the test engineer to focus attention on an additional monitor where statistical histograms and velocity profiles were being displayed. Because of the automatic functioning of the entire data acquisition and reduction procedure, and the audible computer signals, fatigue was significantly reduced.

RESULTS AND DISCUSSION

Surface Pressure

Pressure measurements and calculated lift, drag, and pitching moment coefficients are presented for both 2D and 3D wing configurations, with square- and round-lateral tips, for angles of attack of $0° \leq \alpha \leq 14°$ and Reynolds numbers of $1 \times 10^6 \leq Re \leq 3 \times 10^6$ (tables 1-6). The coordinate system used for presenting the pressure measurements, and the equation for defining the surface of the airfoil, are given in figure 13.

Load calculations– Since there was no provision for making pressure measurements at either the leading edge or the trailing edge, values at these two locations were approximated so that more accurate lift, drag, and pitching moment calculations could be made. The leading-edge pressure coefficient was determined from a theory that is applicable to thin symmetric airfoils (ref. 31). In this theory it is hypothesized that the flow around the leading edge of the airfoil is the same as that for an ellipse (with a trailing fin) that has been

sized to geometrically approximate the leading edge of the airfoil. The first step is to determine the angle of attack for the finned ellipse that produces the same v/V_∞ as calculated for the actual airfoil at the same $\overline{x}/c$. Based on the measured pressure coefficient at a particular location near the leading edge, the velocity is determined from

$$\frac{v}{V_\infty} = \sqrt{1 - C_p} \qquad \text{(incompressible)} \quad (1)$$

The angle of attack that yields the above v/V_∞ at this particular $\overline{x}/c$ is found from

$$\frac{v}{V_\infty} = (1 + \frac{2r}{\tau})\sqrt{\frac{\overline{x}/c}{\overline{x}/c + r/2}} \times \Big(\cos\alpha \pm \sin\alpha\sqrt{\frac{k - \overline{x}/c}{\overline{x}/c}}\Big) \quad (2)$$

where $\pm$ denotes that the expression following it is added for the upper surface and subtracted for the lower surface, and k is a function of the fitting ellipse and is defined by

$$k = \frac{e}{4}(\mu + \frac{1}{\mu} + 2) \quad (3)$$

with

$$\mu = (\frac{2}{e + \tau})\Big(1 - \frac{e}{2} + \sqrt{1 - e(1 - \frac{\tau}{2})}\Big) \quad (4)$$

and $\tau = \sqrt{2re}$ is the actual thickness of the ellipse (in airfoil chords). For the NACA 0015 airfoil, the ratio of the nose radius to the airfoil chord (r) is 0.0236 and the ratio of the ellipse chord to the ellipse chord plus fin (e) is 0.3. Using the α just calculated from equation (2), the theoretical pressure at the leading edge is

$$C_p = 1 - \frac{2(1 + \tau)^2}{r}\sin^2\alpha \qquad \text{at } \overline{x} = 0 \quad (5)$$

With this estimate for the leading-edge pressure and the three nearest data points on either side of $\overline{z}/c = 0$ (fig. 14), a quasi-Hermite spline fit (a continuous curve with a continuous first derivative) is used to define additional values around the leading-edge region of the airfoil.

The trailing-edge pressure coefficient used was simply the average of the linear extrapolations from the upper and lower surfaces (fig. 15). From the approximated values of C_p at the leading and trailing edges, and the curve that was fit to the leading-edge data in the C_p vs. $\overline{z}/c$ plane, the original finite set of actual data points was expanded to a 1,000-point set to improve the accuracy and presentation of the results.

The pitching moment is defined about the quarter-chord axis, and is taken to be positive when it produces an increase in α. The force and moment coefficients were calculated from a trapezoidal-rule integration over the expanded data set. The "local contributions" to these integrals are shown in figures 16 ($\alpha = 0°$) and 17 ($\alpha = 12°$) for equal increments of $\Delta\overline{x}$ (fcr C_n and C_m) and equal increments of $\Delta\overline{z}$ (for C_c). In the $\alpha = 0°$ example, an interesting feature is found in the C_p vs. $\overline{z}/c$ curve. Starting at the leading edge where $C_p = 1.0$, and moving along the upper surface, three regions are encompassed by the time the complete airfoil has been traversed and the curve closes at the leading edge. The regions that are bound in a clockwise sense represent a negative chord force, and those bound in a counterclockwise sense represent a positive chord force. In this case, the positive and negative contributions sum to zero. In the $\alpha = 12°$ example there is a sizable negative chord force as a result of the low pressure distribution over the forward projection of the airfoil. Since only the pressure has been considered, the complete chord force would no doubt be more positive (in all cases) if the viscous component had been available for inclusion. Because the incremental chord force is derived from the local pressure that is acting on an elemental-surface projection in the chord direction, and since ΔC_c is plotted for equal increments of $\Delta\overline{z}$, there will necessarily be a discontinuity in the curve at maximum thickness ($2\overline{z}/c$) where the surface projection changes direction (surface slope changes sign). The discontinuity is not symmetric about $\Delta\overline{z} = 0$ because of the difference in the average pressure over these adjacent segments of the surface.

2D wing– A 2D configuration was established by positioning the image endplate against the tip of the large wing (fig. 5(a)). Representative pressure distributions over the central 45% of the wing are shown for three angles of attack and two Reynolds numbers in figure 18. Recall that the leading- and trailing-edge values (open symbols) are estimates based on data for neighboring locations. The chordwise pressure distribution differs little between the three span stations shown, even for the $\alpha = 12°$ case. However, subtle differences in pressure can result in large variations in the force and moment loads when these pressures are integrated over the surface. When the lift at all 12 span

stations (including those near the endplate where significant boundary-layer interactions are evident) is calculated, it can be seen that some degree of variation is present along the entire span (even over the central portion) and that the variation becomes quite pronounced when $\alpha > 10°$ as the stall angle is approached (fig. 19). The solid line accompanying the results for each α represents the average value for the lift over the part of the span from $0.09 < y/s < 0.90$ (this segment excludes the five points near the tip). The integrated loads over the angle range $0° \leq \alpha \leq 14°$ indicate that the drag and pitching moment are even more sensitive to span location than is the lift (fig. 20). Since the drag and moment are usually small for angles below stall, the scales that were used to plot these loads have exaggerated the impact of spanwise differences in the leading-edge pressure (mostly affecting the drag) and the center of pressure (mostly affecting the pitching moment).

3D wing– The 3D configuration was investigated in two stages. During the first stage, measurements were made over the full wing span, with a square tip only. During the second stage the pressure-tube connections were reconfigured to concentrate on measurements over the outer portion of the wing span, and both round and square tips were examined.

The full-span (square tip) pressures are shown in figures 21 and 22 for all 12 spanwise stations where both upper- and lower-surface measurements were made. Only the results for conditions of $\alpha = 4°$, 8°, and 12° at $Re = 1.5 \times 10^6$ and 2.5×10^6 are presented. For all conditions, there is a gradual reduction in pressure as the tip of the wing is approached, and there is a peculiar distortion over the upper surface along the outermost 3% of the span ($y/s > 0.97$). This distortion in the chordwise pressure distribution has been observed in other experiments (refs. 8, 32–35) and is believed to be due to the vortex (or vortices) that forms on the suction side of the wing tip. The integrated effect of the vortex is to produce an increase in the lift over the region near the wing tip (fig. 23). Back along the span in the inboard direction, the lift is observed to level off except for a slight increase at the innermost location $y/s = 0.094$. This departure from the expected asymptotic value is attributed to the presence of the supporting endplate.

The force and moment variations along the span of the wing for $\alpha = 4°$, 8°, and 12° at different Reynolds numbers (fig. 24) show a large change in the lift as the wing tip is approached, and a comparatively modest increase near the tip itself. This behavior is in contrast to the rather slight change in the drag and the pitching moment as the wing tip is approached, and the significant increase in the drag and the "nose-down" moment that occurs near the tip. The Reynolds number has some effect on the loads at all locations along the span (fig. 24), and, when integrated over the entire span (fig. 25), has an increasing effect as α is increased.

The pressure over the outer portion of the wing is shown for the square-tip case (figs. 26–28) and for the round-tip case (figs. 29–31) under conditions of $\alpha = 4°$, 8°, and 12° at $Re = 1.0 \times 10^6$, 2.0×10^6, and 2.9×10^6. At two spanwise stations near the wing tip the pressure was measured only on the upper surface. The y/s values for these two cases will differ by 2.3% because of the addition of the round tip, which increases the span by half of the airfoil thickness ($t_{max}/2$). For both the square- and round-tip cases, the pressure distortions due to the tip vortex are confined to the upper surface and along the outer 4% of the span ($y/s > 0.96$). This same behavior has been observed in pressure measurements made on a rotor (rectangular and untwisted NACA 0012) with round and square tips (ref. 33). In the region near the tip of the wing, the pressure distributions assume shapes that are distinctive under conditions of high lift ($\alpha \geq 8°$). After the suction peak that occurs near the leading edge, the pressure curve exhibits two strong undulations in the square-tip case and only one undulation in the round-tip case (albeit this chordwise row of pressure orifices is located 2.3% farther inboard after the round tip is installed). The Reynolds number appears to have little effect on the pressure undulations in the square-tip case, whereas the pressure undulation is larger and more responsive to changes in the Reynolds number in the round-tip case. The apparent insensitivity to Reynolds number in the square-tip case may be due to the transition-fixing nature of the sharp edge in this case, as the flow accelerates around the tip of the wing to form the trailing vortex that is developing on the upper surface. While the vortex causes an increase in lift near the wing tip with increasing angle of attack in both the square- and round-tip cases (figs. 32 and 33), the increase becomes noticeably large in the round-tip case for the combination of high angle of attack ($\alpha \geq 8°$) and high Reynolds number (recall, in figs. 29–31, the corresponding large pressure undulation near the trailing edge in the round-tip case). The rather large drag and pitching moment loads that are

observed near the tip of the wing in the square-tip case are seen to be even larger in the round-tip case.

The lift, drag, and pitching moment values for the full wing can be estimated by integrating the section loads over the span and assuming that the innermost value at $y/c = 0.58$ remains constant up to the wing root at $y/c = 0.0$. The results obtained at different Reynolds numbers show a modest and generally increasing spread as α is increased toward stall (fig. 34).

The peculiar distortion in the chordwise pressure distribution near the wing tip (recall fig. 27(c)) was also observed in an earlier experiment (archived run:1/ frame:19 data from ref. 37). In agreement with the present experiment, the earlier results indicate that the distortion is confined to the outermost 3% of the span (fig. 35). The dimensional characteristics of the pressure-instrumented wings used in these two tests are shown in figure 36(a), along with the nondimensional distances from the wing tip (y^*/c) where the results can be compared. Although the results from these two experiments are in good qualitative agreement, the referenced data are consistently lower along the upper surface. By imposing estimates for the lower-surface pressure in the Spivey–Morehouse data at the incomplete spanwise stations (see fig. 35), the pressure can be integrated to obtain the lift and a comparison made at corresponding values of y^*/c (fig. 36(b)). Again, the results are qualitatively similar but significantly different in magnitude. This difference may be attributed to the following two factors: first, wall corrections to the present data have not been made, and second, tuft studies during the Spivey–Morehouse test revealed that a large updraft (along the wing span) from an opening around the base of the floor-mounted model may have produced sizable wing–wall effects when those data were acquired.

Wing Circulation

Calculated wing circulation coefficients are presented for the 3D wing configuration at $Re = 1.5 \times 10^6$ and $\alpha = 12°$, for both a square- and a round-lateral tip. Based on velocity integrations around a rectangular path of fixed size in the x–z plane (figs. 10,11), the calculated circulation ($\sum V_x \Delta x + \sum V_z \Delta z$) at various span stations are presented in table 7 and figure 37. The circulation results are given in nondimensional form as $-2\Gamma/cV_\infty$ since this quantity is stated to be equal to the lift coefficient, C_l, per unit of span, according to the Kutta–Joukowski theorem for 2D incompressible ($M_\infty < 0.3$) flow. In each case, the results are referenced to the tip of that particular wing, and in each figure is included a projection of the wing thickness over its entire span.

Using the smallest wing ($c = 0.305$ m) as a basis for comparison, the addition of a round tip (which causes an increase in y/c of 0.13) does not appear to have proportionately extended the circulation distribution toward the tip (fig. 38(a)). If the circulation distribution were to be physically keyed to the spanwise limits of the wing, then one curve would have overlain the other. It is also evident that a 23% increase in the aspect ratio of the wing (produced by adding a tip section) has no effect on the circulation distribution (fig. 38(b)). This suggests that in both cases the wing aspect ratio is sufficiently large so that neither the wall boundary layer nor the image plane at the root has a detectable effect. Maintaining the same aspect ratio and changing only the chord of the wing yields a similar circulation curve (fig. 38(c)). This result indicates that the chord may be the correct reference length for nondimensionalizing the spanwise distribution of circulation. A final area of interest is the spanwise distribution of lift as it is derived from either circulation or surface pressure (fig. 38(d)). In both cases the same wing is used ($c = 0.518$ m). Without considering wall corrections, it can only be stated that the same trend occurs over the inboard region. Over the region near the tip, however, a major difference in the shape of the lift curve appears. Whereas the circulation-derived lift smoothly diminishes as the tip is approached, the pressure-derived lift displays a substantial perturbation as a result of the trailing vortex that forms over the upper surface. This behavior has been observed in other experiments (refs. 10, 36, and 37), and may indicate a limitation in the application of circulation measurements.

In the circulation–lift relation, it is assumed that the contour of integration contains all of the rotational flow. This is not possible in real flows because the downstream boundary must cut across the viscous wake. Contours taken close to the airfoil, that have downstream boundarles that are perpendicular to the free-stream velocity, will not include any contribution to the lift arising from changes in total pressure across the wake, and will therefore be lower than the correct values (ref. 38). The error may not be significant as long as the enclosed wake contains nearly equal amounts of positive and negative vorticity, but this condition is highly suspect in the tip region of the wing, where

the flow is dominated by the formation of a strong 3D trailing vortex.

Trailing Vortex

Wake velocity measurements are presented for the 3D wing configuration for various combinations of conditions. These conditions include three aspect ratios, three chord lengths, three tip-image plane positions, a square- and a round-lateral tip, presence and absence of a boundary layer trip, angles of attack of $4° \leq \alpha \leq 12°$, and Reynolds numbers of $1 \times 10^6 \leq Re \leq 3 \times 10^6$. Measurements were also made of the trailing vortex at numerous downstream stations ranging from 0.1 to 13.0 chordlengths behind the airfoil. A majority of the velocity measurements were made at various downstream distances from the wing tip (x/c referenced to the trailing edge). A detailed summary of the conditions under which these measurements were made is presented in tables 7–10. Velocity components V_x (oriented parallel to the free-stream direction) and V_z (oriented in the vertical direction) were obtained along a one-dimensional survey (in the spanwise direction) across the core of the vortex (fig. 12(a)). A limited number of measurements was also obtained over a 2D area centered around the core of the vortex (fig. 12(b)).

Streamwise development– To examine the effects of various trailing-vortex determinants (table 11), the square-tip wing with $AR = 6.6$ (referred to as "basic" in the following figures) is used as the reference case. Viewing the vortex from a downstream position, the vertical and streamwise components of velocity are first examined at seven locations (from $x/c = 0.1$ to $x/c = 6$) behind the trailing edge of the basic wing (fig. 39). The flow condition for this case was $Re = 1.5 \times 10^6$ with $V_\infty = 46$ m/sec ($M_\infty = 0.13$). A projection of the wing profile is included in each plot for the convenience of visualizing the relative position of the vortex during its downstream maturation. Just behind the airfoil (at $x/c = 0.1$), the vertical component of velocity reaches nearly 90% of the free-stream velocity. The distortion in the velocity profile (the double inflection before the peak is reached), which is most evident along the outboard portion of the vortex, is probably due to a secondary vortex (refs. 8, 9, 23, and 39). This is the same vortex that was believed to have produced the second undulation in the pressure distribution near the wing tip, in figure 27(c). An alternate view (refs. 14, 24, and 40) is that the distortion in the velocity profile is due to a crossing of the wing-shear layer as it wraps around the trailing vortex. This distortion rapidly fades (completely disappearing by $x/c \approx 1$) as the trailing vortex evolves. The streamwise velocity component initially shows a 50% excess over the free-stream velocity. A distortion in the velocity profile as a result of the secondary vortex is also present. In this case the relative velocity in the vortex core is mostly away from the wing; however, either an excess or a deficit condition is possible, depending on the spanwise load distribution near the tip of the wing (ref. 41). When one examines the velocity profiles at spanwise locations away from the immediate vicinity of the vortex, it is apparent that free-stream characteristics are generally not achieved. For the streamwise velocity component it is expected that $V_x/V_\infty \rightarrow 1$, and for the vertical velocity component that $|V_z/V_\infty|$ (inboard) $> |V_z/V_\infty|$ (outboard), because of downwash behind the wing. Deviations from this expected behavior are believed to be caused by blockage (since an upstream pitot-static probe was used to determine V_∞) and by the effects of the image vortex near the wing tip.

As the trailing vortex moves downstream and the maximum circumferential velocity in the vortex decreases because of viscosity (fig. 40), one can argue that the pressure increases and causes the streamwise component of velocity to decrease (ref. 42). If the distance between the vertical velocity peaks is considered to be a measure of the vortex core, the core diameter appears to grow rapidly in the immediate region downstream of the trailing edge of the wing, and then maintains a somewhat constant value (about 70% of the wing thickness, or 11% of the chord) over the remainder of the first six chordlengths of travel (fig. 41(a)). In an earlier experiment (ref. 16) involving a NACA 0012 with a square tip, the core diameter was found to be about 12% of the wing chord and it remained nearly constant with downstream travel. A core size equaling 10% of the blade chord has also been reported in a model rotor experiment (ref. 43). Since the core is so small, the rotational speed within the vortex can reach very high values. For example, just behind the wing, where the core radius measures about 2.7 cm and the maximum vertical velocity is around 37.7 m/sec, the rotational speed is 13,333 rpm. This explains why the central core region appears clear in many attempts to visualize the vortex (particles that are heavier than air would be rapidly centrifuged out of the core of the vortex). The center of the vortex moves inboard about

25% of the wing chord (fig. 41(b)), and upward to a position slightly above the reference line passing through the quarter-chord pitch axis (fig. 41(c)). Since the vortex would normally be expected to move downward in free air because of the downwash behind the wing, the upward direction of the vortex path is attributed to wall effects (specifically, the image vortex on the opposite side of the wall from the wing tip).

A velocity survey over an area centered around the vortex core is shown in figure 42 for three locations near the wing trailing edge ($x/c = 0.1 \rightarrow 0.5$). The area covered by each survey measures about one chord in the spanwise and vertical directions (in all pictorial contour plots the wing is not shown to scale). The contour plot for the vertical velocity component corroborates the presence of two velocity peaks located inboard from a line projected downstream from the wing tip. The contour and 3D surface plots for the streamwise velocity component show the velocity excess (relative to free stream) within the vortex core and the velocity deficit along the wake of the wing. The streamwise velocity deficit is not uniform along the wake, but instead appears to form islands along the span of the wake that feeds into the trailing vortex along a spiral path.

Chord length effects– Three square-tip wings with the same aspect ratio were used to study the effects of chord length on the trailing vortex. The Reynolds number ($V_\infty c/\nu$) and circulation ($C_l V_\infty c/2$) were fixed by keeping $V_\infty c$ and C_l constant ($\alpha = 12°$, in this case). Specifically, the Reynolds number was 1.5×10^6 and the circulation (Γ) (just downstream of the trailing edge) was about 8 m^2/sec; and the chord and free-stream velocity combinations were 0.305 m at $V_\infty =$ 74 m/sec ($M_\infty = 0.21$), 0.412 m at $V_\infty = 57$ m/sec ($M_\infty = 0.16$) and 0.518 m at $V_\infty = 46$ m/sec ($M_\infty =$ 0.13). Although the Mach number did change, compressibility effects are not considered to be a factor when $M_\infty < 0.3$. Measurements made at $x/c = 0.1$ show (fig. 43) that the general shape of the velocity profiles are the same: the vertical component exhibits the same distortion over the outboard portion of the profile, and the streamwise component exhibits the same number of inflections across the vortex core. The velocity deficit that occurs further inboard ($|y| > 200\ mm$) is caused by the viscous wake that is shed from the trailing edge of the wing. The deficit region appears to scale with the wing chord since it progresses even further inboard as the chord increases. The maximum velocities (relative to free-stream values that vary inversely with the chord) are dependent on the chord length of the wing. The same can be said about the velocity components measured at $x/c = 4$, except that no appreciable deficit is observed in the streamwise profile. The streamwise component within the vortex core has a maximum (velocity excess) value that increases with chord, and a minimum (velocity deficit) value that decreases with chord (figs. 43 and 44). The relative size and position of the vortex core shows a weak dependence on the chord length of each wing at $x/c = 0.1$, and a much stronger dependence on the chord at $x/c = 4$. The relative diameter of the core increases with decreasing chord at the distant streamwise station (fig. 45). The spanwise displacement of the core is observed to move farther inboard with decreasing chord, whereas the vertical displacement increases (moving upward) with increasing chord length. Although the vertical displacement should be downward in all cases (in free air), the fact that the vortex moves farther upward as the chord increases is in keeping with the influence of tunnel wall effects since the wing tip moves progressively closer to the wall as the chord increases (given the same aspect ratio).

Vertical and streamwise velocity contours centered around the vortex core are shown for $x/c = 0.1$ behind the trailing edge of the wing (fig. 46). Distinct islands of velocity excess and deficit can be observed in the streamwise component. Since the physical dimensions of the survey were fixed, a greater extent of the span (in terms of chord length) was covered for the wing with the smallest chord (1.8 chords for the $c = 30$ cm wing and 1.0 chords for the $c = 52$ cm wing). This increased spanwise coverage shows that the 3D character of the viscous wake is not limited to the immediate neighborhood of the tip, but may actually extend over a large portion of the wake.

Reynolds number effects– A single square-tip wing with $c = 52$ cm was used to examine the effects of Reynolds number on the trailing vortex. Because ρ could not be varied in this facility, Re was varied through V_∞. The circulation was held fixed by requiring that $C_l V_\infty$ remain constant, which meant that any increase in the free-stream velocity (V_∞) had to be offset by a decrease in C_l (by reducing α). The three Reynolds number conditions of $Re = 3.0 \times 10^6$, $Re = 1.7 \times 10^6$ and $Re = 1.1 \times 10^6$ were obtained with $V_\infty = 91$ m/sec ($M_\infty = 0.26$) at $\alpha = 4°$, $V_\infty =$ 51 m/sec ($M_\infty = 0.15$) at $\alpha = 7°$ and $V_\infty = 32$ m/sec ($M_\infty = 0.09$) at $\alpha = 10°$, respectively. The circulation for this study was about 5 m^2/sec. The velocity

measurements at $x/c = 0.1$ show that the distortion in the vertical component moves farther outboard and that the extrema in both the vertical and streamwise components increase as the Reynolds number is decreased (fig. 47). The shape of the streamwise profile at $x/c = 4$ indicates a change from a deficit to an excess condition across the vortex core as the Reynolds number is decreased. Although the vertical component (relative to free stream) decreases with Reynolds number (fig. 48), the magnitude of the free-stream velocity increases so that the circulation around the vortex remains constant. In other words, the vertical velocity profiles would have similar magnitudes had they been nondimensionalized using αV_∞ instead of merely V_∞. The diameter of the vortex core appears to be very dependent on Reynolds number just behind the wing (fig. 49(a)); however, this may be deceiving, because the velocity peak (which is used to determine the core diameter) is greatly affected by the outboard distortion of the profile. The core diameter shows no significant dependence on Reynolds number at $x/c = 4$. The spanwise position of the core is insensitive to Reynolds number just downstream of the wing. The vertical position shows a spread which is caused by a combination of Reynolds number and the fact that α is different for each case. The spanwise and vertical positions of the core show some dependence on Reynolds number at $x/c = 4$, with the $Re = 3 \times 10^6$ case being somewhat distinct from the other two cases.

The vertical and streamwise velocity contours around the core of the vortex are presented for each Reynolds number at a location $x/c = 0.1$ behind the trailing edge of the wing (fig. 50). The vertical component shows a progressive increase in the number of contour lines as the Reynolds number is decreased (corresponding to an increase in α). The streamwise component shows a steady growth in velocity excess while the regions of large velocity deficit become more isolated as the Reynolds number is decreased.

Circulation effects– The angle of attack of a square-tip wing with $c = 52$ cm was varied from $\alpha = 4°$ to $\alpha = 12°$ to examine the effects of circulation on the trailing vortex at $Re = 1.5 \times 10^6$. Based on the vertical velocity component near the trailing edge of the wing, the nondimensional circulation (Γ/cV_∞) is estimated to be 0.15 at $\alpha = 4°$, 0.25 at $\alpha = 8°$ and 0.35 at $\alpha = 12°$. Since c and V_∞ were held constant, these values show that Γ varies linearly with α. The velocity measurements at $x/c = 0.1$ indicate that the distortion in the vertical component moves inboard but retains approximately the same magnitude (while the primary vortex peak diminishes) as the circulation (or α) decreases (fig. 51). The streamwise velocity component shows that the velocity excess portion of the profile is a pocket of flow that reverses and becomes a velocity deficit as the circulation is reduced to $\alpha = 4°$. Farther downstream at $x/c = 4$, the streamwise component progresses from a velocity excess condition to a deficit as the circulation is reduced. An earlier experiment on a rectangular wing with the same cross section also showed a streamwise component that changed from a predominantly excess profile to a deficit as α was decreased (ref. 44). The same trend has been reported for wings with different cross sections (ref. 45). The maximum vertical velocity exhibits a strong proportional dependence on circulation at both $x/c = 0.1$ and $x/c = 4$ (fig. 52(a)). The maximum streamwise velocity also shows a strong proportional dependence on circulation at $x/c = 0.1$ (fig. 52(b)), whereas at $x/c = 4$ the core velocity exceeds the surrounding values only for $\alpha = 12°$. The diameter of the vortex core does not appear to have a clear dependence on circulation, especially near the trailing edge, where the distortion in the profile confounds a simple definition for the vortex diameter (fig. 53(a)). The spanwise displacement of the core shows little dependence on circulation at $x/c = 0.1$, whereas there is a sizable (but unordered) dependence at $x/c = 4$ (fig. 53(b)). The vertical displacement of the core follows the angle of attack of the wing and retains that order through $x/c = 4$ (fig. 53(c)).

The vertical and streamwise velocities around the vortex core when $Re = 1.5 \times 10^6$ are shown for three values of circulation at $x/c = 0.1$ behind the trailing edge of the wing (fig. 54). The vertical component shows a progressive decrease in the contour range as the circulation is decreased. The streamwise component shows a decrease in the velocity excess and a more numerous and even distribution of islands of velocity deficit along the wake of the wing that is feeding into the trailing vortex as the circulation is decreased. The same trends were characteristic of the results when Reynolds number was the variable. Since changes in Reynolds number and circulation both involved changes in α, it may be that α is the more fundamental determinant that dictates the behavior of the trailing vortex and its surroundings.

Focusing on the maximum vertical component of velocity, and recalling the results when Γ was varied by changing α at constant V_∞ (fig. 52(a)) as well as

the results when Γ was constant while α and V_∞ were changing (fig. 48(a)), one can see a trend that depends predominantly on α. Combining the results from these two figures shows that there is indeed a nearly linear relationship between V_z/V_∞ and α (fig. 55). The slope of the curve decreases as x/c increases, and there appears to be no obvious dependence on V_∞. This behavior was also observed in an earlier experiment (ref. 30) on a NACA 0015 wing with a square tip.

Aspect ratio effects– Three square-tip wing sections with the same chord ($c = 30$ cm) were combined to study the effects of aspect ratio on the trailing vortex. The Reynolds number and circulation were held constant and the aspect ratio varied from 6.6 to 9.6 (based on wing-tip-to-wing-tip distance). For this study, $Re = 1.5 \times 10^6$ ($V_\infty = 77$ m/sec and $M_\infty = 0.22$) and $\Gamma = 8$ m^2/sec. Measurements made at $x/c = 0.1$ indicate that there are only minor differences between each of the aspect ratio cases (fig. 56). The major distinguishing characteristics, such as the outboard distortion in the vertical velocity profile, the inflections in the streamwise profile as the vortex core is traversed, and the streamwise velocity deficit in the wake of the wing farther inboard, are all present for each aspect ratio. There also appears to be little difference between the velocity profiles at $x/c = 4$, except for the "atypical" streamwise deficit when $AR = 8.1$. Although referred to as atypical, it may be that this case is actually more representative of the flow in all three cases, because the survey was more "centered" across the vortex and/or because the performance of the vortex meter during those particular measurements was better and thereby influenced the choice of data that was admitted for conditional averaging. Overall, the maximum velocities (relative to free stream) do show some dependence on aspect ratio (fig. 57); however, the behavior is too inconsistent to draw any conclusions. The relative size and position of the vortex core show a more rational dependence on aspect ratio (fig. 58). The relative diameter of the vortex core decreases as the aspect ratio is increased (a total reduction of 23% from $AR = 6.6$ to $AR = 9.6$). The spanwise displacement of the core is farther inboard for lower values of aspect ratio. The vertical displacement of the core is increased in an upward direction as the aspect ratio is increased; however, this is believed to be a tunnel-wall effect and therefore not representative of free-air behavior.

Velocity contours showing the vertical and streamwise components over an area around the core of the vortex are presented for each aspect ratio at a location $x/c = 0.1$ behind the trailing edge of the wing (fig. 59). All three cases appear to be qualitatively similar, with the vertical velocity showing a well defined set of closed contours over the outboard portion of the vortex and more open contours over the inboard portion because of the downwash behind the wing. The viscous wake behind the wing can be clearly identified in the contour map of the streamwise velocity component. The numerous pockets of velocity deficit that make up the viscous sheet feeding into the vortex again attest to the three-dimensional character of the wake shed by the wing.

Leading-edge trip effects– A serrated tape was placed along the span near the leading edge of the wing to produce a boundary-layer trip. The effects of the trip on the trailing vortex were examined at $x/c = 4$ for $Re = 1.5 \times 10^6$ and $\alpha = 12°$ with the wing having $c = 30$ cm. Although there is a slight reduction in the maximum vertical velocity with the trip, the most obvious effect appears in the streamwise component of velocity, which changes from a small excess velocity to a large deficit condition (figs. 60 and 61). The trip increases the diameter of the vortex core and decreases its inboard movement along the span, but has no detectable effect on its vertical position (fig. 62).

Image plane effects– To determine what effects the proximity of the test-section wall might have on the trailing vortex, an endplate (equal in size to the wing-support endplate) was placed at different positions away from the tip of the wing (fig. 5). The trailing vortex from the $c = 30$ cm wing (square-tip, $AR = 6.6$) was examined at $x/c = 4$ with $\alpha = 12°$ and $Re = 1.5 \times 10^6$. Without an image endplate, the test-section wall became the image plane and represented the "far image" condition. In this case the far-image plane was located 5.7 chords away from the tip of the wing. When the image endplate was in the "near image" position, the distance between the image plane and the wing tip was 1.9 chords. This configuration corresponded geometrically to the $c = 52$ cm wing case, which had the same aspect ratio and was also 1.9 chords away from the opposing wall. The largest effect of the presence of the image plane is on the streamwise component of velocity (fig. 63). The maximum vertical velocity increases slightly and the streamwise velocity deficit increases significantly as the image plane approaches the wing tip (fig. 64). The diameter of the vortex core remains nearly the same while the path of the core is drawn toward the tip and

upwards as the image plane approaches the wing tip (fig. 65). This diversion of the path of the trailing vortex is in keeping with the anticipated influence of the imaginary vortex on the other side of the image plane, and seems to offer a convincing explanation of why the trailing vortex was observed to move up instead of down as it traveled downstream.

Round-lateral edge effects– Each square-tip wing could be converted to a round-tip wing by the addition of an end cap (fig. 1). The conversion to a round tip causes the planform to be extended by an amount equal to half of the thickness profile of the wing. When viewed along a line from the trailing edge to the leading edge of the wing, the tip appears to be extended by a semicircular section with a radius equal to half the maximum thickness of the wing. The trailing vortex was examined at $x/c = 4$ using a $c = 30$ cm wing with $Re = 1.5 \times 10^6$, and in more detail at $x/c = 0.1$ using a $c = 52$ cm wing with $Re = 2.0 \times 10^6$ ($V_\infty = 59$ m/sec and $M_\infty = 0.17$). Velocity measurements at $x/c = 0.1$ show that the round tip not only eliminates the distortion along the outboard portion of the vertical component, but also reduces the number of inflections in the streamwise component within the vortex (fig. 66). At $x/c = 4$ however, the profiles appear to be quite similar. The maximum vertical velocity is significantly higher for the round tip at $x/c = 0.1$, although it becomes lower than that for the square tip after reaching $x/c = 4$ (fig. 67). The maximum streamwise velocity remains higher for the round-tip case, but the difference is barely distinguishable at $x/c = 4$. The diameter of the vortex core is smaller with the round tip, but reverses after reaching $x/c = 4$ (fig. 68). When the behavior of the core diameter and that of the maximum vertical velocity are looked at together, the circulation associated with the vortex development for both the square and round tips appears about the same. The vortex leaves the trailing edge at the same spanwise location, but at $x/c = 4$ it has moved farther inboard when the tip is round. Since the round tip extends the wing span by 7.5% of the chord, the position of the trailing vortex relative to the wing root is about the same in both cases. The vertical position of the vortex is initially higher for the round tip, but at $x/c = 4$ the vortex from the square tip is slightly higher.

The velocity contours around the vortex at $x/c = 0.1$ are very similar (fig. 69). Therefore, it appears that the distinguishing features that were evident in the profiles taken across the center of the vortex (fig. 66) are due to factors that do not have an area-wide influence. Examination of the contours in more detail (fig. 70) only confirms the presence of steep gradients and high velocities already observed for the vortex from the round-tip wing. Both contour maps are irregular and contain several isolated islands of peak velocity, but no specific features appear that would explain or corroborate the distortions always observed at $x/c = 0.1$ for the square-tip wings along the outboard portion of the vertical-velocity profile.

CONCLUDING REMARKS

The effects of the round-lateral edge appear to be confined to the pressure near the wing tip and the velocity distribution within the trailing vortex near the wing trailing edge. The round edge eliminates the additional pressure undulation on the wing surface as well as the outboard distortion in the vertical velocity component, indicating that a secondary vortex over the wing (and in the near wake) is a characteristic of wings with square tips.

The lift distribution (from pressure integrations) diminishes along the wing span as the tip is approached, but exhibits an abrupt increase over the outermost 4% of the wing in both the round- and square-tip cases. Drag and pitching moment deviations in the tip region are even greater. These force and moment increases are due to the presence of the trailing vortex over the upper surface of the wing tip. The Reynolds number had some effect on the pressure distribution over the wing in the square-tip case, and greatly affected the pressure on the suction side near the wing tip in the round-tip case. The section load variations along the wing were largest for the round-tip case, as were the maximum velocities within the trailing vortex close to the wing.

Circulation-box measurements did not capture the effect of the tip vortex in either the round- or square-tip cases, but instead showed a smooth decline in the lift all the way to the wing tip. This result may indicate a limitation in the application of simple circulation contours to obtain lift in regions of a wing with highly three-dimensional flow.

Within the trailing vortex, the vertical velocity can reach 110% of free stream and the streamwise velocity can reach 50% of free stream when the vortex is close to the wing. Given the small size of the vortex core, the rotational speed can be as high as 44,000 rpm. In

all cases, the peak values of velocity diminish with downstream distance from the wing. The streamwise velocity within the viscous wake that is shed from the wing is not uniform; instead, islands of peak velocity occur in the spiraling sheet that feeds into the trailing vortex. Near the wing the trailing vortex appears to be asymmetric (both components), and it has definite zones where the streamwise velocity both exceeds and falls behind the free-stream value. As the trailing vortex moves downstream, a streamwise deficit condition generally prevails at low α and an excess condition prevails at high α (except when the boundary layer is tripped and when the opposing image plane is brought close to the wing tip). When referenced to the free-stream velocity, the maximum vertical velocity of the vortex is directly dependent on α (almost linearly) and is independent of Re.

The center of the vortex leaves the wing with an inboard displacement from the tip equal to about 5% of the wing chord, and a vertical displacement that depends on α. Tracing the downstream path of the vortex shows a continuing inboard movement of the core that can be as large as 20% of the wing chord in the spanwise direction. Increasing the aspect ratio is similar to decreasing the distance to the image plane (opposite the wing tip), in that both result in a spanwise decrease and a vertical increase in the displacement of the path of the trailing vortex. The round-lateral edge does not cause any permanent change to the vortex. At a distance of 4 chords downstream from the wing, the round- and square-tip velocity profiles are quite similar and even the path of the trailing vortex from the round tip adjusts to match that of the square-tip wing. The boundary-layer trip had the largest effect on the downstream diameter of the vortex core (causing a 30% increase), but in general the diameter at $x/c = 4$ was about 65% of the wing thickness (or 10% of the wing chord).

APPENDIX

WALL CORRECTIONS

Solid and Wake Blockage

When measurements are obtained on a lifting airfoil in a flow that is confined by wind tunnel walls, certain aerodynamic quantities (such as the pressure and lift coefficients) are altered from their free-air values because of blockage and a distortion of the streamlines. In a closed test section, blockage has the effect of producing a more dense flow and a higher velocity in the region where the airfoil is located. These increases are due to a streamwise continuity adjustment that can be modeled by an infinite array of airfoil images located beyond the actual tunnel walls. A change in streamline curvature (caused by these airfoil images) has the effect of imparting greater "apparent" camber to the airfoil (ref. 46) and inducing a higher angle of attack (or an increase in the effective airfoil incidence).

In the present experiment, the lift coefficient is ultimately derived from the measured pressure distribution on the surface of the airfoil. Considering pressure first, the nondimensional pressure coefficients are based on the "free-stream" static and dynamic pressures that are obtained from a pitot-static probe placed upstream in the test section. To emphasize that these reference pressures will be different from the local tunnel values because of density and velocity changes arising from blockage effects, the corrected pressure coefficient is stated as

$$C_p = \frac{p - (p_{\infty u} + \Delta p_\infty)}{q_{\infty u} + \Delta q_\infty} \qquad \text{(A-1)}$$

where the subscript u denotes an uncorrected value and the symbol Δ stands for the difference between corrected and uncorrected values. Letting ϵ represent the total correction factor accounting for both solid and wake blockage, the corrected free-stream velocity becomes

$$V_\infty = (1 + \epsilon) V_{\infty u} \qquad \text{(A-2)}$$

In other words, $V_{\infty u}$ is the "free-stream" velocity at an upstream location that is not influenced by the airfoil (measured with an upstream pitot-static probe), while V_∞ is a corrected value that is more representative of the constricted flow in the test section where the airfoil is actually positioned. If the flow is incompressible (thereby justifying $p_\infty + q_\infty$ = constant), and use is made of the approximation $(1+\epsilon)^{-2} \approx (1 - 2\epsilon)$, then the corrected pressure coefficient from equation (A-1) becomes:

$$C_p = C_{pu}(1 - 2\epsilon) + 2\epsilon \qquad \text{(incompressible)} \quad \text{(A-3)}$$

where C_{pu} is the pressure coefficient that would be formed using upstream reference pressures ($p_{\infty u}$ and $q_{\infty u}$), without regard for blockage effects. To illustrate the impact of blockage on the measured pressure distribution, results from the present experiment are compared with blockage-adjusted values (fig. 71) under the arbitrary assumption that $\epsilon = 0.05$ (corresponding to a 5% increase in free-stream velocity). To more directly reflect the change that is observed in the pressure distribution, equation (A3) is rearranged to read

$$\Delta C_p = 2\epsilon(1 - C_{pu}) \qquad \text{(incompressible)} \quad \text{(A-4)}$$

This arrangement makes clear (for incompressible flows) that no change in the pressure coefficient occurs at the stagnation point (where $C_{pu} = 1$), and since elsewhere $C_{pu} < 1$ always, the resulting change is everywhere positive; that is, C_p always becomes more positive, if it changes at all, as a result of blockage in a closed test section. Integrating the pressure distribution over the airfoil surface yields a vector from which the lift coefficient can be obtained (if the viscous component is neglected). Comparing the uncorrected with the blockage-corrected value of the lift shows that for the example case of 5% blockage, an 11% decrease in C_l results (fig. 71). The lift coefficient will decrease even more once the correction for streamline curvature is included.

Considering now the more general compressible flow case, the corrections explicitly feature the Mach number and can be summarized (ref. 47) as

$$\Delta Re = \epsilon Re_u \qquad \text{(A-5)}$$

$$\Delta q_\infty = \epsilon\left(2 - M^2_{\infty u}\right) q_{\infty u} \qquad \text{(A-6)}$$

$$\Delta M_\infty = \epsilon\left(1 + 0.2 M^2_{\infty u}\right) M_{\infty u} \qquad \text{(A-7)}$$

$$\Delta C_p = \epsilon\left(2 - [2 - M^2_{\infty u}] C_{pu}\right) \qquad \text{(A-8)}$$

The above relations governing the corrections to Re, q_∞, M_∞, and C_p are assumed to apply to both 2D

and 3D configurations. Next comes the more difficult task of specifying a value for the blockage factor, ϵ, that appears in each of these relations. Numerous formulations have been rigorously developed for cases where the object causing the blockage can be simply described and imaged with potential-flow equations. However, models and supports are often complicated, and in such cases a rough approximation for the blockage factor (applicable to either 2D or 3D configurations) based on a simple area reduction in the test section may have to suffice (ref. 46):

$$\epsilon = \kappa \frac{\text{object frontal area}}{\text{test section area}} \qquad \text{(A-9)}$$

The coefficient $\kappa = \frac{1}{4}$ is appropriate when the airfoil for which the aerodynamic quantities are to be corrected is itself responsible for the blockage. The effect of blockage on elements that are located away from a given blocking object will be greater, and therefore a much larger value than $\frac{1}{4}$ may be more suitable. The frontal projection for the NACA 0015 airfoil at various angles of incidence is shown in figure 72.

2D Blockage Factor

If the flow is considered to be two dimensional and incompressible, then the solid and wake contributions to the total blockage for a symmetrical airfoil (ref. 46) become

$$\epsilon = \epsilon_{solid} + \epsilon_{wake} \qquad \text{(A-10)}$$

$$\epsilon = \frac{\pi^2}{22.6}\left(1 + 0.8\frac{c}{t}\right)\left(\frac{t}{h}\right)^2 + \frac{c}{4h}C_{du} \qquad \text{(A-11)}$$

In the more general case, compressible effects may be present and the blockage-producing object may also be off center in the test section as well as at some angle of incidence to the oncoming flow. For these conditions the blockage factor (ref. 47) becomes

$$\epsilon = \delta\eta\epsilon_{solid} + \epsilon_{wake} \qquad \text{(A-12)}$$

$$\epsilon = \delta\eta\frac{\pi}{6}\left(1 + 1.2\beta\frac{t}{c}\right)\frac{A_a}{\beta^3 h^2} + \frac{c}{4h\beta^2} \times \left(1 + 0.4M_{\infty u}^2\right)C_{du} \qquad \text{(A-13)}$$

where $\delta \geq 1$ and is introduced to account for objects that are offset from the centerline of the test section (fig. 73):

$$\delta = \left(1 + \frac{3}{4}\cot^2\frac{\pi d}{h}\right) \qquad \text{(A-14)}$$

and η accounts for the increase in blockage due to angle of incidence:

$$\eta = \left(1 + 1.1\beta\frac{c}{t}\alpha^2\right) \qquad \text{(A-15)}$$

The symbol A_a represents the cross-sectional area of the airfoil (fig. 74), and β is a compressibility factor:

$$\beta = \left(1 - M_{\infty u}^2\right)^{1/2} \qquad \text{(A-16)}$$

The uncorrected drag coefficient C_{du}, which consists of both pressure and viscous contributions, was not measured in this experiment. However, an estimate for the drag should be sufficient for determining the blockage, so it was taken from data already published (fig. 75, based on ref. 48). For the airfoil used to measure pressure in the present experiment, with no offset, $\alpha = 10°$, and $M_{\infty u} = 0.3$, the predicted blockage factor as calculated from equation (A-13) is $\epsilon = 0.0065$.

The above relations have been derived for somewhat ideal configurations. The actual "2D" setup in this experiment (fig. 76) consisted of an airfoil supported between two endplates that were not centered in the test section. In addition, a large fairing was attached to the wall side of one of the endplates to cover the pressure tubes that extended from the airfoil. Clearly some approximations will be necessary.

If the blockage factor due to the endplates is to be roughly estimated by equation (A-9), then the coefficient should be increased (say, to unity) since the midspan of the airfoil will be in the far field relative to each endplate. A better treatment of each endplate and its respective offset can be given with equation (A-13). In this case, the endplate (with leading- and trailing-edge fairings) is assumed to be a long ellipse at $\alpha = 0°$ with an estimated drag coefficient of 0.011 (ref. 49). In addition, w will need to be substituted for h in equations (A-13) and (A-14) because the endplates span the vertical dimension of the tunnel.

To illustrate the magnitudes of the blockage factors predicted for the airfoil and its various supports, results using the different methods that have been discussed are shown in figure 77. It can be seen that the airfoil contributes a comparatively modest amount of blockage, whereas the endplates account for about 70% of the blockage. The "approximate" estimates for the endplates are based simply on the projected frontal area of each endplate relative to the cross-sectional area of the test section. Because the endplates have a much greater blockage effect on the flow around the airfoil

than the airfoil has on itself, blockage estimates using equation (A-9) should be made with $\kappa = 1$ for each endplate and $\kappa = \frac{1}{4}$ for the airfoil. No consideration is given to where each endplate is placed in the test section, and therefore both endplates are assigned the same blockage factor. However, using equation (A-13) to calculate the blockage factors for the endplates shows that the support endplate produces a significantly higher blockage than the image endplate because of its close proximity to the tunnel wall. Since equation (A-14) is not recommended for objects that are offset much over 10% from the centerline of the test section (ref. 47), the blockage value for the support endplate is expected to be excessive. Taking this into consideration, the approximations obtained using equation (A-9) appear to be in good agreement with those obtained from the more rigorous approach based on equation (A-13).

3D Blockage Factor

When the body is three dimensional, a doubly infinite system of images is needed to specify the blockage factor. Assuming that the airfoil is not offset from the center of the test section, the solid and wake blockage factor (ref. 47) is

$$\epsilon = \eta\lambda\frac{A_a s}{4\pi h^3\beta^3}\left(1 + 1.2\beta\frac{t}{c}\right) + \frac{A_p}{4bh\beta^2} \times \left(1 + 0.4M_{\infty u}^2\right) C_{d0u} \qquad \text{(A-17)}$$

where A_p is the planform area of the wing ($A_p = cs$ for a rectangular wing), C_{d0u} is the uncorrected drag coefficient at zero lift, and the test-section shape parameter λ is given by (ref. 50, with σ replaced by λ)

$$\lambda = \sum_{m=-\infty}^{\infty}\sum_{n=-\infty}^{\infty}\frac{2m}{\xi_1\xi_2}[(m+\frac{s}{b})\xi_2 + (m-\frac{s}{b})\xi_1]^{-1} + \sum_{n=-\infty}^{\infty} n^{-2}[n^2 + (\frac{s}{h})^2]^{-1/2} \qquad \text{(for } m \neq 0 \text{ and } n \neq 0\text{)} \qquad \text{(A-18)}$$

The terms ξ_1 and ξ_2 are introduced for convenience and are defined by

$$\begin{aligned} \xi_1 &= [n^2 + (m + \tfrac{s}{b})^2(\tfrac{b}{h})^2]^{1/2} \\ \xi_2 &= [n^2 + (m - \tfrac{s}{b})^2(\tfrac{b}{h})^2]^{1/2} \end{aligned} \qquad \text{(A-19)}$$

The indices in equation (A-18) range over all values except for those that define the physical location of the airfoil at $(m, n) = (0, 0)$. When the airfoil is supported off a side wall of the test section (half-span model), the blockage is assumed to be that for a full-span model (2s) in an imaginary test section (fig. 78) twice the actual width (b = 2w). These equations can be applied to compressible flows over a test-section size range of $0.3 < b/h < 3.5$ and a model span range of $0 < 2s/b < 1$ (ref. 47). Taking values from the present experiment, for a direct wall-mounted model with $b/h = 2.86$ and $2s/b = 0.56$, the test-section shape parameter becomes $\lambda = 2.78$ (this is equivalent to $\tau = 0.5\lambda(b/\pi h)^{1.5} = 1.2$, in ref. 50). For the airfoil in the present experiment, at $\alpha = 10°$ and $M_{\infty u} = 0.3$, the predicted blockage factor is $\epsilon = 0.0021$.

2D Lift Interference

Not only do the walls of a closed test section impose a choking effect on the flow, but they also cause the streamlines to be distorted around the lifting airfoil, and these distorted streamlines produce slightly different aerodynamic characteristics than would result in free air. In modeling the confining effect of the tunnel walls (vanishing normal velocity), the airfoil images induce a curvature in the flow that causes the lift as well as the angle of attack to be too high. In an incompressible flow around a thin airfoil with a short chord relative to the tunnel height, these quantities can be corrected (ref. 46) by

$$\Delta\alpha_{sc} = \frac{\sigma}{2\pi}(C_{lu} + 4C_{m_{\frac{1}{4}u}}) \text{ (incompressible)} \qquad \text{(A-20)}$$

$$\Delta C_{lsc} = -\sigma C_{lu} \qquad \text{(incompressible)} \qquad \text{(A-21)}$$

with the subscript "sc" denoting that the correction is for streamline curvature (the result of lift interference) only. The coefficient σ is defined as $\sigma \equiv \frac{1}{3}(\frac{\pi c}{4h})^2$.

For cases when compressibility and airfoil thickness and length are significant (especially when $c/h > 0.4\beta$), more accurate corrections to the angle of attack and lift (ref. 47) are given by

$$\Delta\alpha_{sc} = \frac{\pi\beta}{96}\left(\frac{c}{\beta h}\right)^2(1 + \beta(-C_0 + C_1 + C_2))C_{lu} - \frac{\pi^3\beta}{92160}\left(\frac{c}{\beta h}\right)^4(41 + \beta(79C_0 + 11C_1 + C_2 + 31C_3 + 42C_4))C_{lu} \qquad \text{(A-22)}$$

$$\Delta C_{lsc} = -\frac{\pi^2}{96}\left(\frac{c}{\beta h}\right)^2 (2 + \beta(14C_0 - 2C_1 - 5C_2))C_{lu} + \frac{\pi^4}{92160}\left(\frac{c}{\beta h}\right)^4 \times (210 + \beta(1004C_0 - 190C_1 - 96C_2 + 106C_3 - 69C_4))C_{lu} \quad \text{(A-23)}$$

where

$$C_0 = \frac{2}{\pi}\int_0^\pi \frac{\bar{z}}{c\sin\theta}d\theta$$

$$C_n = \frac{4}{\pi}\int_0^\pi \frac{\bar{z}\cos n\theta}{c\sin\theta}d\theta \qquad (n > 0) \quad \text{(A-24)}$$

$$\cos\theta = 1 - \frac{2x}{c}$$

The coefficients C_0 and C_n are defined above for the case of a symmetric airfoil, and $\bar{z}$ is the ordinate of the upper surface of the airfoil. For the present case of a NACA 0015 airfoil, the coefficients are

$$C_0 = \ \ 0.1205$$
$$C_1 = \ \ 0.0755$$
$$C_2 = -0.0211$$
$$C_3 = -0.0084$$
$$C_4 = -0.0181$$

Note that equations (A-22) and (A-23) reduce to equations (A-20) and (A-21) when (1) the flow is incompressible ($\beta = 1$); (2) $\bar{z}/c << 1$; (3) $c/h << 1$; and (4) the airfoil is approximated by a single vortex at the quarter chord. If the airfoil completely spans the center of the tunnel, and $C_{lu} = 1.0$, $M_{\infty u} = 0.3$, and $c/h = 0.24$, then the corrections predicted by equations (A-22) and (A-23) are $\Delta\alpha_{sc} = 0.11°$ and $\Delta C_{lsc} = -0.022$.

3D Lift Interference

The approach for determining the 3D lift interference for a wing is similar to that for a 2D model, except that now the image system is doubly infinite. Although the wing may actually be a half-span model that is mounted on a reflection plane in the test section (thereby allowing the use of a larger chord model to achieve a higher Reynolds number), the configuration is treated as though it were a full-span model in a rectangular test section that is double the breadth-to-height ratio (fig. 78). Even though the interference upwash causes an increase in the lift as well as a more forward inclination of the force vector, it has generally been found more convenient to apply the correction entirely to the angle of attack (refs. 46 and 51). This means that the angle of attack for closed-tunnel compressible-flow data will have to be decreased (refs. 47, 51, and 52) according to

$$\Delta\alpha_{sc} = \delta_E\left(1 + \frac{c\delta_1}{2\beta h\delta_0}\right)\frac{A_p}{A_t}C_{lu} \quad \text{(A-25)}$$

where A_t is the cross-sectional area of the tunnel ($A_t = bh$ for a rectangular tunnel, and b is twice the actual tunnel breadth for a half-span model), and other terms are defined as follows:

$$\delta_0 = \frac{\pi}{24}\frac{h}{b} + \pi\frac{h}{b}\sum_{n=1}^{\infty}\frac{n}{\exp(2\pi nh/b) + 1}$$

$$\delta_1 = \frac{\pi}{24} + \frac{1}{4\pi}\left(\frac{h}{b}\right)^2 \times \left(\sum_{n=1}^{\infty} n^{-3} + \sum_{n=1}^{\infty}(-1)^n S_1\{\frac{nh}{b}\}\right)$$

$$S_1\{\xi\} = \frac{2}{\xi^2} + \sum_{m=-\infty}^{+\infty}\frac{m^2 - 2\xi^2}{(m^2 + \xi^2)^{2.5}} \quad \text{(A-26)}$$

$$\delta_E = \frac{1}{2}\frac{h}{b}F\{\chi\} + 4\pi\frac{h}{b}\sum_{n=1}^{\infty}\frac{n}{\exp(2\pi nh/b) + 1} \times \left(\frac{J_1\{\pi n\chi\}}{\pi n\chi}\right)^2$$

$$F\{\chi\} = \frac{1}{2\pi}\sum_{n=0}^{\infty}\frac{(2n+1)!(2n+2)!}{n!(n+1)!(n+1)!(n+2)!} \times \left(\frac{\chi}{4}\right)^{2n}\sum_{p=1}^{\infty} p^{-2(n+1)}$$

where $\xi \equiv nh/b$, $\chi \equiv 2s/b$, and J_1 is a Bessel function of the first order. If it is assumed that the half-span pressure model in the present experiment ($c/h = 0.24$) is mounted directly on a side wall of the test section ($h/b = 0.35$ and $\chi = 0.56$) and that $M_{\infty u} = 0.3$ and $C_{lu} = 1.0$, then the complete lift-interference correction can be determined from equations (A-25) and (A-26) to be $\Delta\alpha_{sc} = 0.51°$.

In summary, the corrected V_∞ is determined from equation (A-2) and Re, q_∞, M_∞, and C_p are determined from equations (A-5)–(A-8), where it is assumed that the uncorrected free-stream temperature and velocity are measured upstream of the airfoil. These corrections all require a value for the blockage factor, which in the case of a single obstruction can either be estimated using equation (A-9) or calculated more precisely using either equation (A-13) in the 2D case or equation (A-17) in the 3D case. Some judgment is required in deciding which blockage equation best accounts for a particular obstruction in the test section. The total blockage factor will be equal to the sum of the individual factors that describe each of the flow disturbances. Finally, the integrated loads that are derived from the corrected surface pressure must be adjusted. Both α and C_l must be corrected according to equations (A-22) and (A-23) in the 2D case, whereas only α is corrected, according to equation (A-25), in the 3D case.

Ames Research Center
National Aeronautics and Space Administration
Moffett Field, CA 94035-1000, August 20, 1991

REFERENCES

1. Schmitz, F. H.; and Yu, Y. H.: Helicopter Impulsive Noise: Theoretical and Experimental Status. International Symposium on Recent Advances in Aerodynamics and Aeroacoustics, Stanford University, Stanford, California, 1983.
2. Caradonna, F. X.; Strawn, R. C.; and Bridgeman, J. O.: An Experimental and Computational Study of Rotor-Vortex Interactions. Fourteenth European Rotorcraft Forum, Milano, Italy, 1988.
3. Scheiman, J.; Megrail, J. L.; and Shivers, J. P.: Exploratory Investigation of Factors Affecting the Wing Tip Vortex. NASA TM X-2516, 1972.
4. Staufenbiel, R. W.: Structure of Lift-Generated Rolled-Up Vortices. J. Aircraft, vol. 21, no. 10, 1984, pp. 737-744.
5. Bliss, D. B.: Prediction of Tip Vortex Self-Induced Motion Parameters in Terms of Rotor Blade Loading. Proceedings of the American Helicopter Society, Arlington, Texas, 1987.
6. Srinivasan, G. R.; McCroskey, W. J.; Baeder, J. D.; and Edwards, T. A.: Numerical Simulation of Tip Vortices of Wings in Subsonic and Transonic Flows. AIAA/ASME 4th Fluid Mechanics, Plasma Dynamics and Lasers Conference, Atlanta, Georgia, 1986.
7. Tung, C.; Pucci, S. L.; Caradonna, F. X.; and Morse, H. A.: The Structure of Trailing Vortices Generated by Model Rotor Blades. Vertica, vol. 7, no. 1, 1983, pp. 33-43.
8. Spivey, R. F.: Blade Tip Aerodynamics - Profile and Planform Effects. 24th Annual National Forum Proceedings of the American Helicopter Society, Washington, D.C., 1968.
9. Thompson, D. H.: A Flow Visualisation Study of Tip Vortex Formation. Aeronautical Research Laboratories, Aerodynamics Note 421, Melbourne, Victoria, Australia, 1983.
10. Francis, M. S.; and Kennedy, D. A.: Formation of a Trailing Vortex. J. Aircraft, vol. 16, no. 3, 1979, pp. 148-154.
11. Bilanin, A. J.; and Donaldson, C. duP.: Estimation of Velocities and Roll-Up in Aircraft Vortex Wakes. J. Aircraft, vol. 12, no. 7, 1975, pp. 578-585.
12. Brown, C. E.: Aerodynamics of Wake Vortices. AIAA J., vol. 11, no. 4, 1973, pp. 531-536.
13. Hoerner, S. F.; and Borst, H. V.: Fluid-Dynamic Lift. Hoerner Fluid Dynamics, Brick Town, N.J., 1975.
14. El-Ramly, Z.; Rainbird, W. J.; and Earl, D. G.: Wind Tunnel Measurements of Rolling Moment in a Swept-Wing Vortex Wake. J. Aircraft, vol. 13, no. 12, 1976, pp. 962-967.
15. Jordan, P. F.: Structure of Betz Vortex Cores. J. Aircraft, vol. 10, no. 11, 1973, pp. 691-693.
16. Mason, W. H.; and Marchman III, J. F.: Far-Field Structure of Aircraft Wake Turbulence. J. Aircraft, vol. 10, no. 2, 1973, pp. 86-92.
17. Spreiter, J. R.; and Sacks, A. H.: The Rolling Up of the Trailing Vortex Sheet and Its Effect on the Downwash Behind Wings. J. Aeronautical Sciences, vol. 18, no. 1, 1951, pp. 21-32.
18. McCormick, B. W.; Tangler, J. L.; and Sherrieb, H. E.: Structure of Trailing Vortices. J. Aircraft, vol. 5, no. 3, 1968, pp. 260-267.
19. Lee, H.; and Schetz, J. A.: Computational and Experimental Study of Tip Vortices. AIAA Paper 83-1868, 1983.
20. Higuchi, H.; Quadrell, J. C.; and Farell, C.: Vortex Roll-Up for an Elliptically-Loaded Wing at Moderately Low Reynolds Numbers. AIAA Paper 86-0562. AIAA 24th Aerospace Sciences Meeting, 1986.
21. Freymuth, P.; Finaish, F.; and Bank, W.: Visualization of Wing Tip Vortices in Unsteady and Steady Wind. AIAA/ASME 4th Fluid Mechanics, Plasma Dynamics and Lasers Conference, 1986.
22. Ikohagi, T.; Higuchi, H.; and Arndt, R. E. A.: The Structure of Trailing Vortices. Advancement in Aerodynamics, Fluid Mechanics and Hydraulics, AIAA/ASME/ASCE Symposium, Univ. of Minnesota, 1986.
23. Corsiglia, V. R.; Schwind, R. G.; and Chigier, N. A.: Rapid Scanning, Three-Dimensional Hot-Wire Anemometer Surveys of Wing-Tip Vortices. J. Aircraft, vol. 10, no. 12, 1973, pp. 752-757.
24. Rorke, J. B.; and Moffitt, R. C.: Wind Tunnel Simulation of Full Scale Vortices. NASA CR-2180, 1973.
25. Iversen, J. D.: Correlation of Turbulent Trailing Vortex Decay Data. J. Aircraft, vol. 13, no. 5, 1976, pp. 338-342.
26. Betz, A.: Behavior of Vortex Systems. NACA TM-713, 1932.

27. Donaldson, C. duP.: A Brief Review of the Aircraft Trailing Vortex Problem. AFOSR Scientific Report, AFOSR-TR-71-1910, 1971.
28. Saffman, P. G.: Structure of Turbulent Line Vortices. Phys. Fluids, vol. 16, no. 8, 1973, pp. 1181-1188.
29. Dosanjh, D. S.; Gasparek, E. P.; and Eskinazi, S.: Decay of a Viscous Trailing Vortex. Aeron. Q., vol. 13, part 2, 1962, pp. 167-188.
30. Orloff, K. L.: Trailing Vortex Wind-Tunnel Diagnostics with a Laser Velocimeter. J. Aircraft, vol. 11, no. 8, 1974, pp. 477-482.
31. Roshko, A.: Pressure Distribution at the Nose of a Thin Lifting Airfoil. Douglas Aircraft Company Report No. SM-23368, 1958.
32. Chigier, N. A.; and Corsiglia, V. R.: Tip Vortices - Velocity Distributions. Presented at 27th Annual National V/STOL Forum of the American Helicopter Society, Preprint No. 522, 1971.
33. Gray, R. B.; McMahon, H. M.; Shenoy, K. R.; and Hammer, M. L.: Surface Pressure Measurements at Two Tips of a Model Helicopter Rotor in Hover. NASA CR-3281, 1980.
34. Shivananda, T. P.; McMahon, H. M.; and Gray, R. B.: Surface Pressure Measurements at the Tip of a Model Helicopter Rotor in Hover. J. Aircraft, vol. 15, no. 8, 1978, pp. 460-467.
35. Triebstein, H.: Unsteady Pressure Measurements in Rotor Blade Tips with Incidence in Incompressible Flow. European Space Agency, Technical Translation, ESA-TT-374 Revised, 1977.
36. Fage, A.; and Simmons, L. F. G.: An Investigation of the Air-Flow Pattern in the Wake of an Airfoil of Finite Span. Royal Society of London, Philosophical Transactions, Series A, vol. 225, 1925, pp. 303-330.
37. Spivey, W. A.; and Morehouse, G. G.: New Insights into the Design of Swept-Tip Rotor Blades. 26th Annual National Forum Proceedings of the American Helicopter Society, Washington, D.C., 1970.
38. Taylor, G. I.: Note on the Connection between the Lift on an Airfoil in a Wind and the Circulation Round it. Royal Society of London, Philosophical Transactions, Series A, vol. 225, 1925, pp. 238-245.
39. Hoffman, J. D.; and Velkoff, H. R.: Vortex Flow Over Helicopter Rotor Tips. J. Aircraft, vol. 8, no. 9, 1971, pp. 739-740.
40. Caradonna, F. X.; Laub, G. H.; and Tung, C.: An Experimental Investigation of the Parallel Blade-Vortex Interaction. NASA TM-86005, 1984.
41. Moore, D. W.; and Saffman, P. G.: Axial Flow in Laminar Trailing Vortices. Proceedings of the Royal Society of London, vol. 333, no. 1595, 1973, pp. 491-508.
42. Batchelor, G. K.: Axial Flow in Trailing Line Vortices. J. Fluid Mech., vol. 20, part 4, 1964, pp. 645-658.
43. Simons, I. A.; Pacifico, R. E.; and Jones, J. P.: The Movement, Structure and Breakdown of Trailing Vortices from a Rotor Blade. Aerodynamic Problems Associated with V/STOL Aircraft, Propeller and Rotor Aerodynamics, vol. 1, USAAVLABS Symposium Proceedings, 1966.
44. Chigier, N. A.; and Corsiglia, V. R.: Wind-Tunnel Studies of Wing Wake Turbulence. J. Aircraft, vol. 9, no. 12, 1972, pp. 820-825.
45. Thompson, D. H.: Experimental Study of Axial Flow in Wing Tip Vortices. J. Aircraft, vol. 12, no. 11, 1975, pp. 910-911.
46. Rae, W. H.; and Pope, A.: Low-Speed Wind Tunnel Testing. John Wiley & Sons, Inc., 1984.
47. Garner, H. C.; Rogers, E. W. E.; Acum, W. E. A.; and Maskell, E. C.: Subsonic Wind Tunnel Wall Corrections. AGARDograph 109, 1966.
48. Pope, A.: The Forces and Moments Over an NACA 0015 Airfoil. Aero Digest, vol. 58, no. 4, 1949, pp. 76-100.
49. Hoerner, S. F.: Fluid-Dynamic Drag. Hoerner Fluid Dynamics, 1965.
50. Herriot, J. G.: Blockage Corrections for Three-Dimensional-Flow Closed-Throat Wind Tunnels, with Consideration of the Effect of Compressibility. NACA Report 995, 1950.
51. Glauert, H.: Wind Tunnel Interference on Wings, Bodies and Airscrews. ARC R&M No. 1566, 1933.
52. Glauert, H.: Interference on Characteristics of Aerofoil in Wind Tunnel of Rectangular Section. ARC R&M No. 1459, 1932.

Table 1. Pressure distribution along span (2D configuration)

α	Re (nominal)				
	1×10^6	1.5×10^6	2×10^6	2.5×10^6	3×10^6
0°		●		●	
2°					
4°					
6°		●		●	
8°					
10°					
12°		●		●	
14°					

Table 2. Pressure-derived lift distribution along span (2D configuration)

α	Re (nominal)				
	1×10^6	1.5×10^6	2×10^6	2.5×10^6	3×10^6
0°		●		●	
2°		●		●	
4°		●		●	
6°		●		●	
8°		●		●	
10°		●		●	
12°		●		●	
14°		●		●	

Table 3. Pressure distribution over full wing span (square tip)

α	*Re* (nominal)				
	1×10^6	1.5×10^6	2×10^6	2.5×10^6	3×10^6
0°					
2°					
4°		●		●	
6°					
8°		●		●	
10°					
12°		●		●	
14°					

Table 4. Pressure-derived lift distribution along full wing span (square tip)

α	*Re* (nominal)				
	1×10^6	1.5×10^6	2×10^6	2.5×10^6	3×10^6
0°					
2°	●	●		●	
4°	●	●		●	
6°	●	●	●	●	●
8°	●	●	●	●	●
10°	●	●	●	●	●
12°	●	●	●	●	
14°	●	●	●	●	

Table 5. Pressure distribution over outer portion of wing
(square and round tips)

α	*Re* (nominal)				
	1×10^6	1.5×10^6	2×10^6	2.5×10^6	3×10^6
0°					
2°					
4°	●		●		●
6°					
8°	●		●		●
10°					
12°	●		●		●
14°					

Table 6. Pressure-derived lift distribution over outer portion of wing
(square and round tips)

α	*Re* (nominal)				
	1×10^6	1.5×10^6	2×10^6	2.5×10^6	3×10^6
0°					
2°					
4°	●	●	●	●	●
6°					
8°	●	●	●		●
10°					
12°	●	●	●	●	●
14°					

Table 7. Circulation measurements along wing span

Tip shape	α, deg					c, cm			$Re \times 10^{-6}$					AR		
	4	7	8	10	12	30	41	52	1.1	1.5	1.7	2.0	3.0	6.6	8.1	9.6
Square					●	●				●				●		
Round					●	●				●				●		
Square					●	●				●					●	
Round					●			●		●				●		

Table 8. Velocity measurements of wing-tip vortex (round tip)

α, deg					c, cm			$Re \times 10^{-6}$					AR			x/c							
4	7	8	10	12	30	41	52	1.1	1.5	1.7	2.0	3.0	6.6	8.1	9.6	.1	.2	.5	1	2	4	6	13
				●	●				●				●								●			
				●			●				●		●			●								*

*2D survey around vortex core also available.

Table 9. Velocity measurements of wing-tip vortex (square tip with boundary-layer trip and square tip with different image planes)

α, deg					c, cm			$Re \times 10^{-6}$					AR			x/c							
4	7	8	10	12	30	41	52	1.1	1.5	1.7	2.0	3.0	6.6	8.1	9.6	.1	.2	.5	1	2	4	6	13
				●	●				●				●								●		

Table 10. Velocity measurements of wing-tip vortex (square tip)

α, deg					c, cm			$Re \times 10^{-6}$					AR			x/c								
4	7	8	10	12	30	41	52	1.1	1.5	1.7	2.0	3.0	6.6	8.1	9.6	.1	.2	.5	1	2	4	6	13	
				●	●				●				●			●								*
				●	●				●				●						●					
				●	●				●				●							●				*
				●	●				●				●								●			
				●	●				●				●									●		
				●	●				●				●										●	
				●	●				●					●							●			
				●			●		●				●			●								*
				●			●		●				●				●							*
				●			●		●				●						●					*
				●			●		●				●							●				
				●			●		●				●								●			
				●			●		●				●									●		
				●			●		●				●										●	
		●					●		●				●			●								*
●							●		●				●			●								*
		●					●		●				●								●			
●							●		●				●								●			
●							●					●	●			●								*
	●						●			●			●			●								*
			●				●	●					●			●								*
●							●					●	●								●			
	●						●			●			●								●			
			●				●	●					●								●			
				●	●				●						●						●			
				●		●			●				●			●								*
				●		●			●				●									●		
				●	●				●					●		●								*
				●	●				●						●	●								*
				●			●				●		●			●								*

*2D survey around vortex core also available.

Table 11. Wing-tip vortex structure determinants

c	Re $(V_\infty c/\nu)$	Γ $(C_l V_\infty c/2)$	AR (s/c)	Method
CHANGE	fixed	fixed	fixed	$V_\infty c$ = constant
fixed	CHANGE	fixed	fixed	$C_l V_\infty$ = constant
fixed	fixed	CHANGE	fixed	vary α
fixed	fixed	fixed	CHANGE	add tip extensions

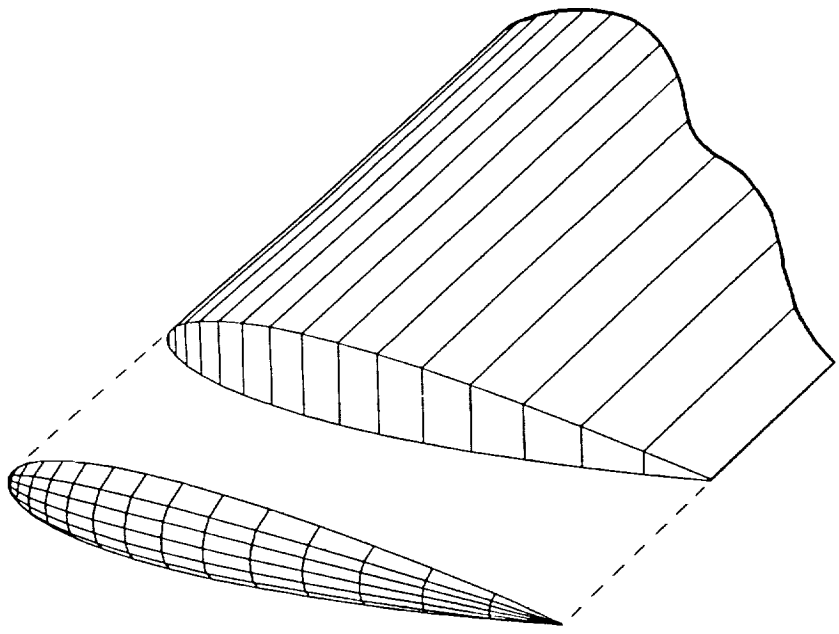

Figure 1. NACA 0015 wing with square tip, and end cap for forming round tip.

ORIGINAL PAGE
BLACK AND WHITE PHOTOGRAPH

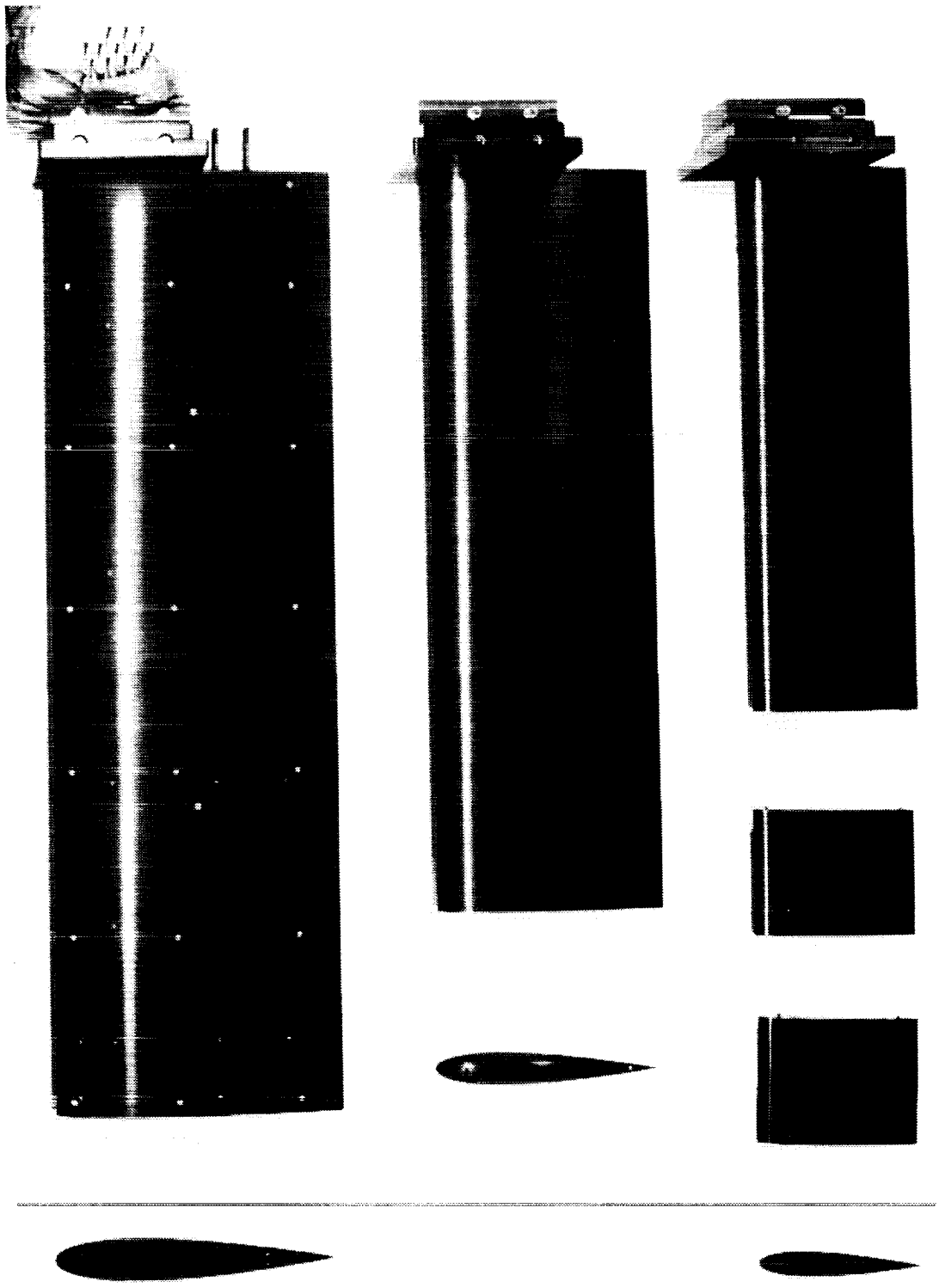

Figure 2. NACA 0015 wings with round end caps and extensions.

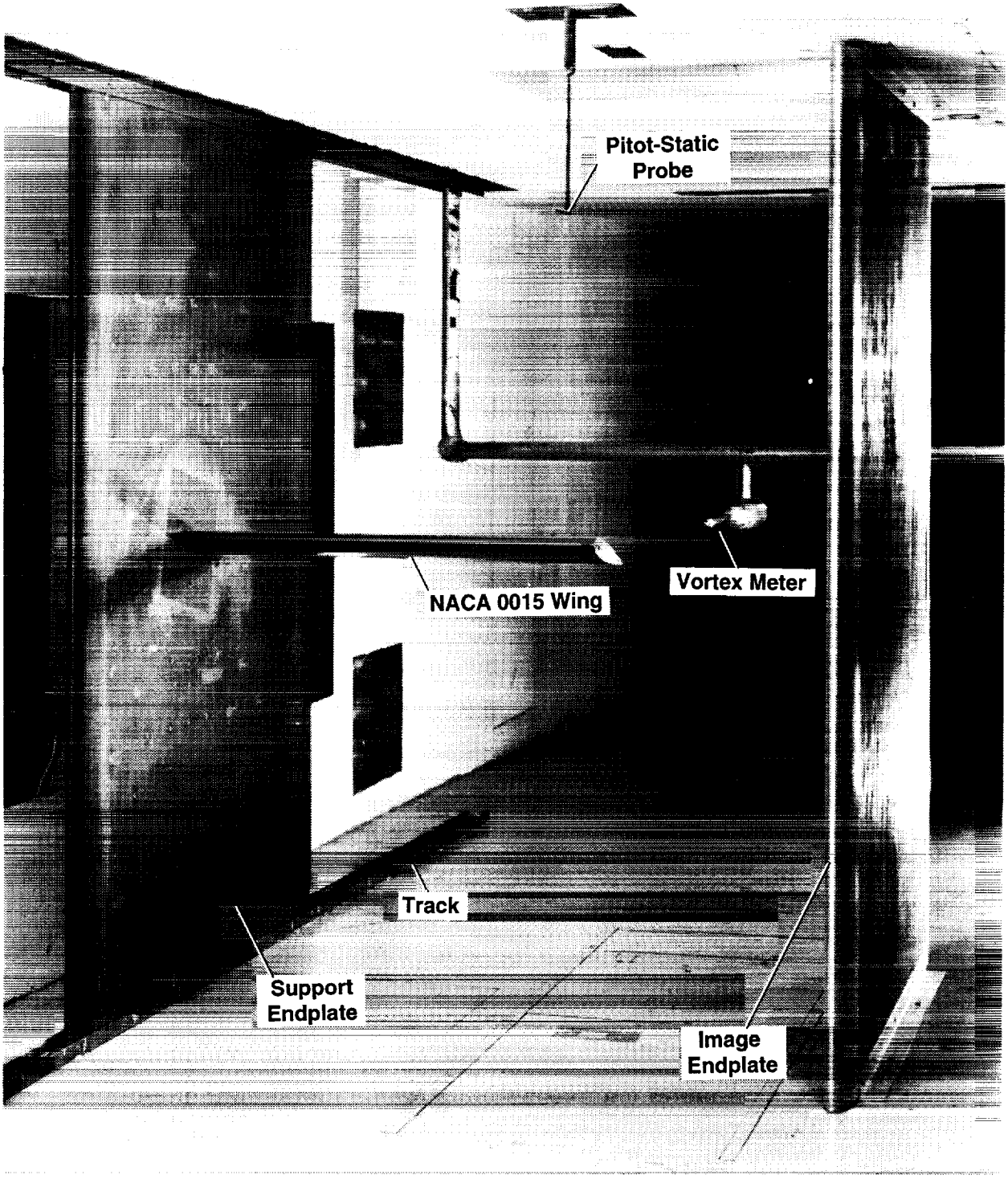

Figure 3. Installation of wing and endplates in the 7- by 10-foot wind tunnel.

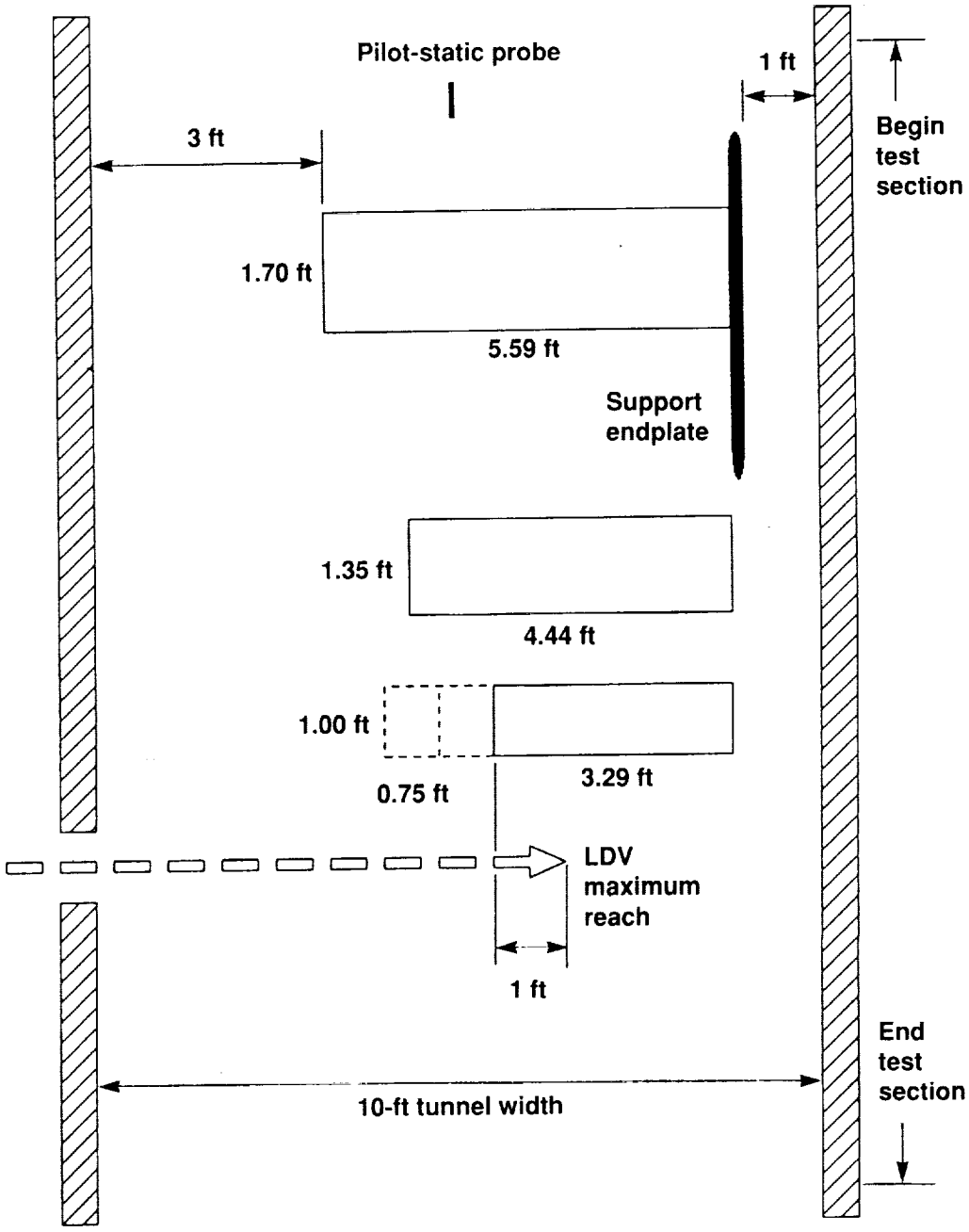

Figure 4. Plan view of test section showing relative sizes of wings tested.

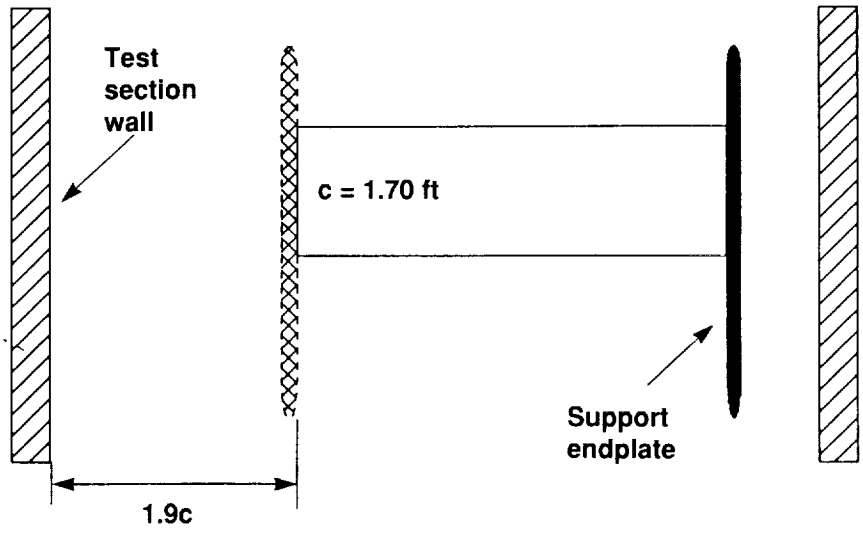

(a) Image endplate in 2D configuration

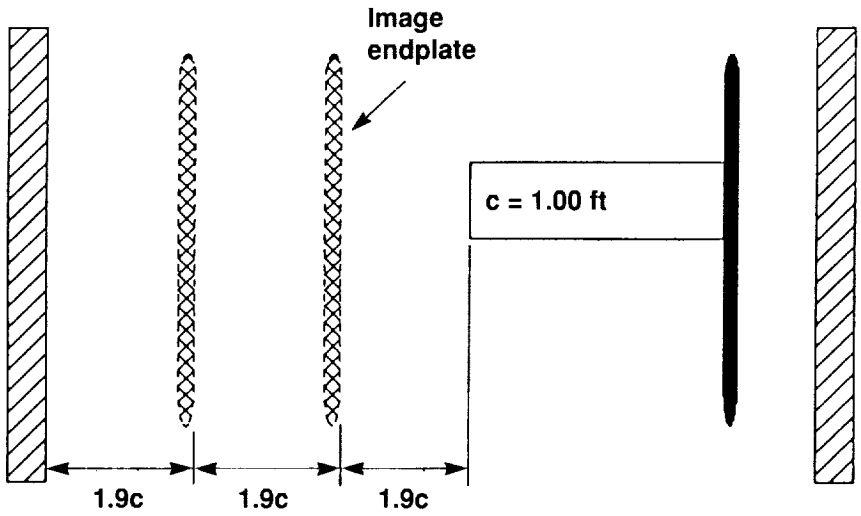

(b) Endplate positions in image-vortex study

Figure 5. Plan view of test section showing positions of the image endplate.

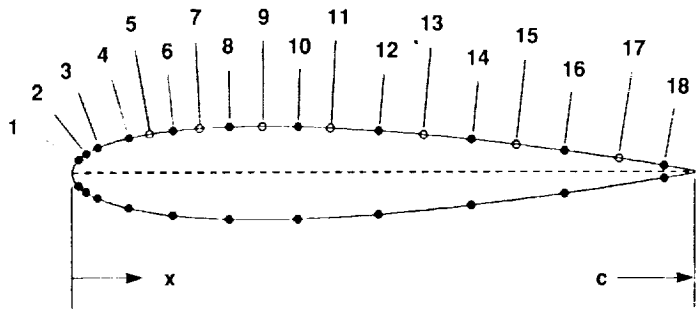

Chord locations		Span locations	
Station	x/c	Station	y/s
1	0.010	1	0.994
2	0.022	2*	0.984
3	0.040	3	0.974
4	0.090	4*	0.959
5*	0.123	5	0.944
6	0.160	6	0.899
7*	0.203	7	0.843
8	0.250	8	0.773
9*	0.303	9	0.692
10	0.360	10	0.597
11*	0.412	11	0.491
12	0.490	12	0.370
13*	0.563	13	0.238
14	0.640	14	0.094
15*	0.712		
16	0.790		
17*	0.877	*Upper surface only	
18	0.950		

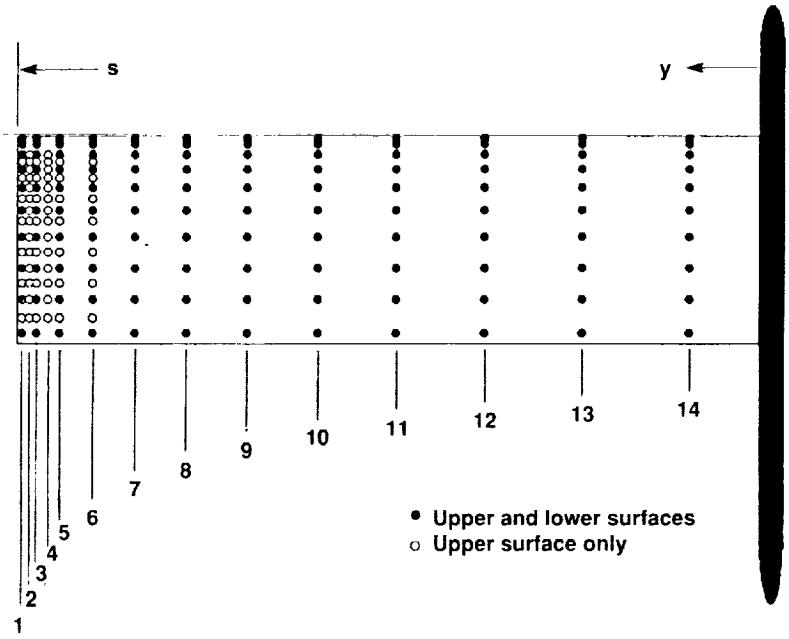

Figure 6. Pressure measurement locations.

ORIGINAL PAGE
BLACK AND WHITE PHOTOGRAPH

Figure 7. Laser velocimeter setup in 7- by 10-foot wind tunnel.

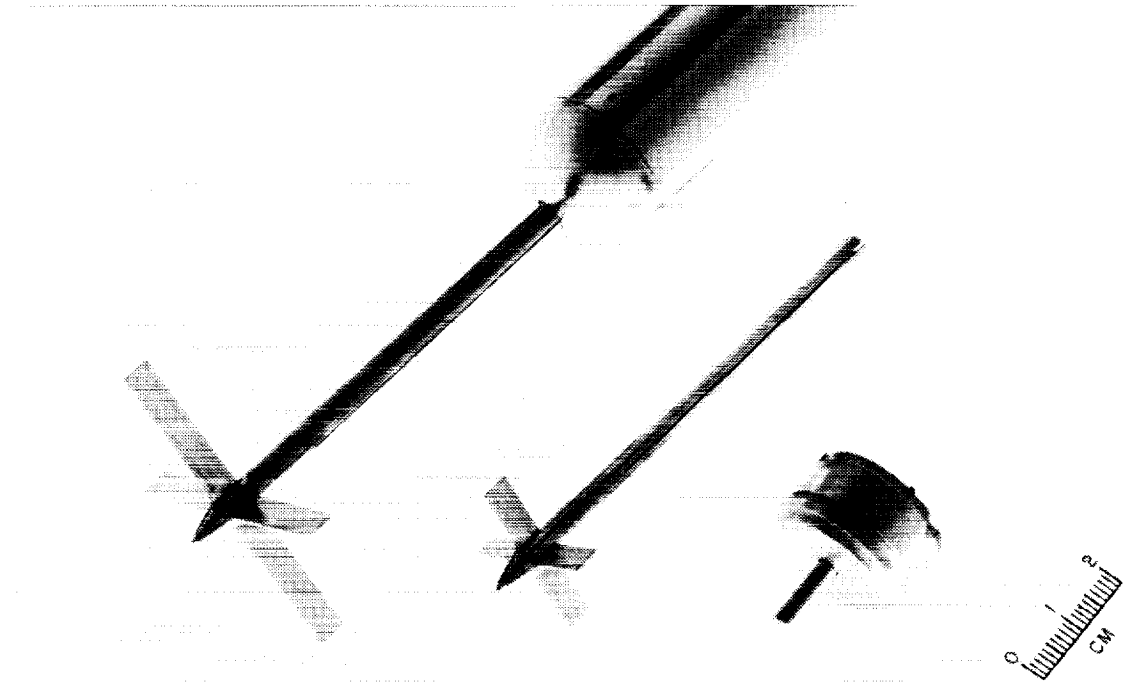

(a)

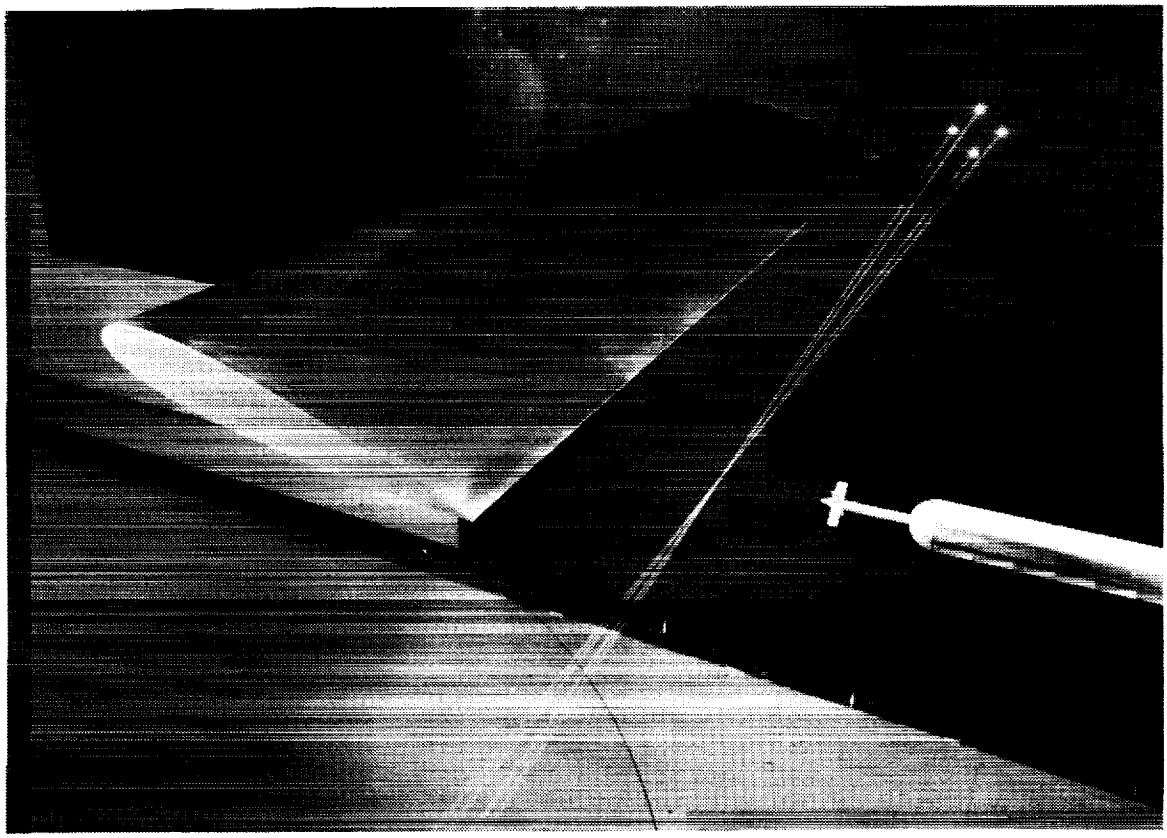

(b)

Figure 8. Vortex meter used to locate trailing-vortex core. (a) Cruciform and Hall-effect transducer elements of vortex meter. (b) Vortex meter positioned near wing tip.

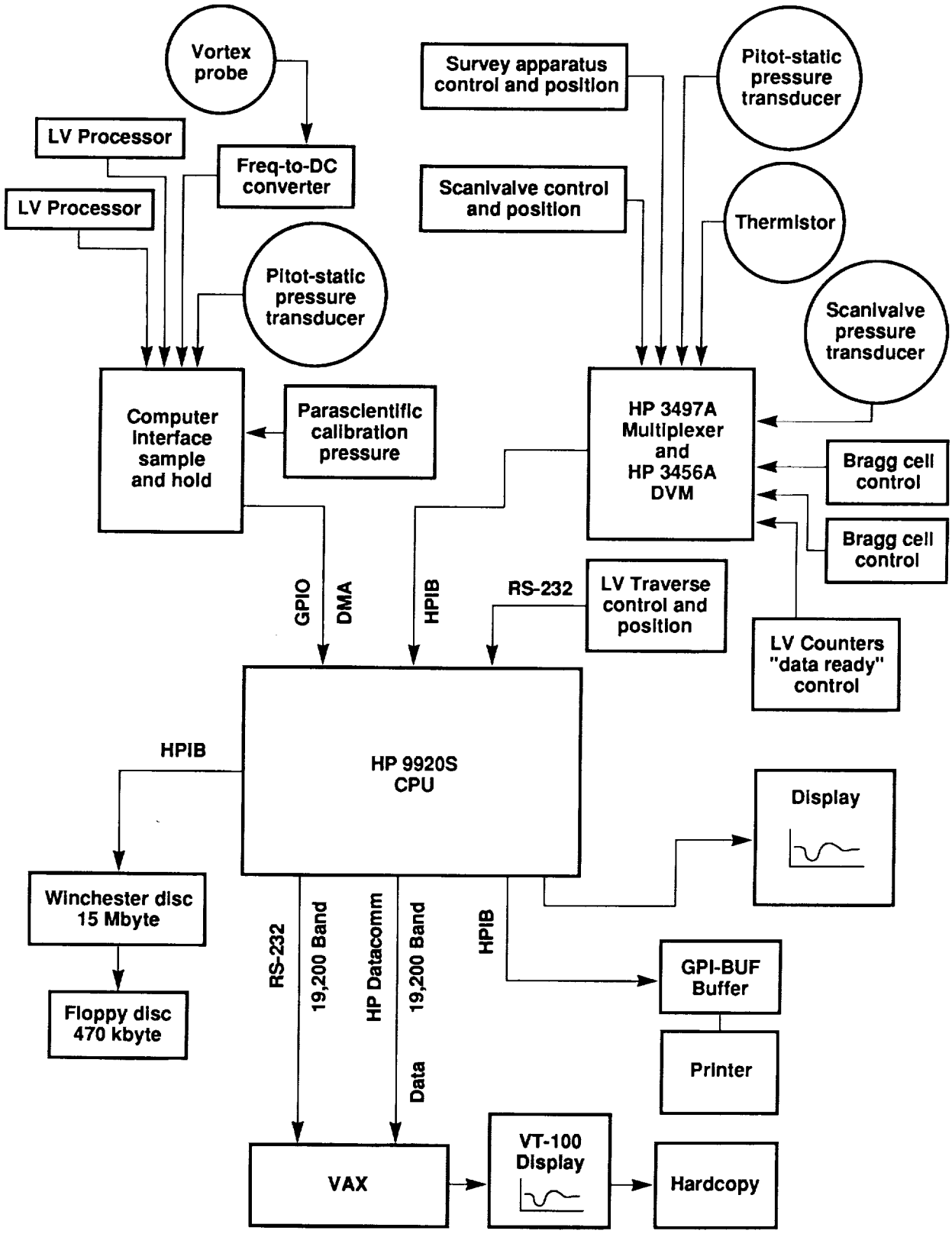

Figure 9. Network required for control, acquisition, and display of test data.

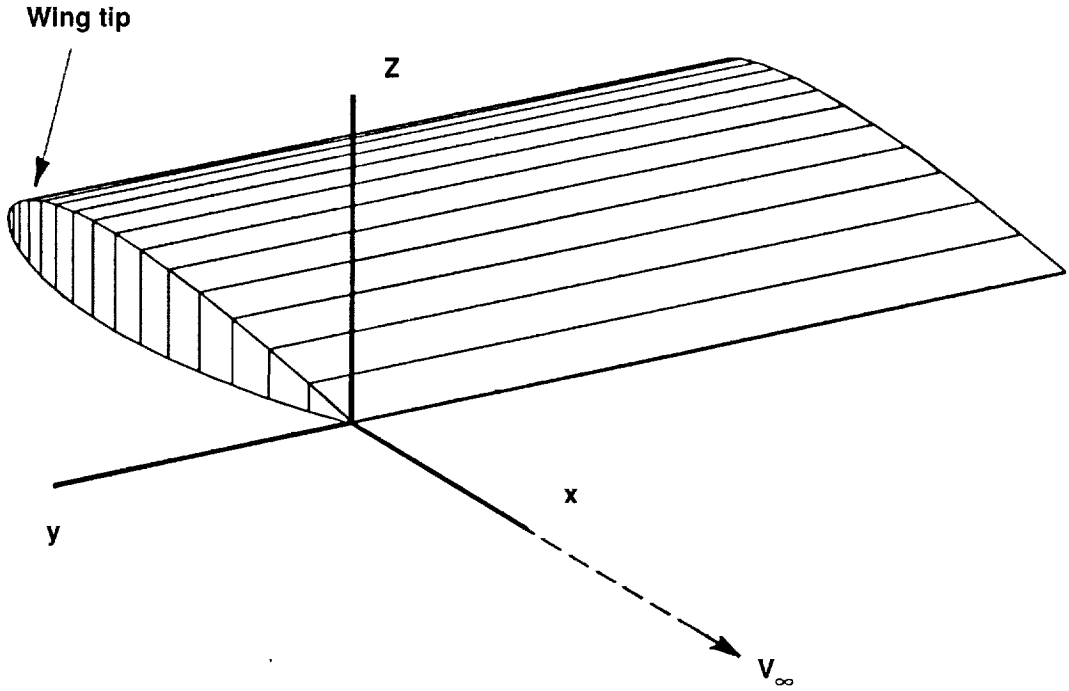

Figure 10. Coordinate system used for trailing-vortex measurements.

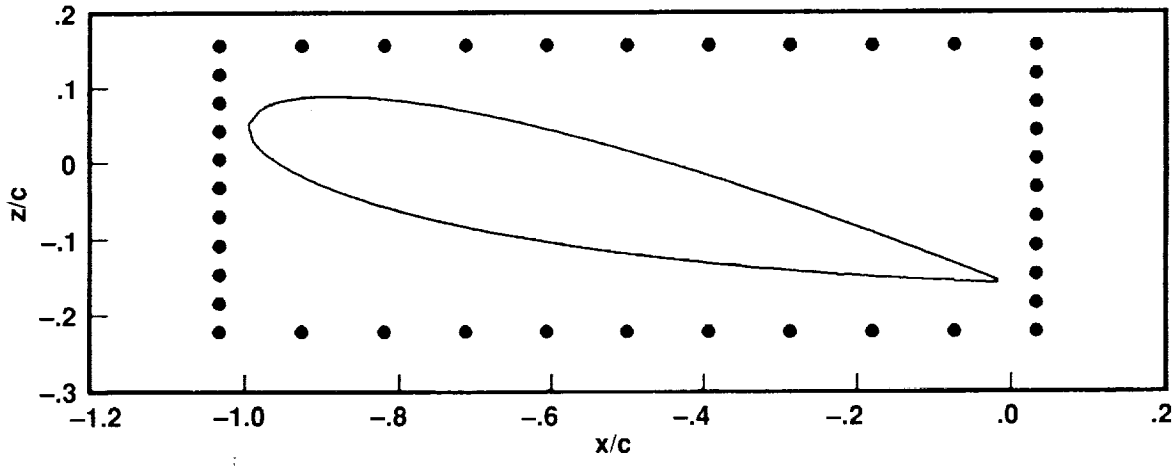

Figure 11. Measurement locations for determining wing circulation.

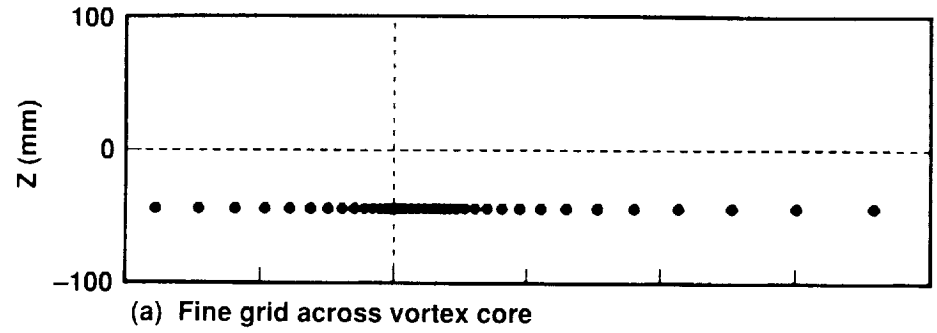

(a) Fine grid across vortex core

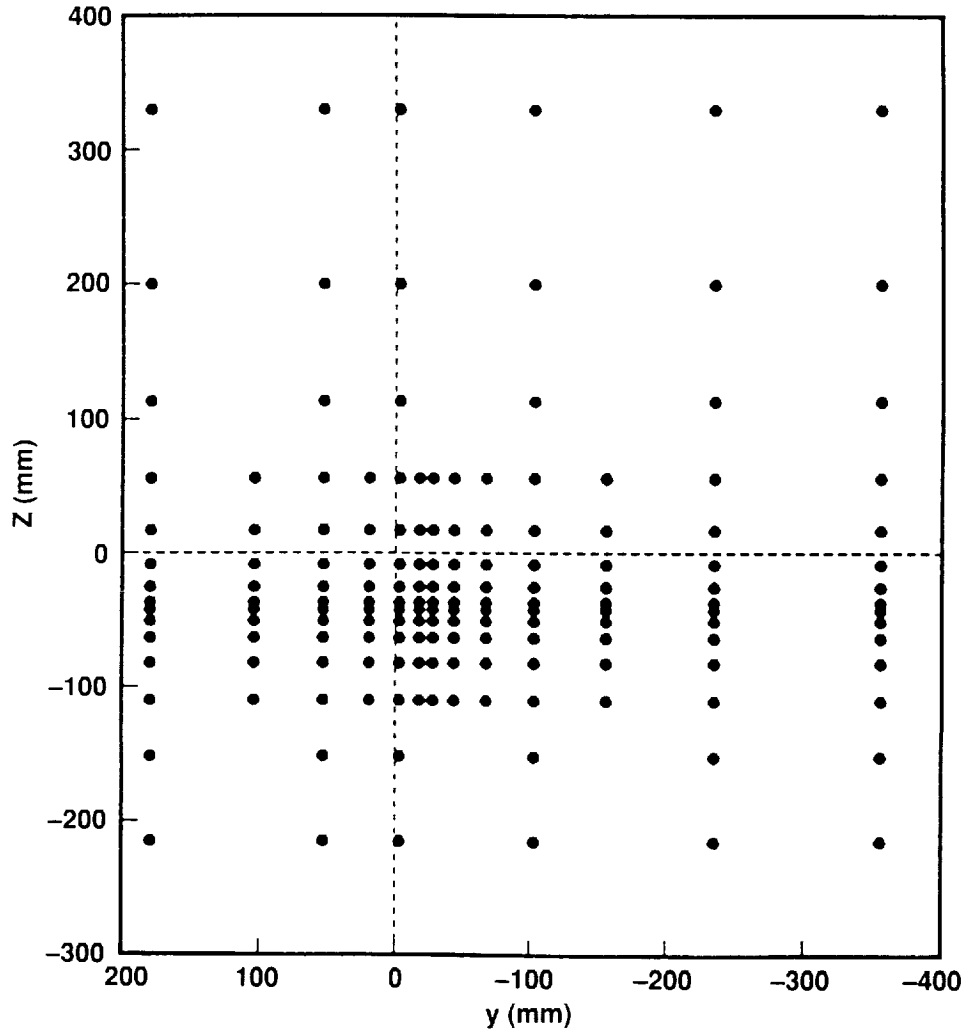

(b) Coarse grid around vortex core

Figure 12. Typical grids used to survey the trailing vortex.

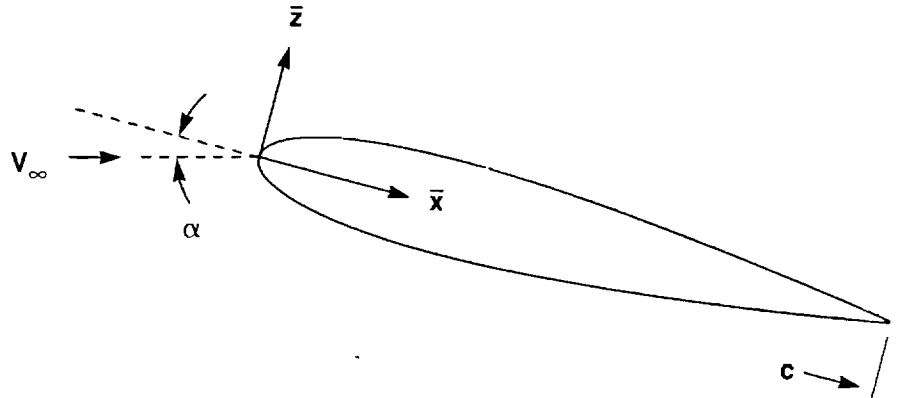

t/c = +0.1500
c_1 = +1.4845
c_2 = −0.6300
c_3 = −1.7580
c_4 = +1.4215
c_5 = −0.5075

$$\bar{z}/c = (t/c)\left(c_1\sqrt{\bar{x}/c} + c_2(\bar{x}/c) + c_3(\bar{x}/c)^2 + c_4(\bar{x}/c)^3 + c_5(\bar{x}/c)^4\right)$$

Figure 13. Coordinate system used for pressure measurements and equation for defining the NACA 0015 surface.

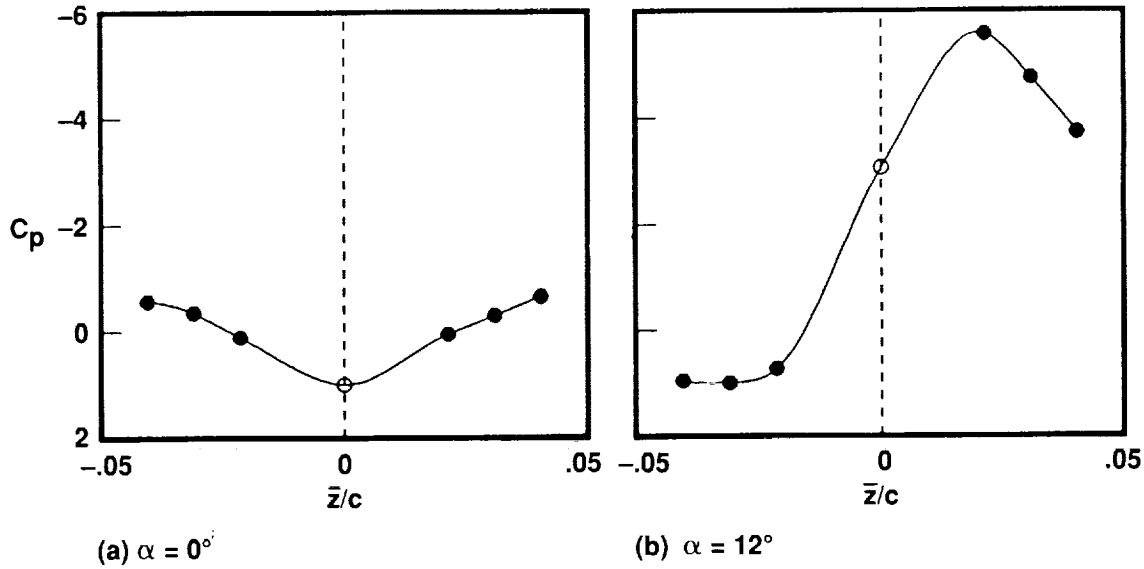

Figure 14. Example of approximation of leading-edge pressure from theory (ref. 31).

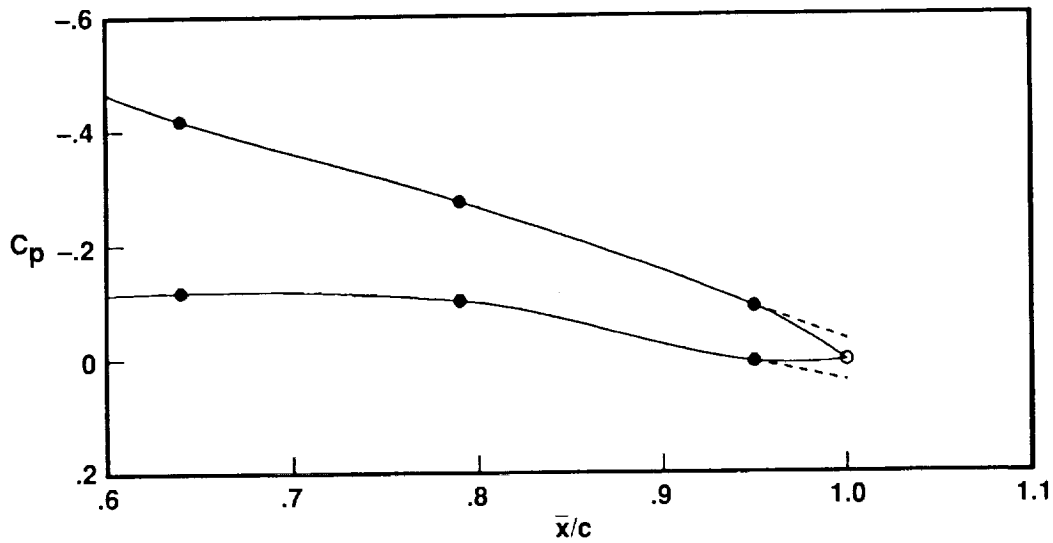

Figure 15. Example of approximation of trailing-edge pressure from linear extrapolations.

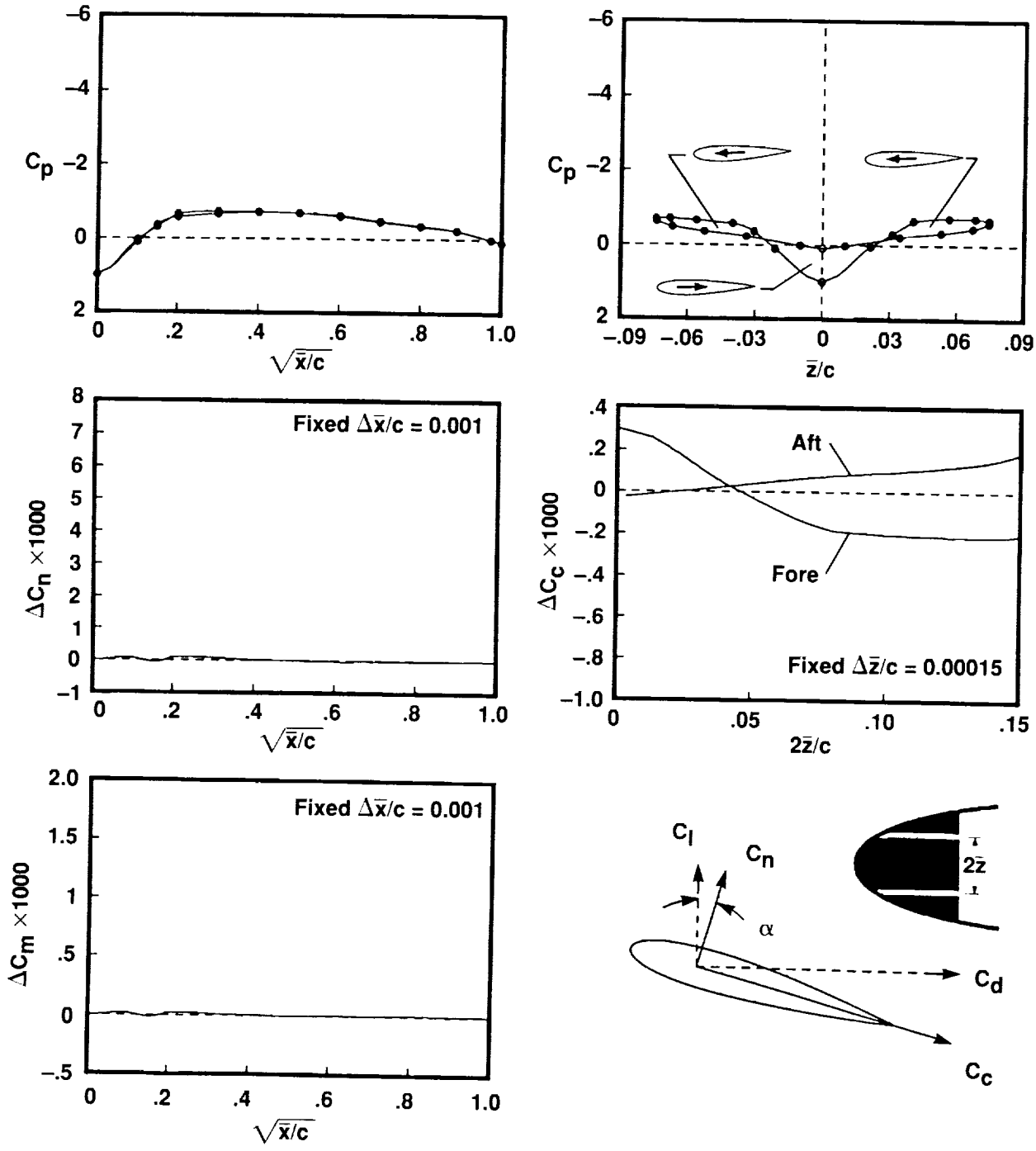

Figure 16. Example curve fit to pressure data and resulting local contributions to the force and moment integrals. Data taken from 2D configuration, span location #9, $Re = 2.5 \times 10^6$ and $\alpha = 0°$. The integrated loads are $C_n = 0.00$, $C_c = 0.00$, $C_l = 0.00$, $C_d = 0.00$ and $C_m = 0.00$.

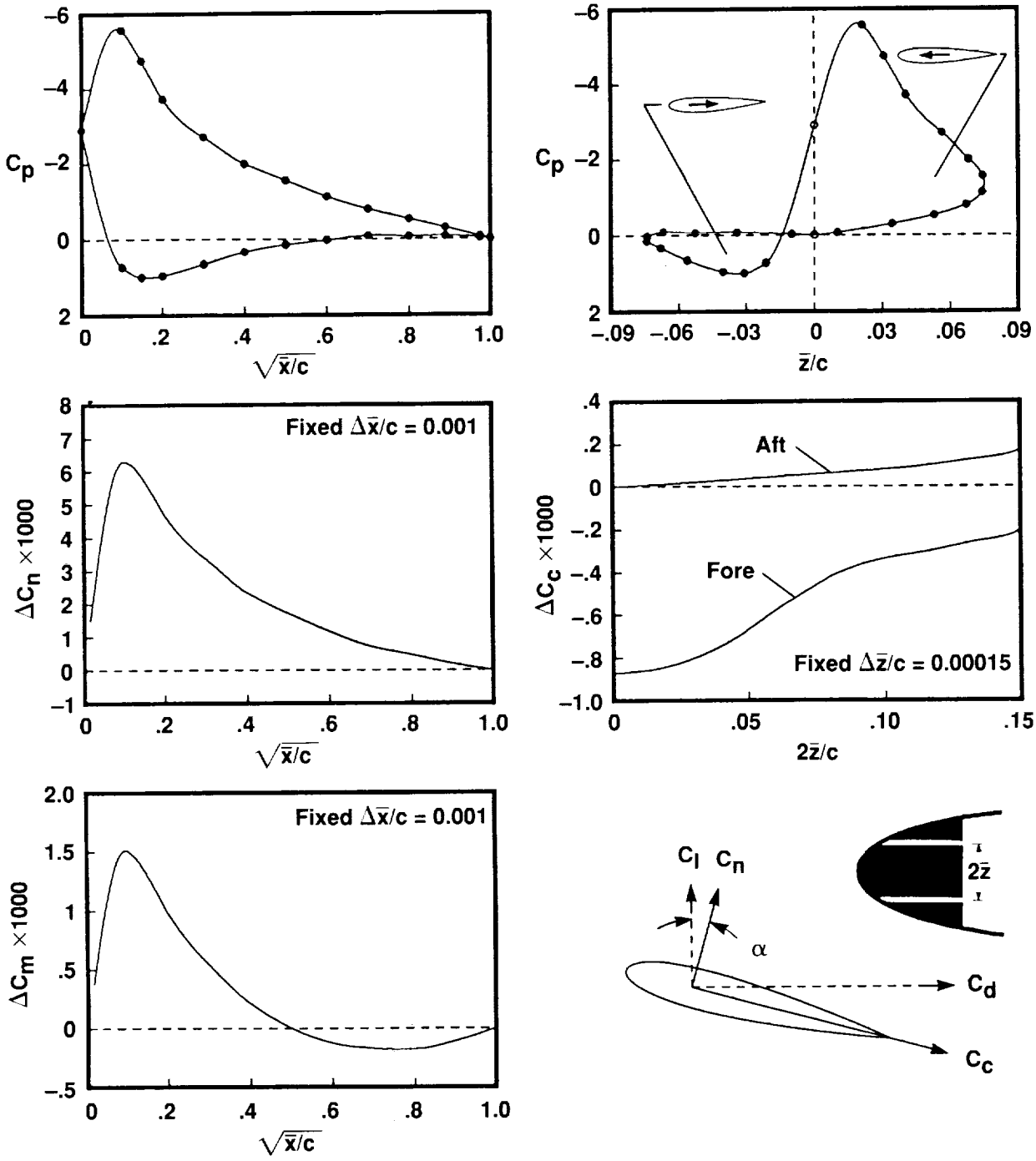

Figure 17. Example curve fit to pressure data and resulting local contributions to the force and moment integrals. Data taken from 2D configuration, span location #9, $Re = 2.5 \times 10^6$ and $\alpha = 12°$. The integrated loads are $C_n = 1.22$, $C_c = -0.23$, $C_l = 1.24$, $C_d = 0.03$ and $C_m = 0.03$.

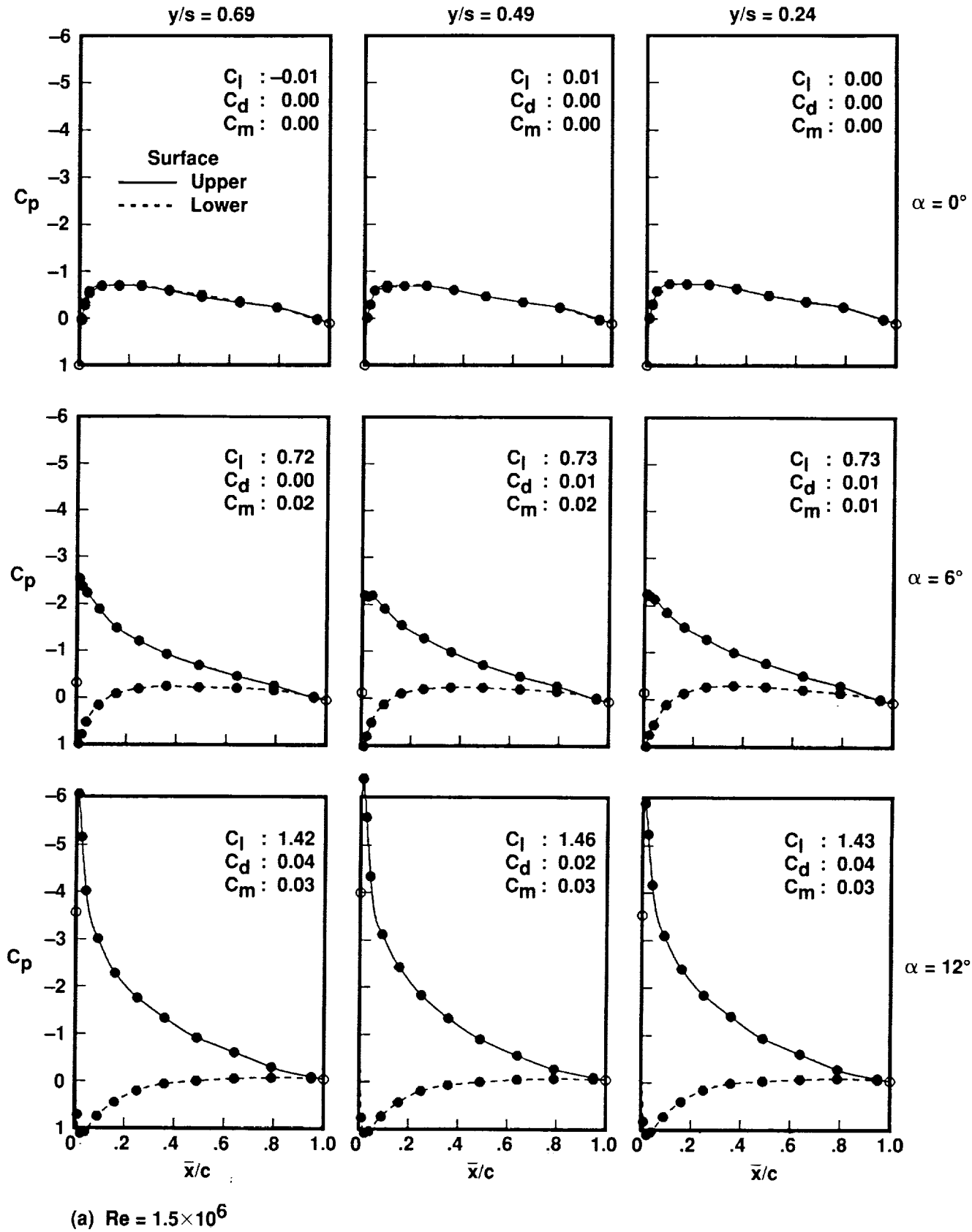

(a) Re = 1.5×10^6

Figure 18. Pressure distribution along span in 2D configuration.

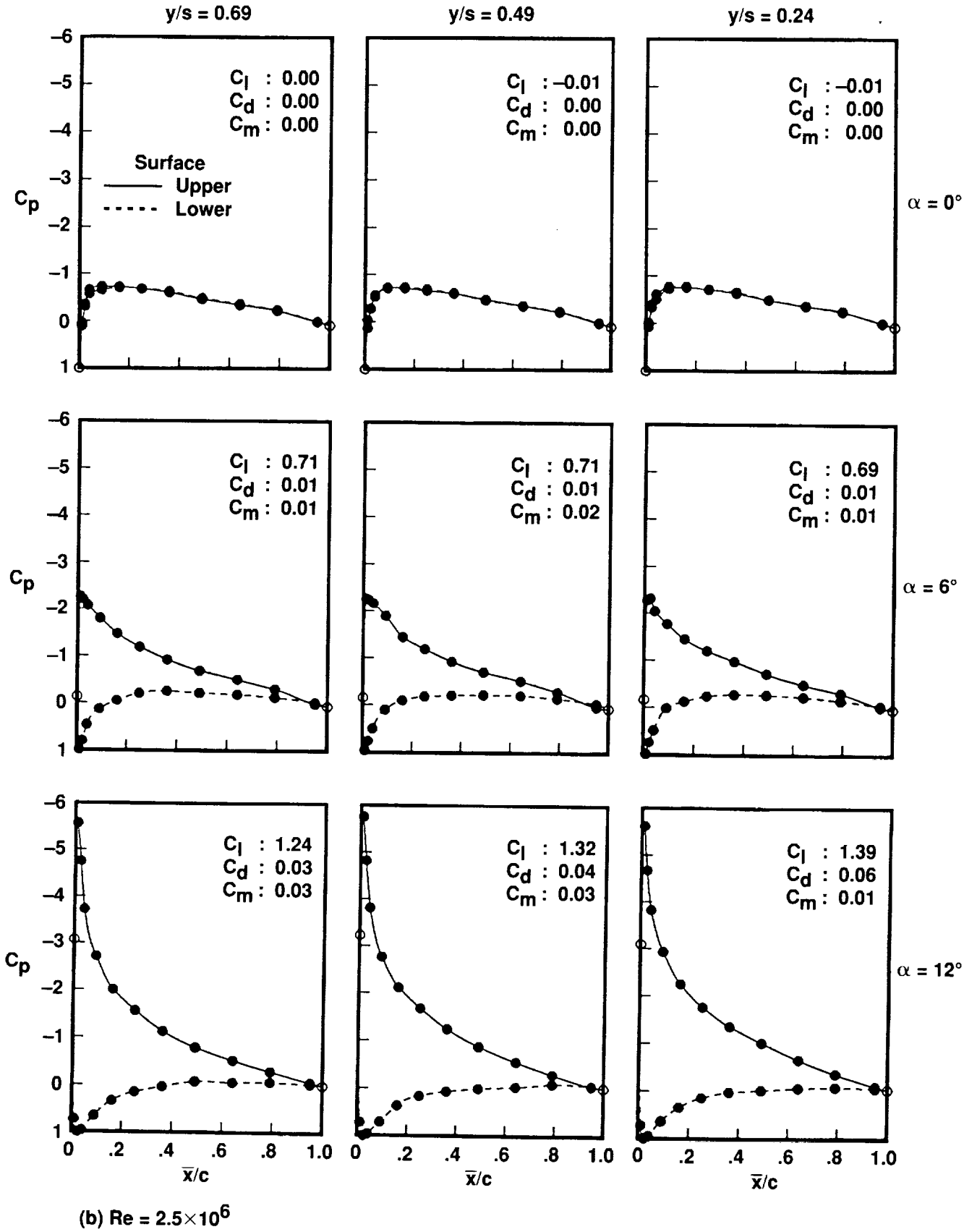

(b) Re = 2.5×10^6

Figure 18. Concluded.

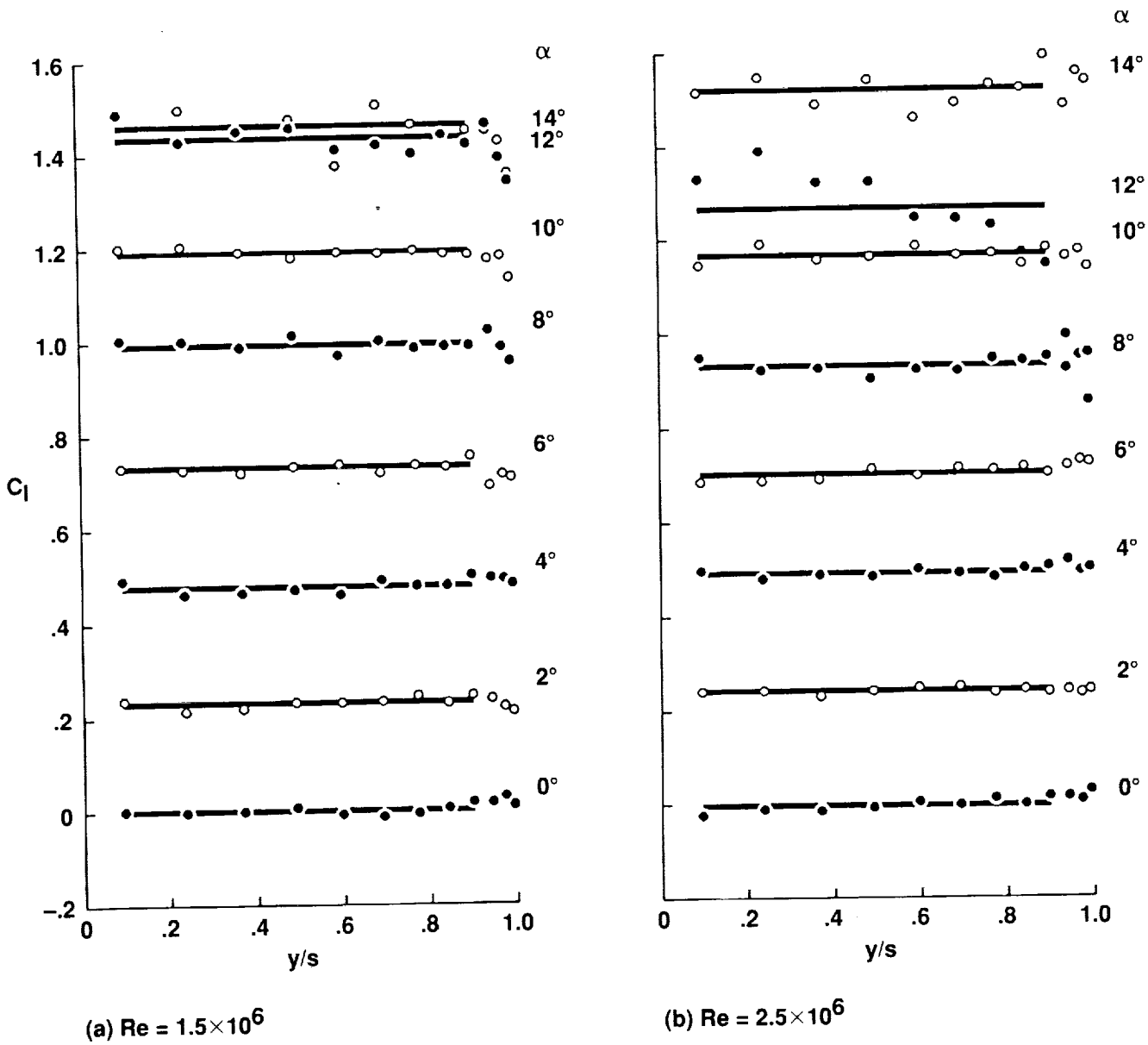

Figure 19. Pressure-derived lift distribution along span in 2D configuration (solid line represents average C_l over $0.09 < y/s < 0.90$).

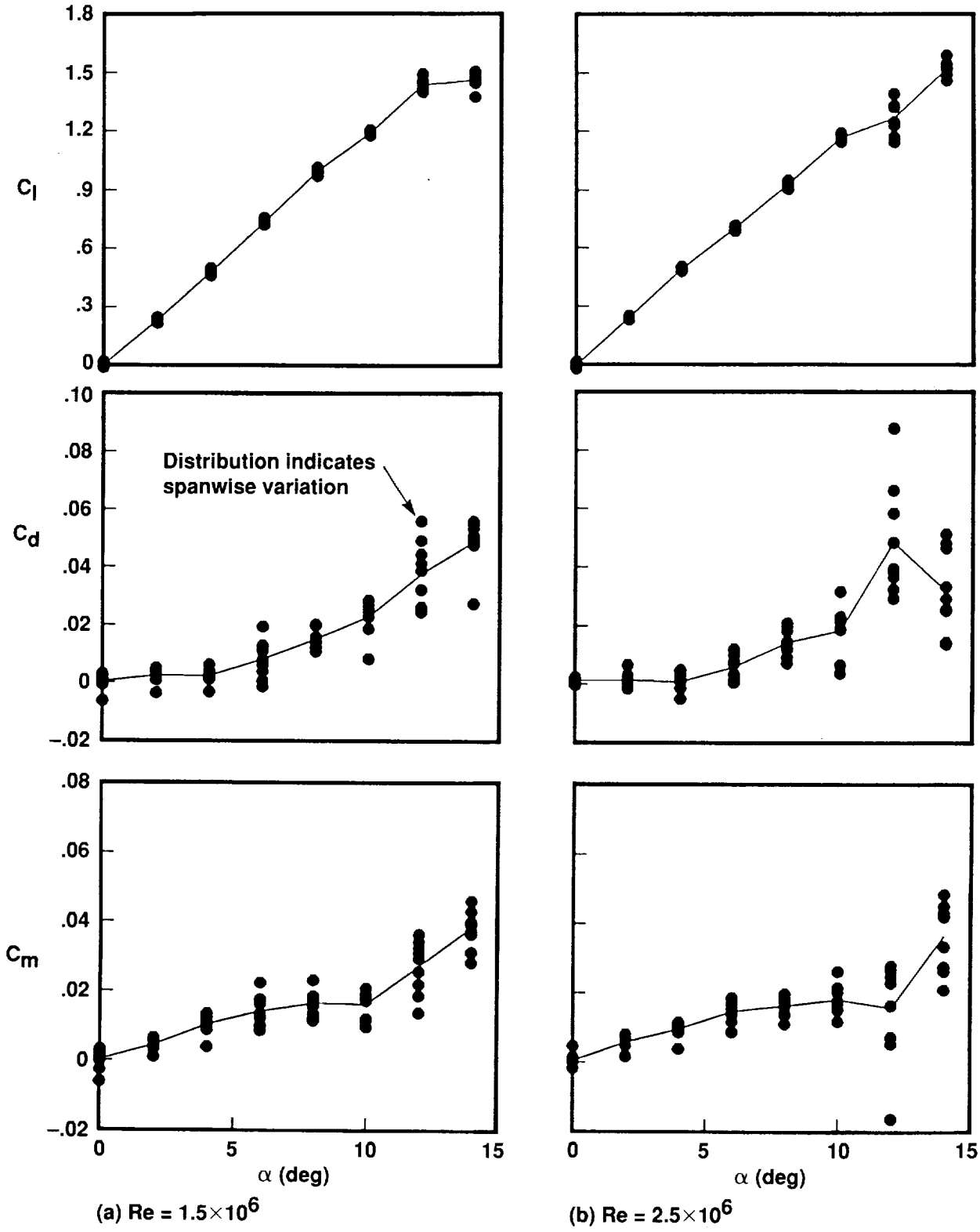

Figure 20. Pressure-derived force and moment variation with angle of attack for 2D configuration (limited to $0.09 < y/s < 0.90$; solid line represents average).

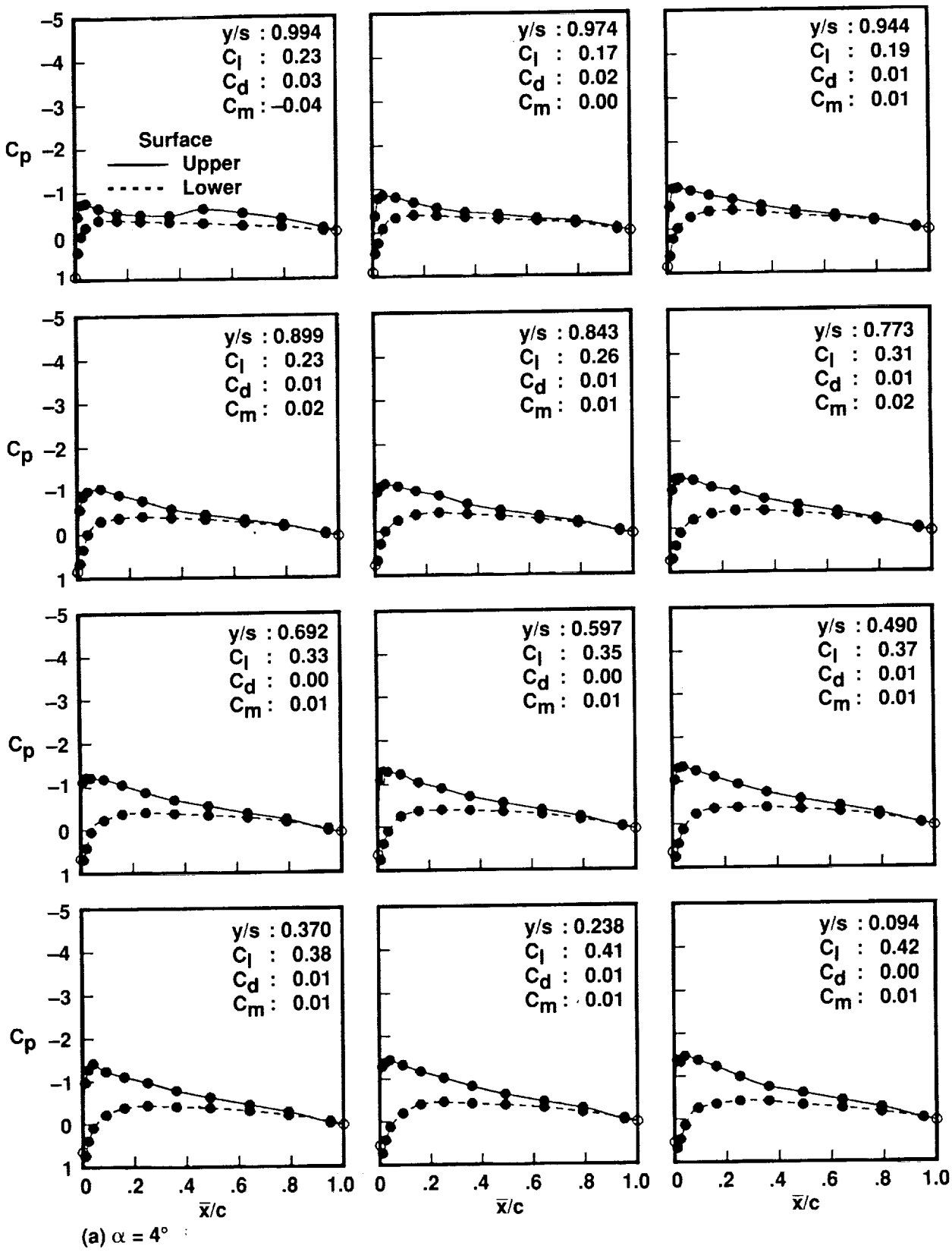

(a) $\alpha = 4°$

Figure 21. Pressure over full wing span with square tip at $Re = 1.5 \times 10^6$.

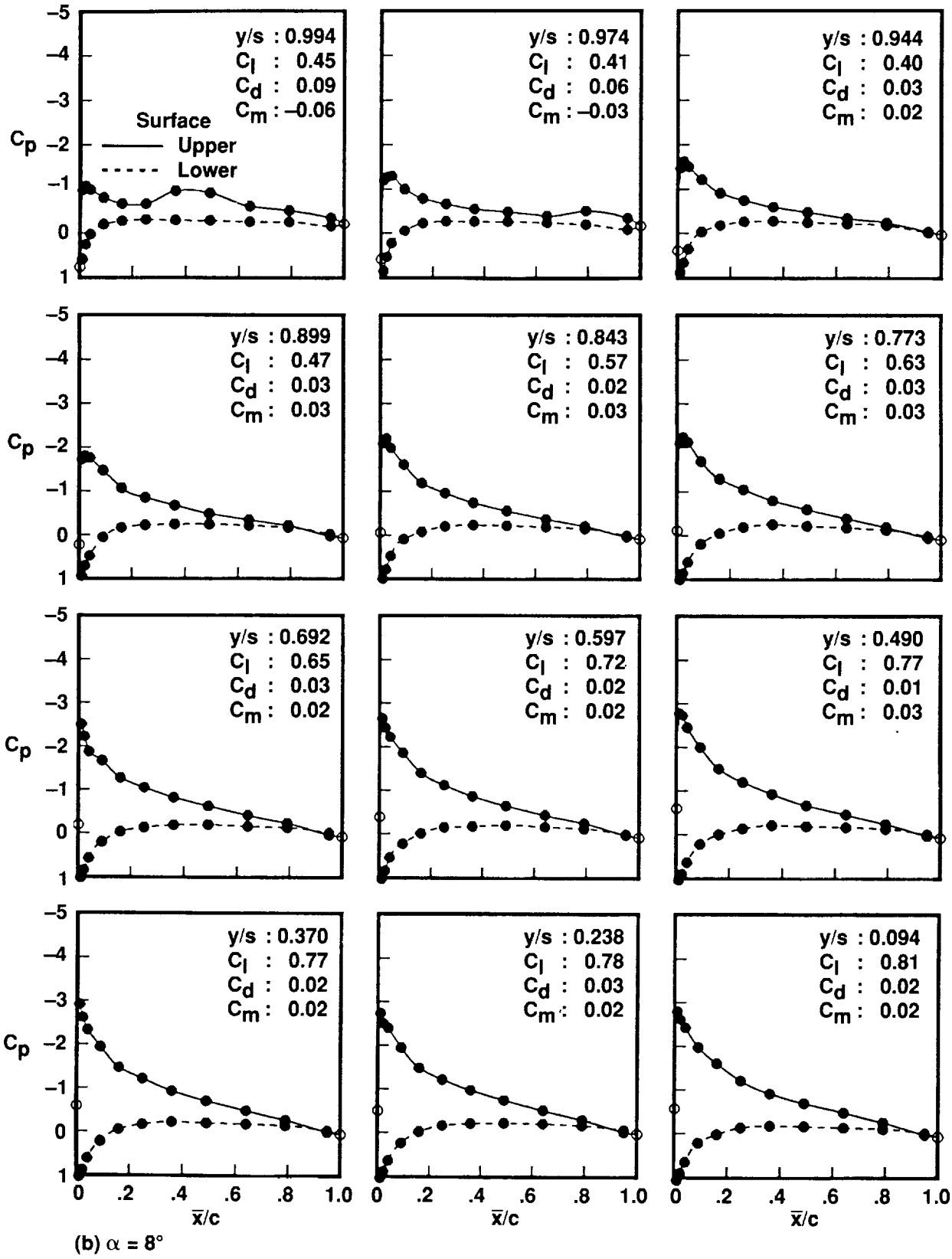

(b) $\alpha = 8°$

Figure 21. Continued.

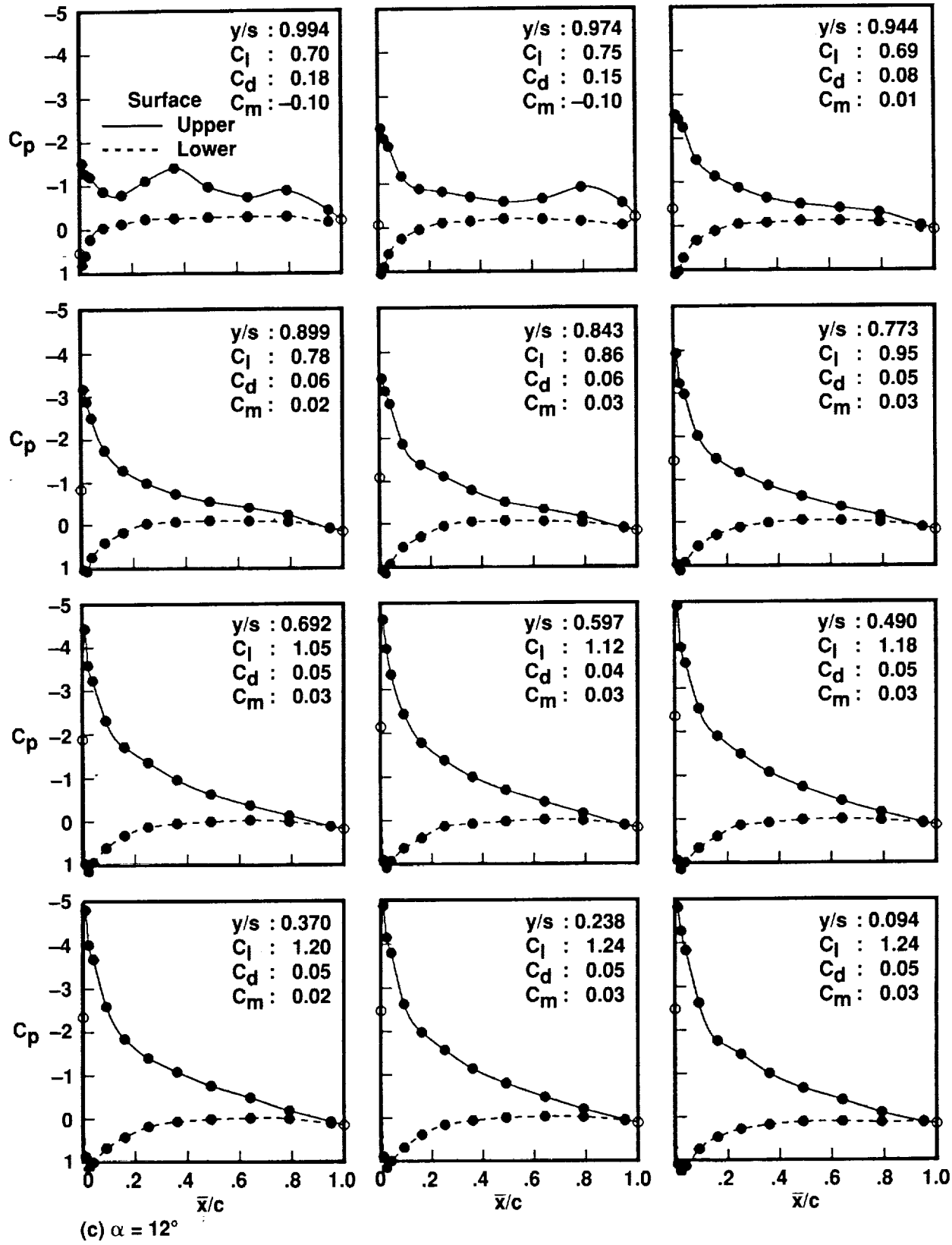

Figure 21. Concluded.

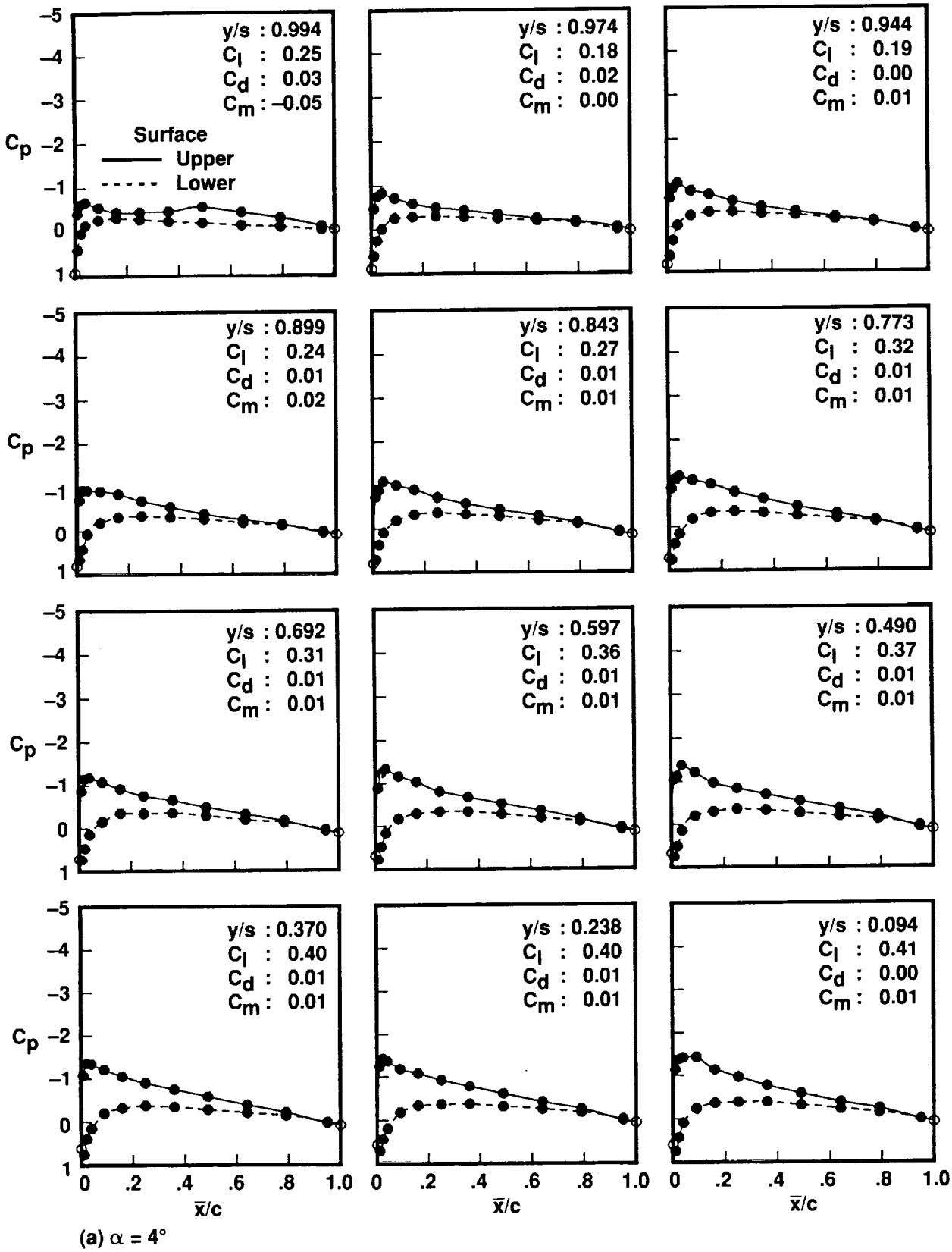

Figure 22. Pressure over full wing span with square tip at $Re = 2.5 \times 10^6$.

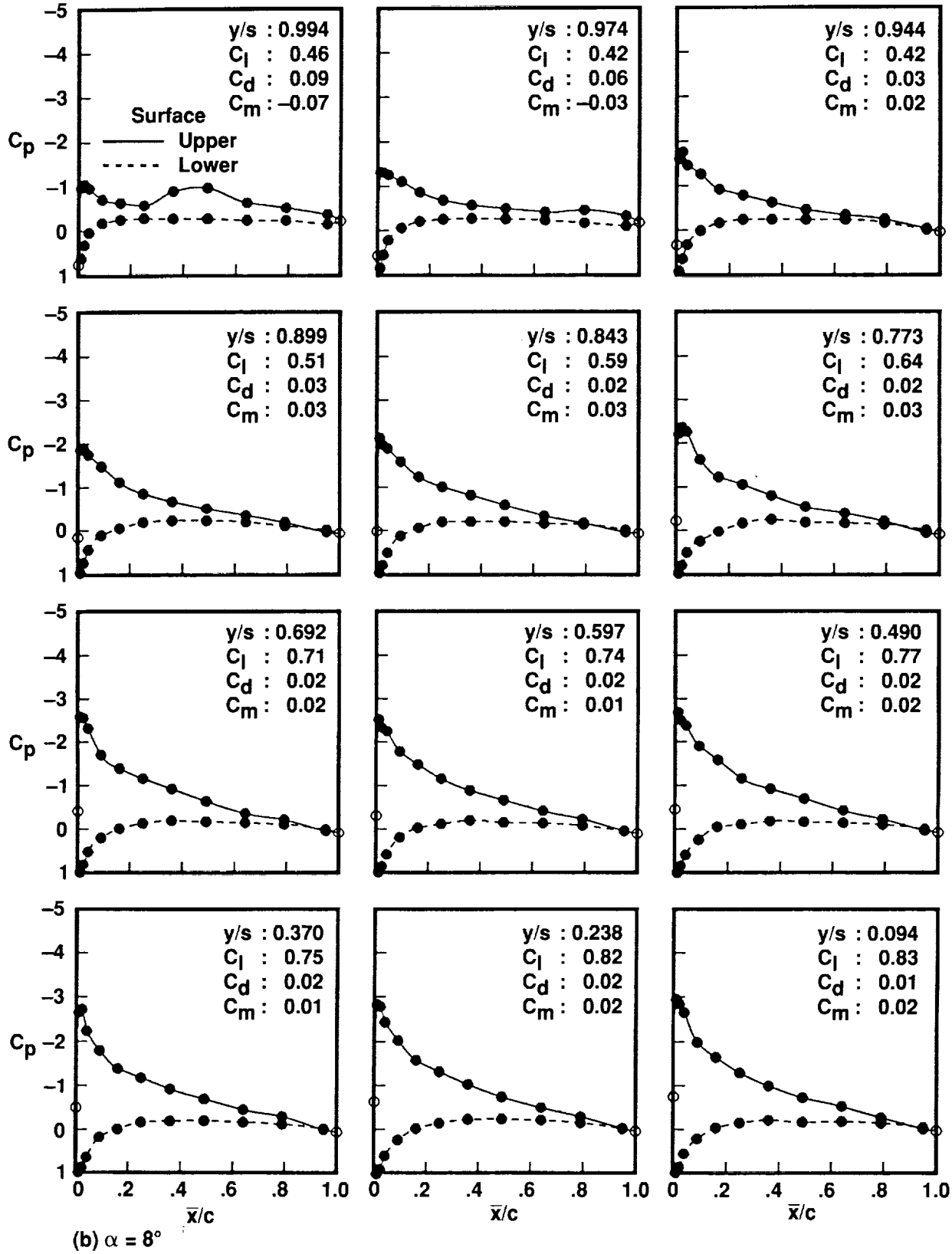

Figure 22. Continued.

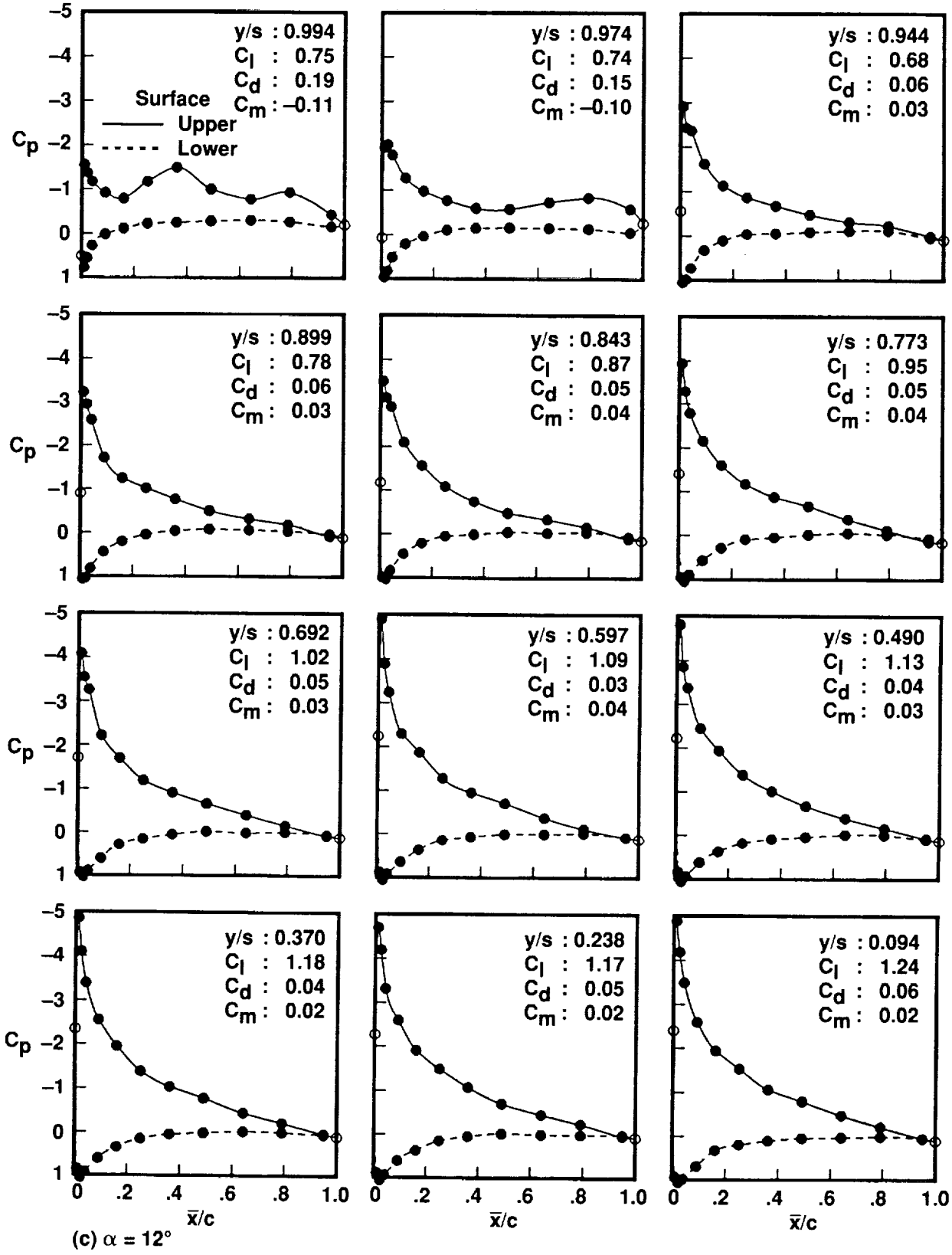

Figure 22. Concluded.

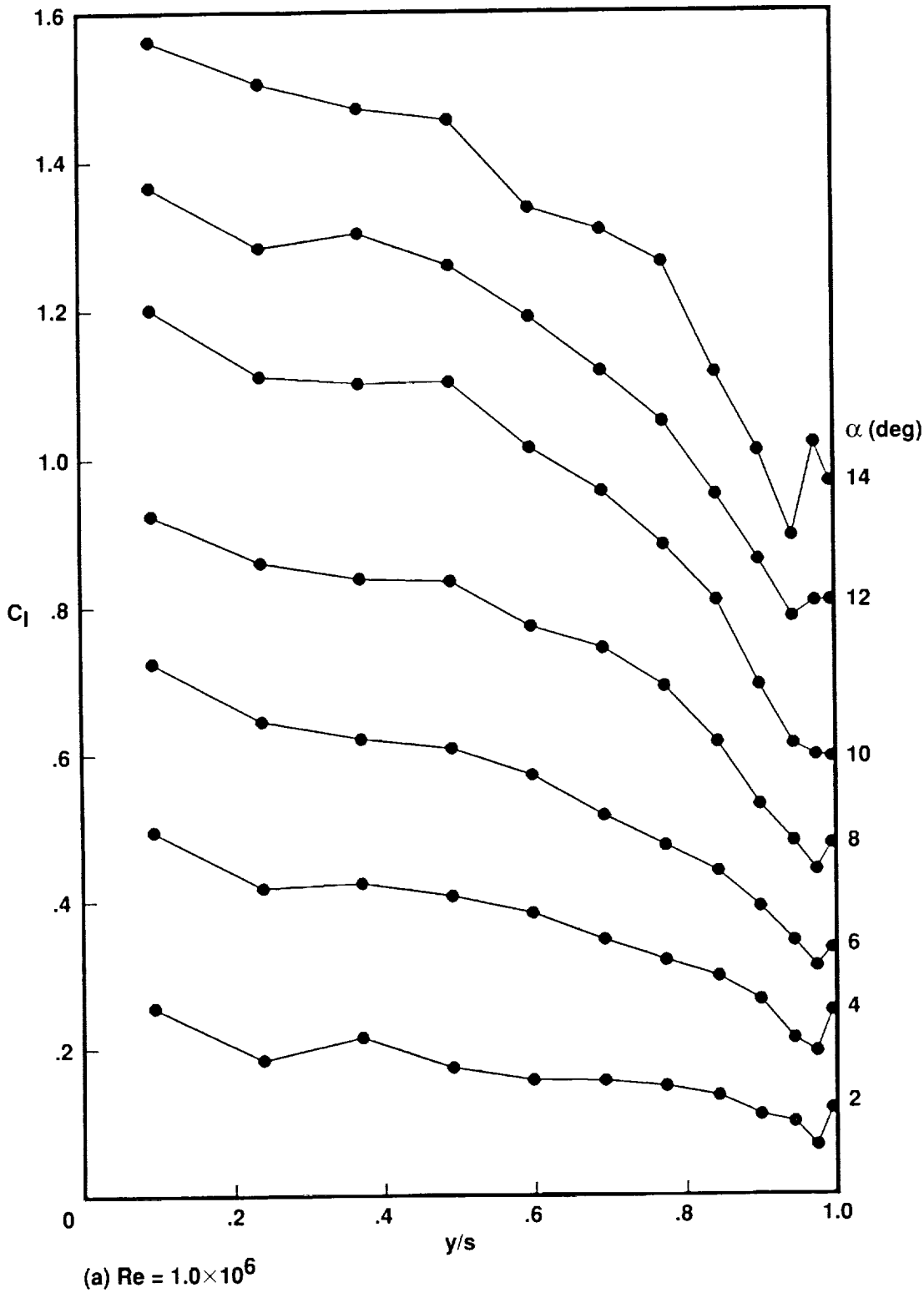

Figure 23. Pressure-derived lift distribution along full wing span with square tip.

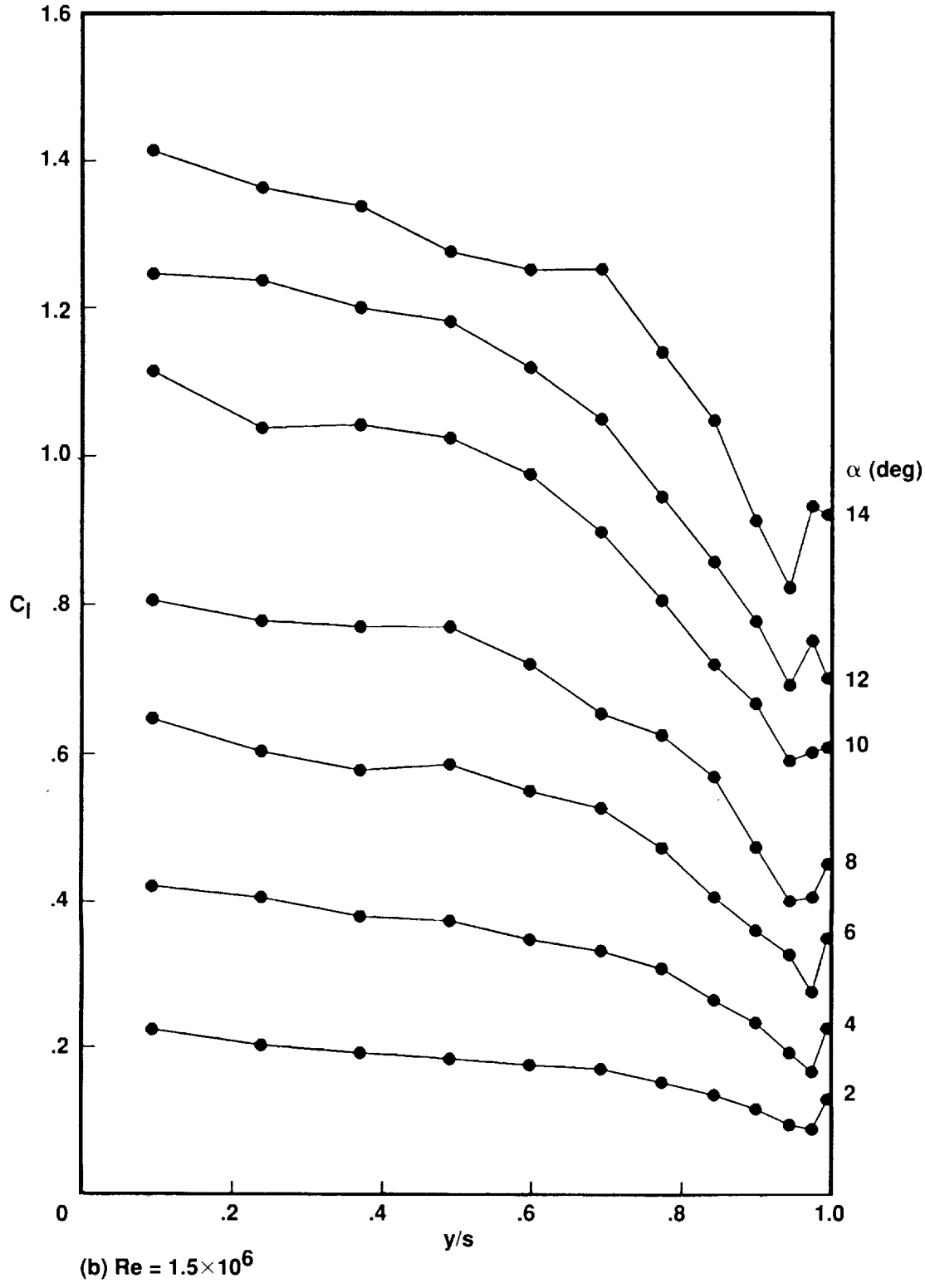

Figure 23. Continued.

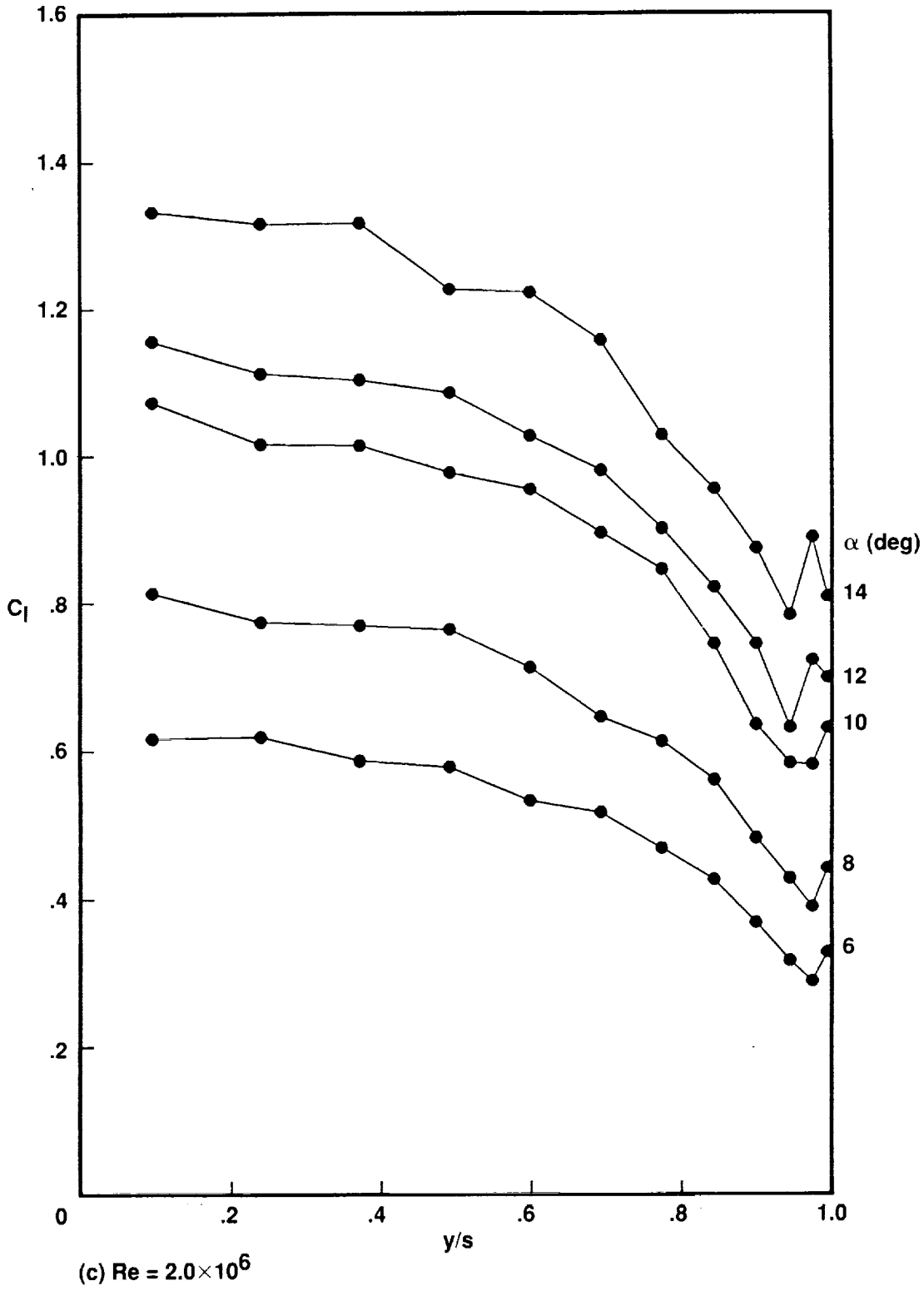

Figure 23. Continued.

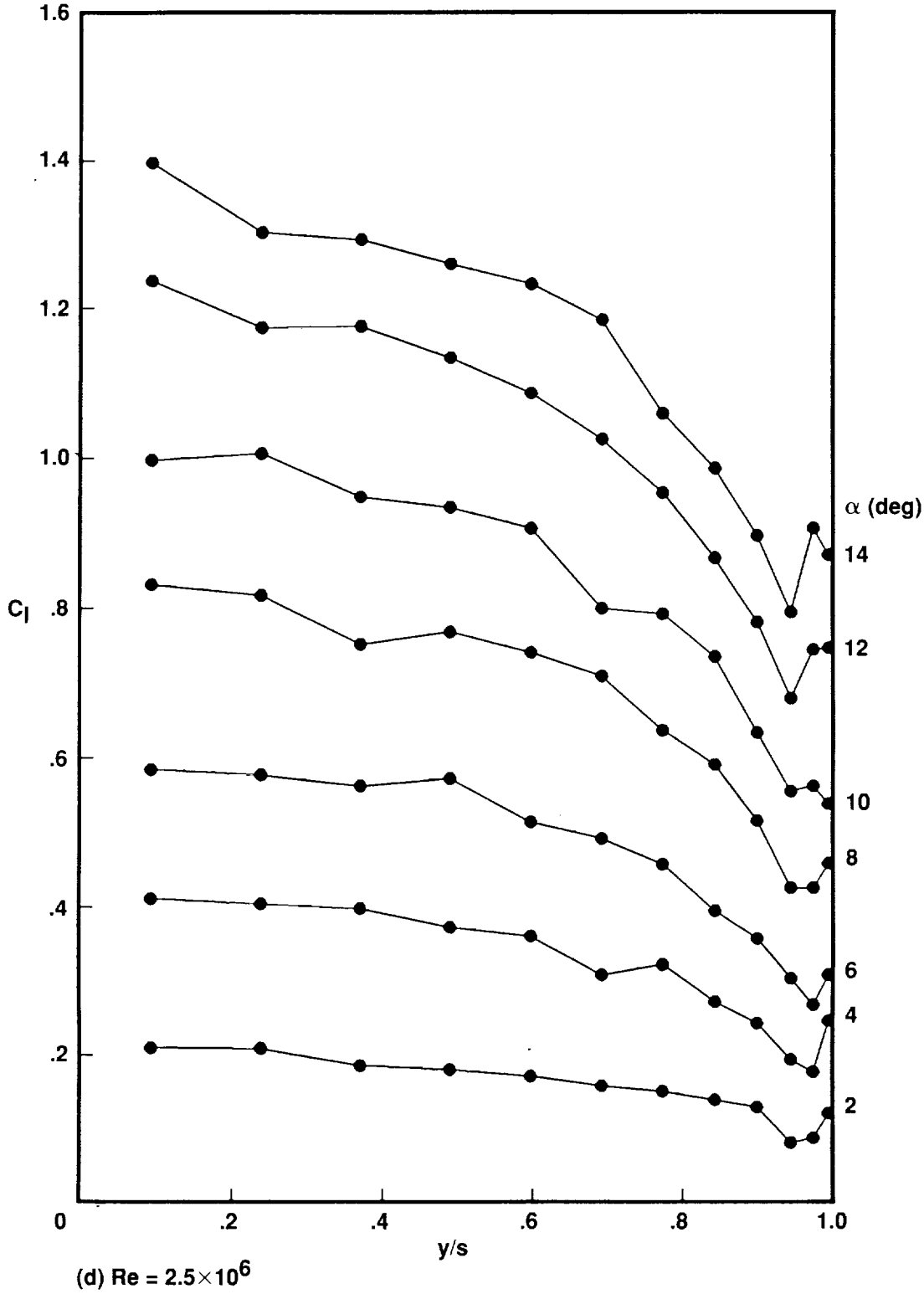

Figure 23. Continued.

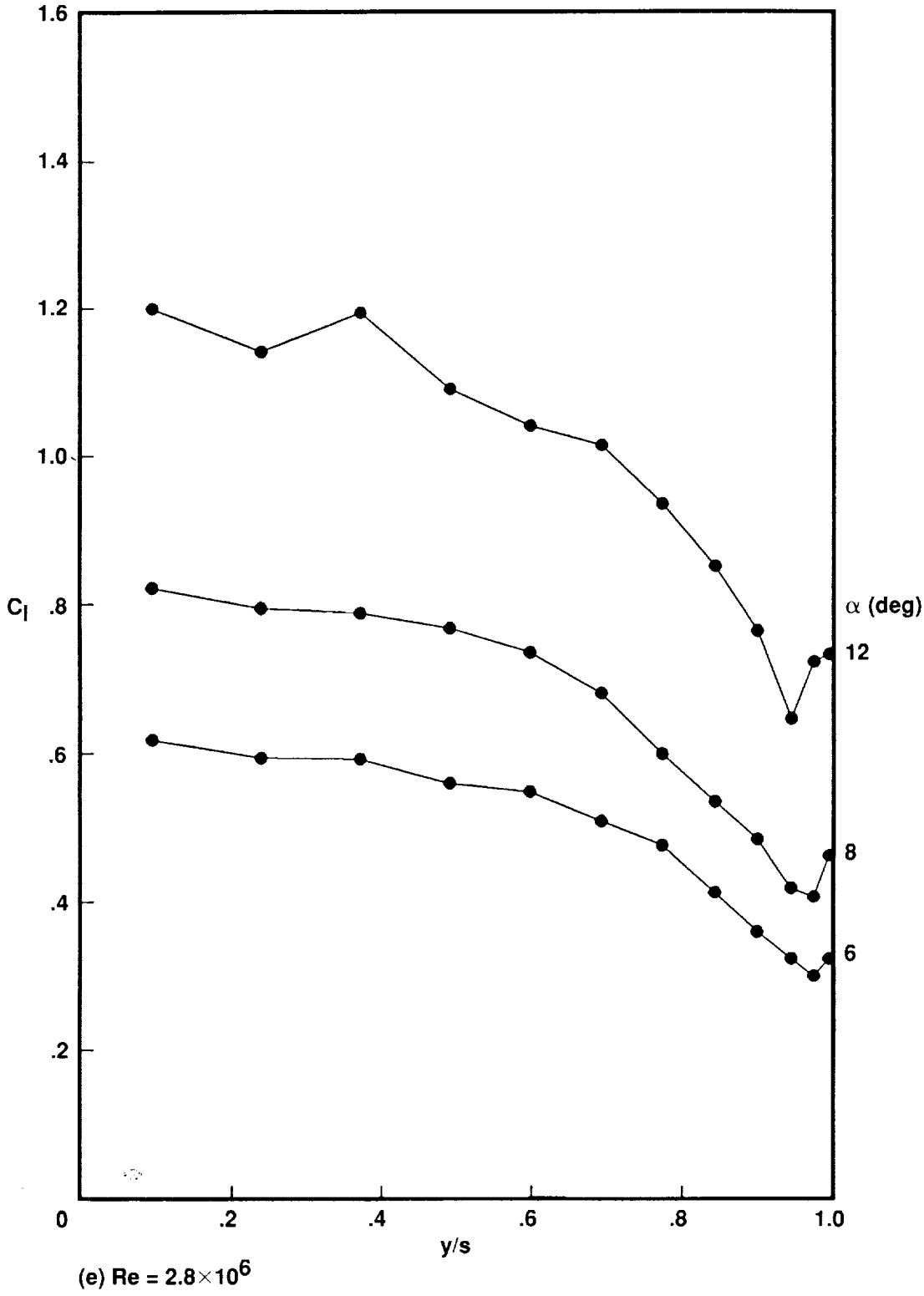

Figure 23. Concluded.

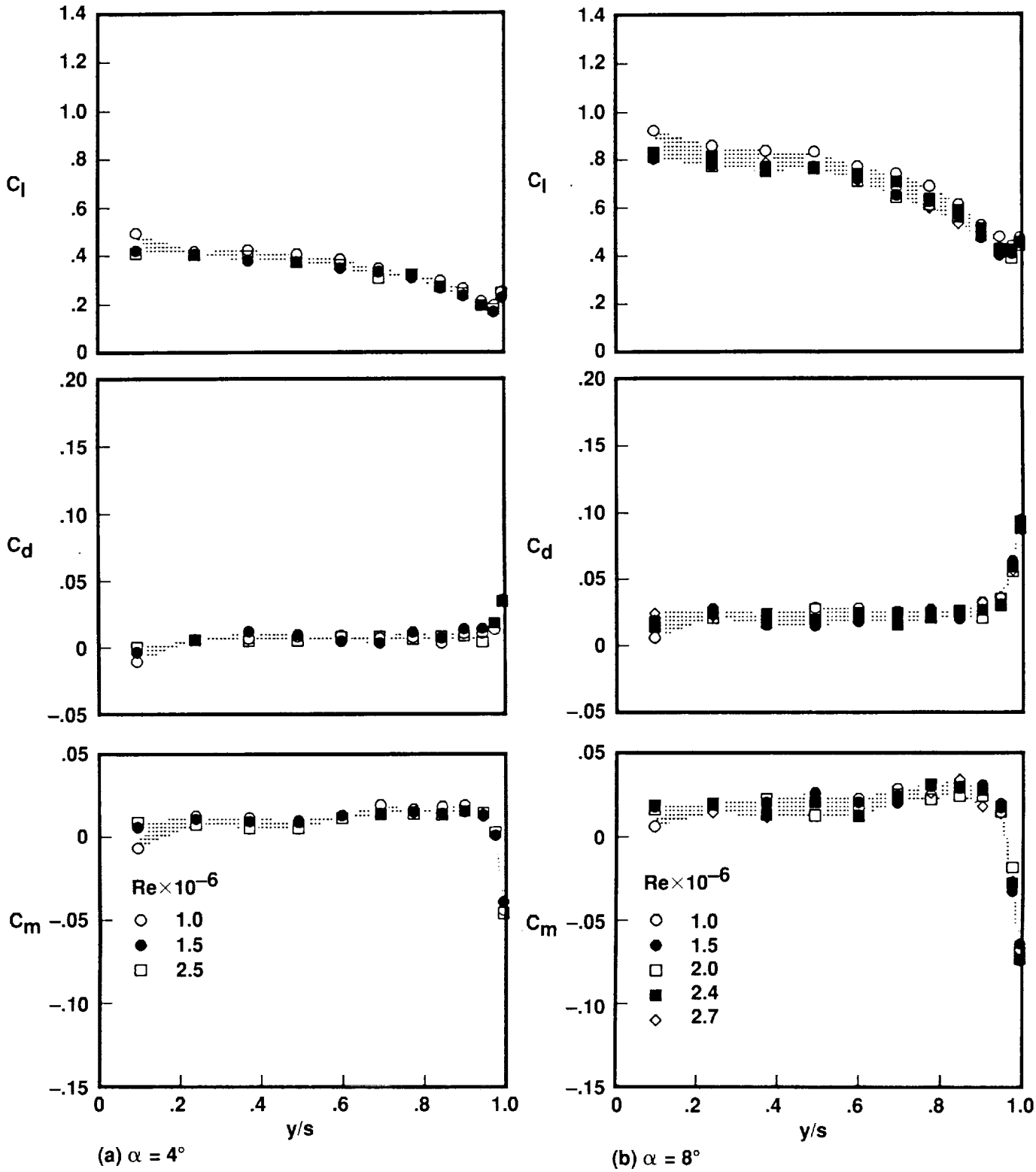

Figure 24. Load variation along full wing span with square tip for different *Re*.

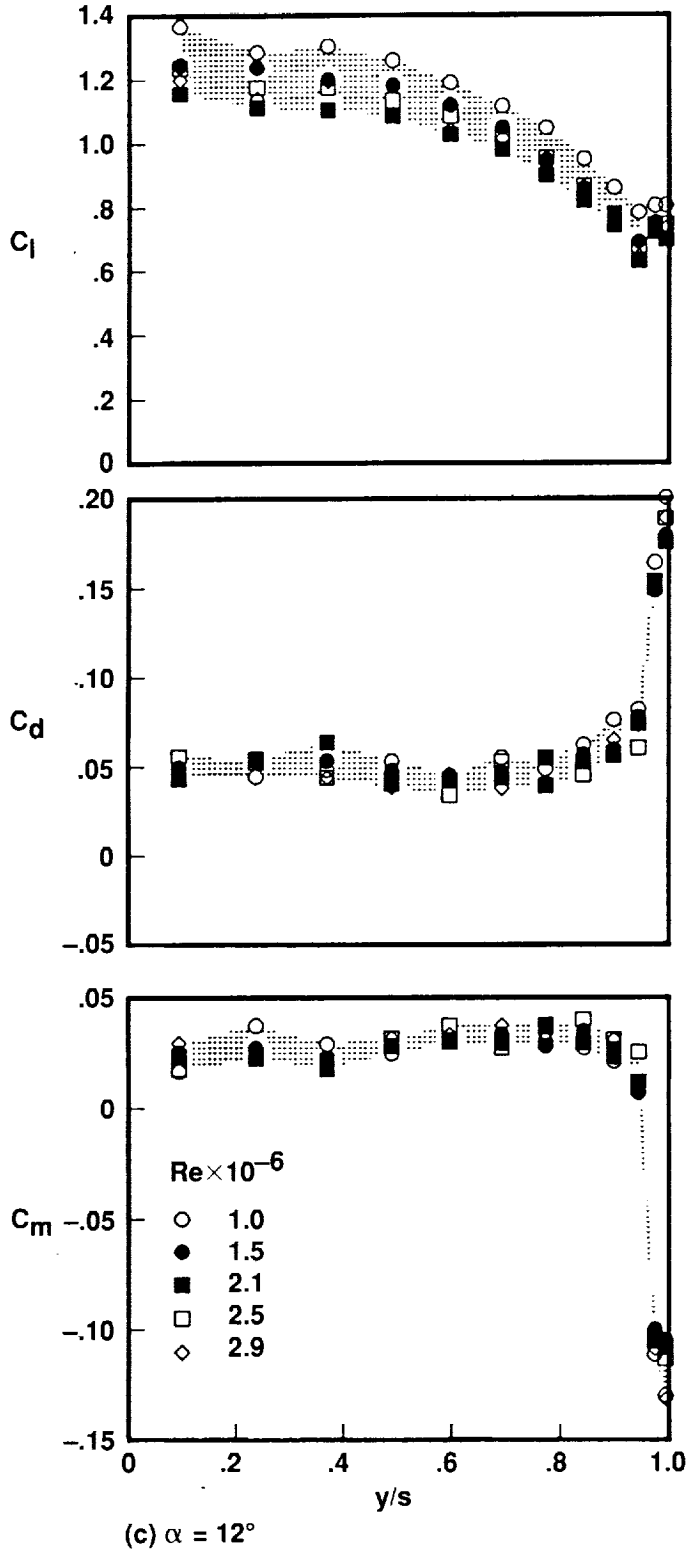

(c) $\alpha = 12°$

Figure 24. Concluded.

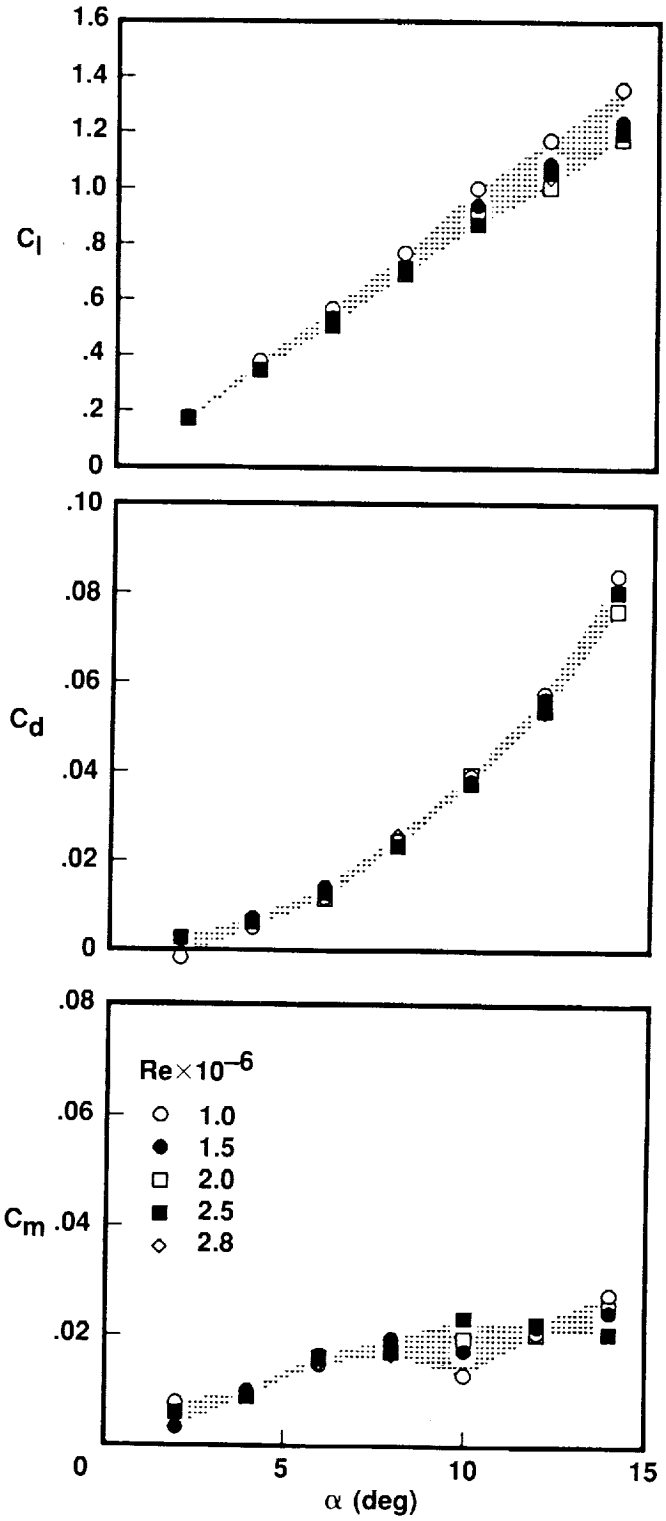

Figure 25. Integrated loads over full wing span with square tip for different *Re*.

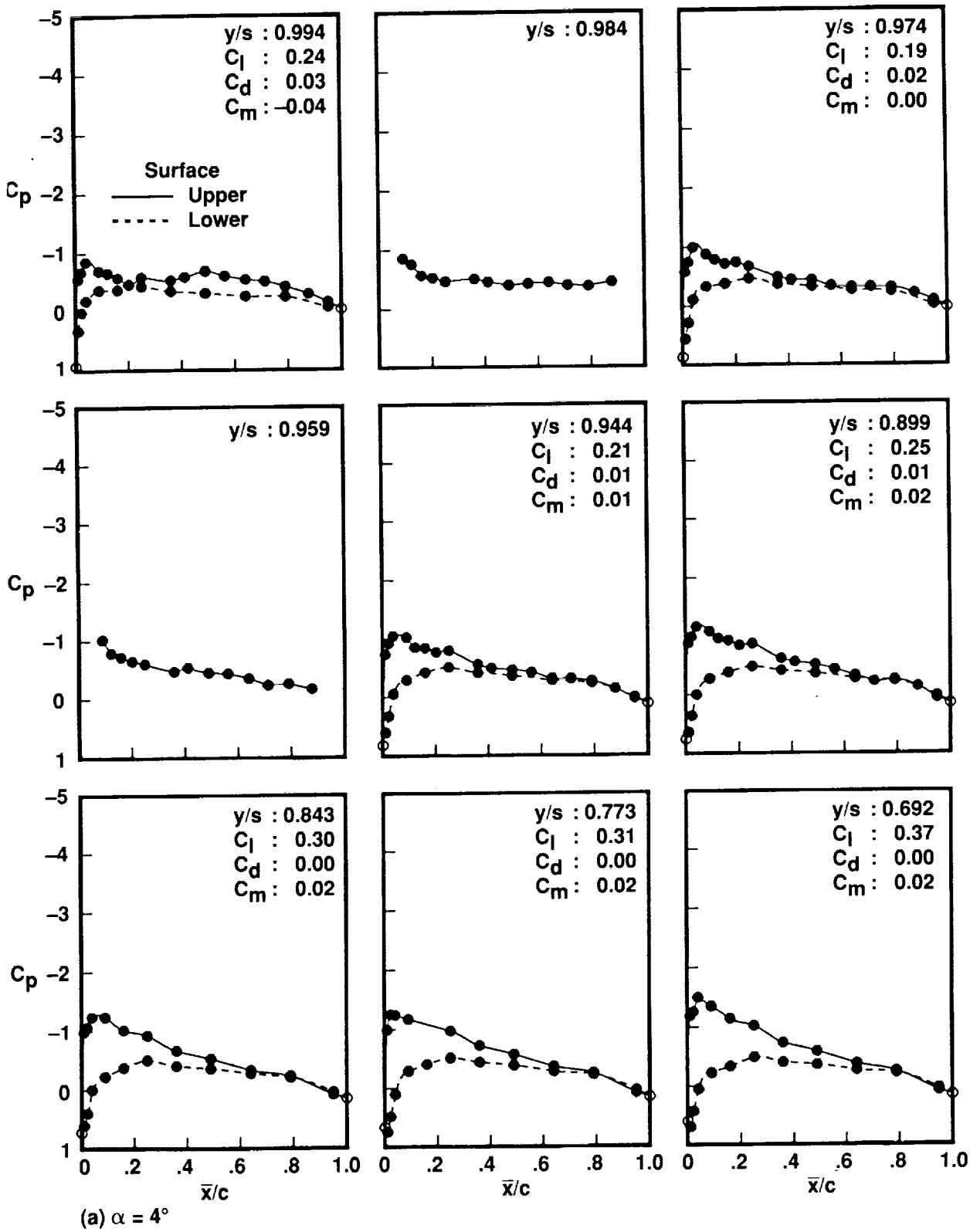

Figure 26. Pressure over outer portion of wing with square tip at $Re = 1.0 \times 10^6$.

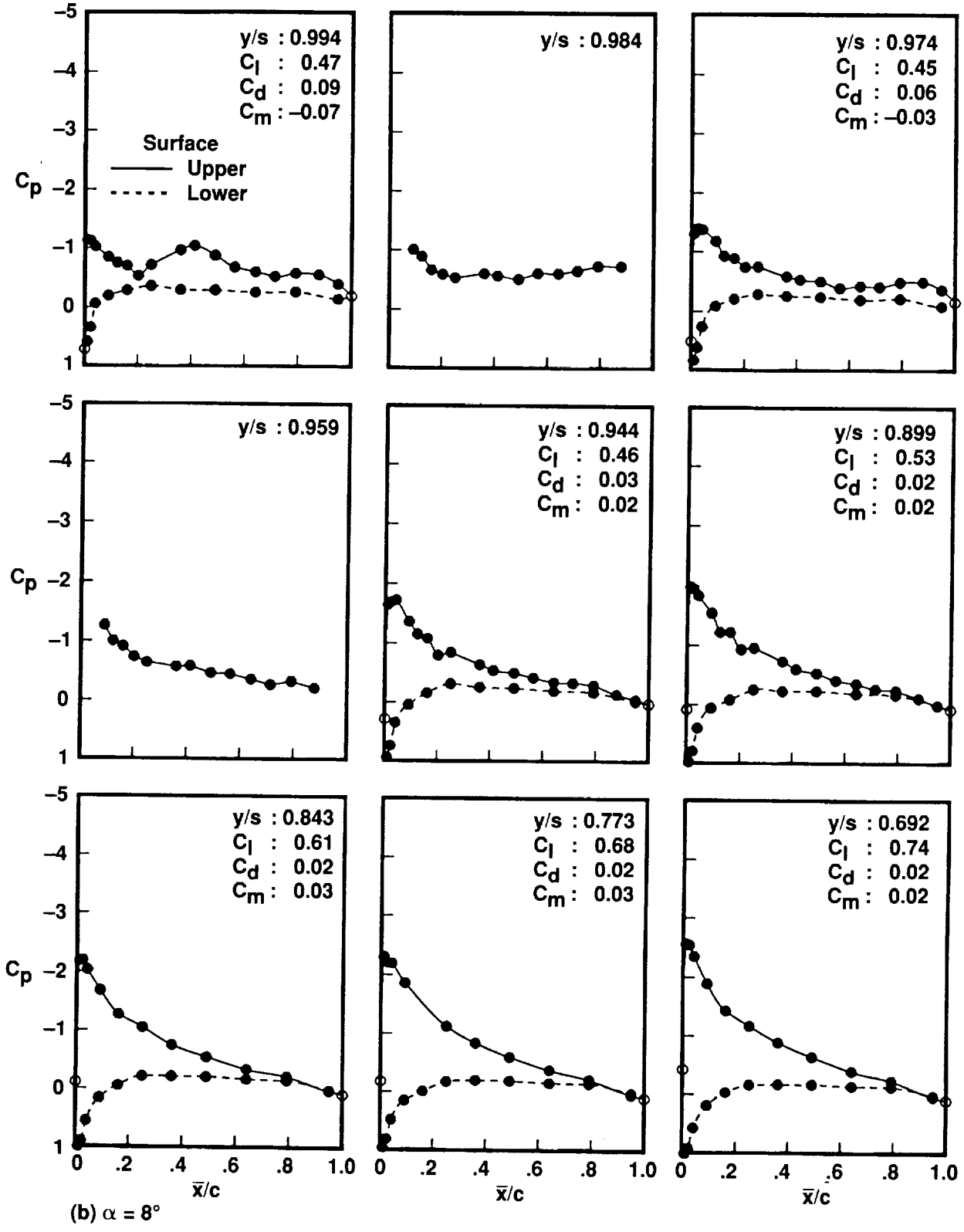

Figure 26. Continued.

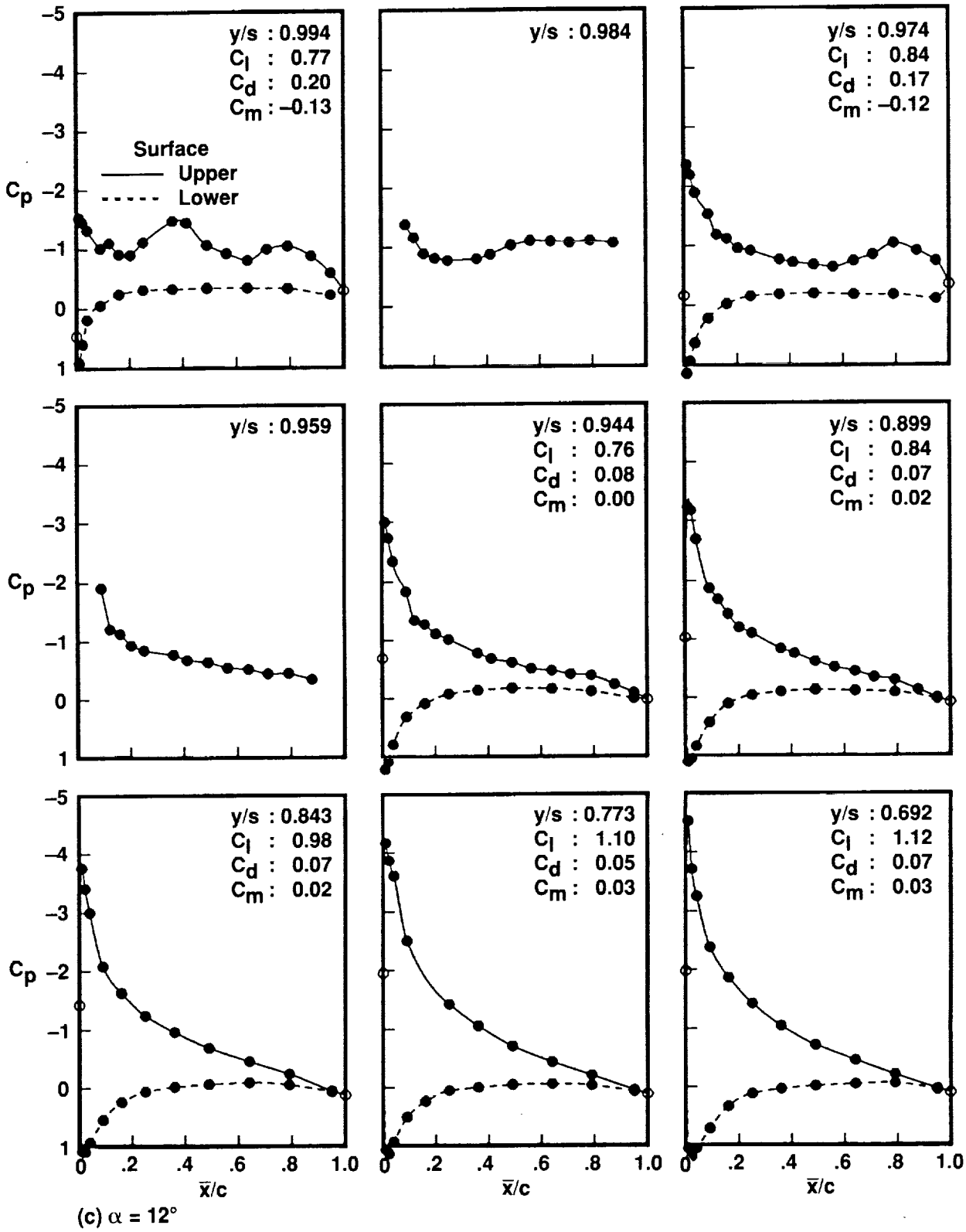

Figure 26. Concluded.

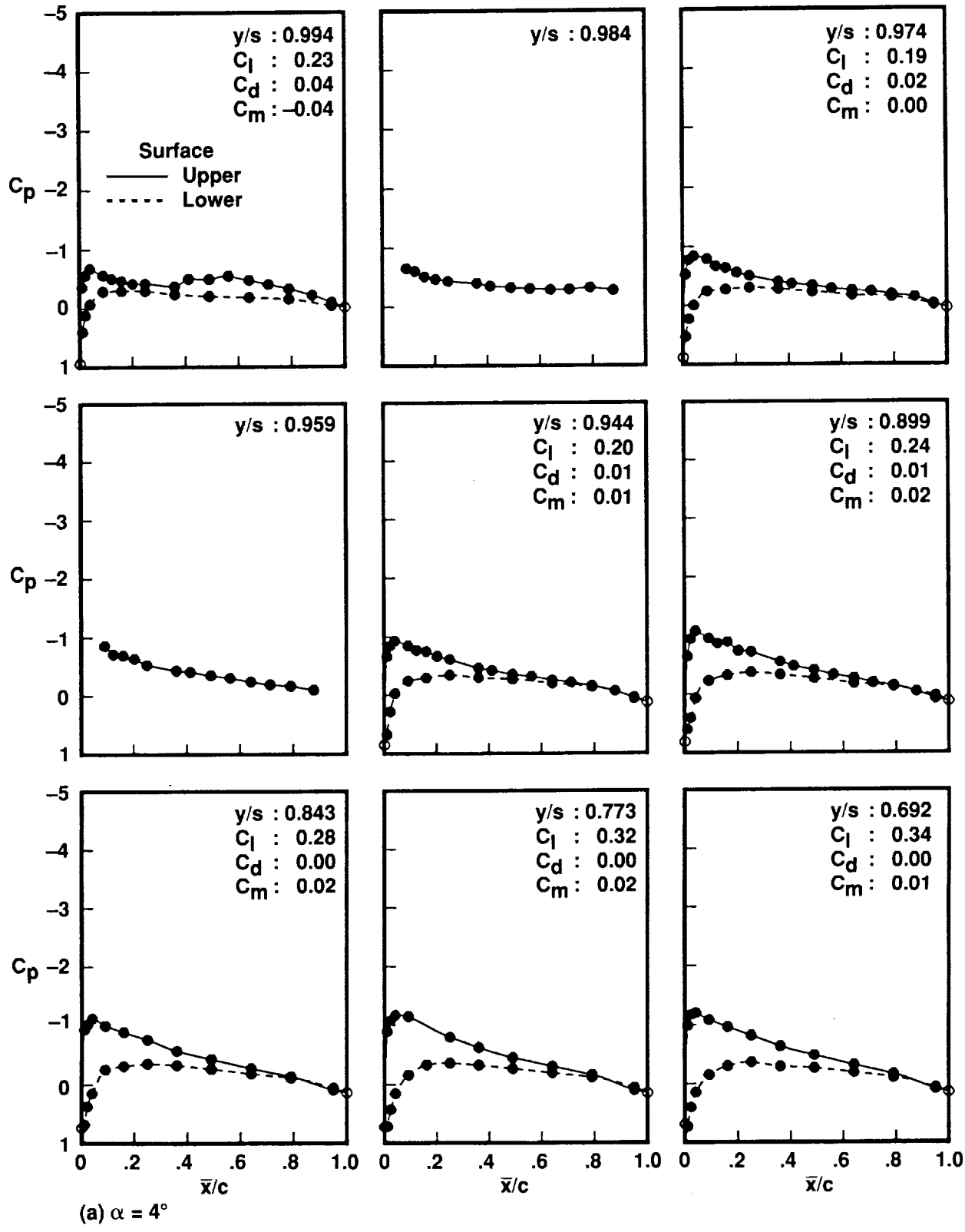

Figure 27. Pressure over outer portion of wing with square tip at $Re = 2.0 \times 10^6$.

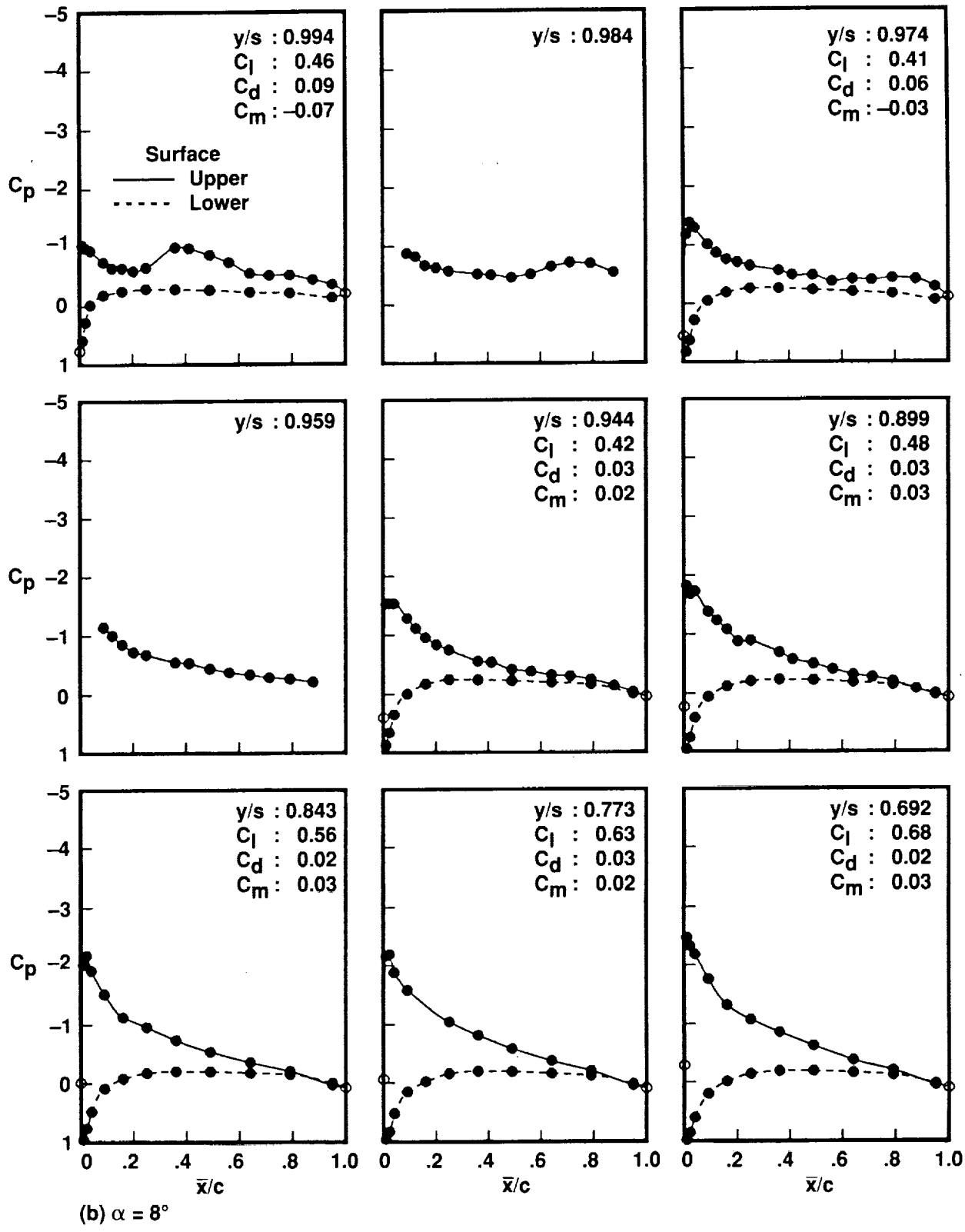

Figure 27. Continued.

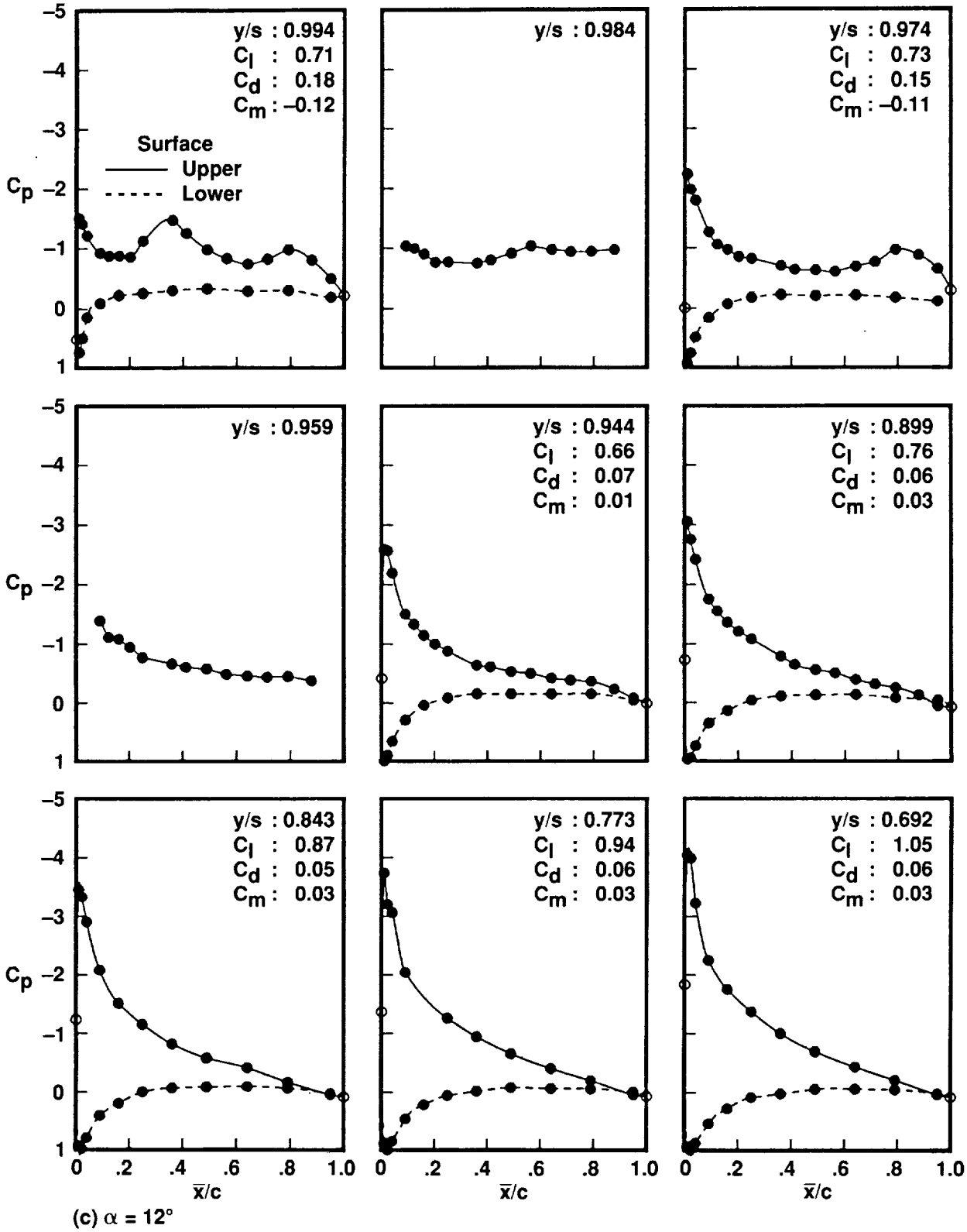

Figure 27. Concluded.

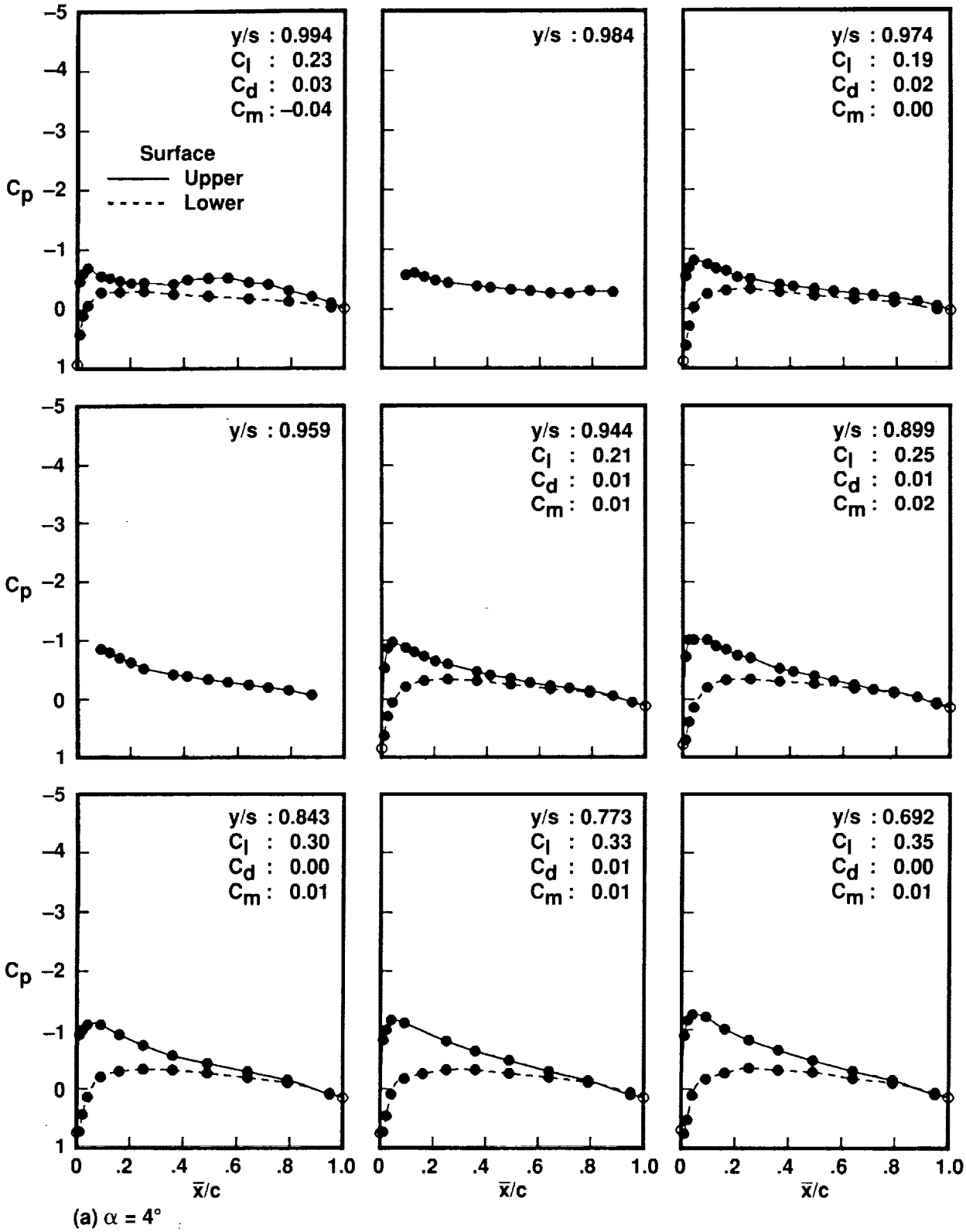

Figure 28. Pressure over outer portion of wing with square tip at $Re = 2.9 \times 10^6$.

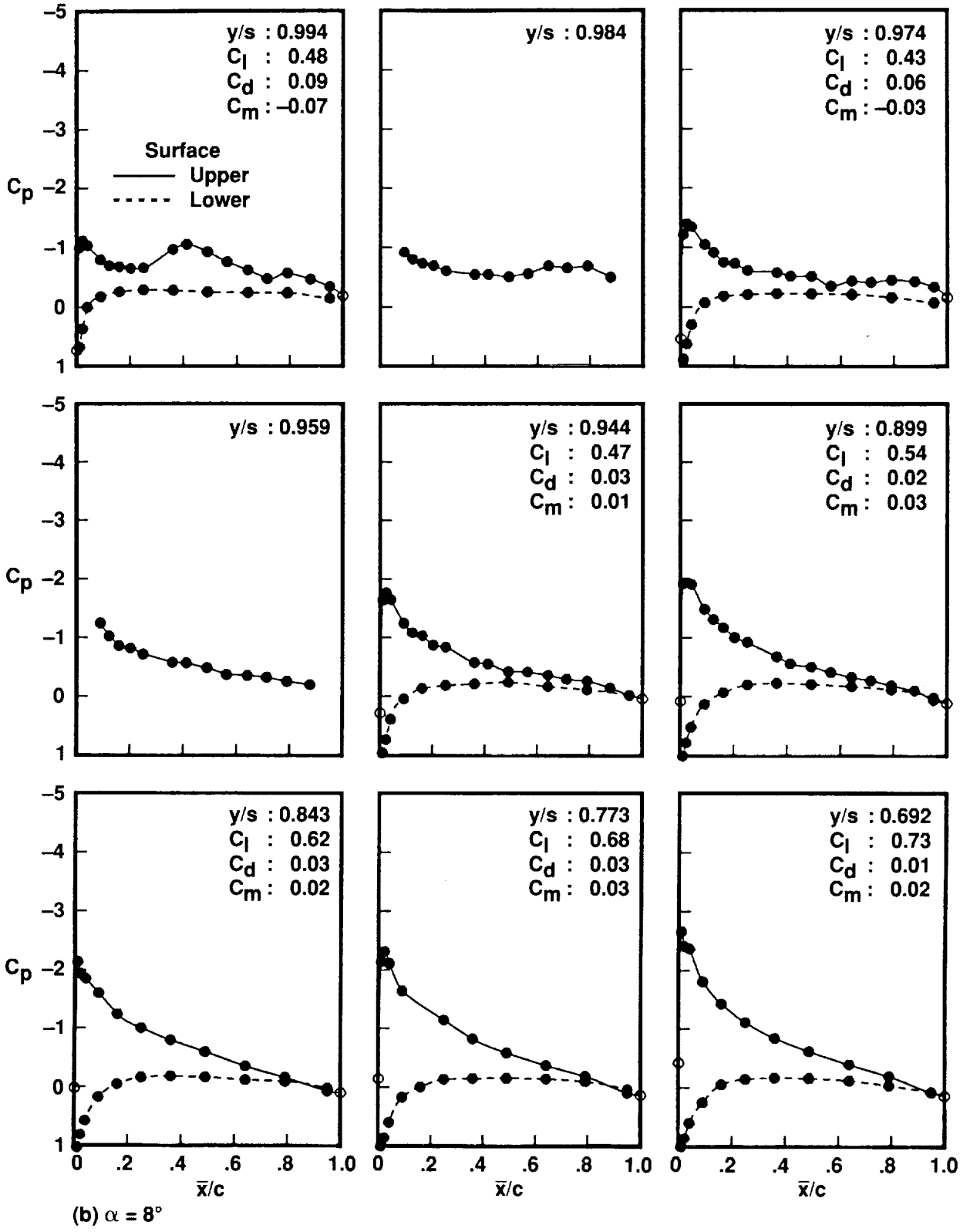

Figure 28. Continued.

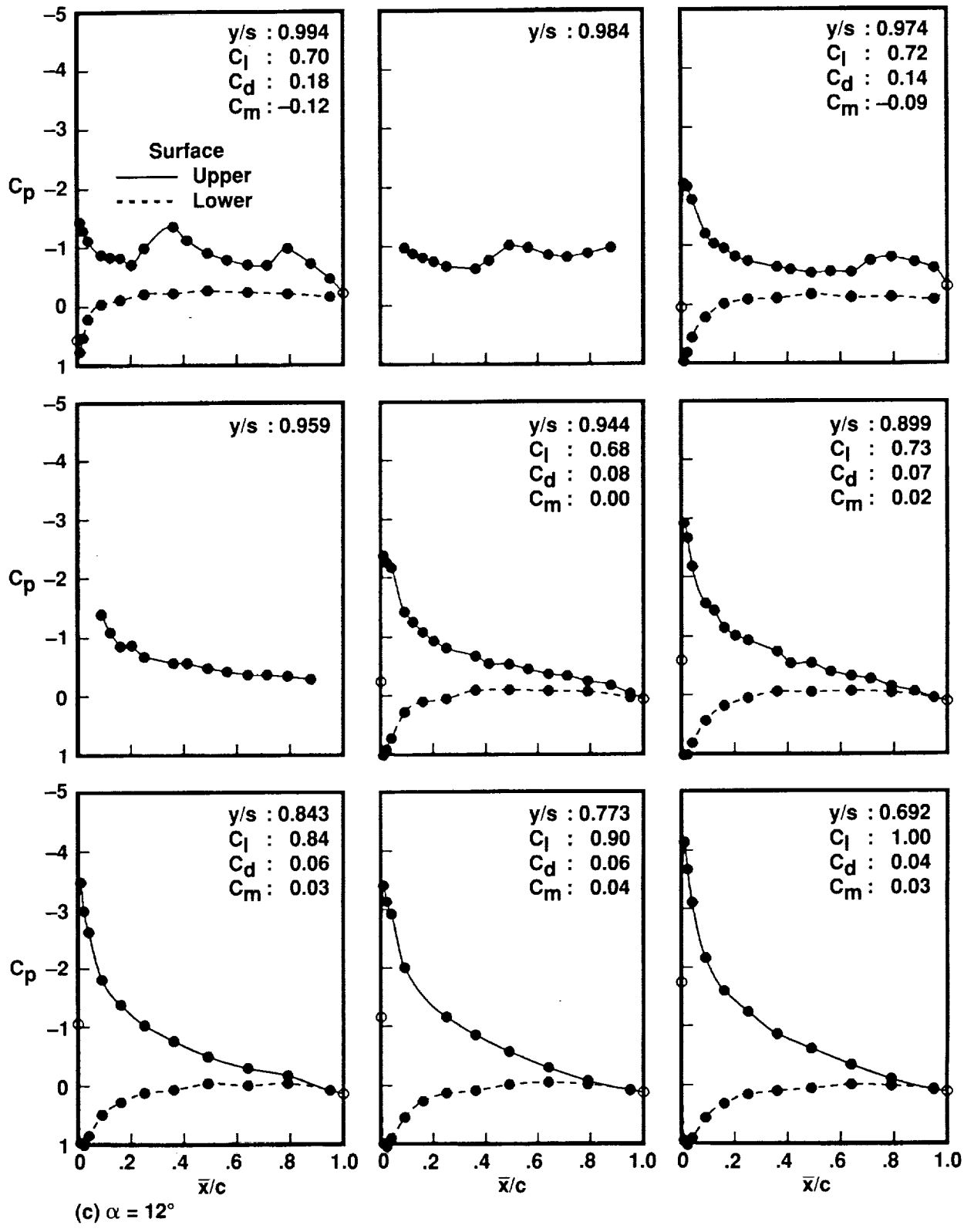

Figure 28. Concluded.

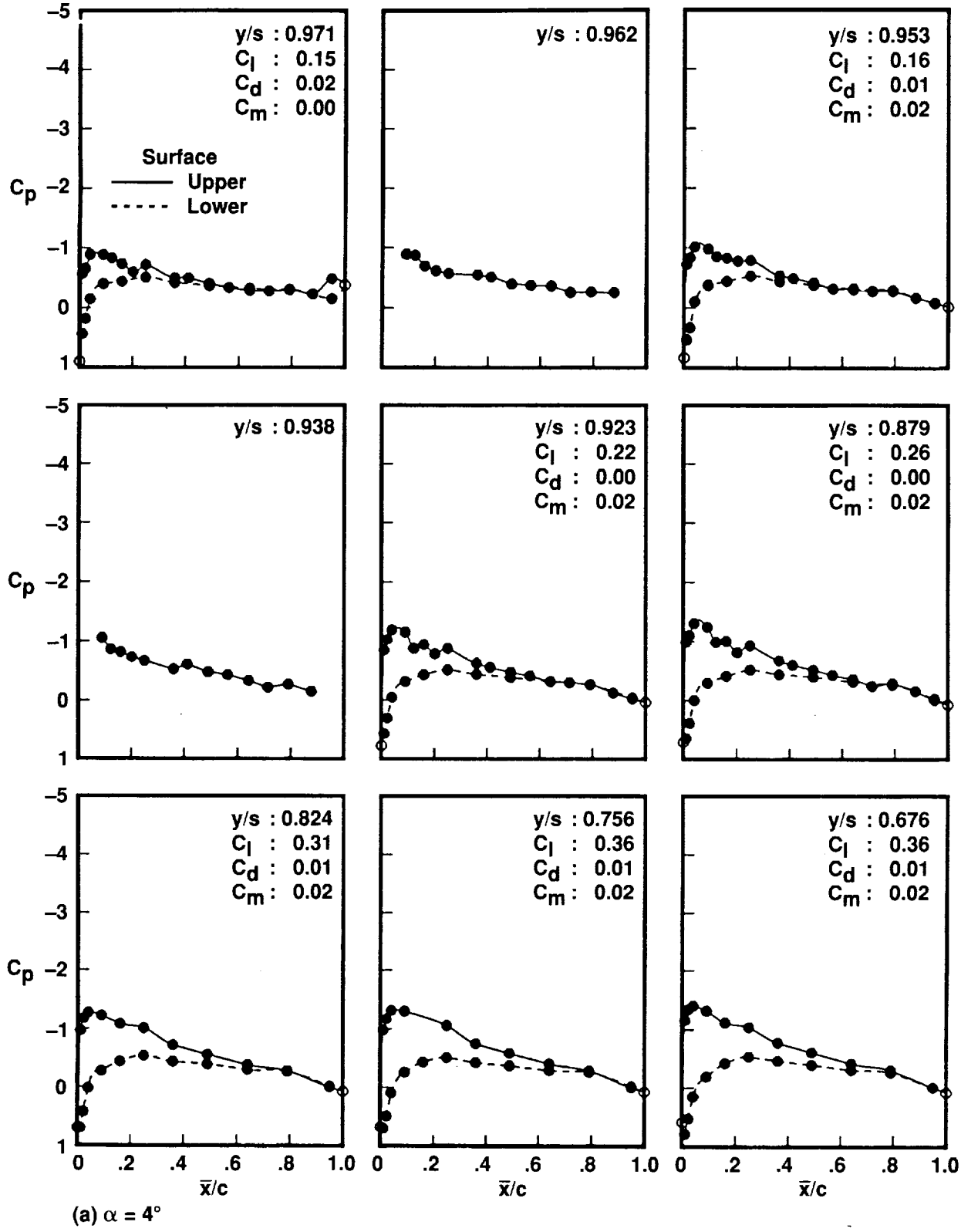

Figure 29. Pressure over outer portion of wing with round tip at $Re = 1.0 \times 10^6$.

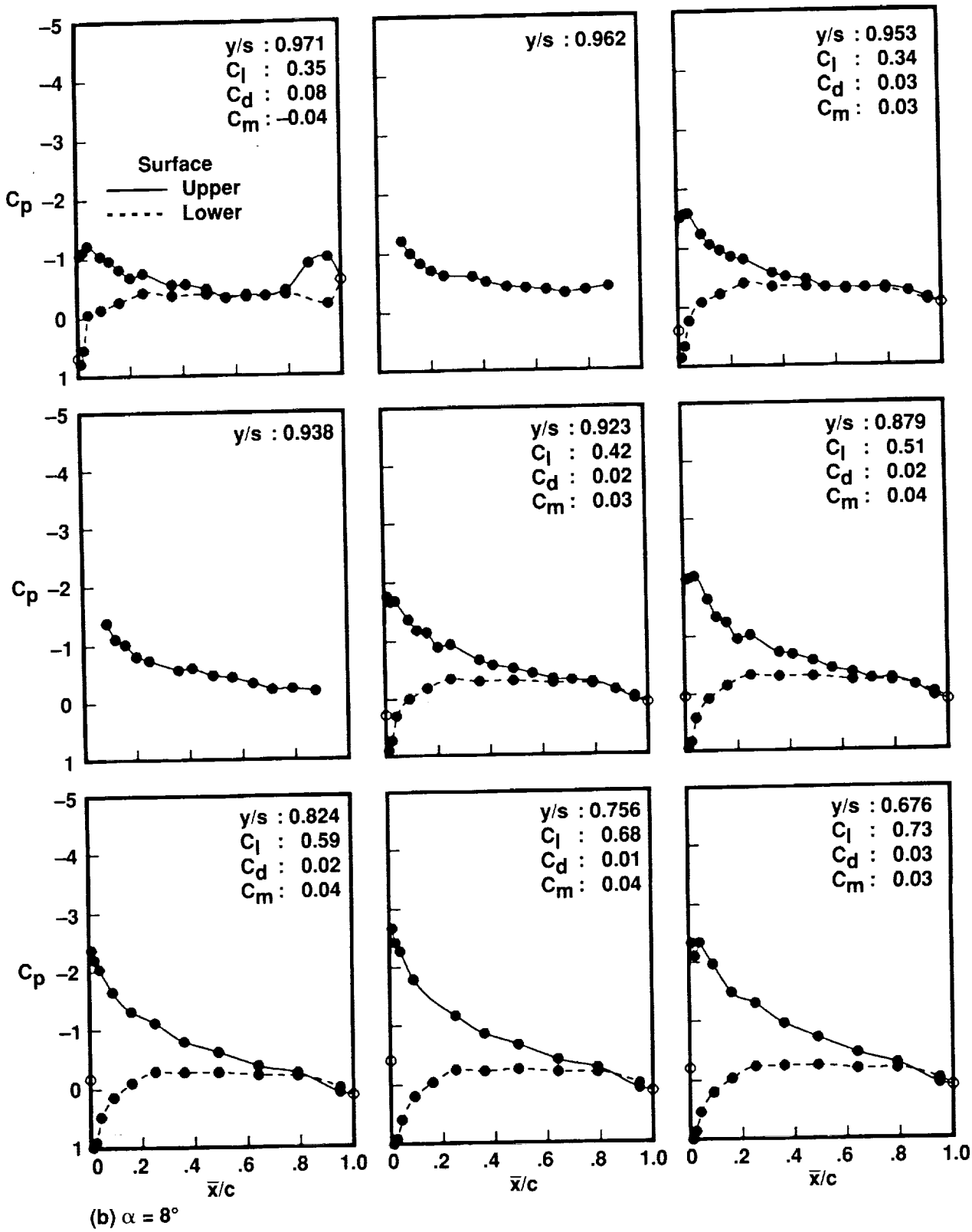

Figure 29. Continued.

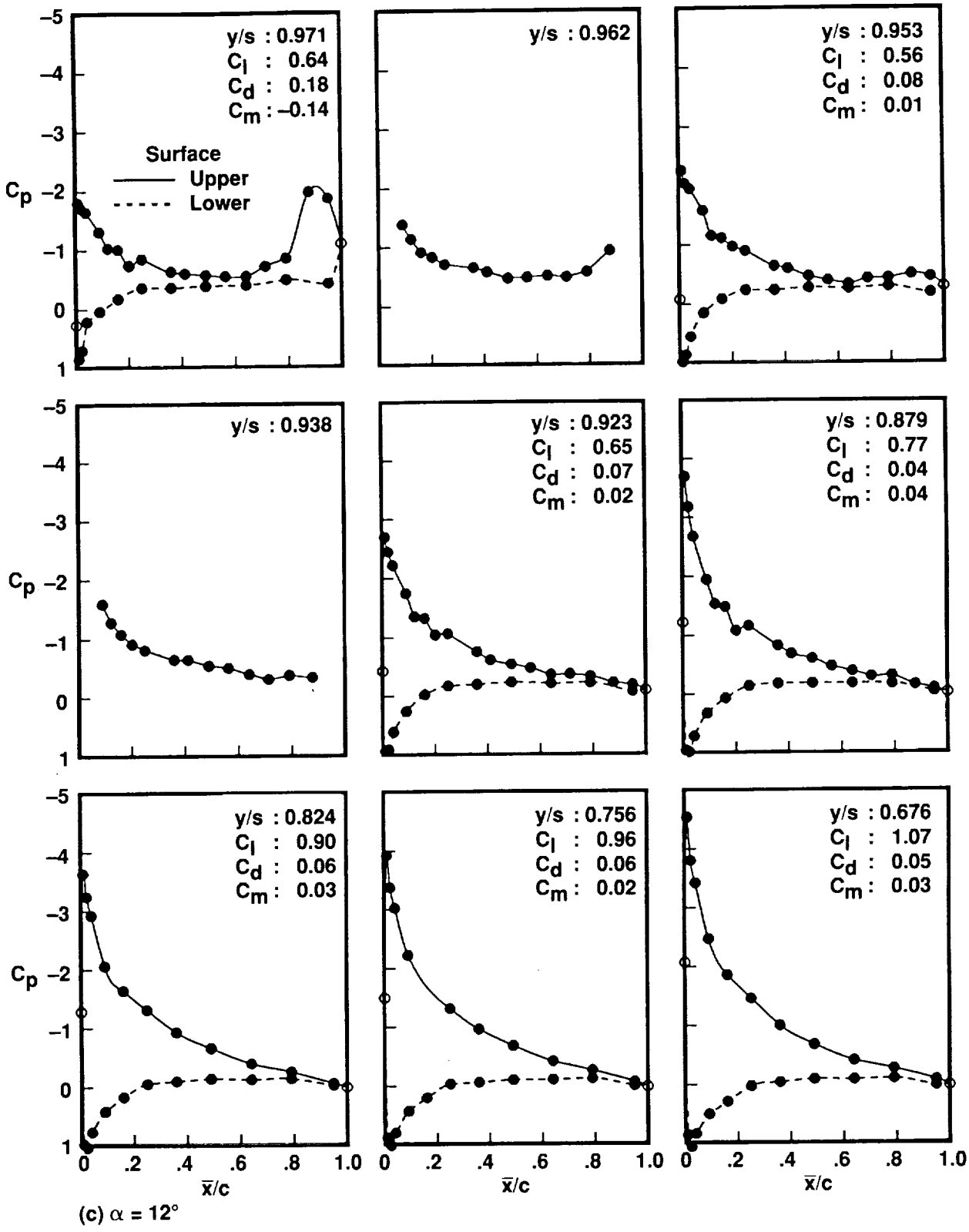

Figure 29. Concluded.

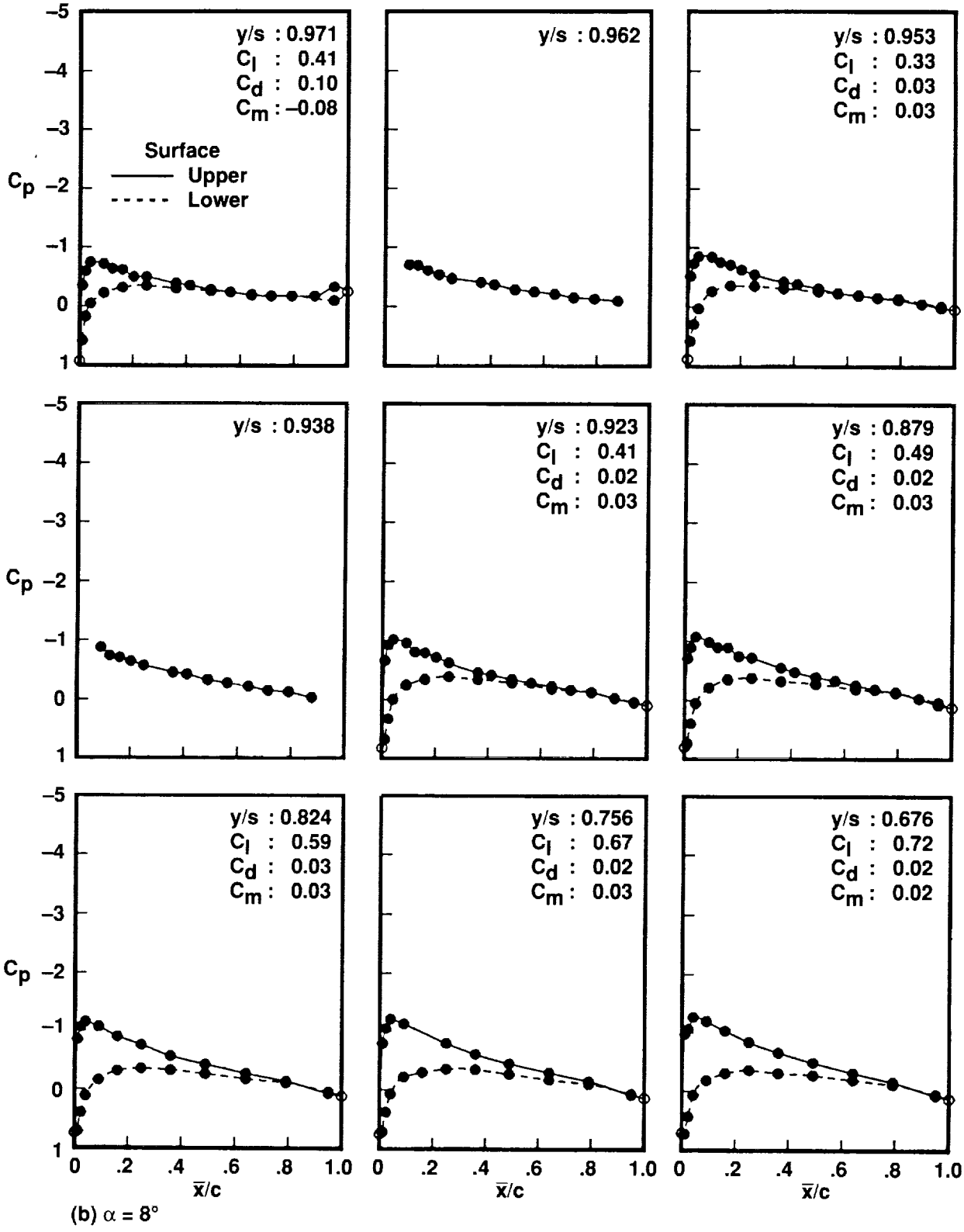

Figure 30. Pressure over outer portion of wing with round tip at $Re = 2.0 \times 10^6$.

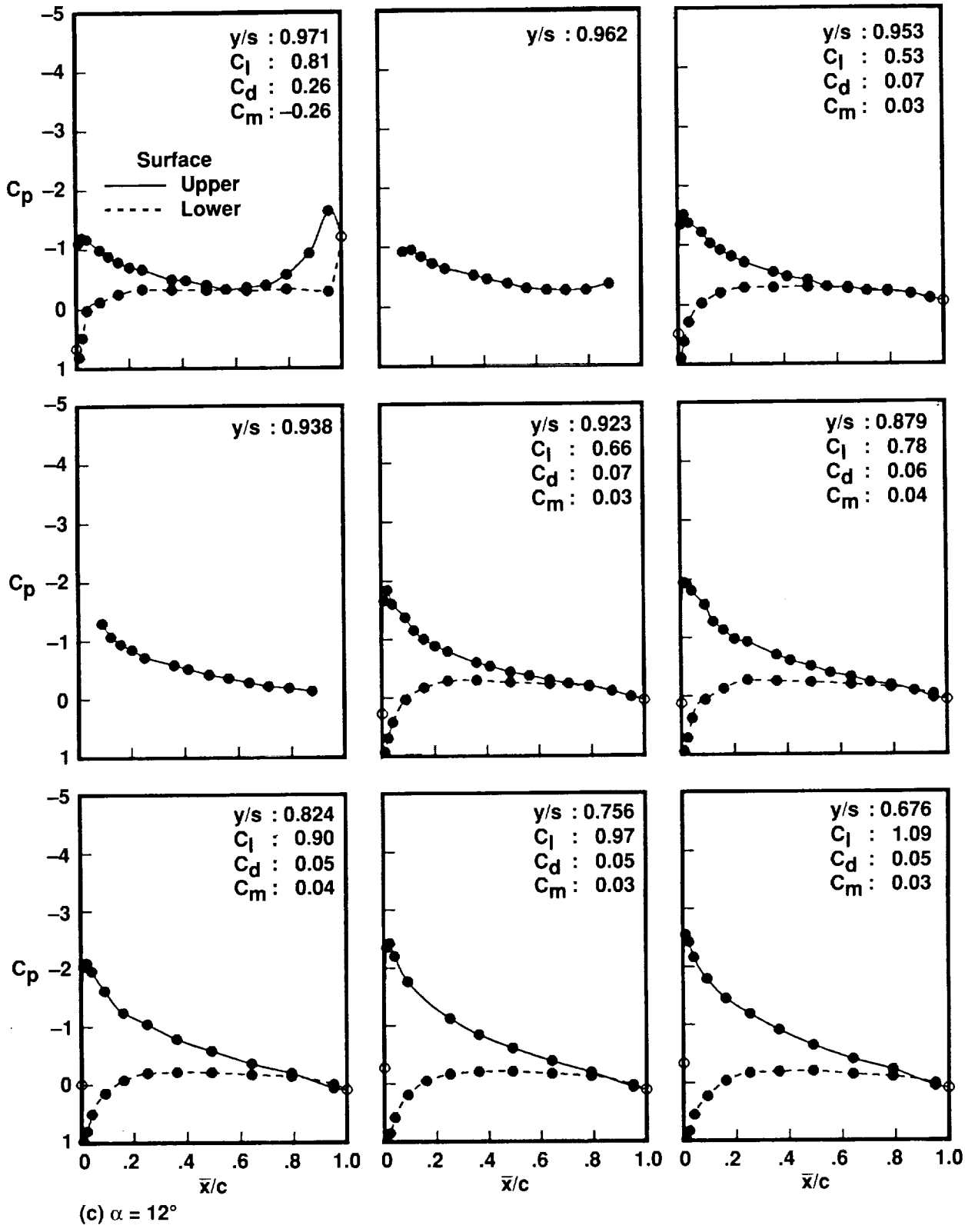

Figure 30. Continued.

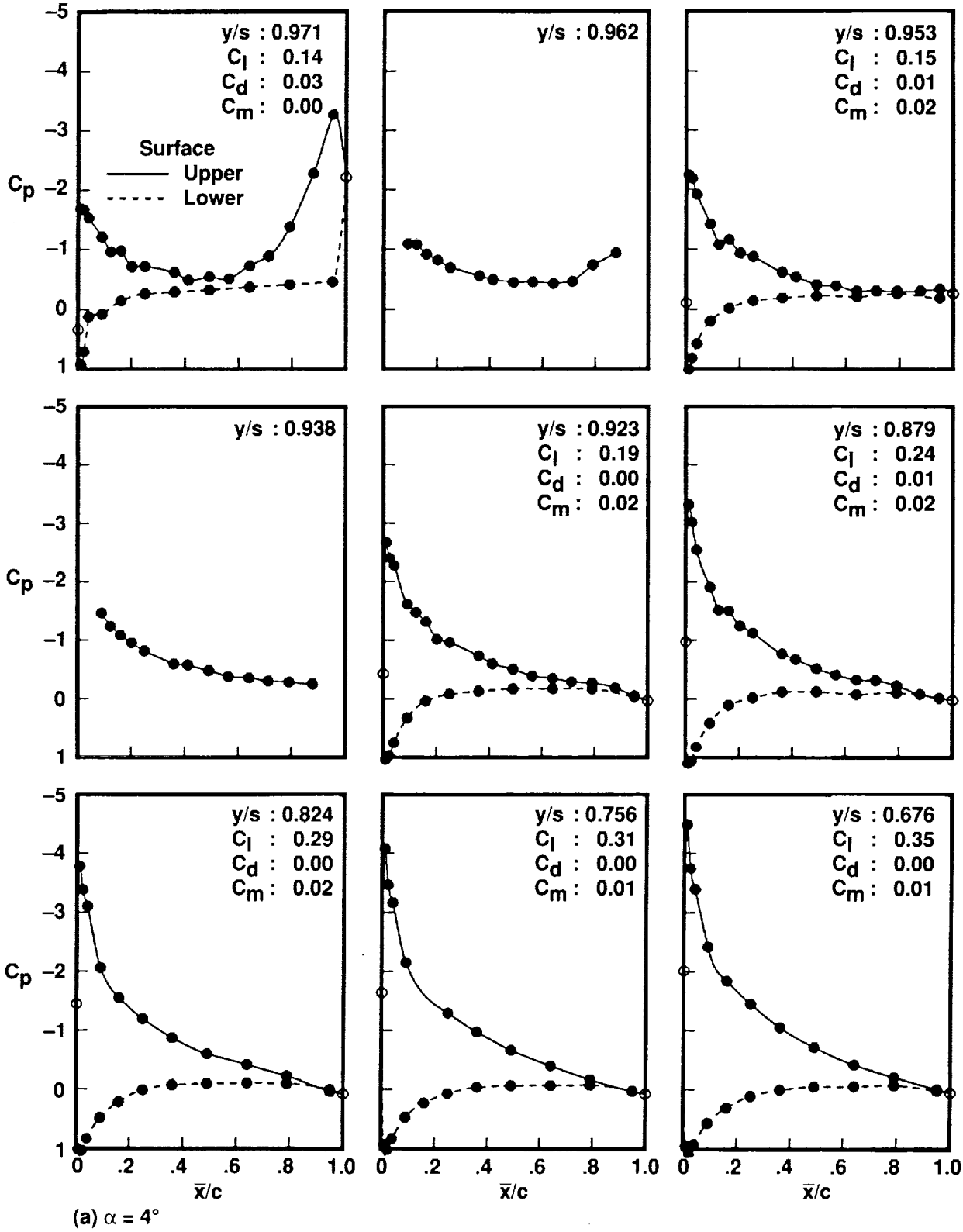

Figure 30. Concluded.

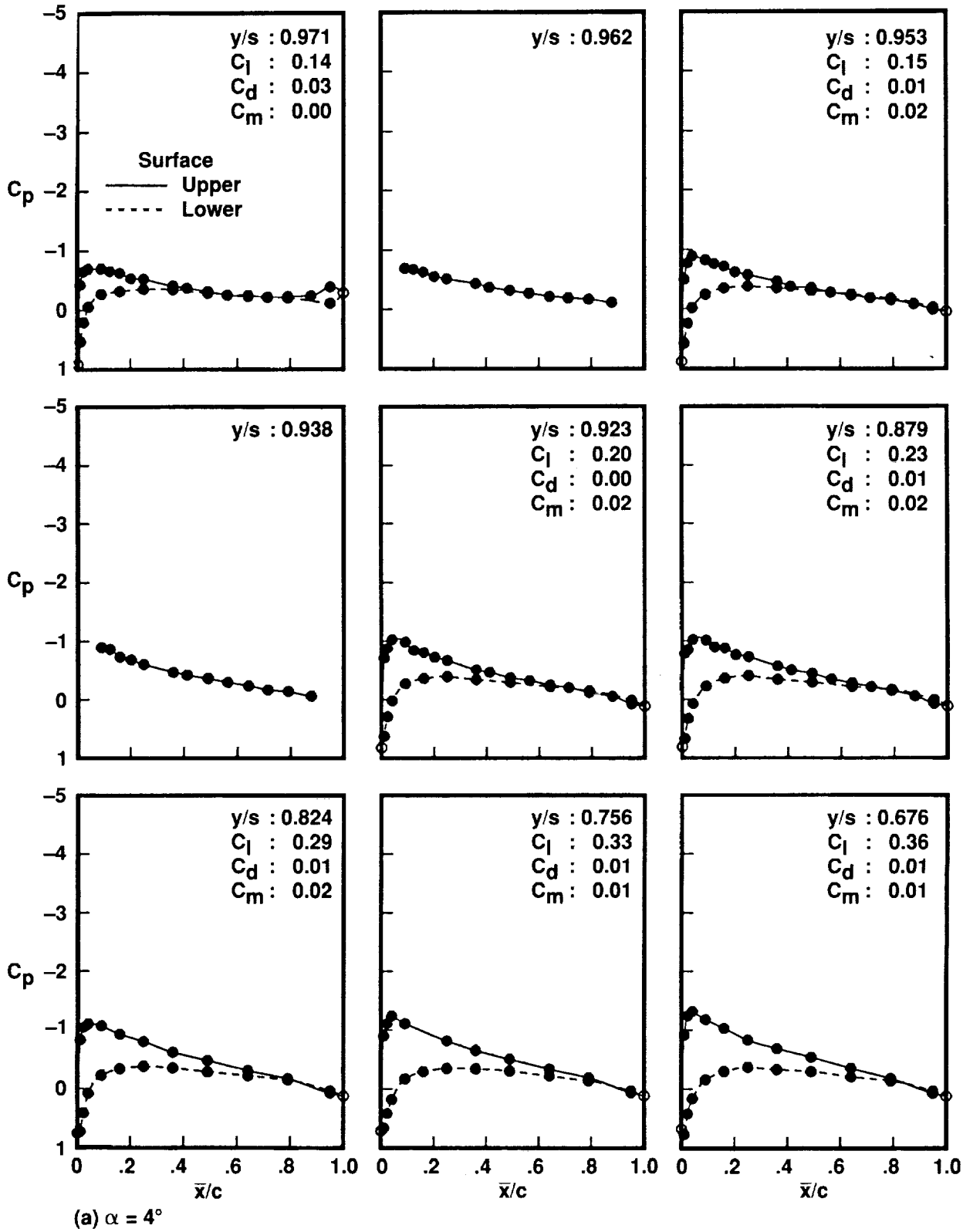

Figure 31. Pressure over outer portion of wing with round tip at $Re = 2.9 \times 10^6$.

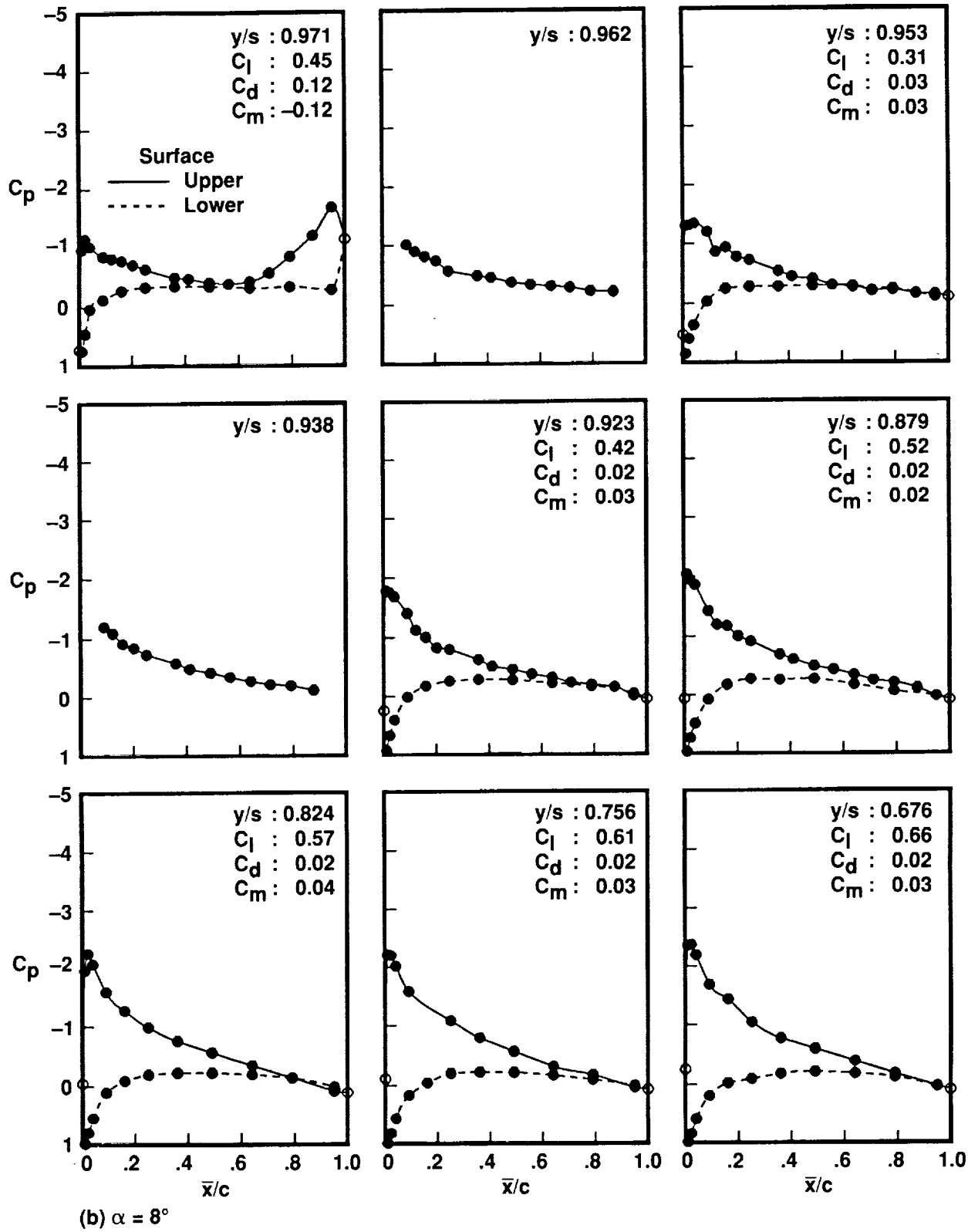

Figure 31. Continued.

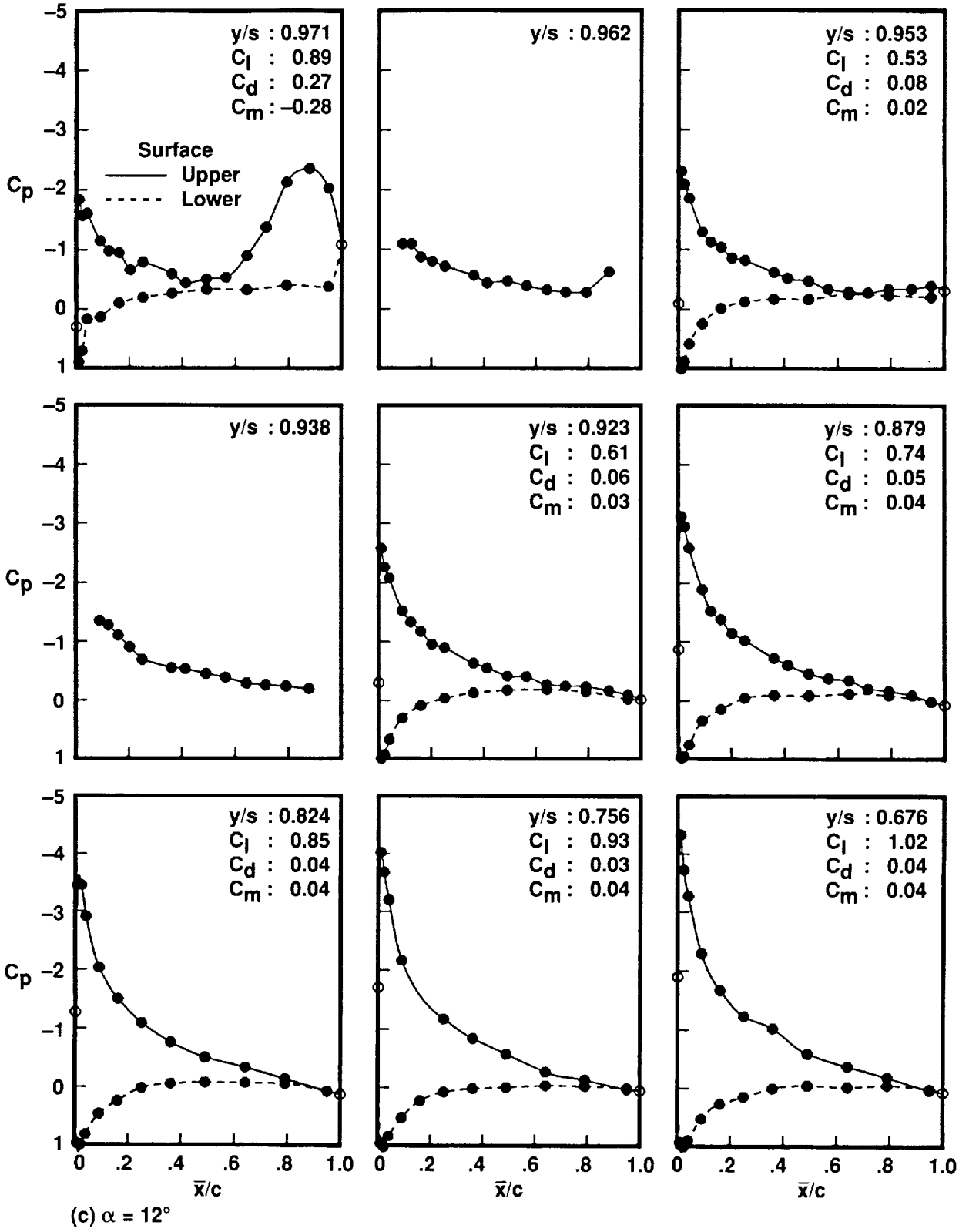

Figure 31. Concluded.

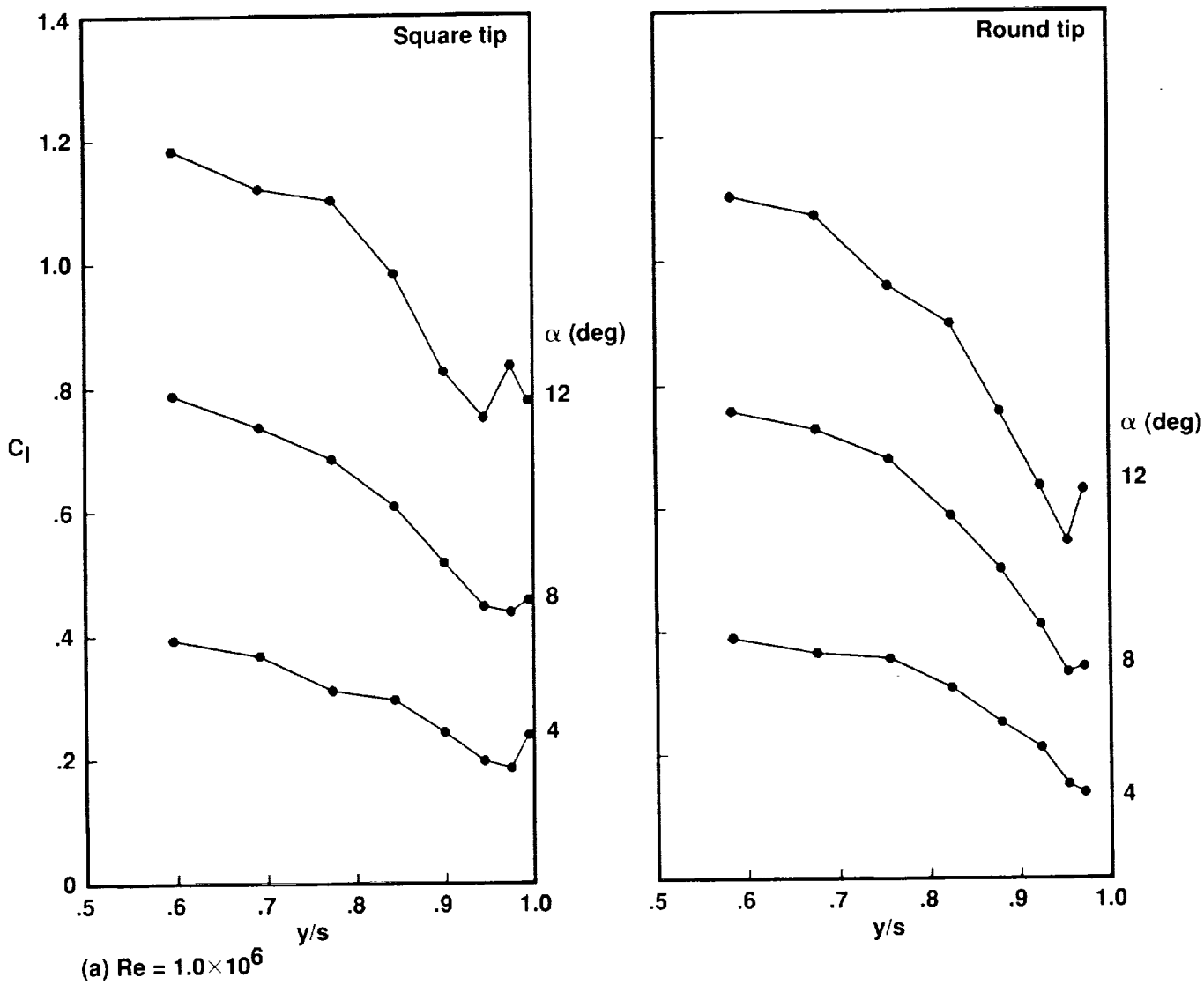

Figure 32. Pressure-derived lift distribution over outer portion of wing.

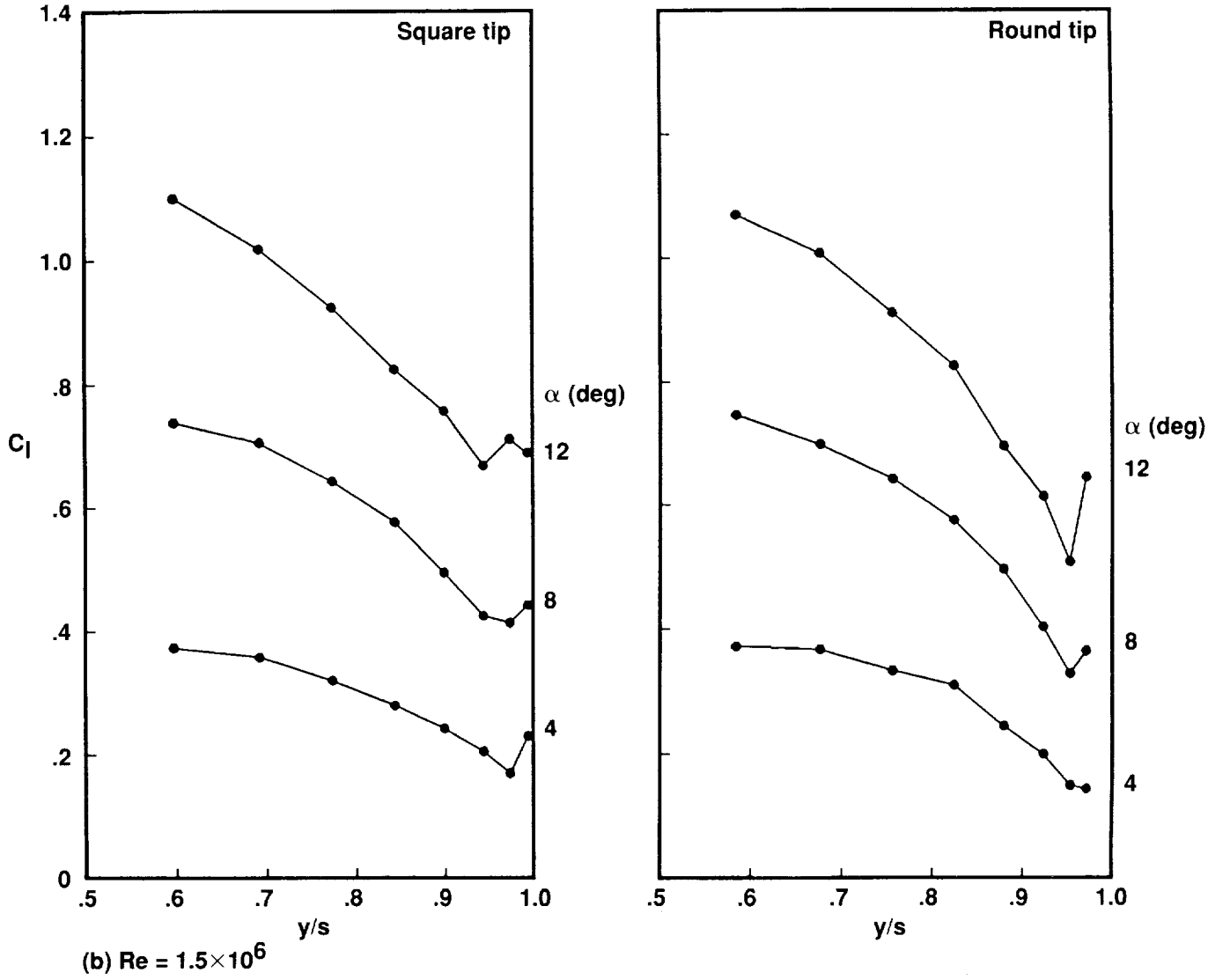

Figure 32. Continued.

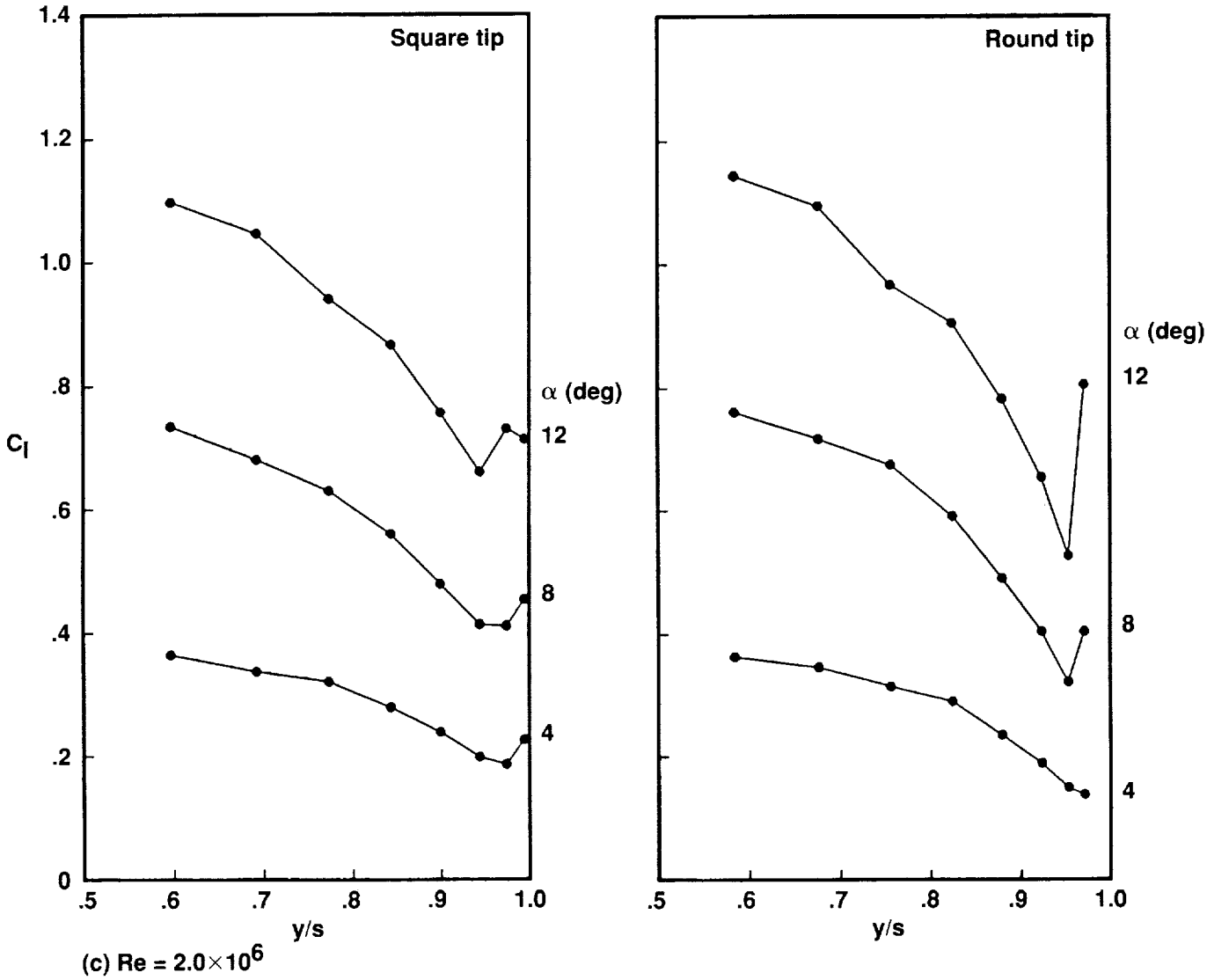

Figure 32. Continued.

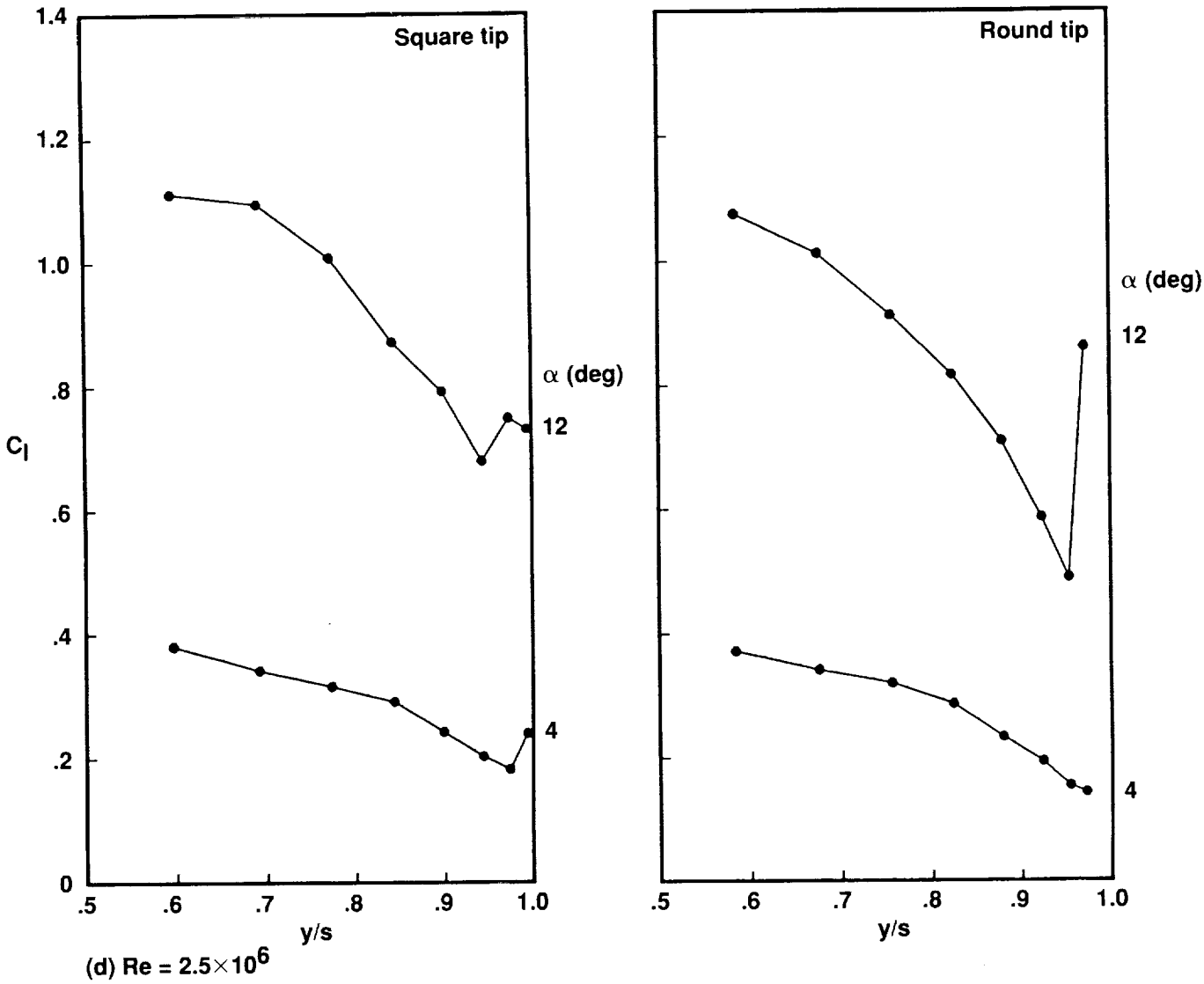

Figure 32. Continued.

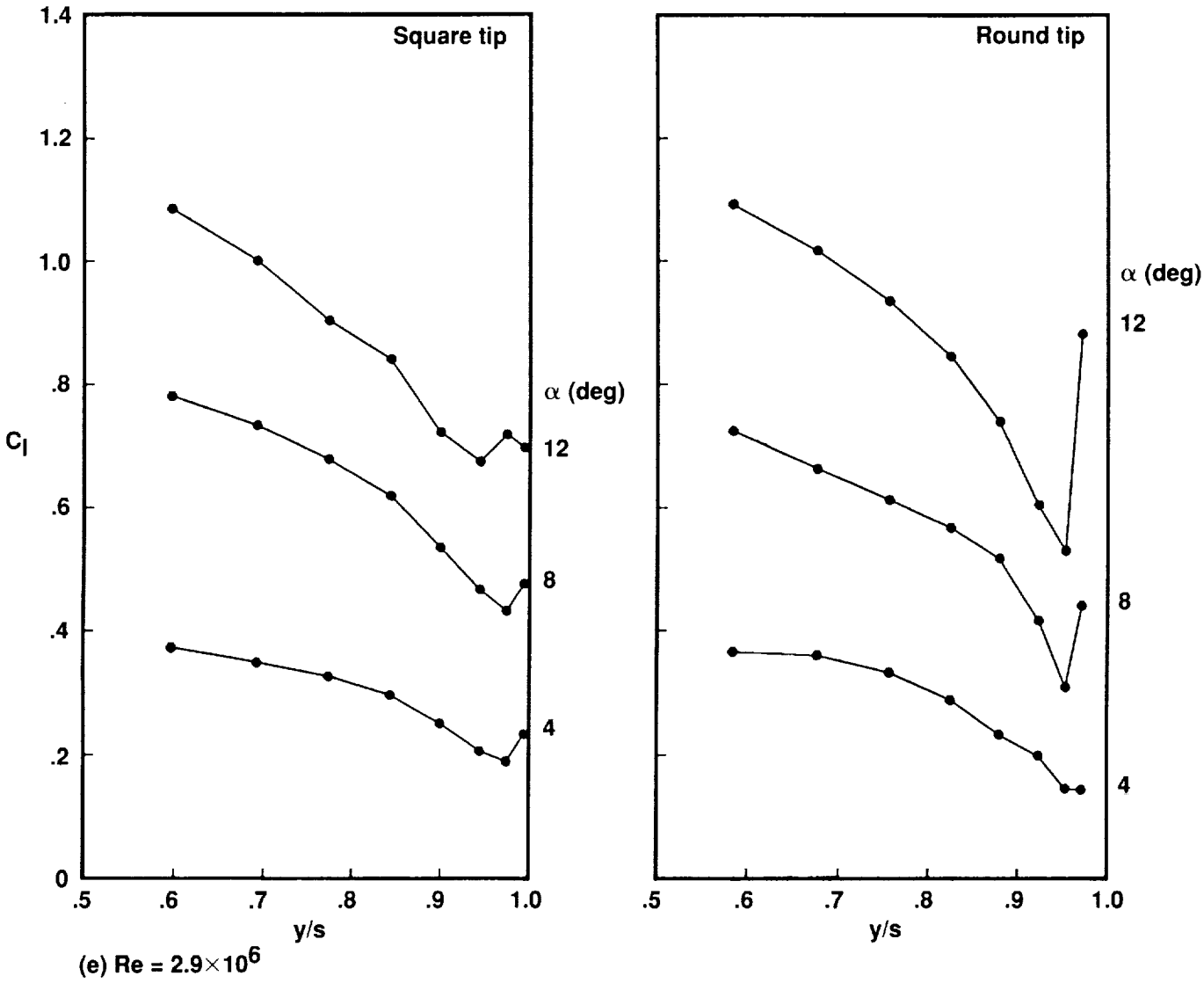

Figure 32. Concluded.

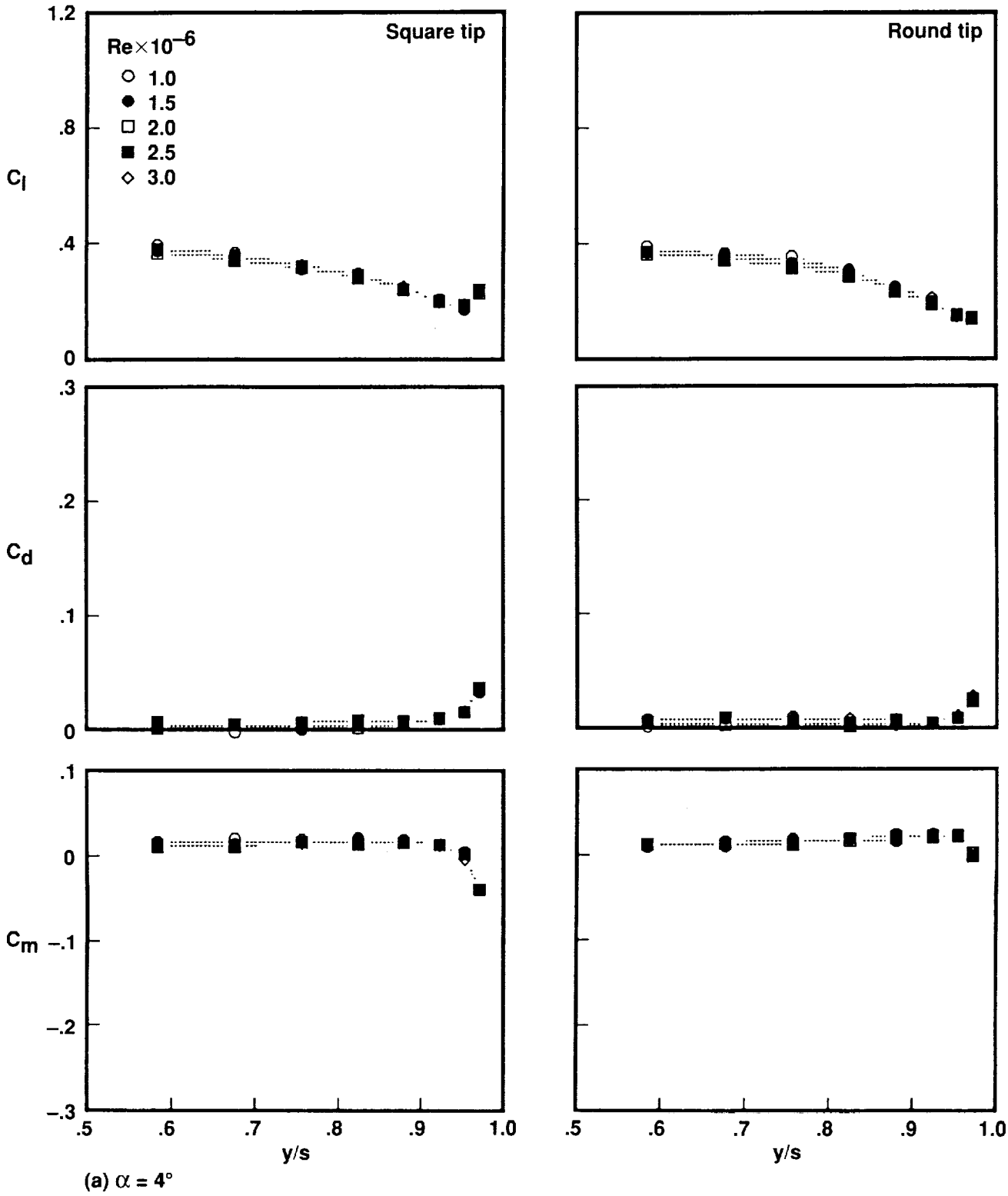

Figure 33. Load variation over outer portion of wing span at different Reynolds numbers.

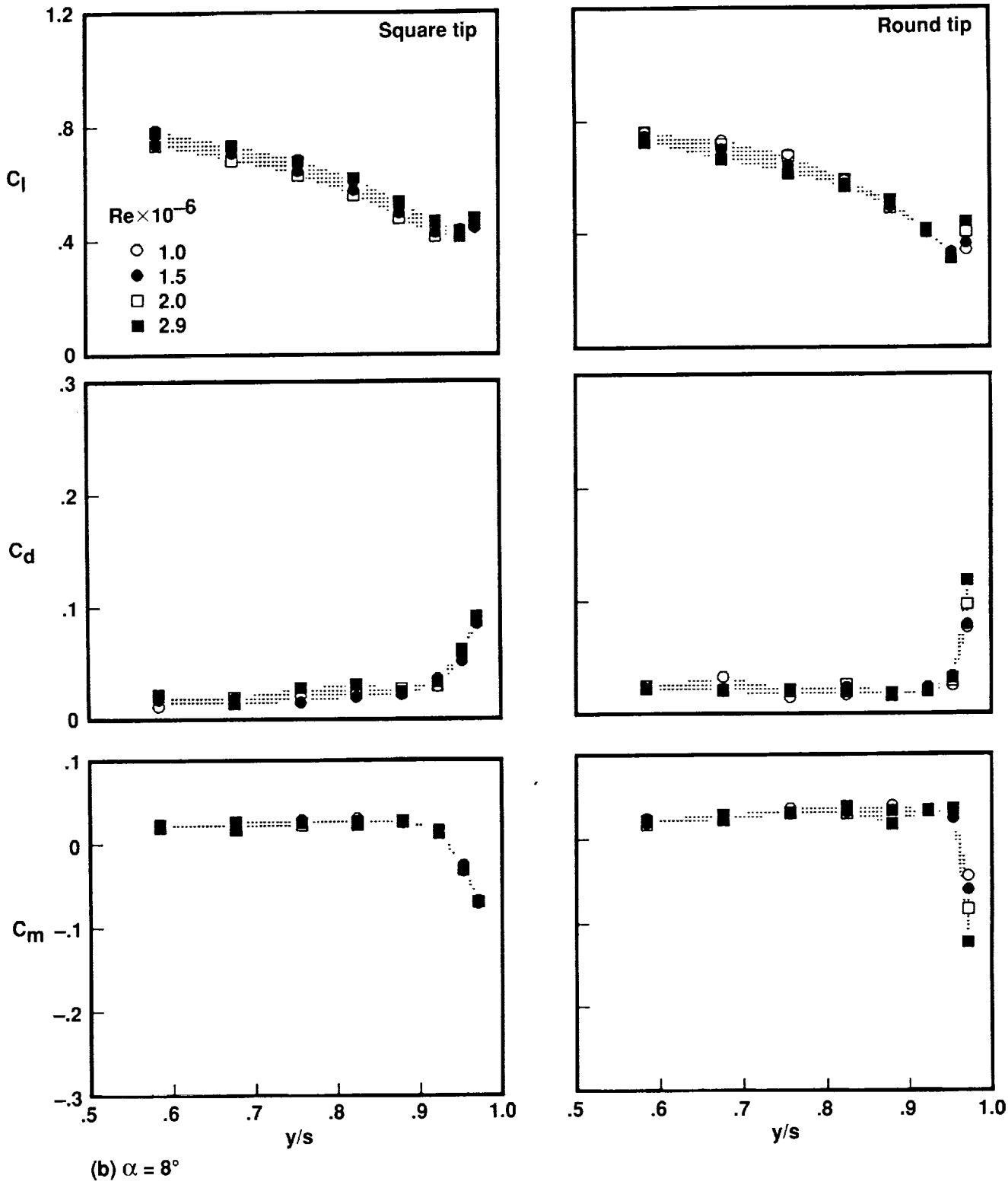

Figure 33. Continued.

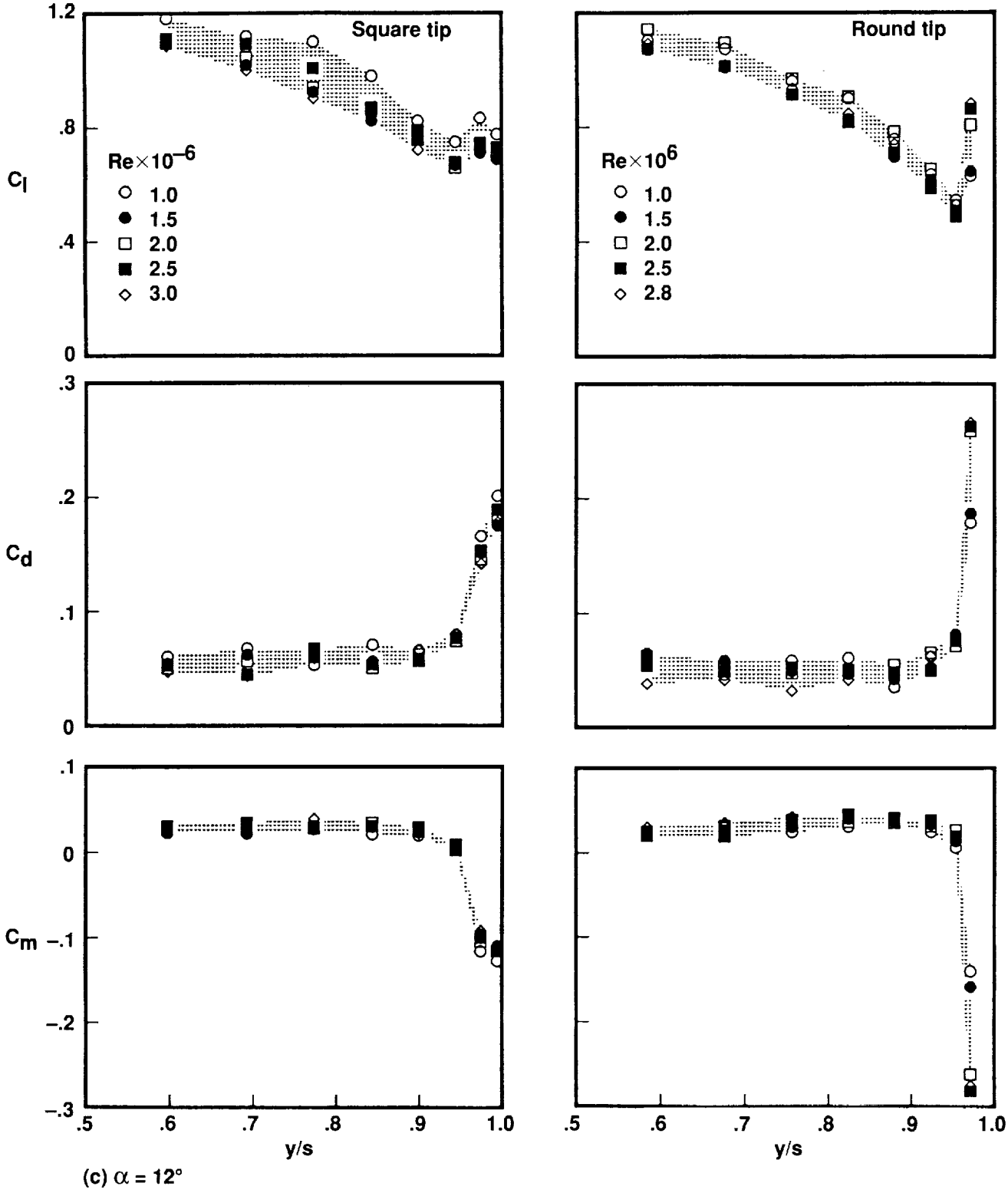

Figure 33. Concluded.

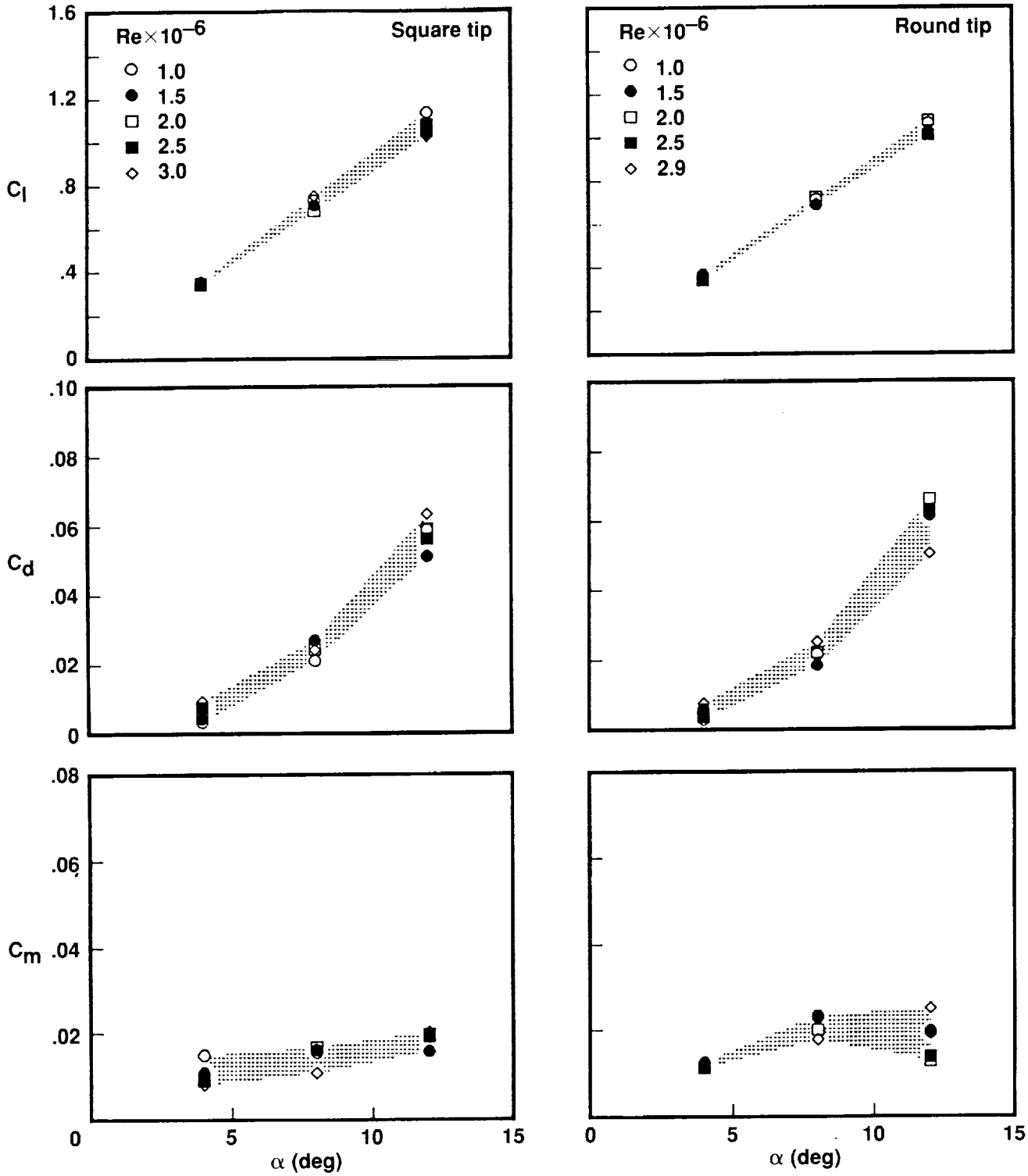

Figure 34. Integrated loads over full wing span with square and round tips at different Reynolds numbers.

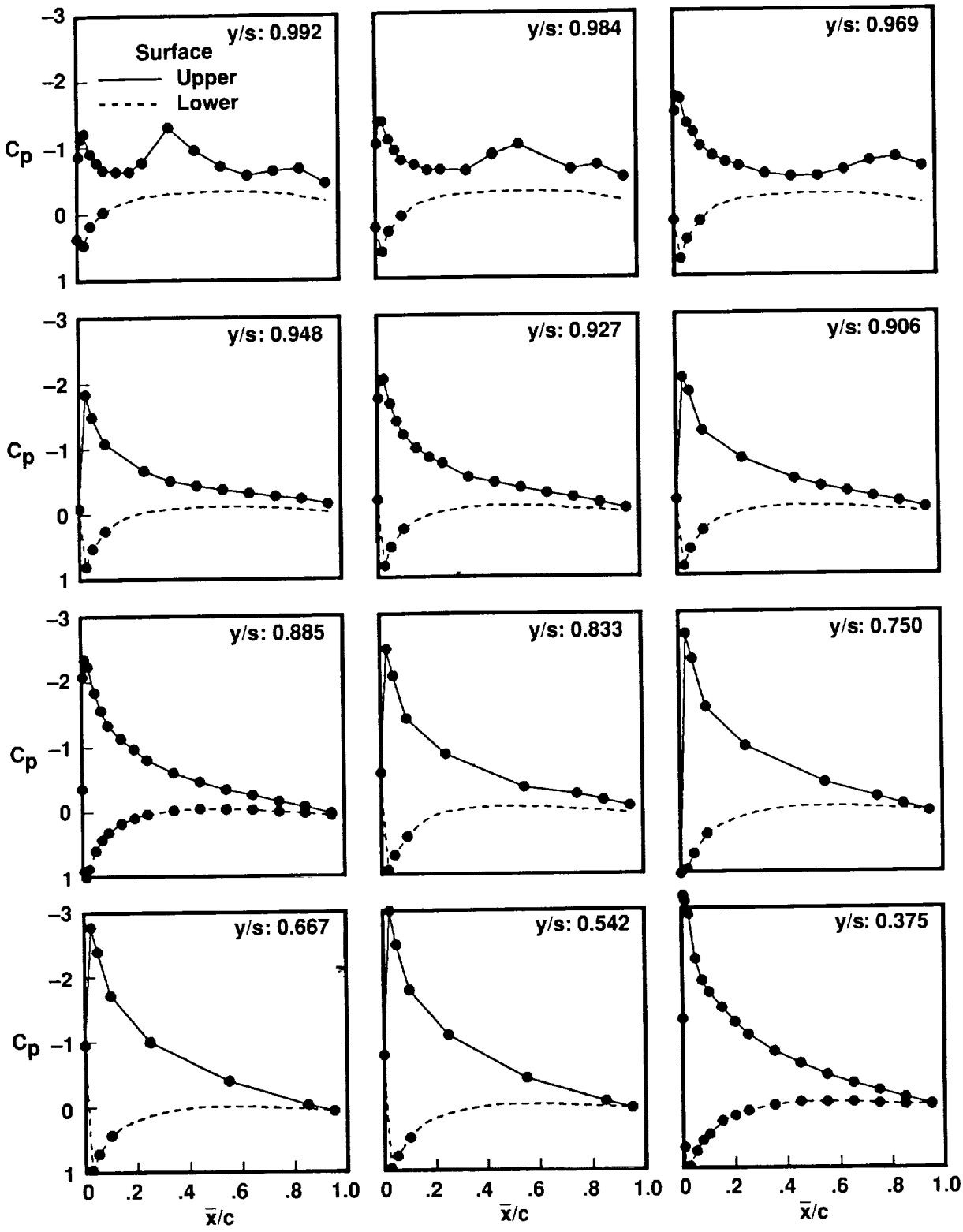

Figure 35. Pressure along wing with square tip from Spivey–Morehouse experiment (ref. 37) with test conditions $\alpha = 11.8°$, $M_\infty = 0.17$ and $Re = 1.8 \times 10^6$.

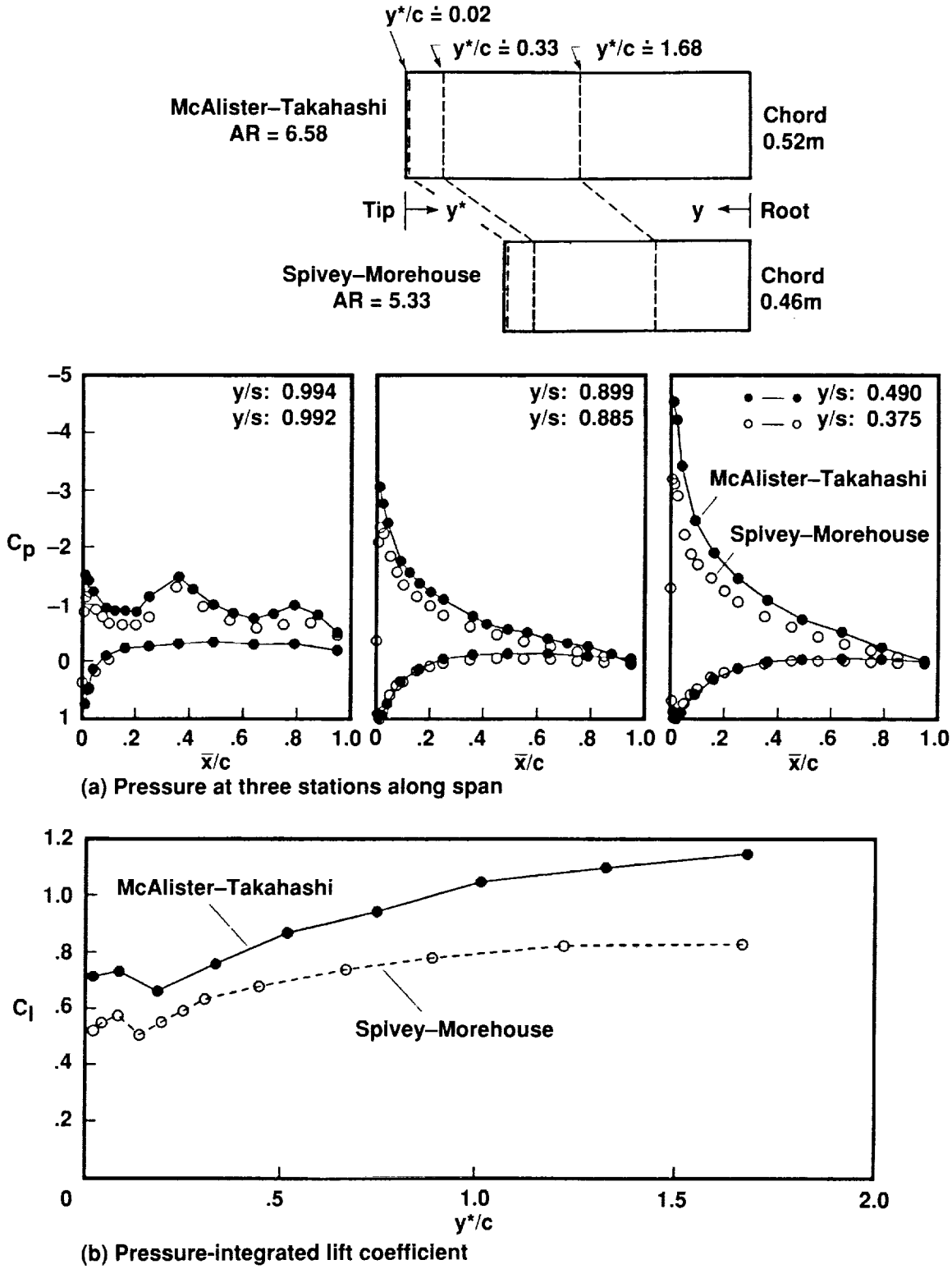

Figure 36. Measurements along wing span with square tip compared with results from Spivey–Morehouse experiment (ref. 37) with test conditions $\alpha \approx 12°$ and $Re \approx 2 \times 10^6$.

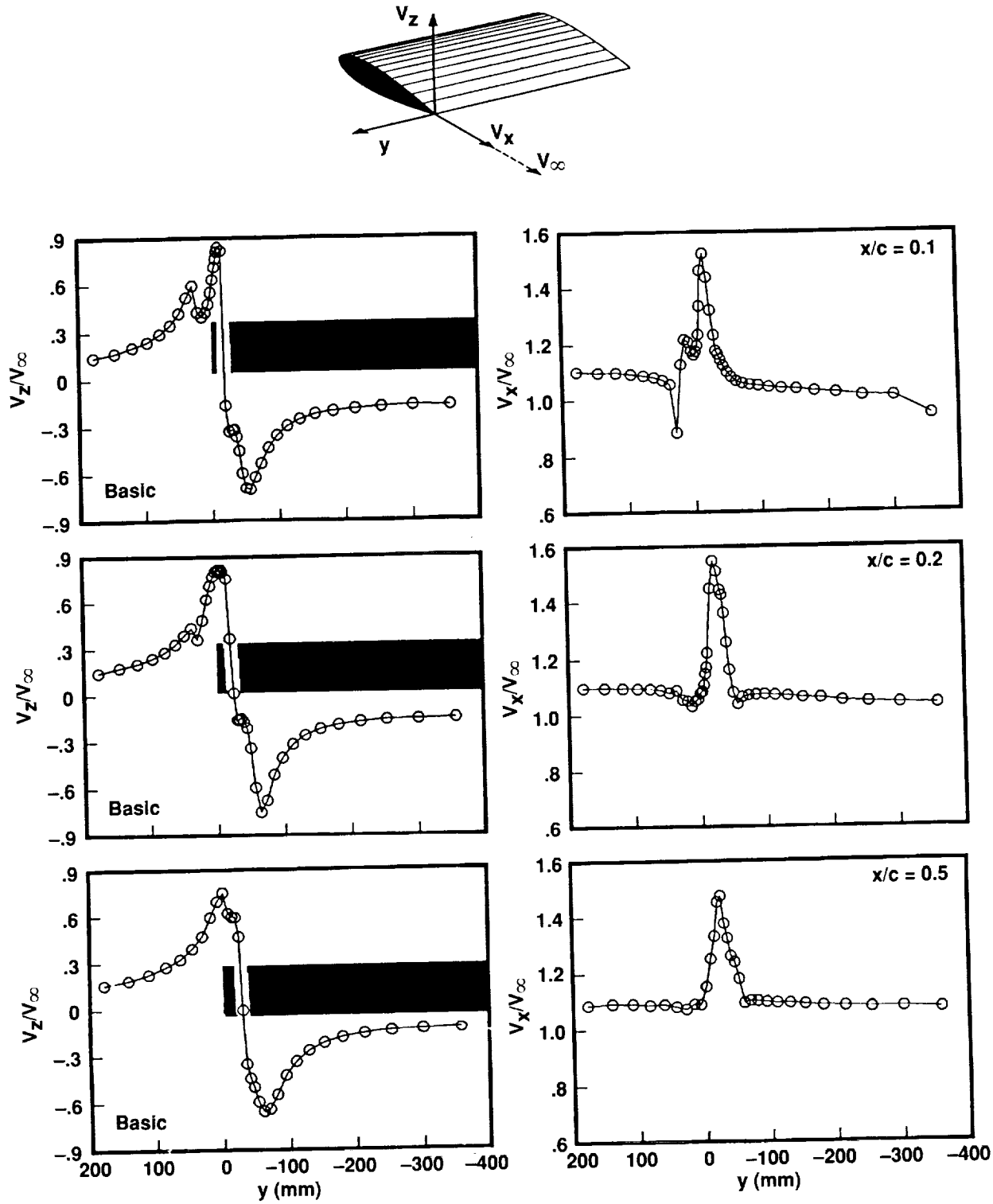

Figure 39. Downstream development of trailing vortex from "basic" wing (square tip, AR = 6.6) with $c = 52$ cm at $Re = 1.5 \times 10^6$ and $\alpha = 12°$.

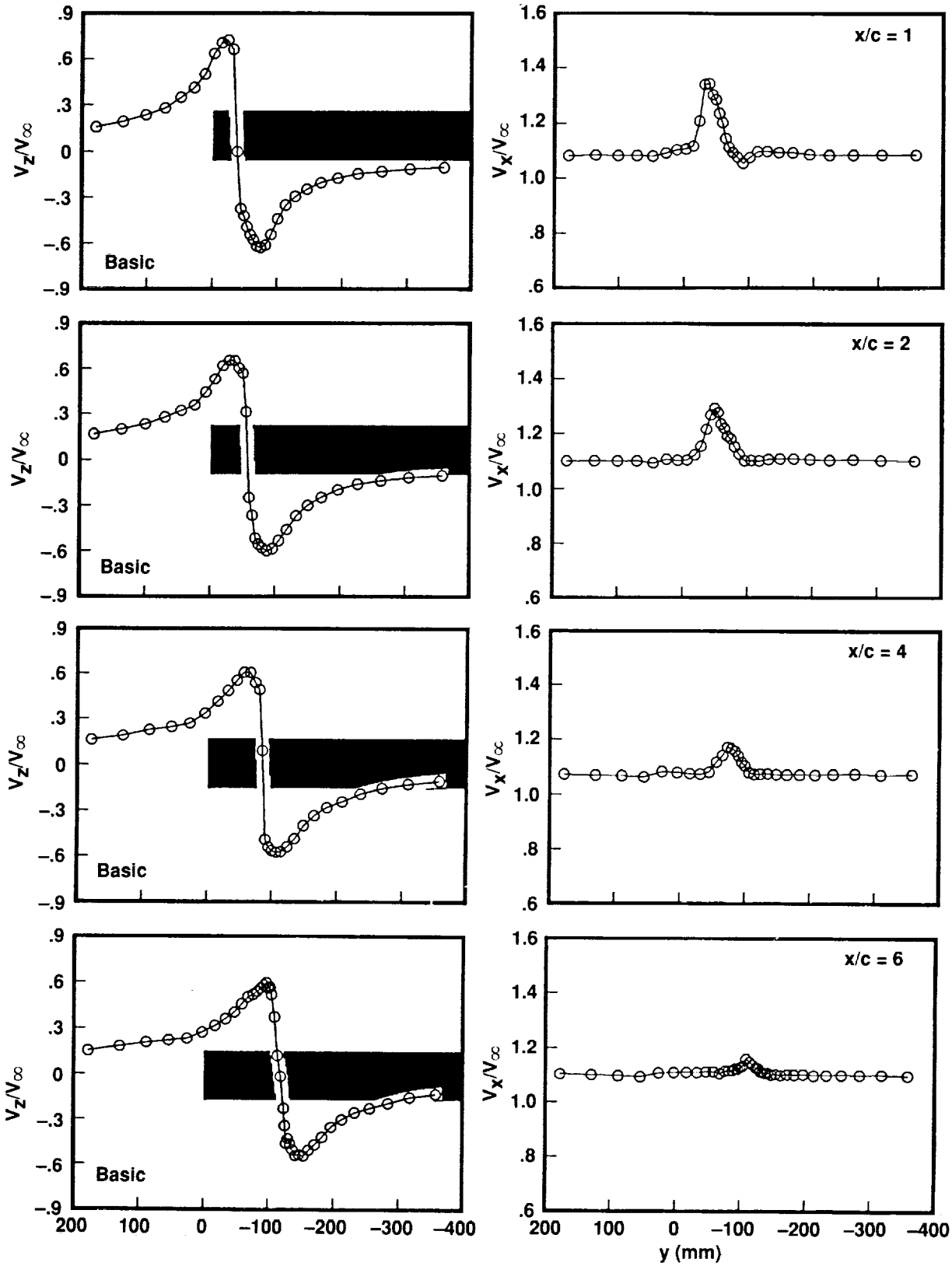

Figure 39. Concluded.

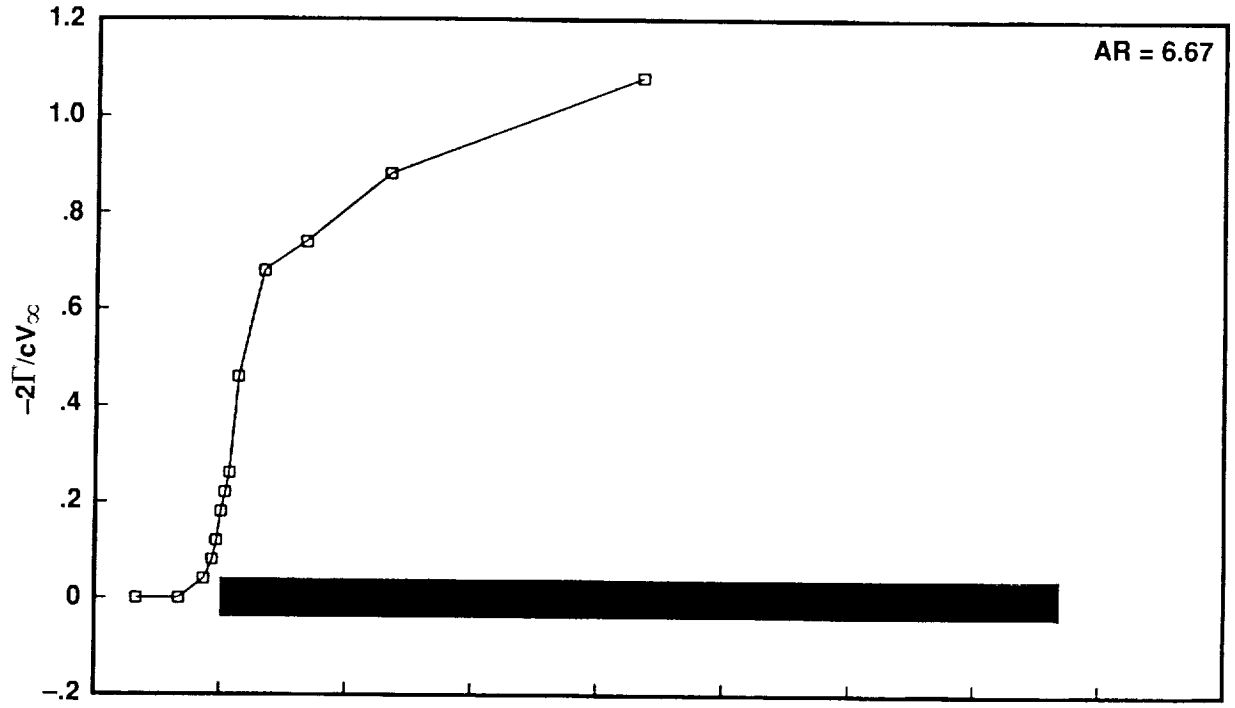

(a) Wing c = 0.30m and s = 1.00m with square tip

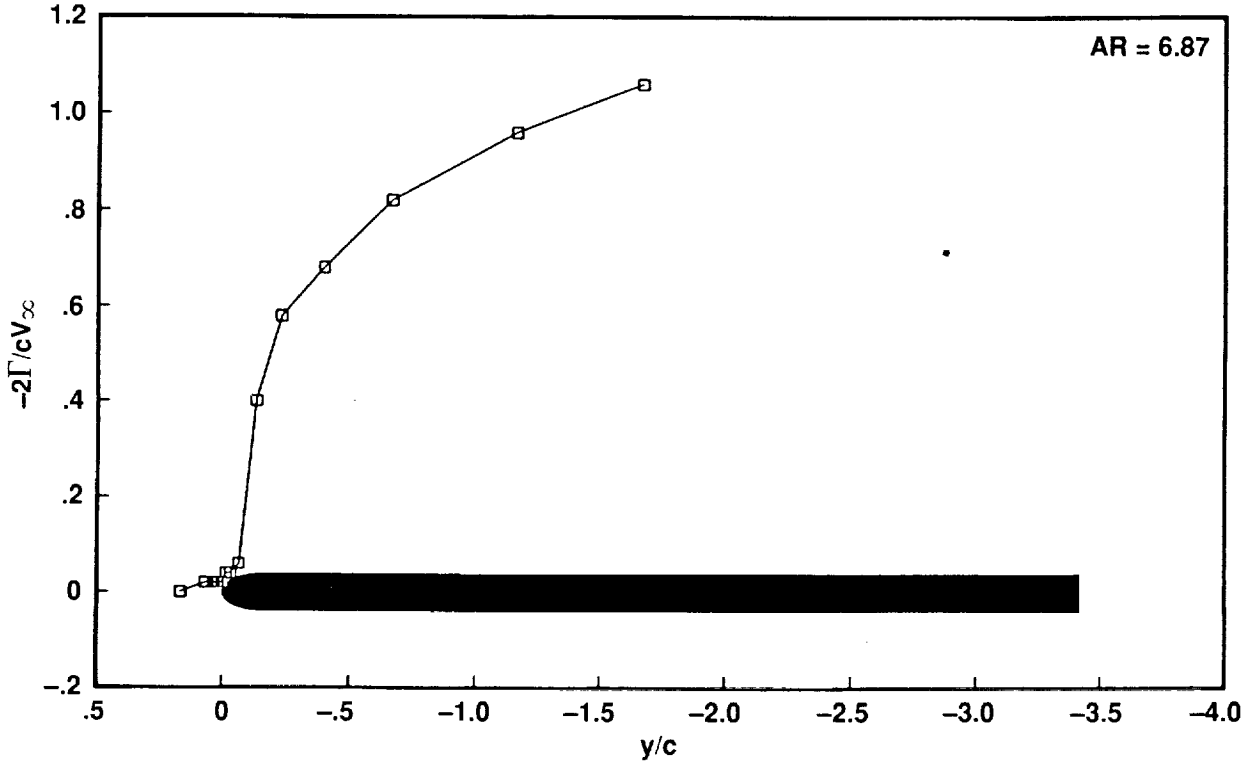

(b) Wing c = 0.30 and s = 1.03m with round tip

Figure 37. Circulation along wing span at $\alpha = 12°$ and $Re = 1.5 \times 10^6$.

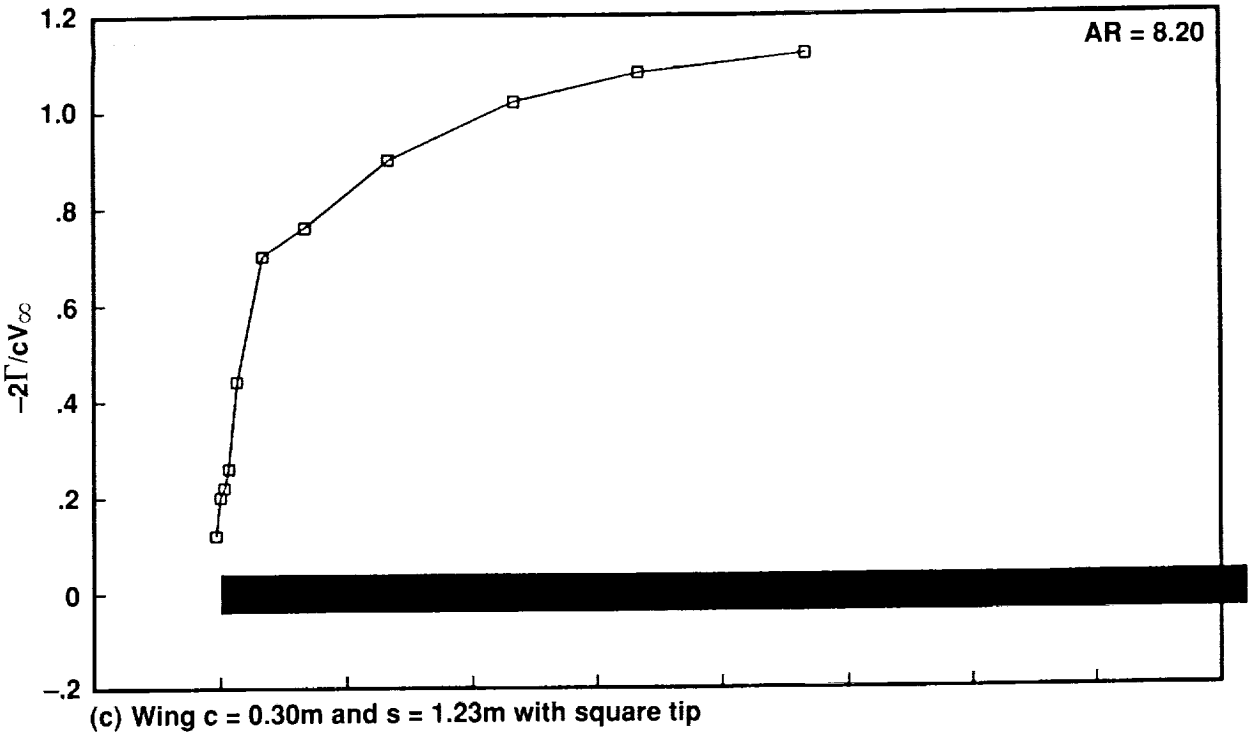

(c) Wing c = 0.30m and s = 1.23m with square tip

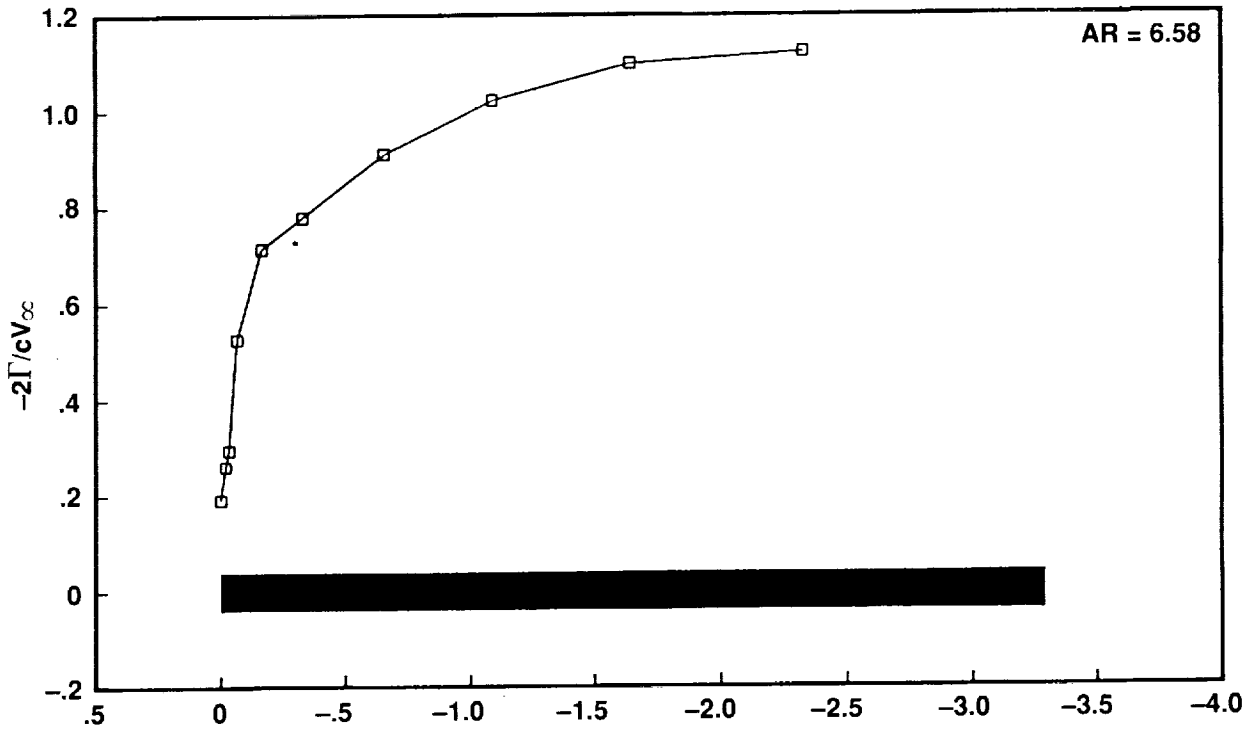

(d) Wing c = 0.52m and s = 1.71m with square tip

Figure 37. Concluded.

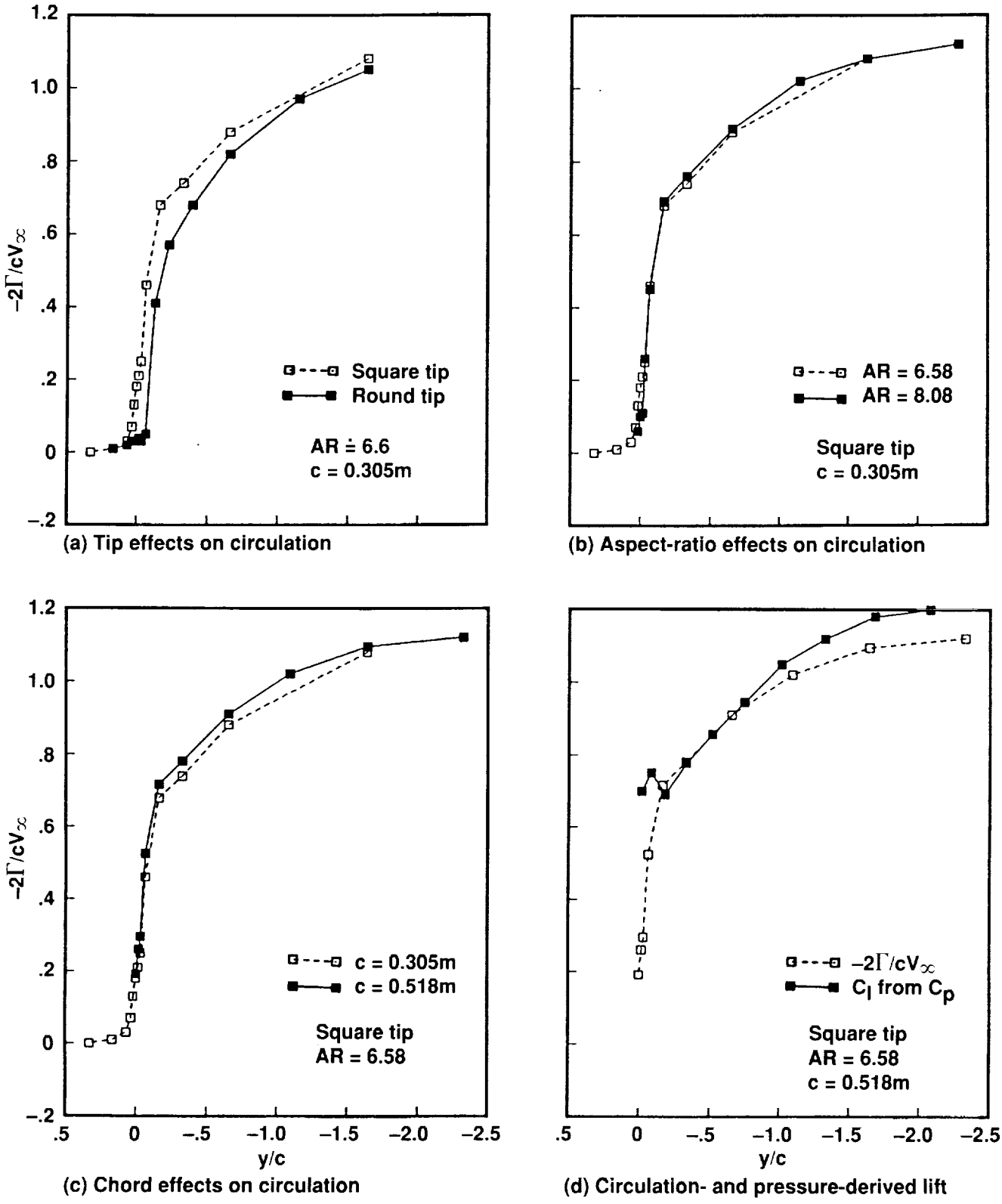

Figure 38. Comparison of circulation along wing span at $\alpha = 12°$ and $Re = 1.5 \times 10^6$.

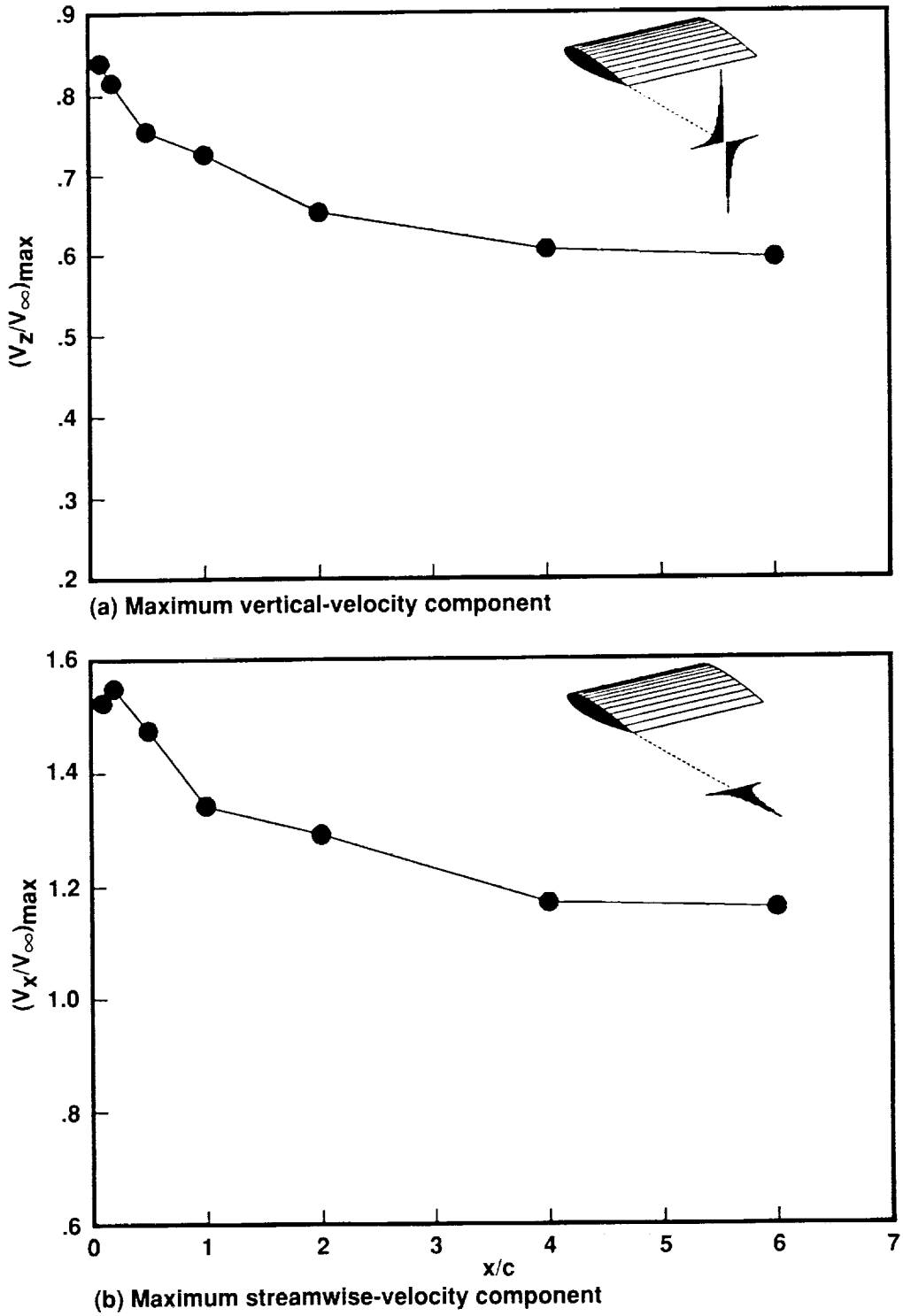

Figure 40. Downstream change in maximum vertical and streamwise velocities within trailing vortex from basic wing with $c = 52$ cm at $Re = 1.5 \times 10^6$ and $\alpha = 12°$.

C-2

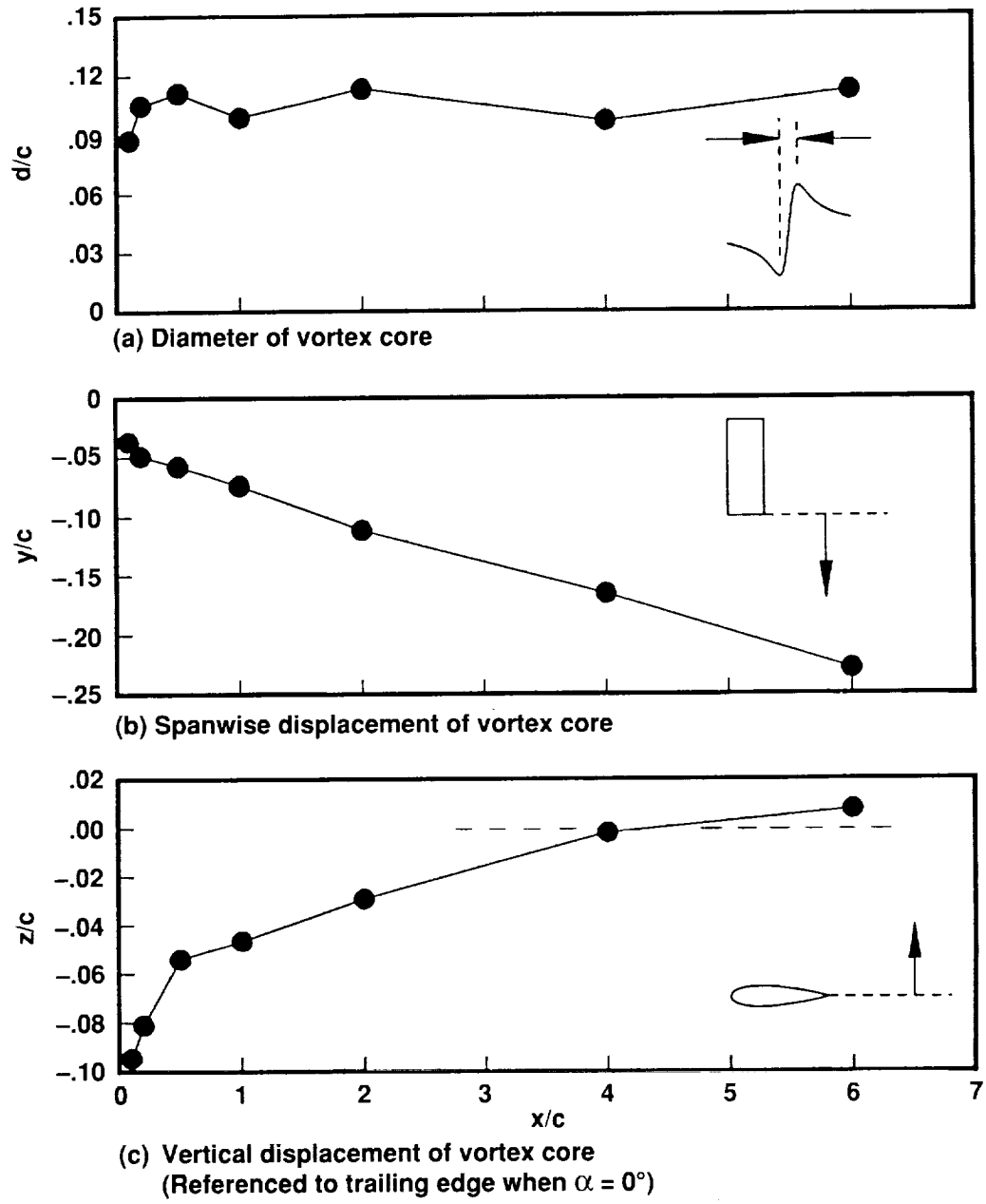

Figure 41. Downstream change in size and position of vortex core trailing from basic wing with $c = 52$ cm at $Re = 1.5 \times 10^6$ and $\alpha = 12°$.

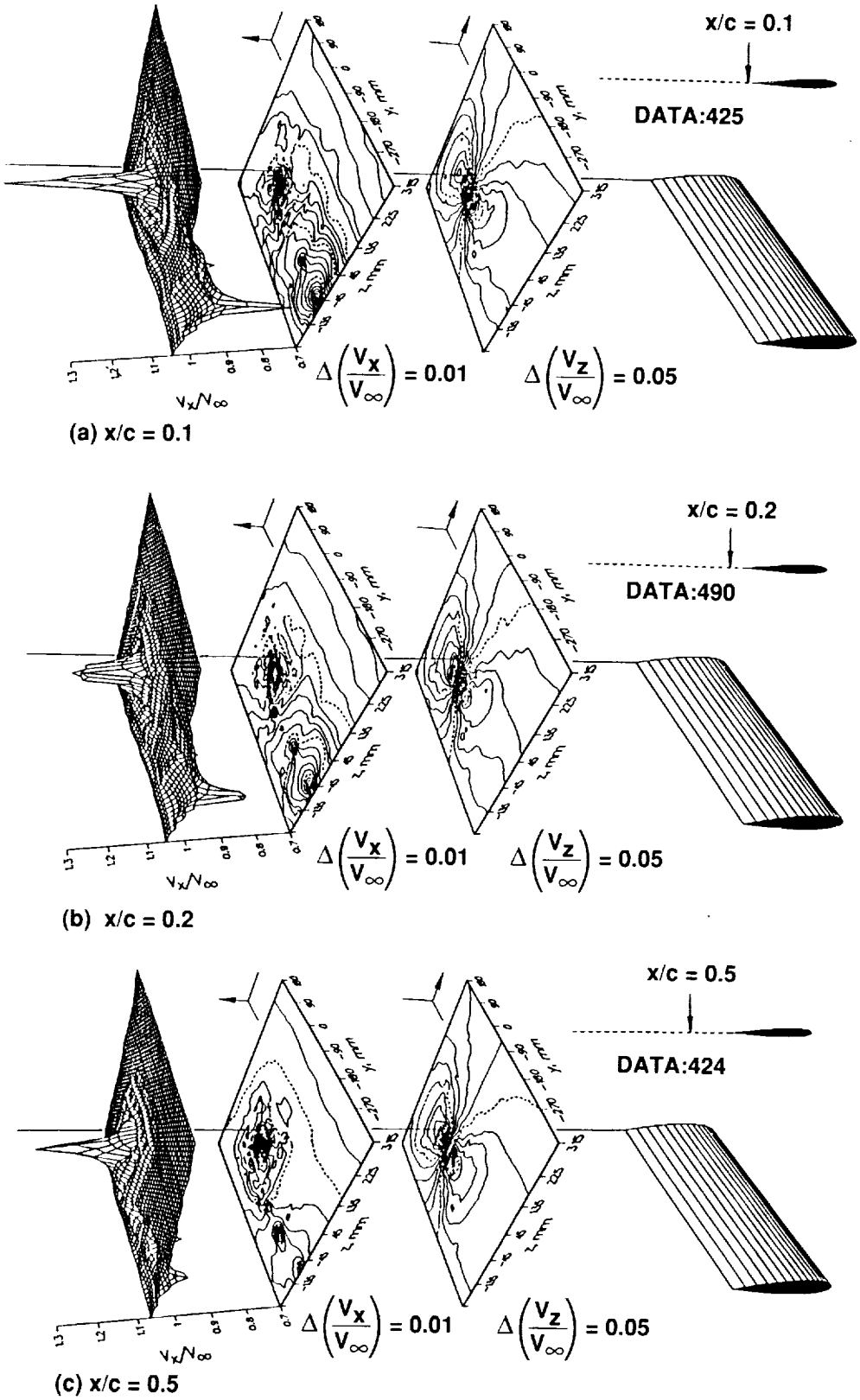

Figure 42. Vertical and streamwise velocity contours around trailing vortex from basic wing with $c = 52$ cm at $Re = 1.5 \times 10^6$ and $\alpha = 12°$ measured at different downstream stations.

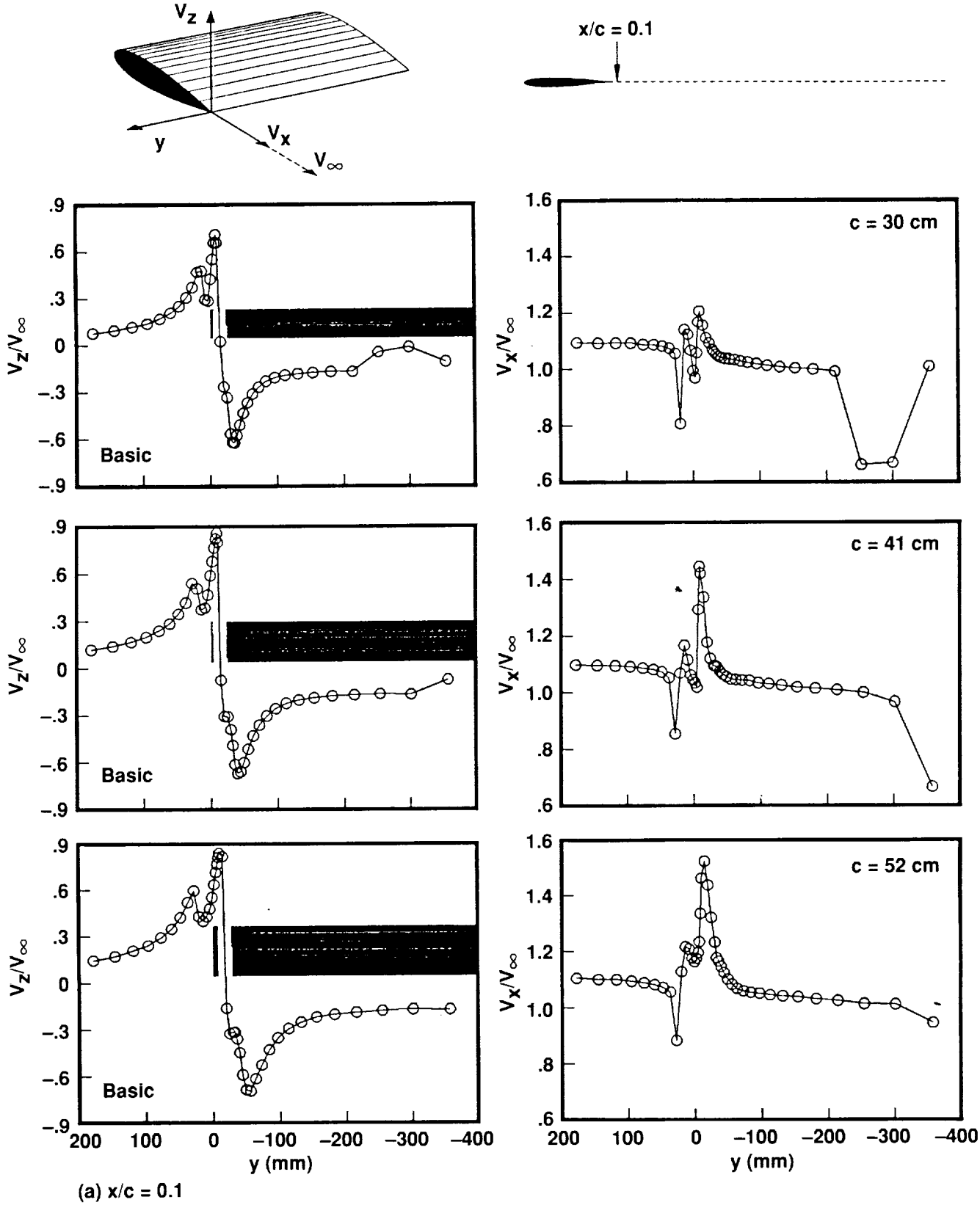

Figure 43. Vertical and streamwise velocity components across trailing vortex from basic wing with $Re = 1.5 \times 10^6$ and $\alpha = 12°$ for different chord lengths while maintaining $C_l V_\infty$ = constant.

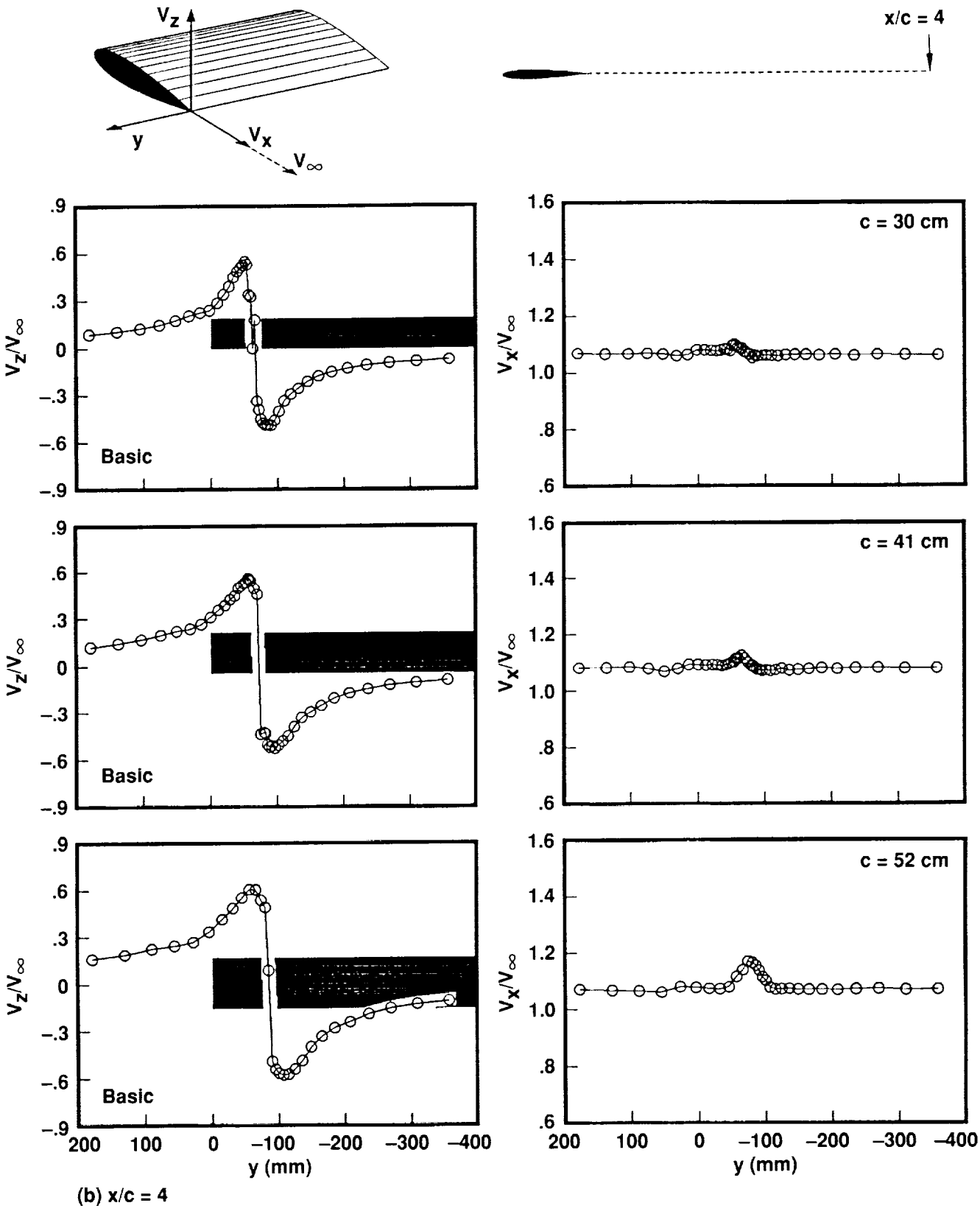

(b) x/c = 4

Figure 43. Concluded.

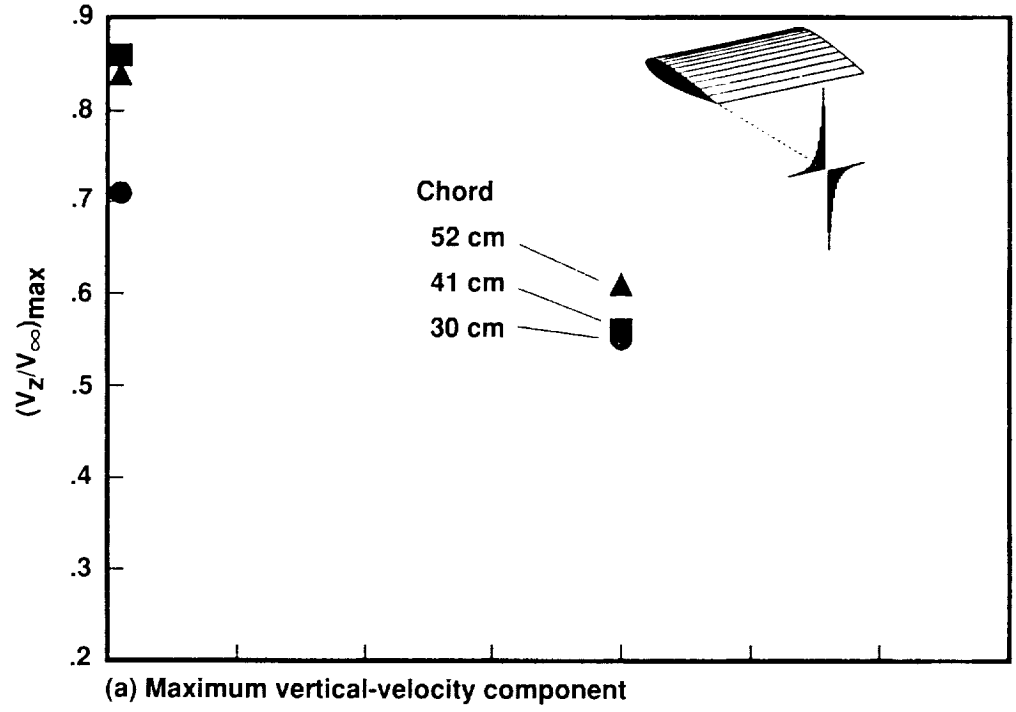

(a) Maximum vertical-velocity component

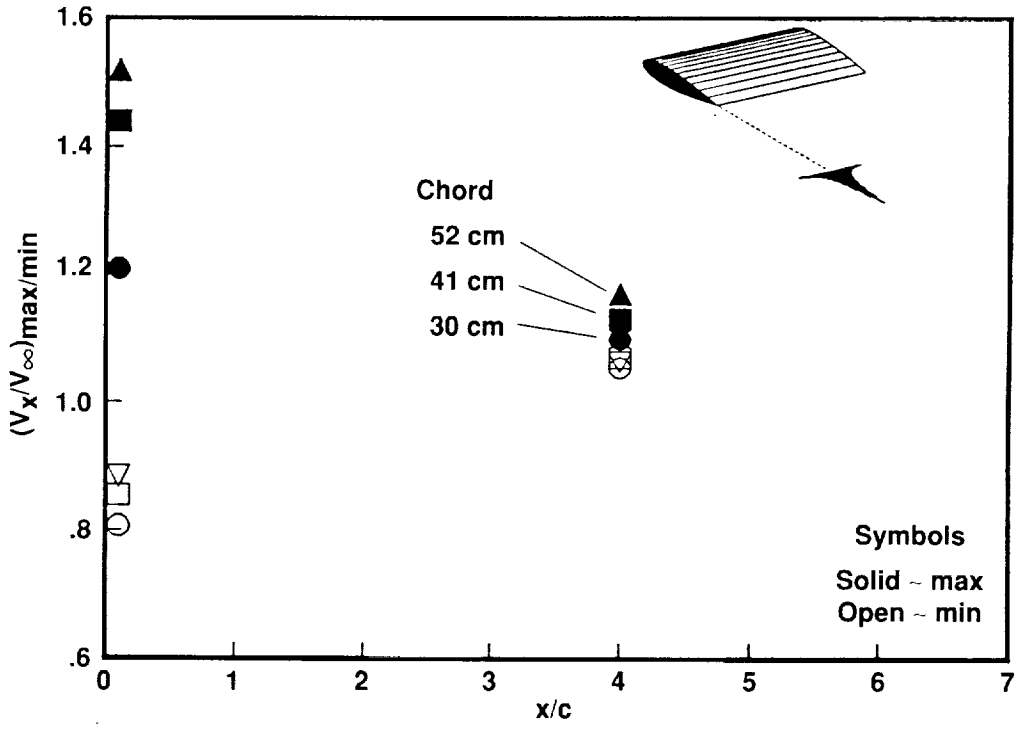

(b) Maximum streamwise-velocity component

Figure 44. Maximum vertical and streamwise velocities within trailing vortex from basic wing at $Re = 1.5 \times 10^6$ and $\alpha = 12°$ for different chord lengths while maintaining $C_l V_\infty$ = constant.

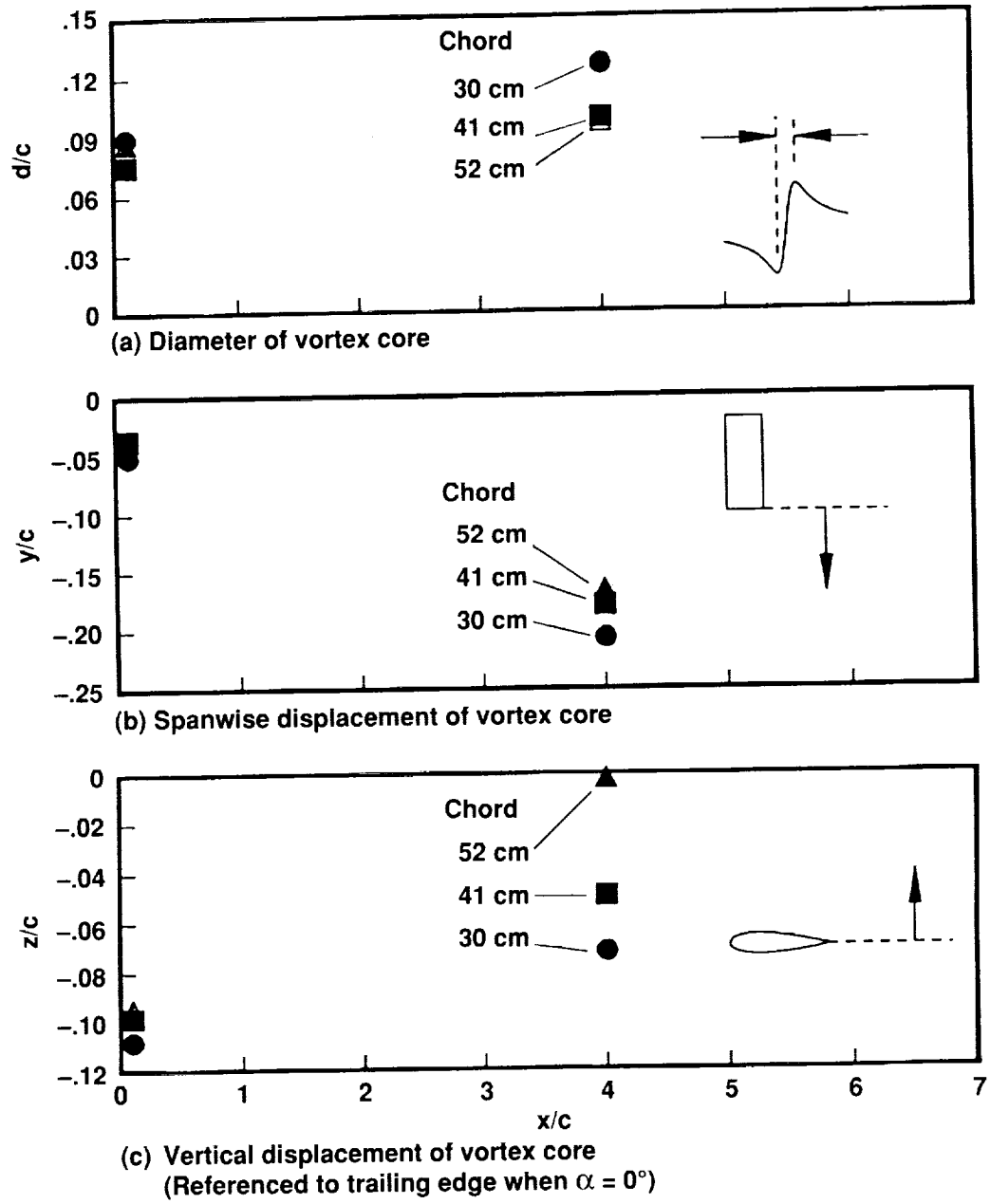

Figure 45. Size and position of vortex core trailing from basic wing at $Re = 1.5 \times 10^6$ and $\alpha = 12°$ for different chord lengths while maintaining $C_l V_\infty$ = constant.

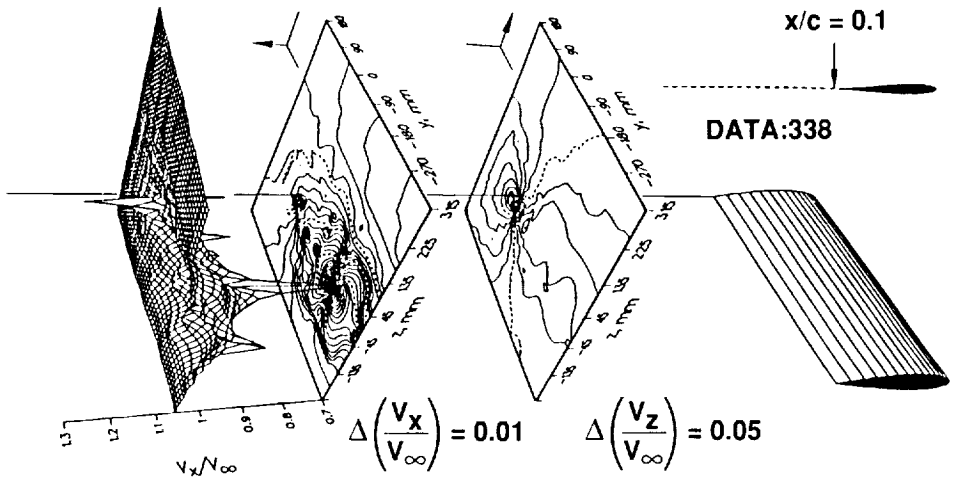

(a) c = 30 cm

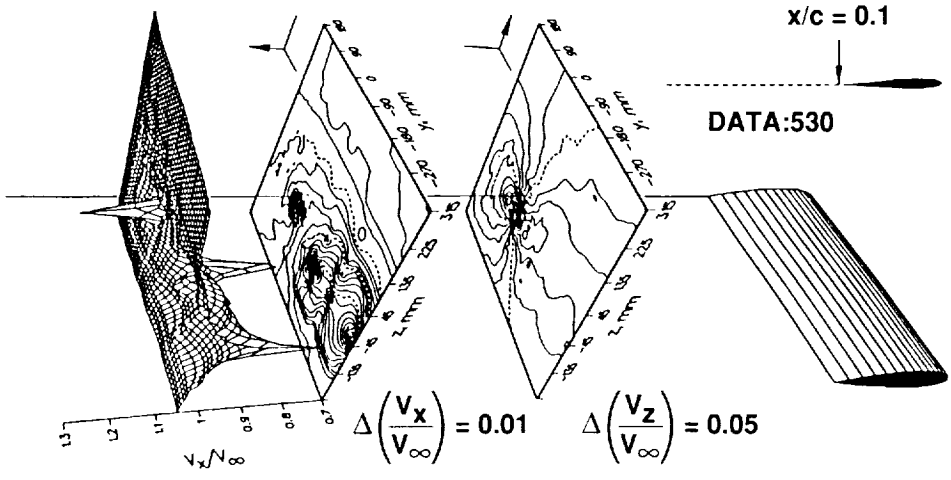

(b) c = 41 cm

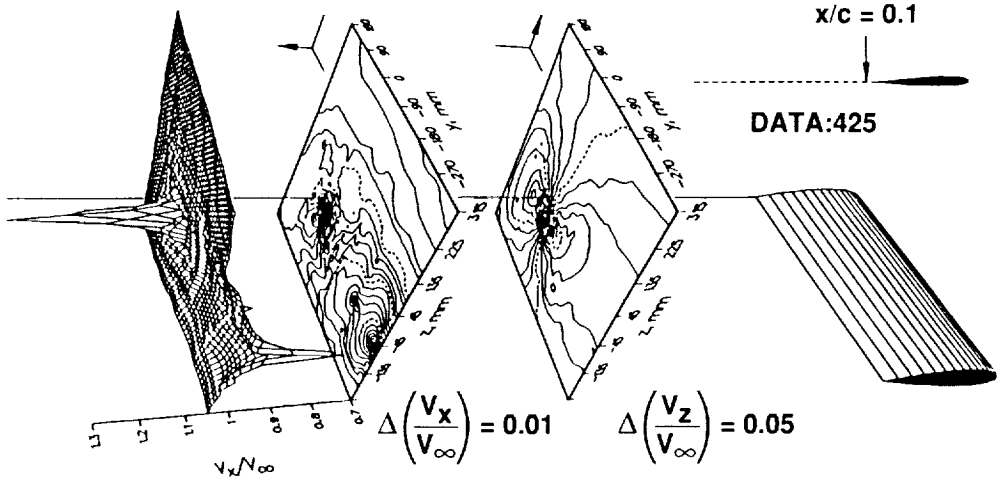

(c) c = 52 cm

Figure 46. Vertical and streamwise velocity contours around trailing vortex from basic wing at $x/c = 0.1$ with $Re = 1.5 \times 10^6$ and $\alpha = 12°$ for different chord lengths while maintaining $C_l V_\infty$ = constant.

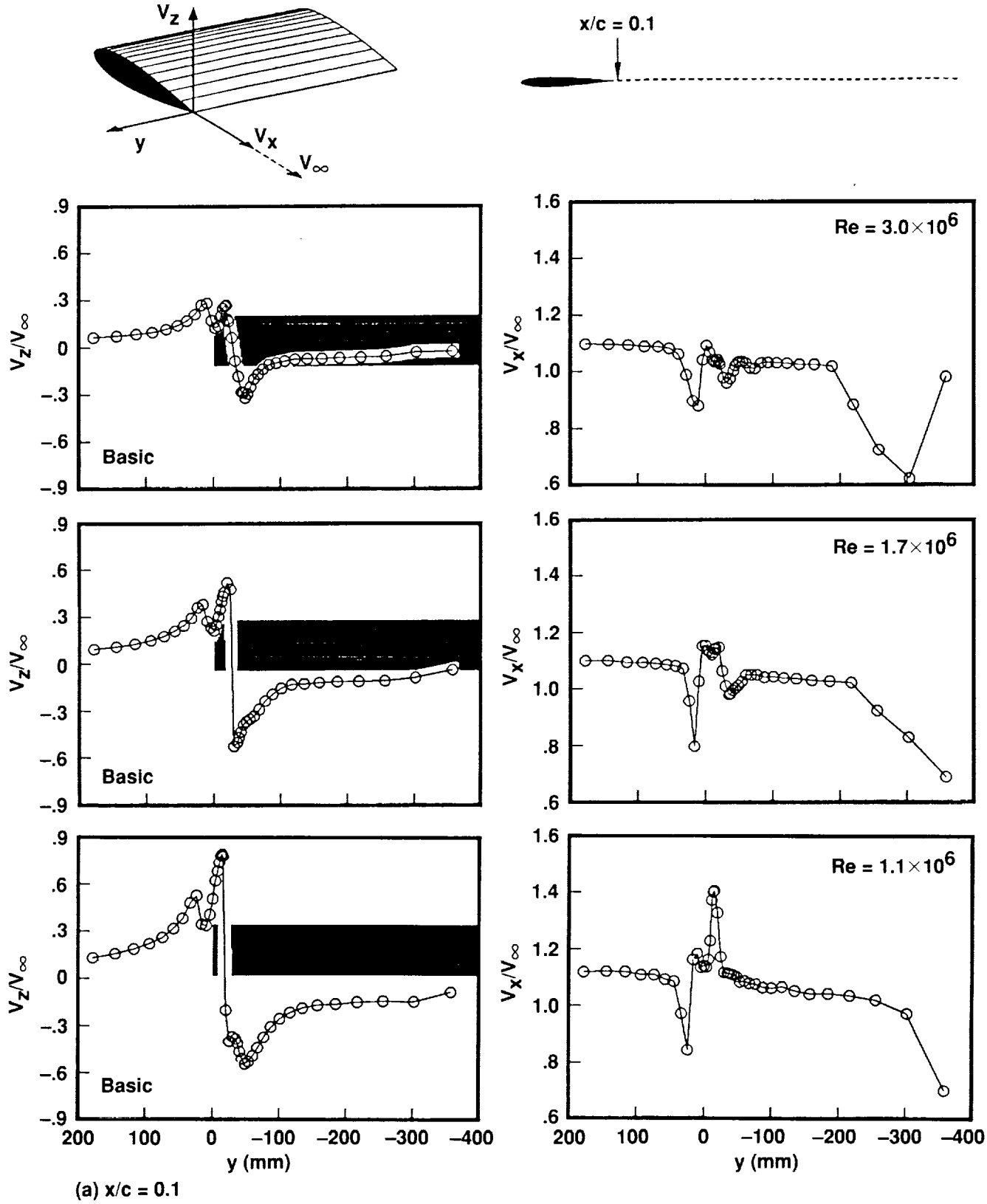

Figure 47. Vertical and streamwise velocity components across trailing vortex from basic wing with $c = 52$ cm for different Reynolds numbers while maintaining $C_l V_\infty$ = constant.

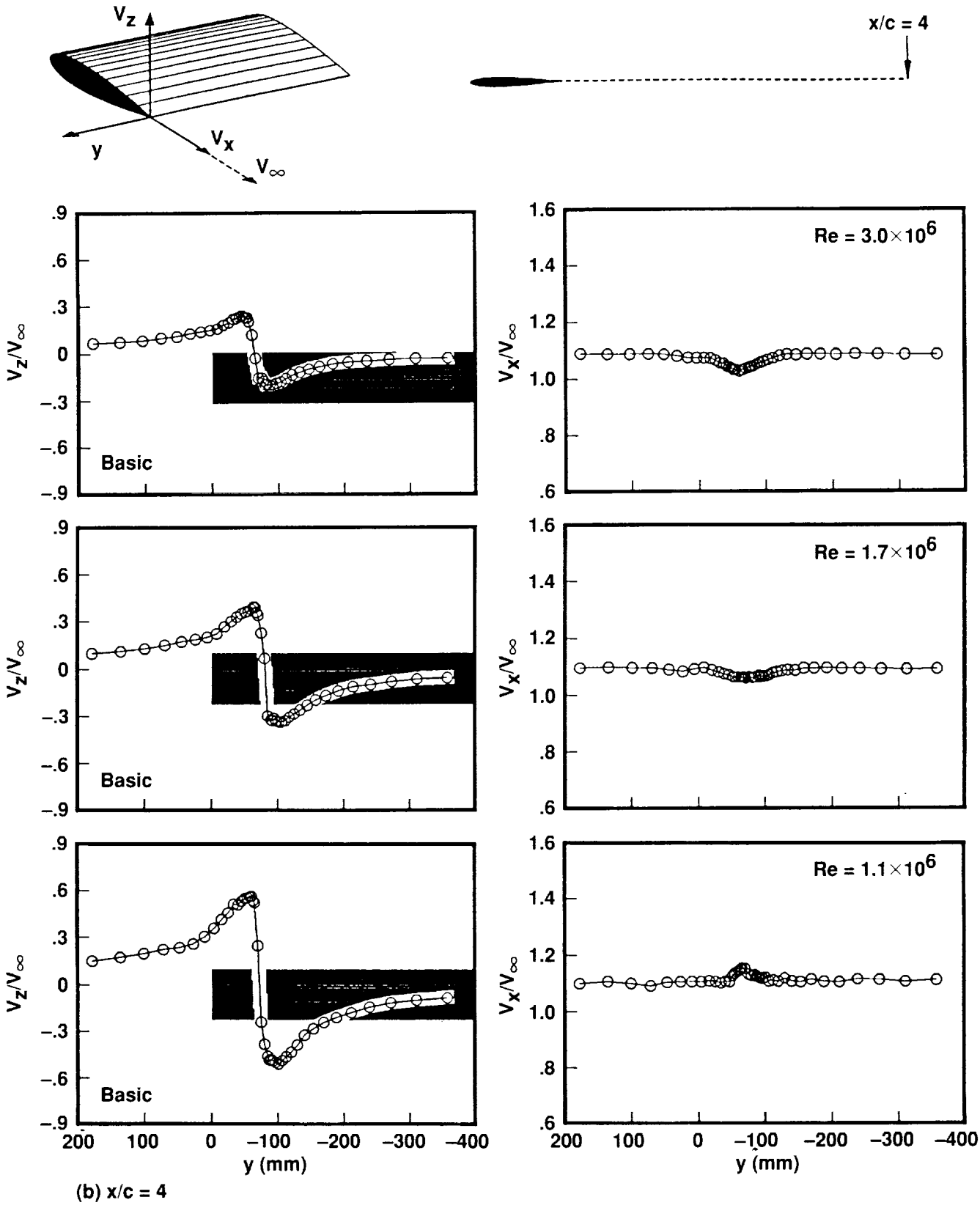

Figure 47. Concluded.

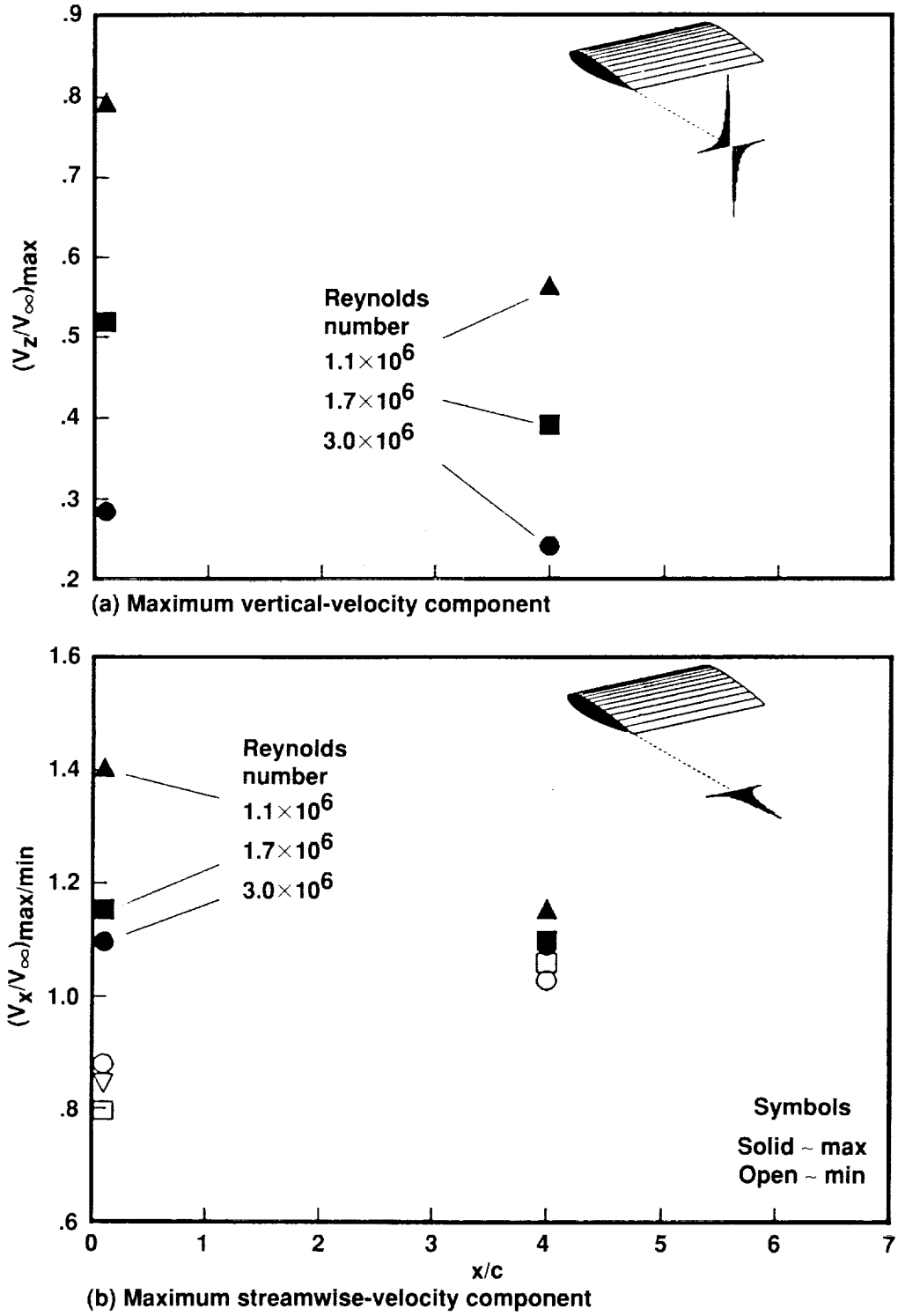

Figure 48. Maximum vertical and streamwise velocities within trailing vortex from basic wing with $c = 52$ cm for different Reynolds numbers while maintaining $C_l V_\infty$ = constant.

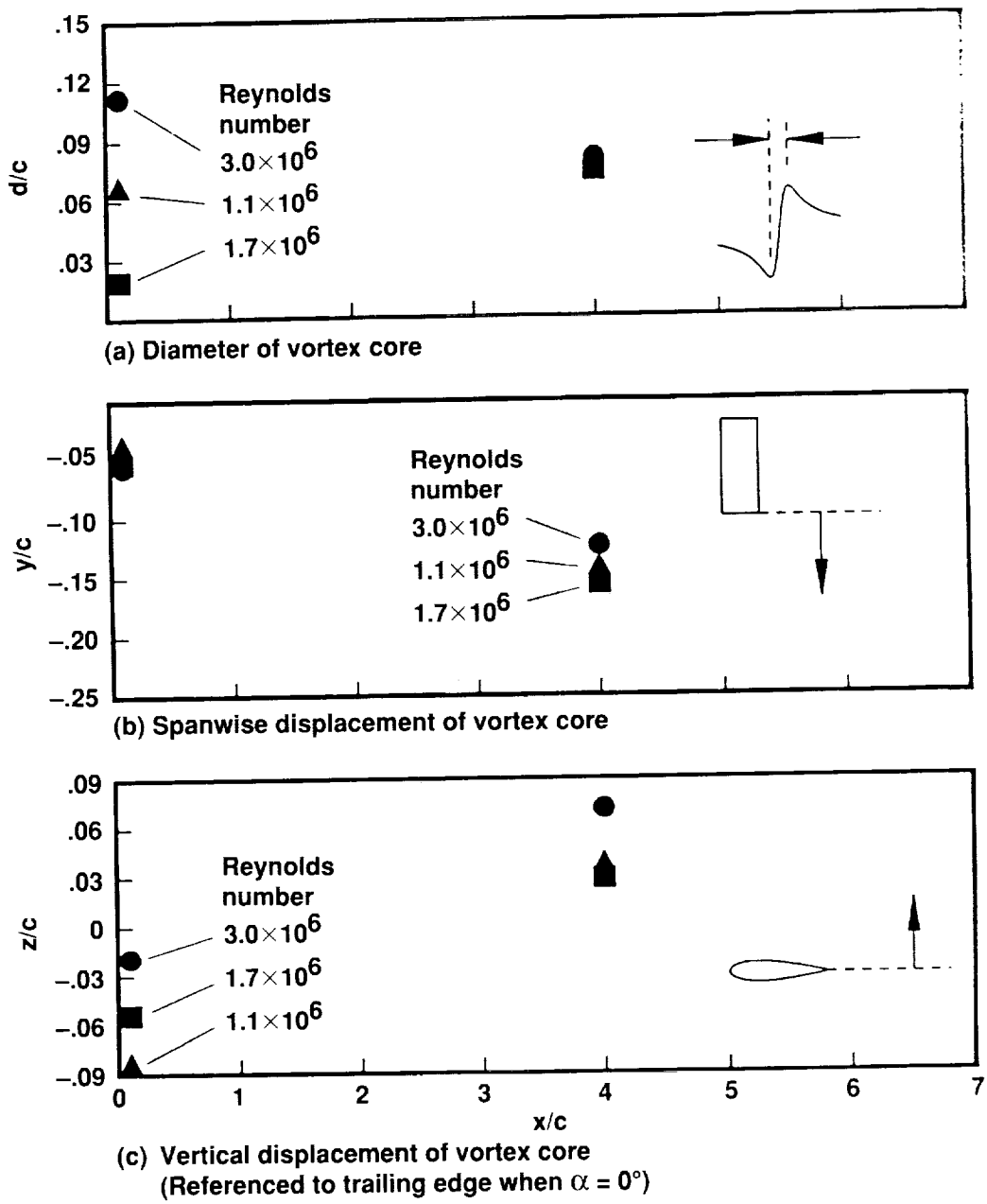

Figure 49. Size and position of vortex core trailing from basic wing with $c = 52$ cm for different Reynolds numbers while maintaining $C_l V_\infty$ = constant.

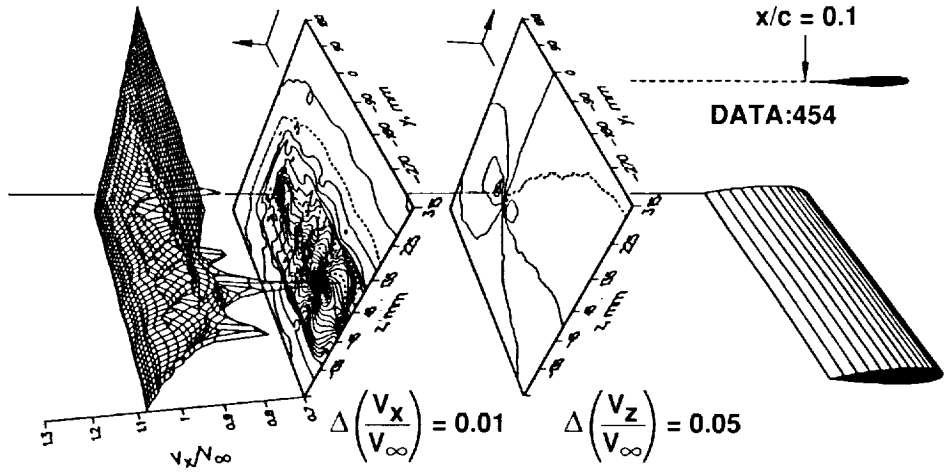

(a) Re = 3.0×10^6

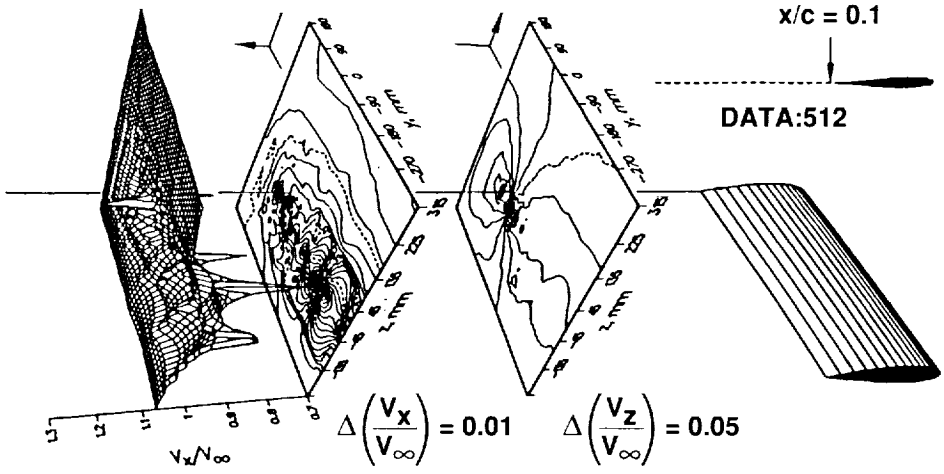

(b) Re = 1.7×10^6

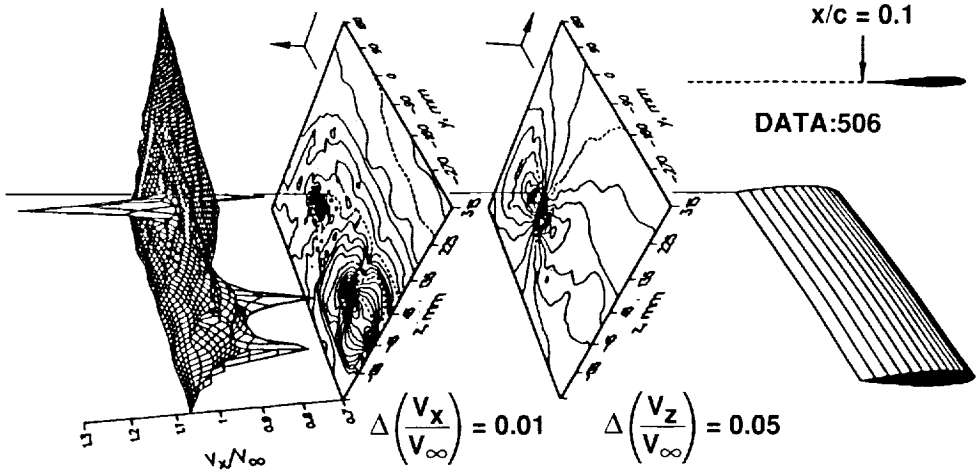

(c) Re = 1.1×10^6

Figure 50. Vertical and streamwise velocity contours around trailing vortex from basic wing with $c = 52$ cm at $x/c = 0.1$ for different Reynolds numbers while maintaining $C_l V_\infty$ = constant.

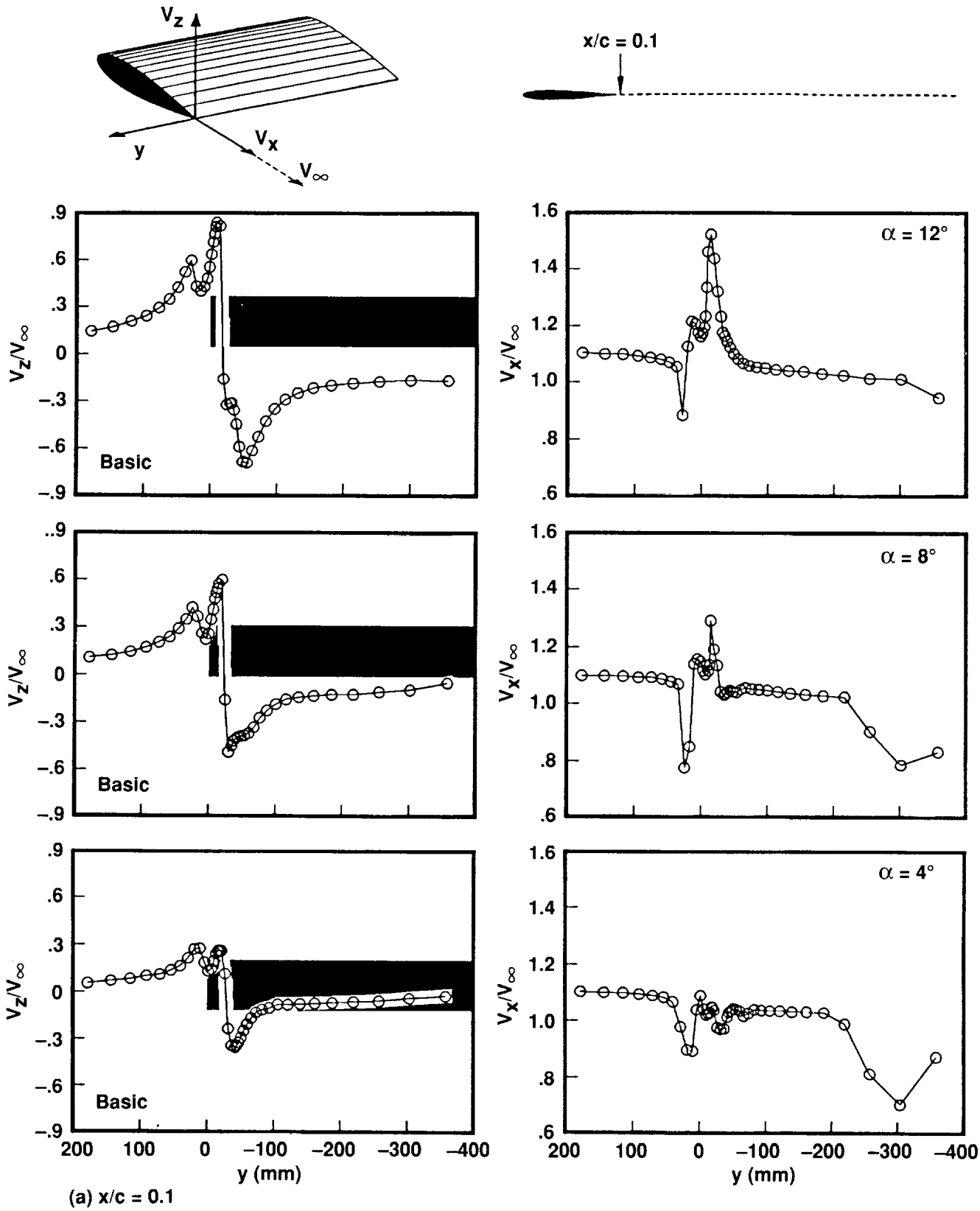

Figure 51. Vertical and streamwise velocity components across trailing vortex from basic wing with $c = 52$ cm and $Re = 1.5 \times 10^6$ for different values of circulation.

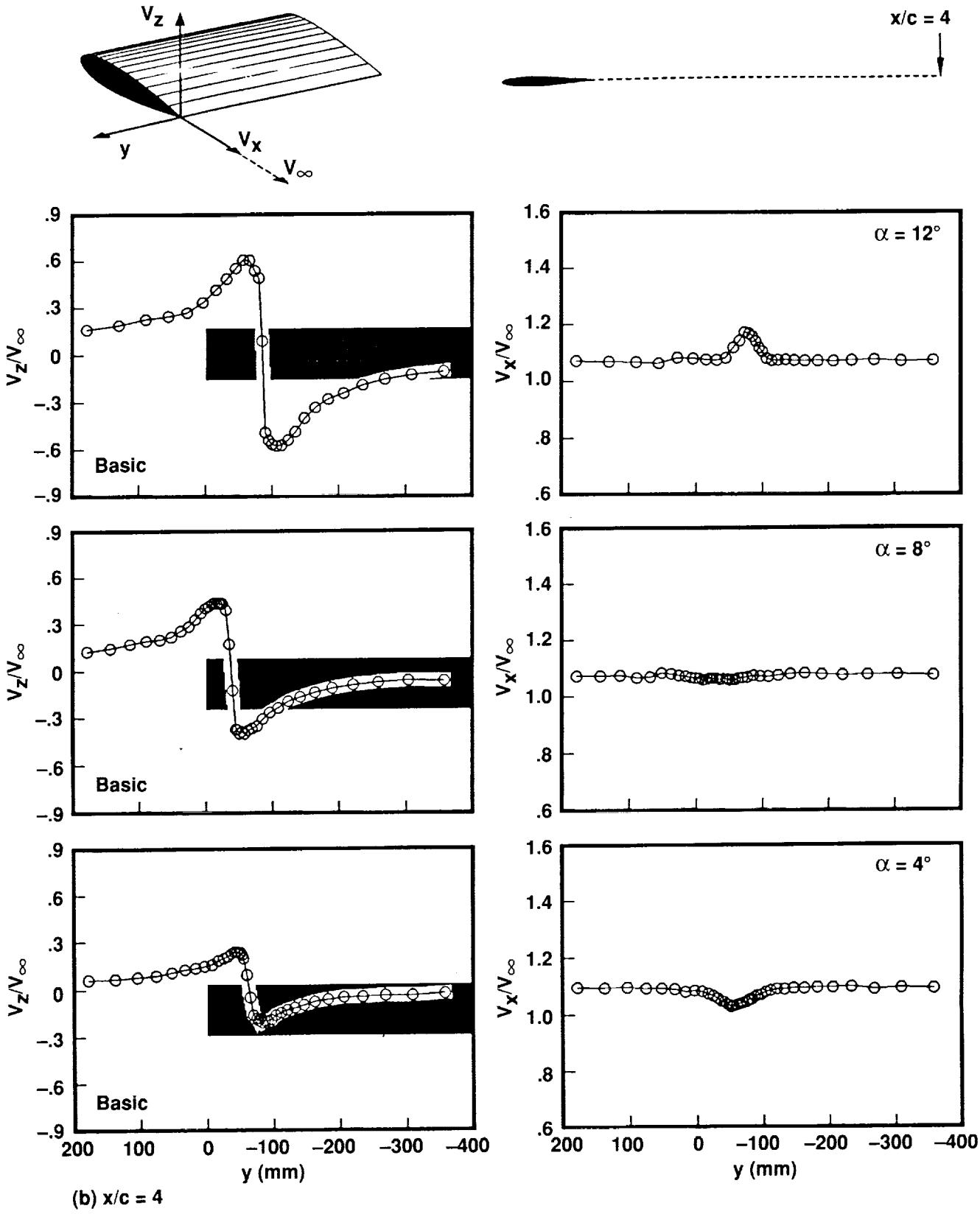

Figure 51. Concluded.

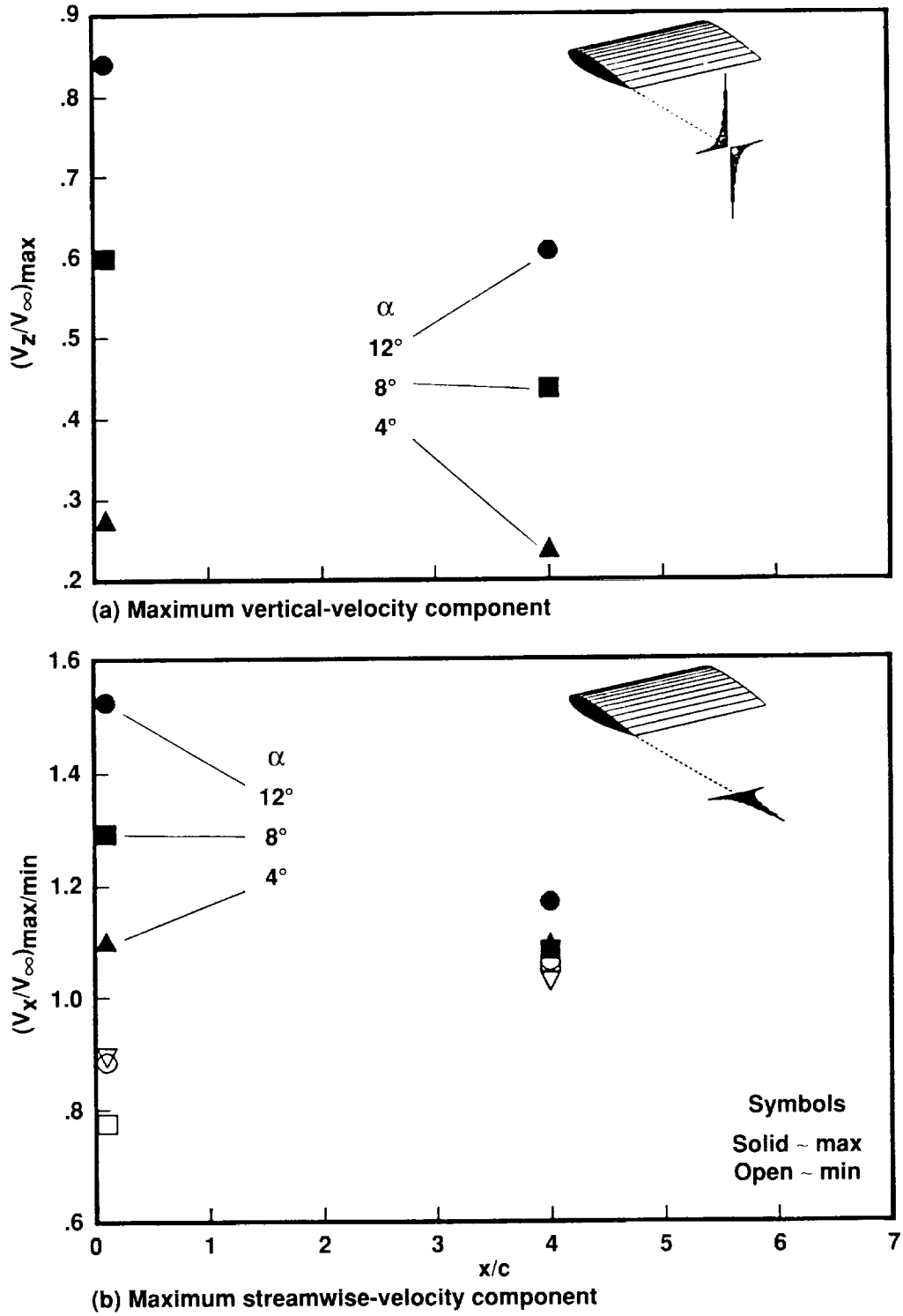

Figure 52. Maximum vertical and streamwise velocities within trailing vortex from basic wing with $c = 52$ cm and $Re = 1.5 \times 10^6$ for different values of circulation.

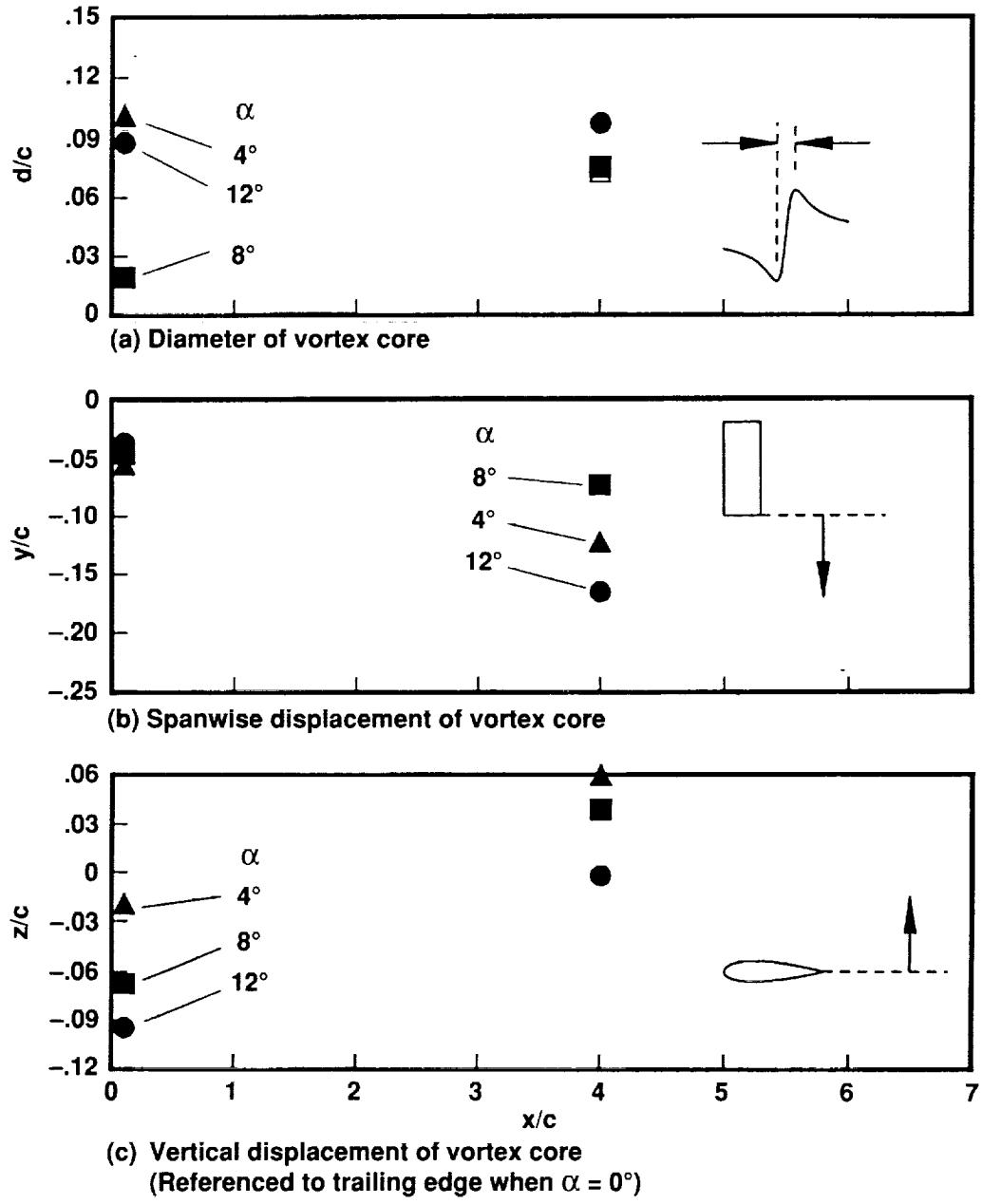

Figure 53. Size and position of vortex core trailing from basic wing with $c = 52$ cm and $Re = 1.5 \times 10^6$ for different values of circulation.

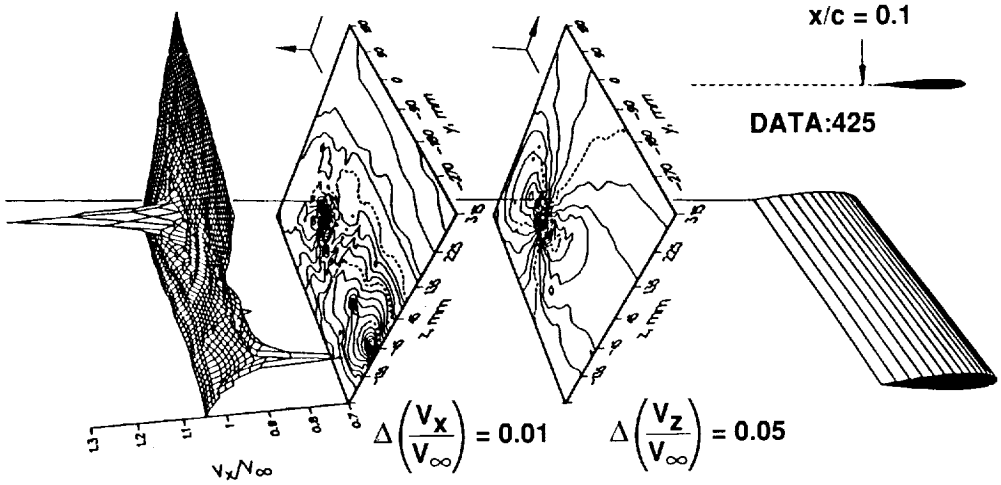

(a) $\alpha = 12°$

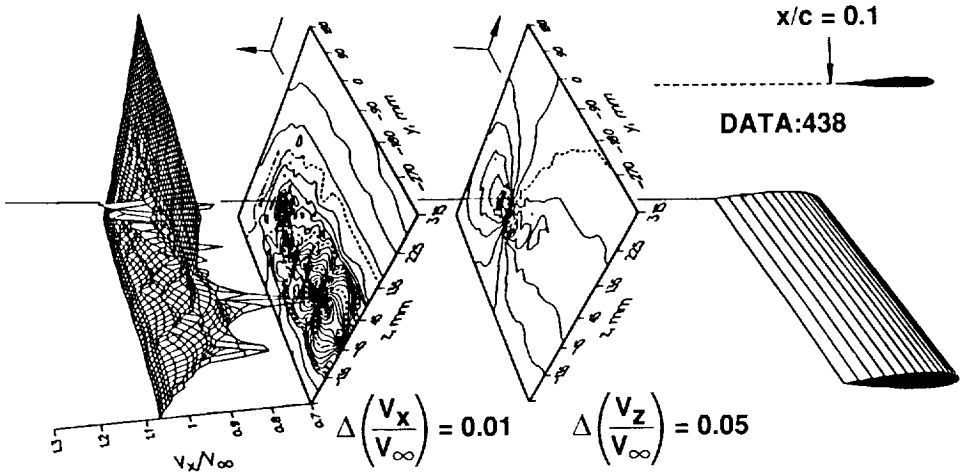

(b) $\alpha = 8°$

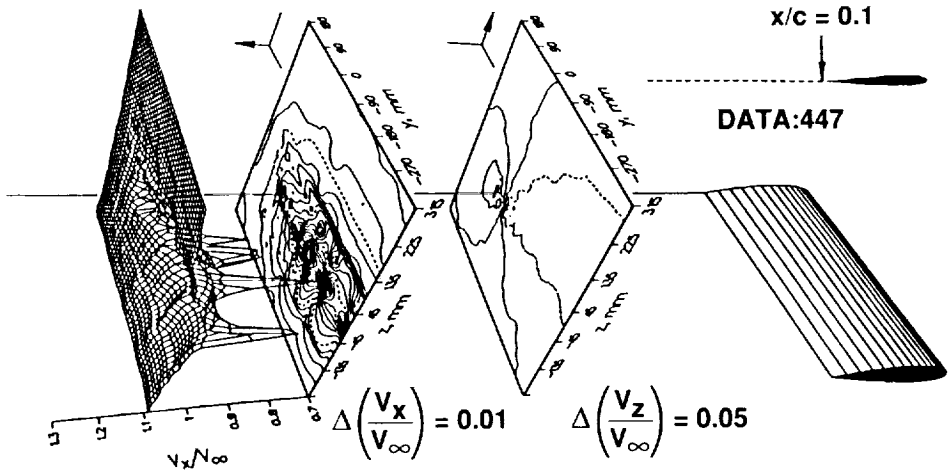

(c) $\alpha = 4°$

Figure 54. Vertical and streamwise velocity contours around trailing vortex from basic wing with $c = 52$ cm at $x/c = 0.1$ and $Re = 1.5 \times 10^6$ for different values of circulation.

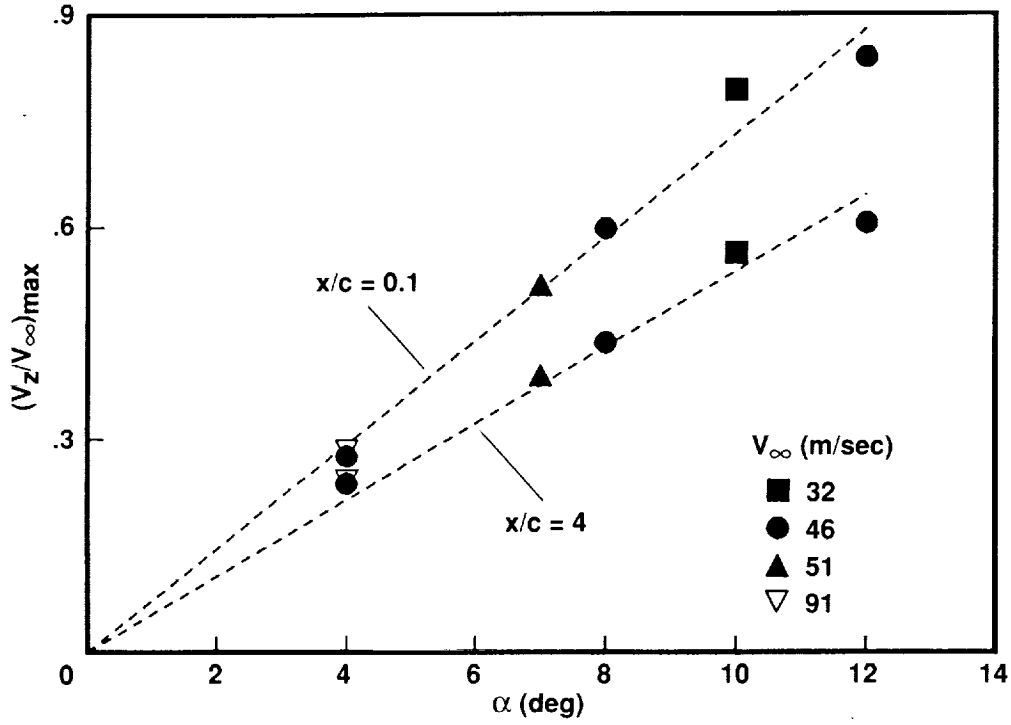

Figure 55. Maximum vertical component of velocity within trailing vortex from basic wing with $c = 52$ cm for different α and V_∞.

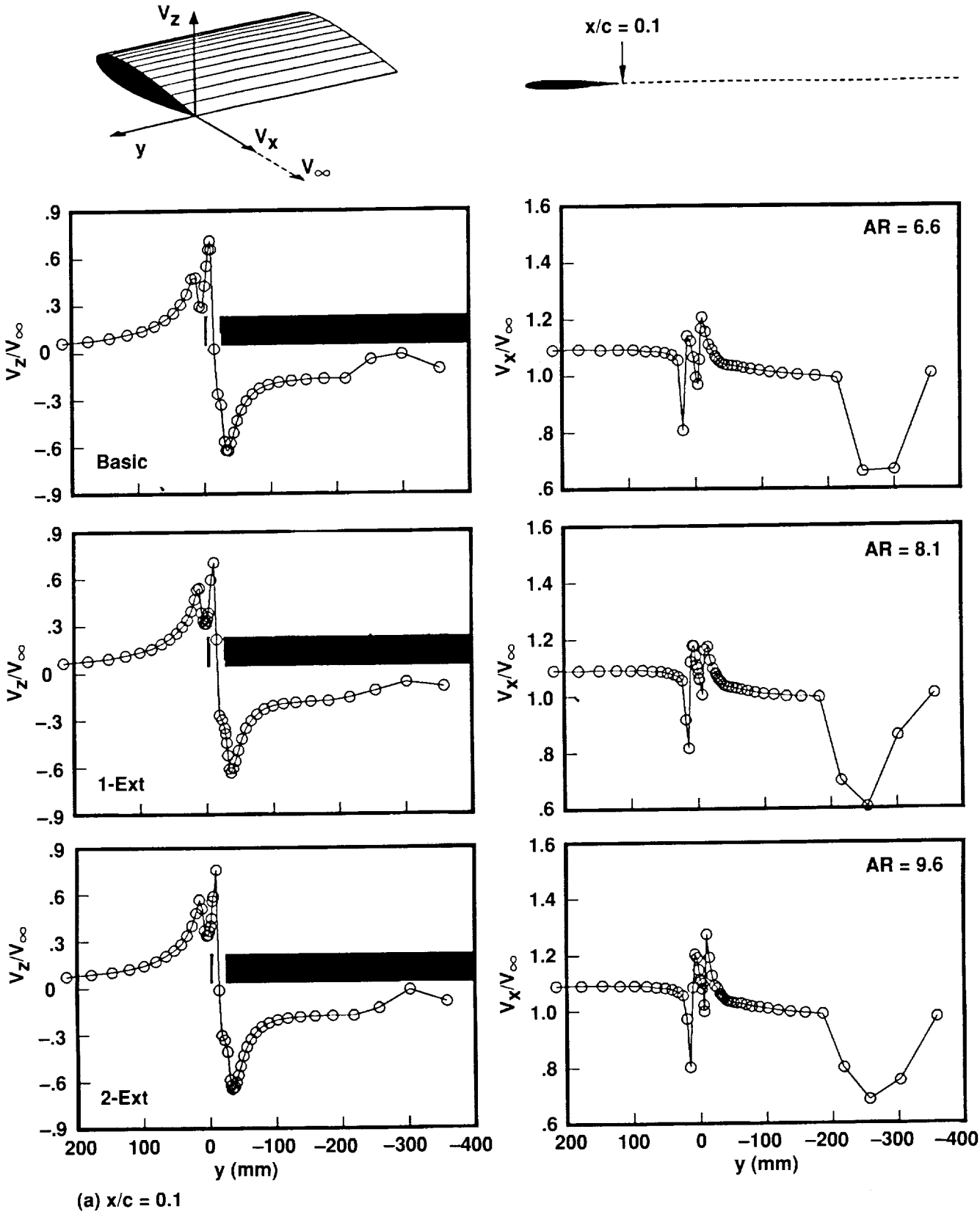

Figure 56. Vertical and streamwise velocity components across trailing vortex from $c = 30$ cm wing (square tip) at $Re = 1.5 \times 10^6$ and $\alpha = 12°$ for different aspect ratios.

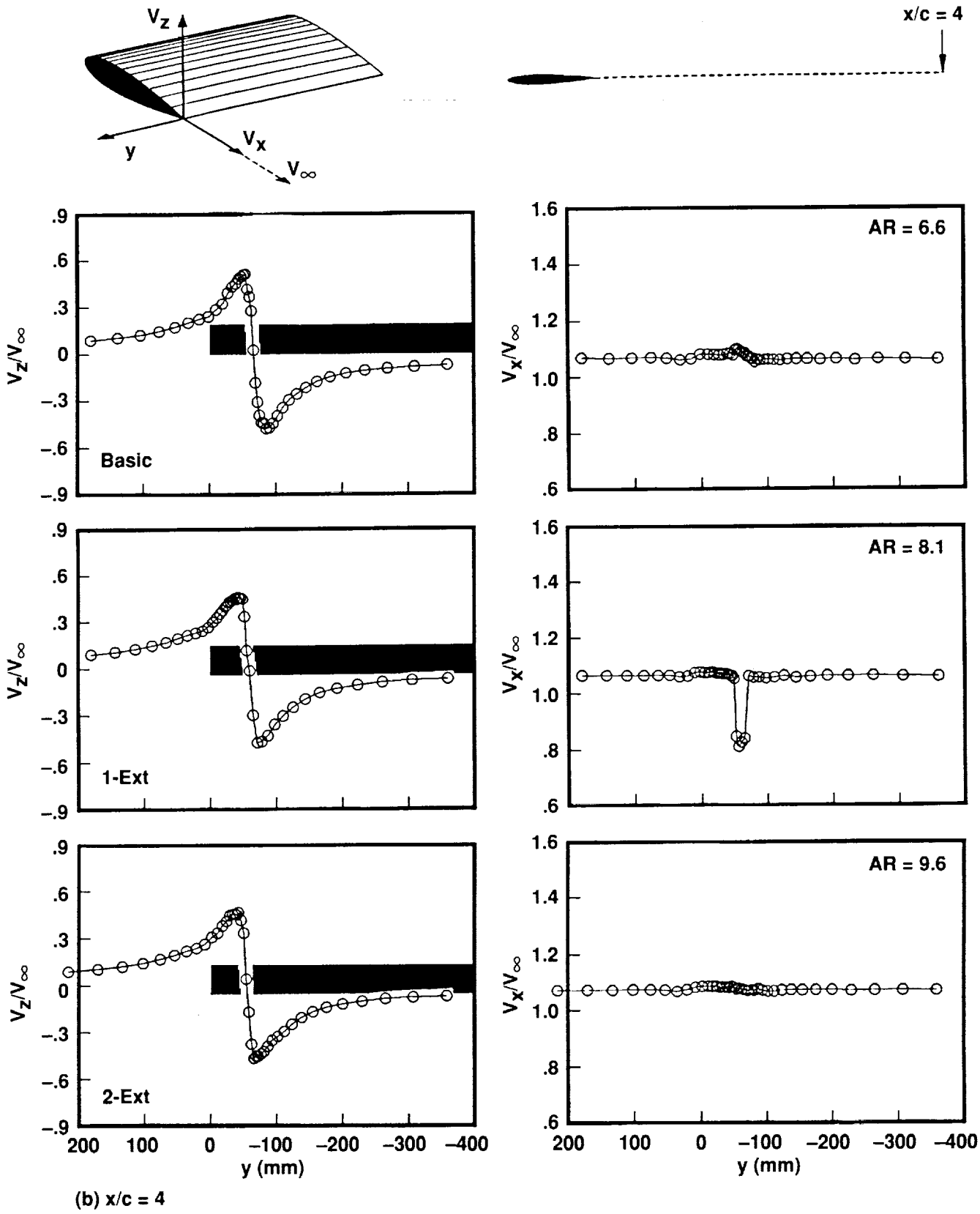

Figure 56. Concluded.

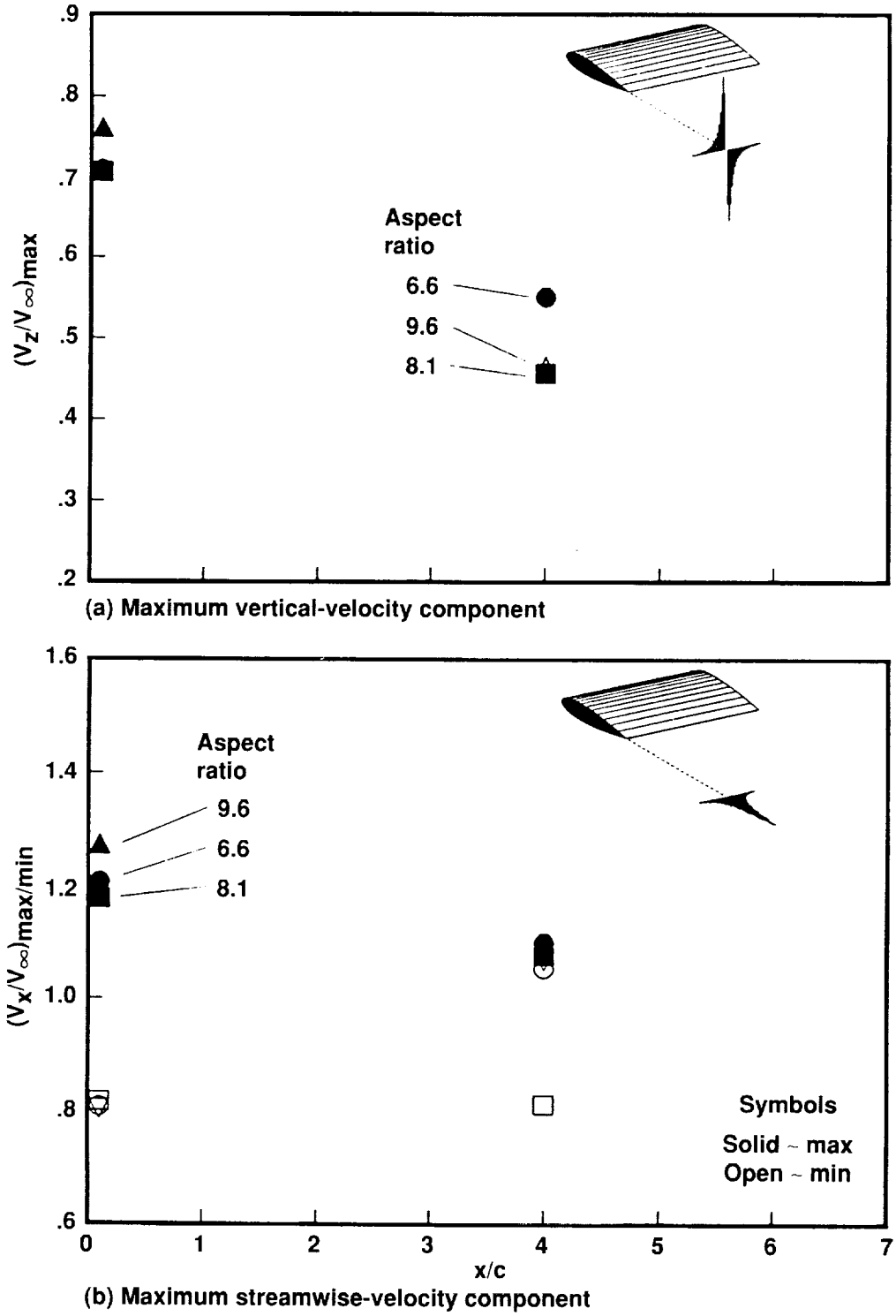

Figure 57. Maximum vertical and streamwise velocities within trailing vortex from $c = 30$ cm wing (square tip) at $Re = 1.5 \times 10^6$ and $\alpha = 12°$ for different aspect ratios.

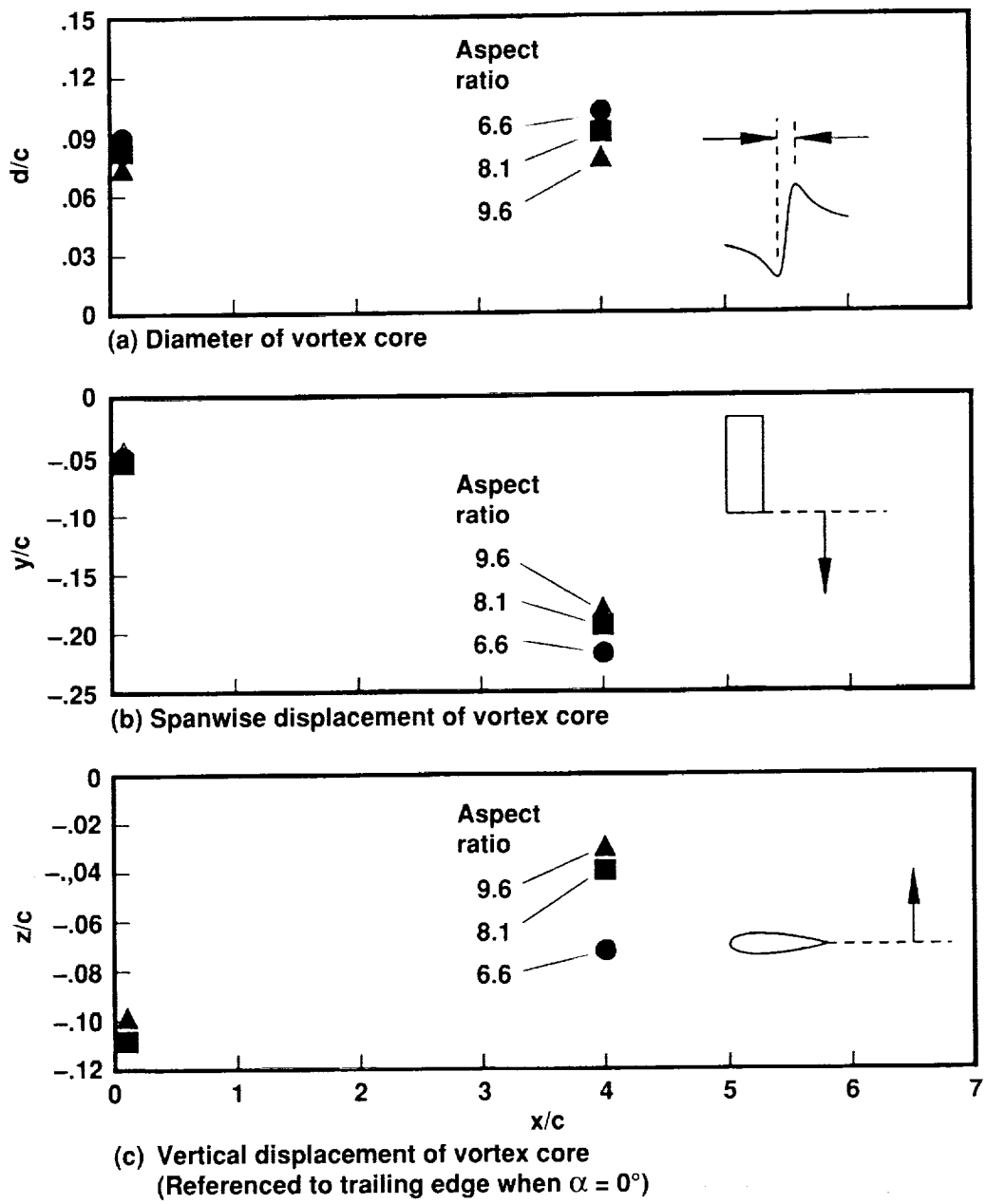

Figure 58. Size and position of vortex core trailing from $c = 30$ cm wing (square tip) at $Re = 1.5 \times 10^6$ and $\alpha = 12°$ for different aspect ratios.

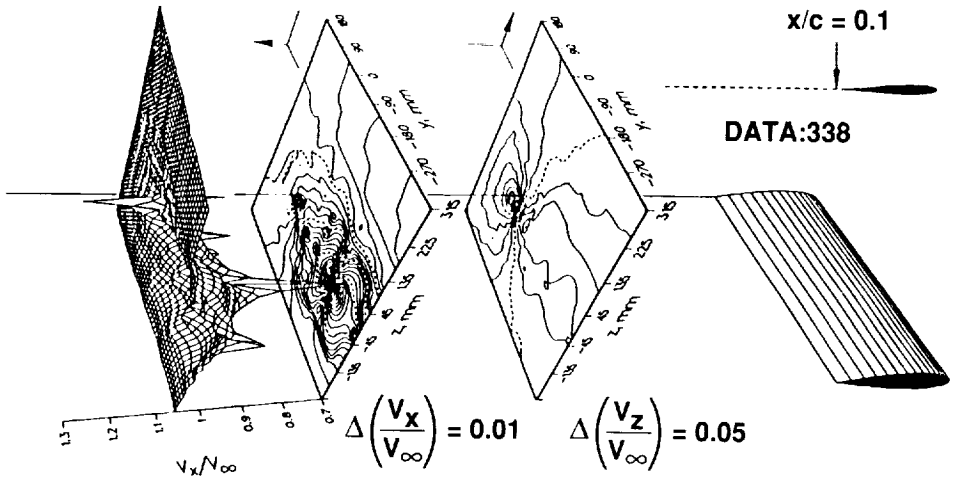

(a) AR = 6.6

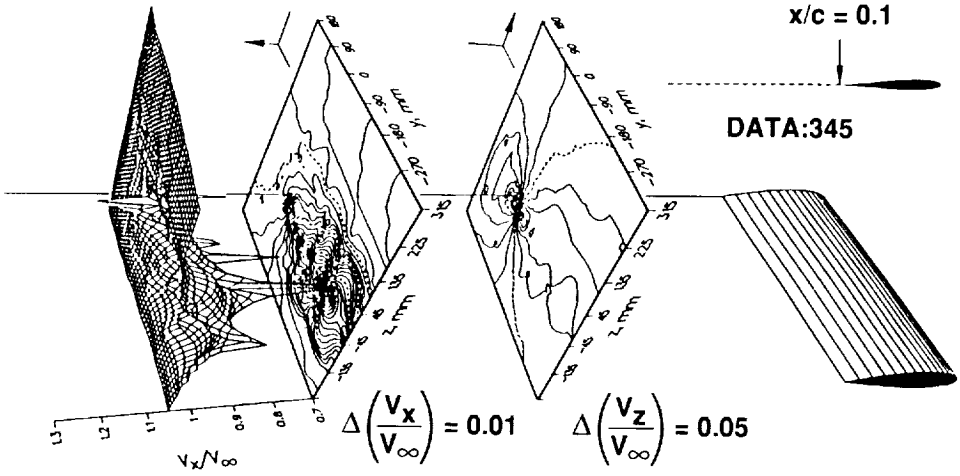

(b) AR = 8.1

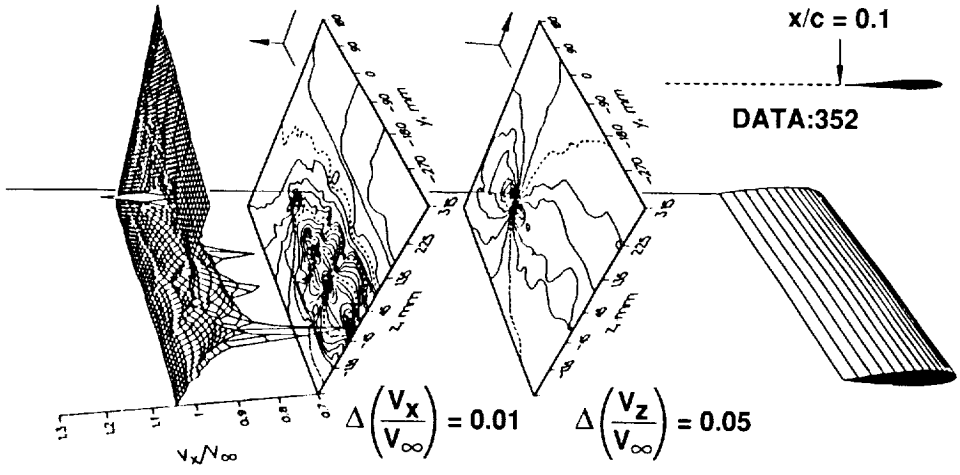

(c) AR = 9.6

Figure 59. Vertical and streamwise velocity contours around trailing vortex from $c = 30$ cm wing (square tip) at $x/c = 0.1$ with $Re = 1.5 \times 10^6$ and $\alpha = 12°$ for different aspect ratios.

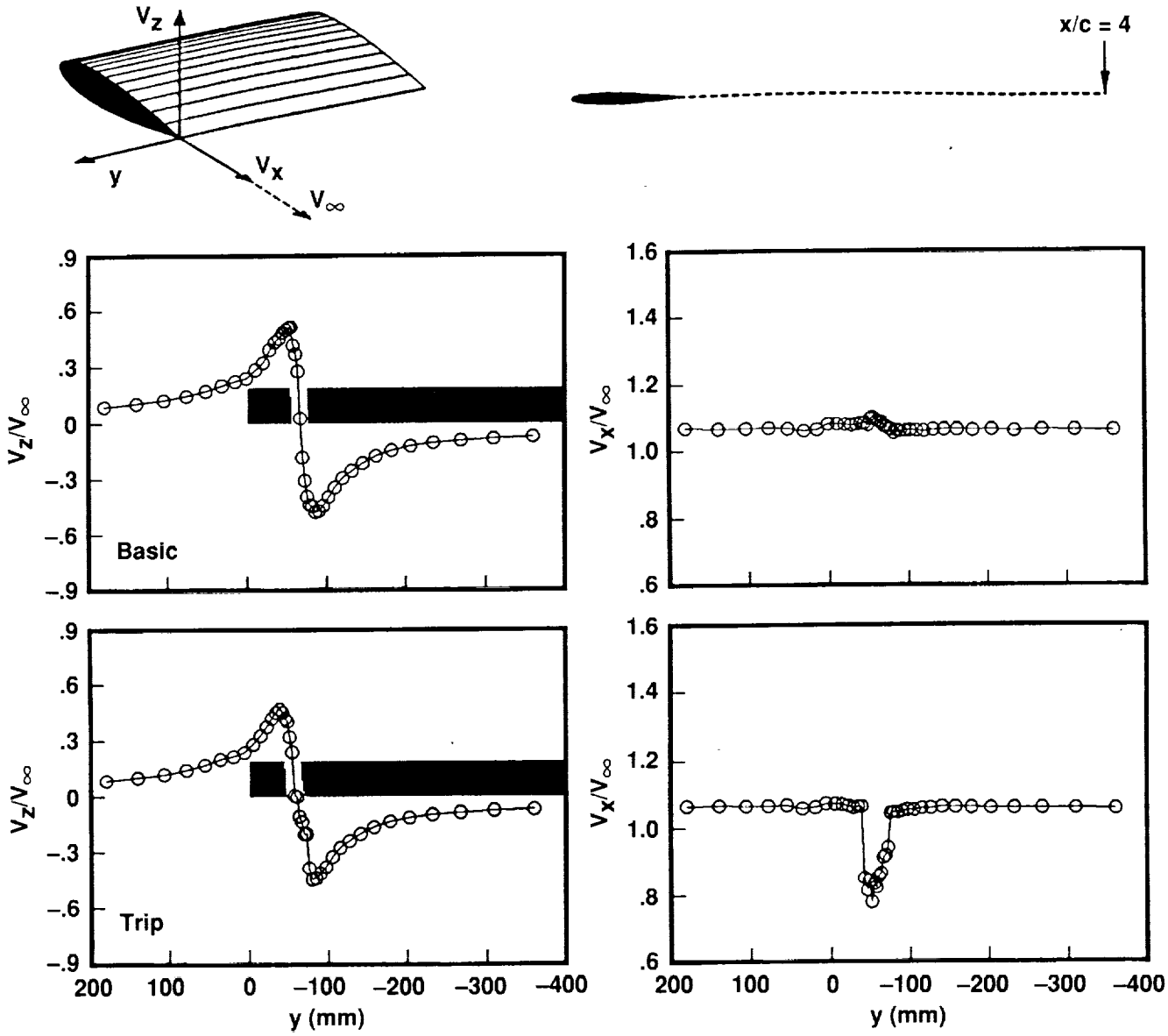

Figure 60. Vertical and streamwise velocity components across trailing vortex from basic wing with $c = 52$ cm at $x/c = 4$ with $Re = 1.5 \times 10^6$ and $\alpha = 12°$ with and without boundary-layer trip.

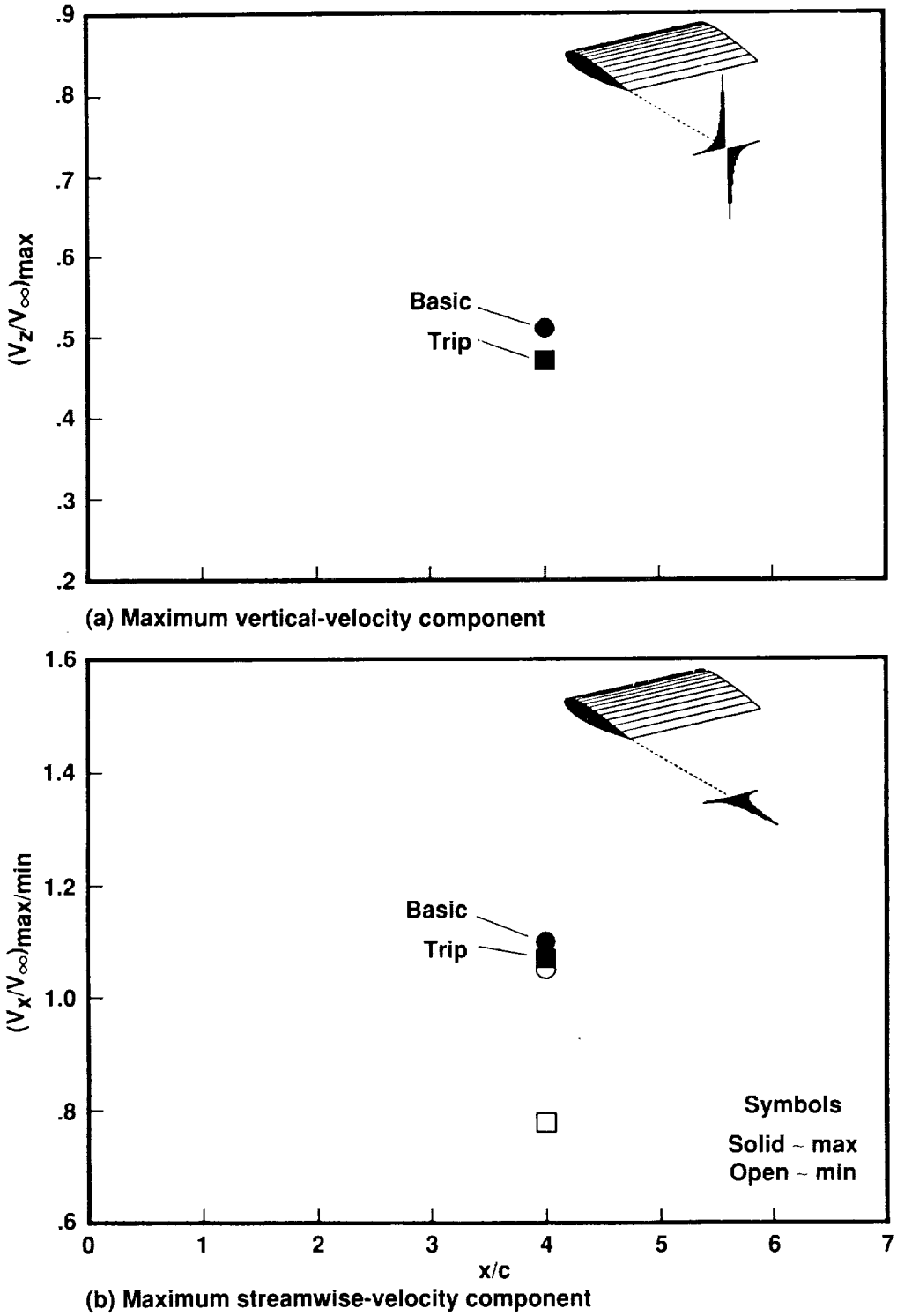

Figure 61. Maximum vertical and streamwise velocities within trailing vortex from basic wing with $c = 52$ cm at $Re = 1.5 \times 10^6$ and $\alpha = 12°$ with and without boundary-layer trip.

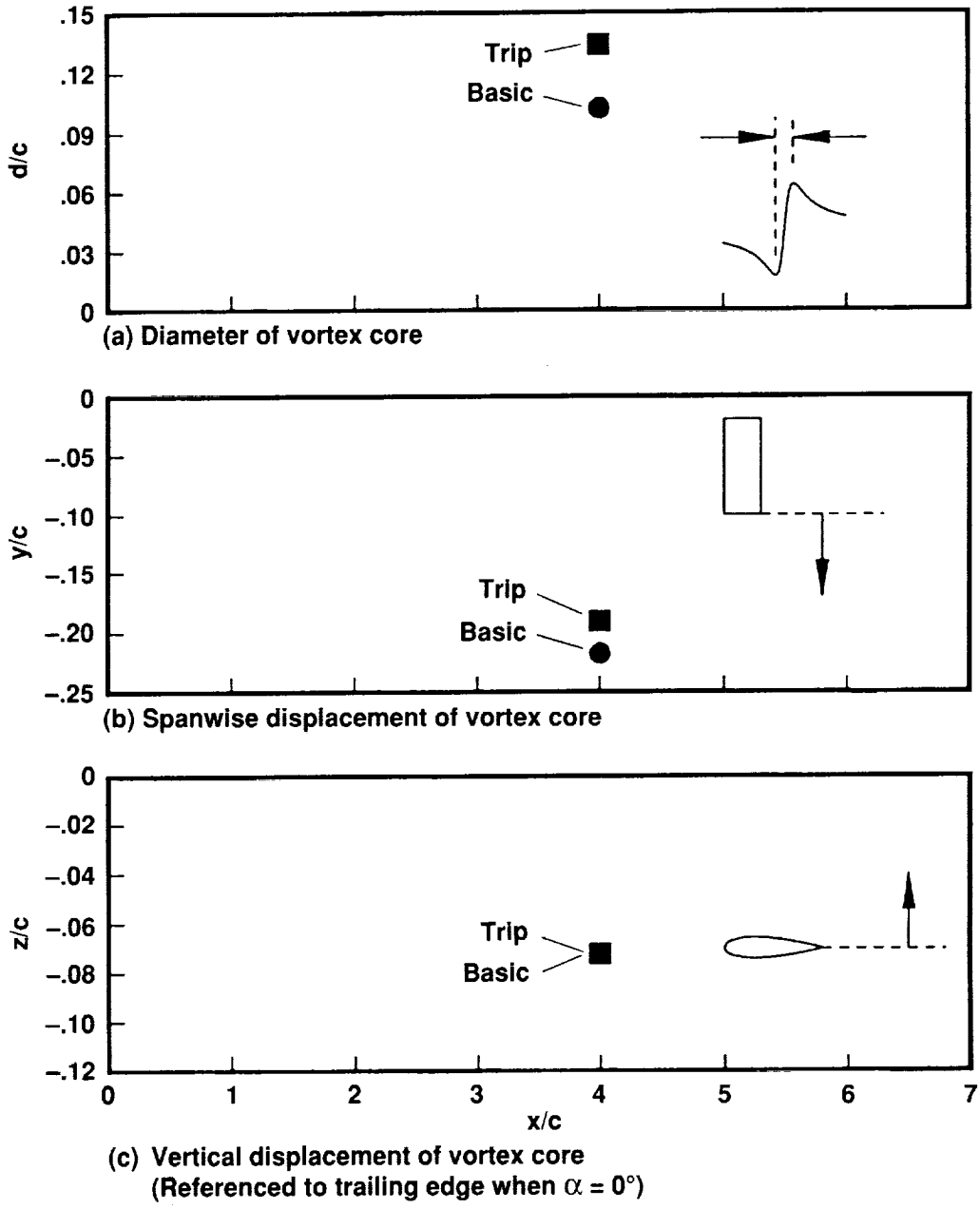

Figure 62. Size and position of vortex core trailing from basic wing with $c = 52$ cm at $Re = 1.5 \times 10^6$ and $\alpha = 12°$ with and without boundary-layer trip.

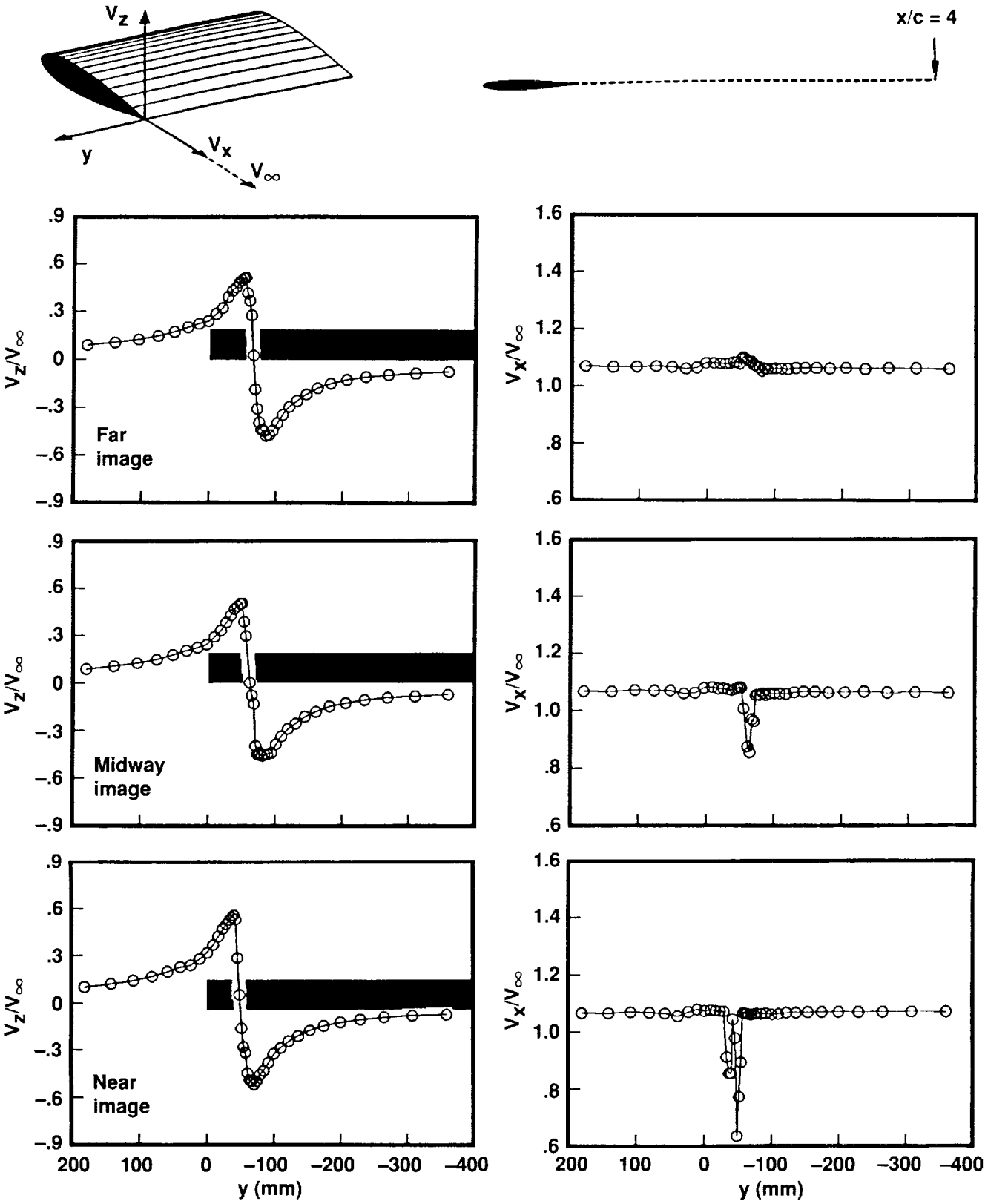

Figure 63. Vertical and streamwise velocity components across trailing vortex from basic wing with $c = 30$ cm at $x/c = 4$ with $Re = 1.5 \times 10^6$ and $\alpha = 12°$ for different image plane positions.

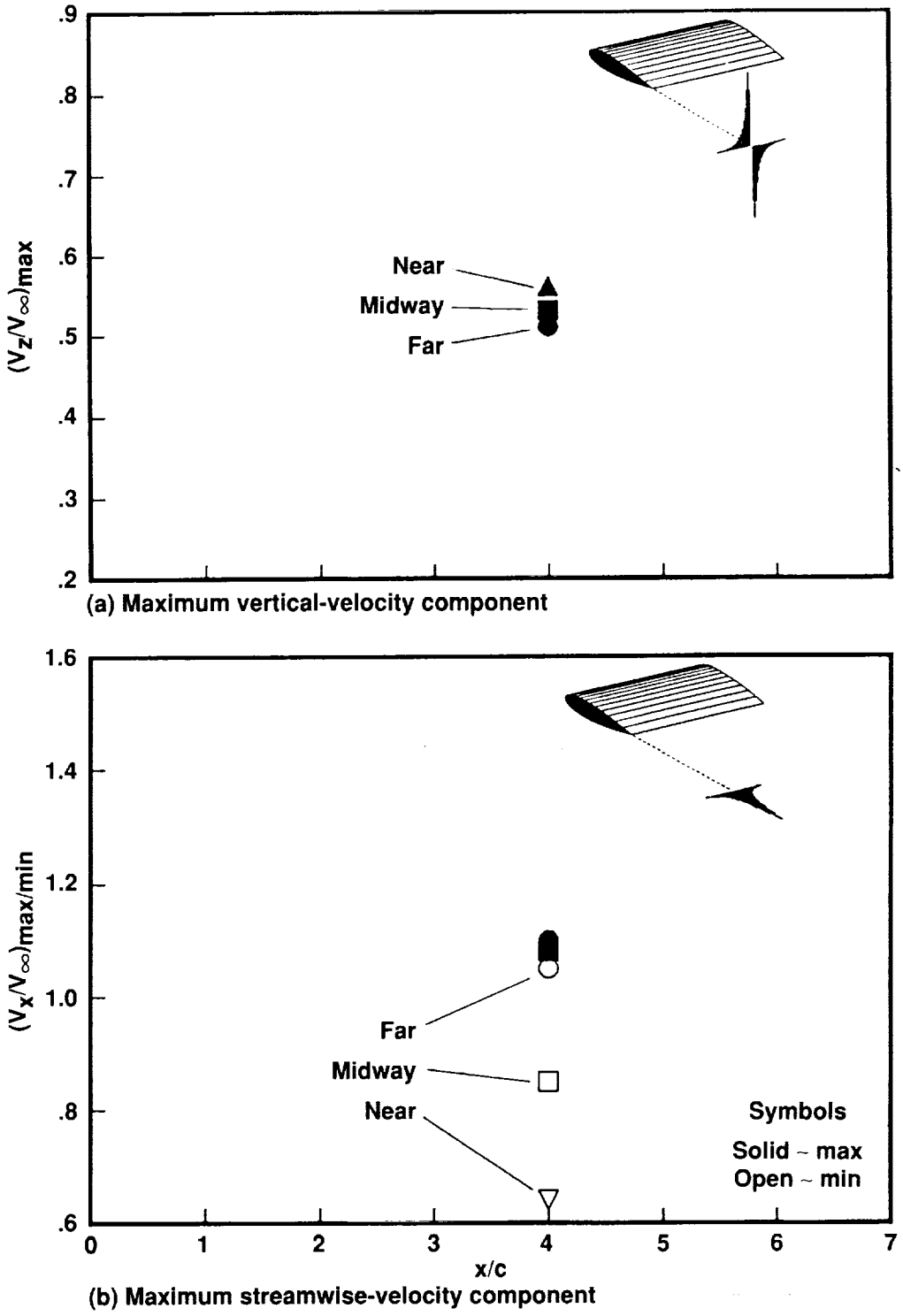

Figure 64. Maximum vertical and streamwise velocities within trailing vortex from basic wing with $c = 30$ cm at $Re = 1.5 \times 10^6$ and $\alpha = 12°$ for different image plane positions.

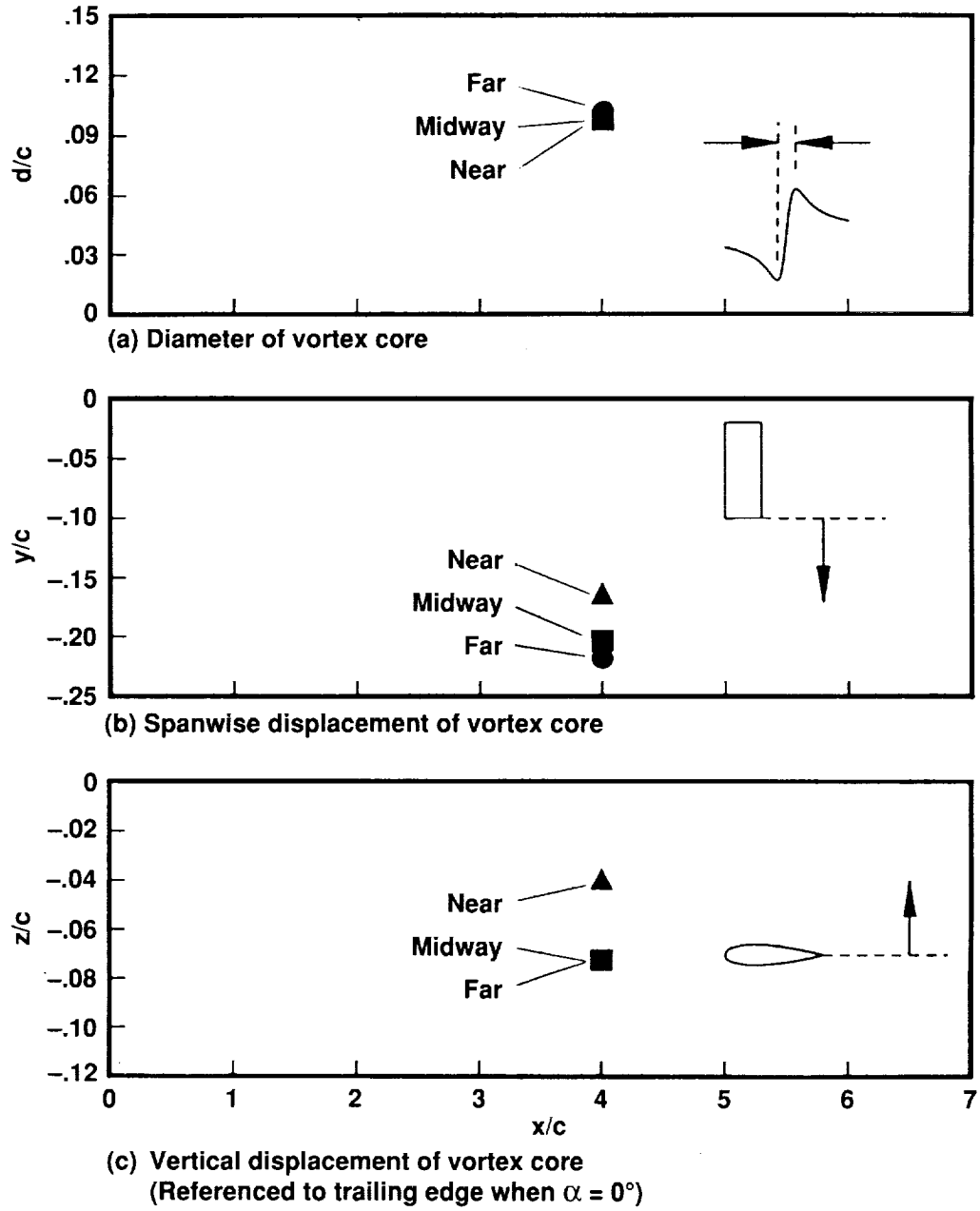

Figure 65. Size and position of vortex core trailing from basic wing with $c = 30$ cm at $Re = 1.5 \times 10^6$ and $\alpha = 12°$ for different image plane positions.

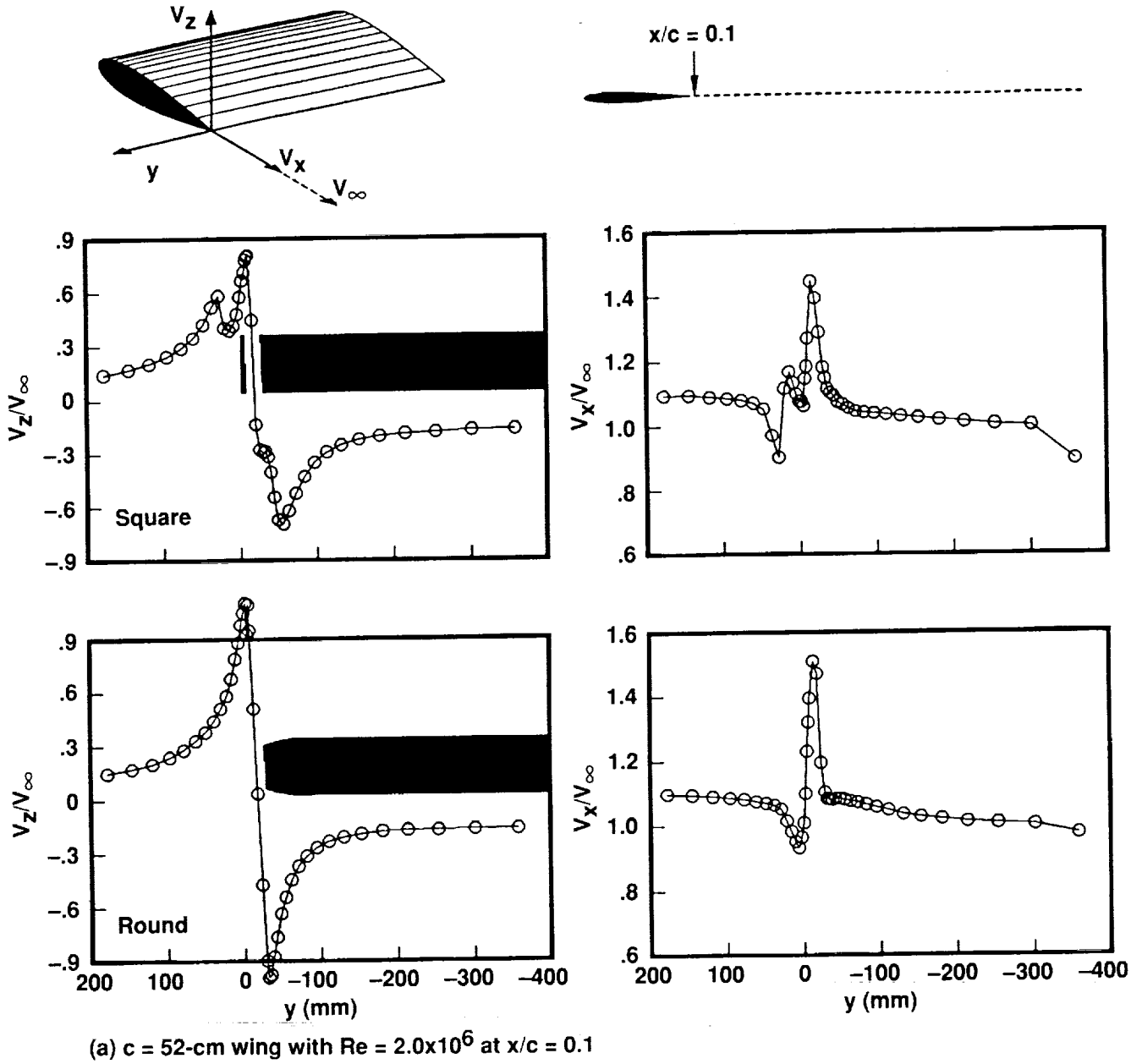

Figure 66. Vertical and streamwise velocity components across trailing vortex from wing ($AR = 6.6$) at $\alpha = 12°$ for square- and round-lateral edges.

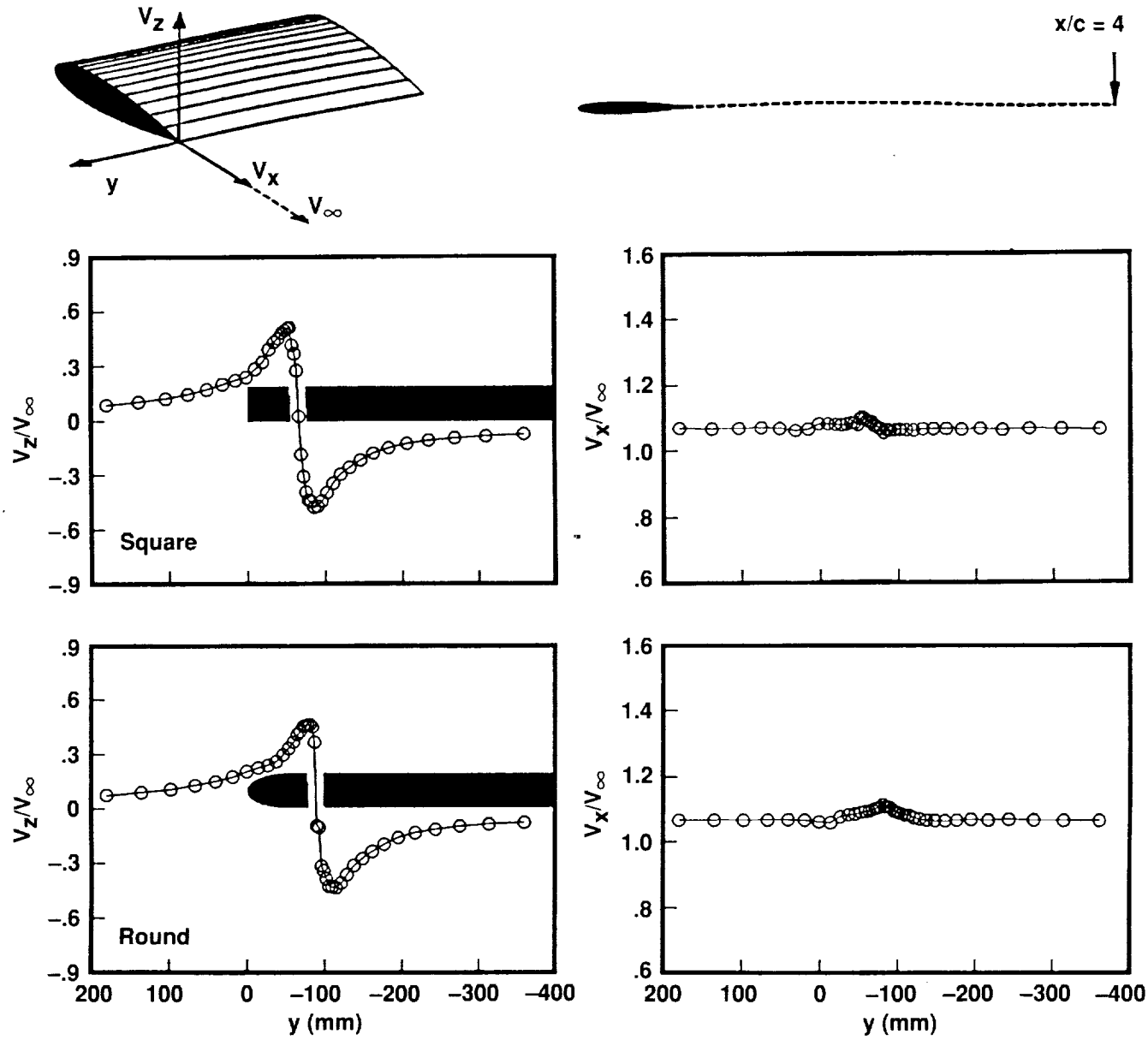

(b) c = 30-cm wing with Re = 1.5×10^6 at x/c = 4

Figure 66. Concluded.

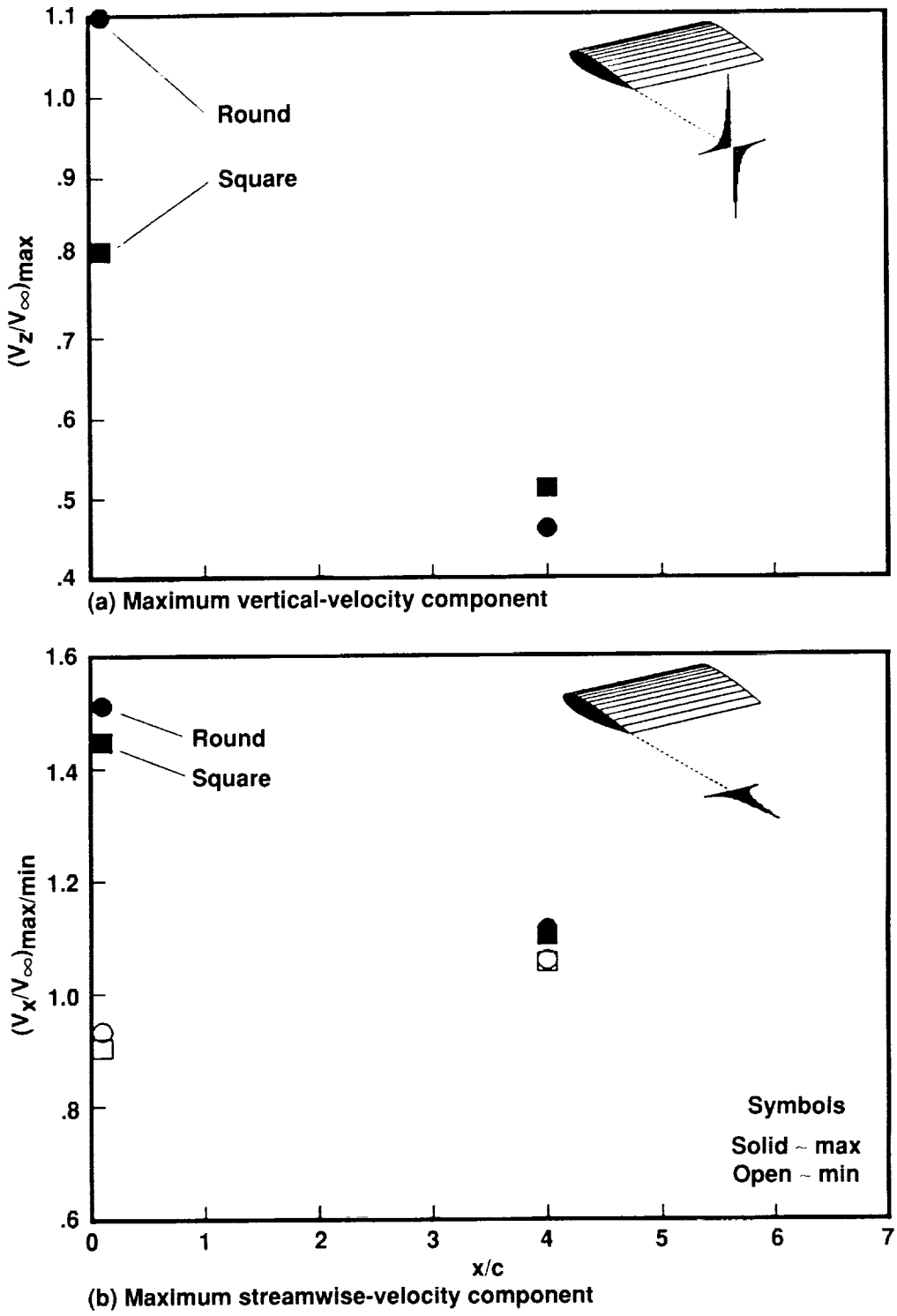

Figure 67. Maximum vertical and streamwise velocities within trailing vortex from wing ($AR = 6.6$) at $\alpha = 12°$ for square- and round-lateral edges. Values at $x/c = 0.1$ for $c = 52$ cm wing with $Re = 2.0 \times 10^6$ and those at $x/c = 4$ for $c = 30$ cm wing with $Re = 1.5 \times 10^6$.

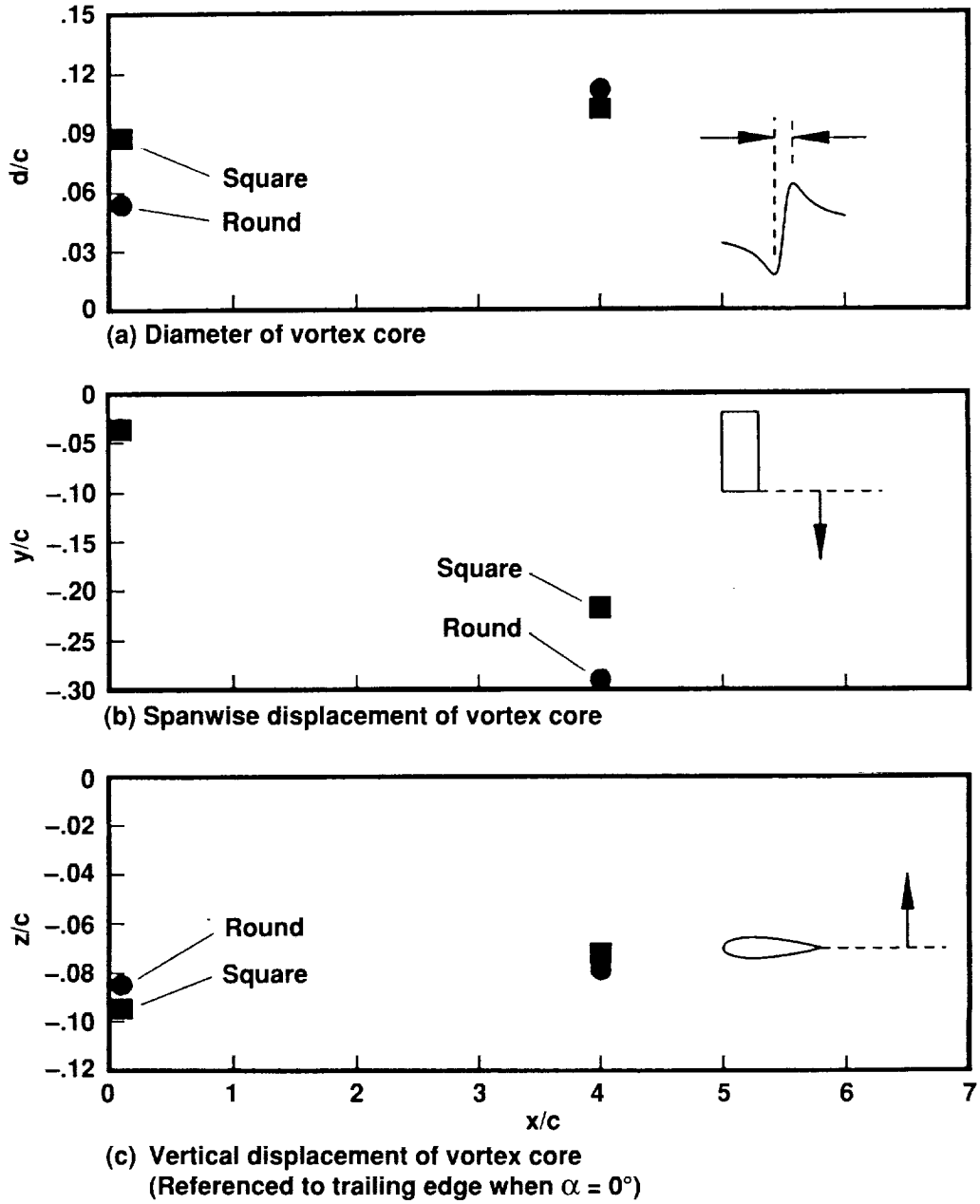

Figure 68. Size and position of vortex core trailing from wing ($AR = 6.6$) at $\alpha = 12°$ for square- and round-lateral edges. Values at $x/c = 0.1$ for $c = 52$ cm wing with $Re = 2.0 \times 10^6$ and those at $x/c = 4$ for $c = 30$ cm wing with $Re = 1.5 \times 10^6$.

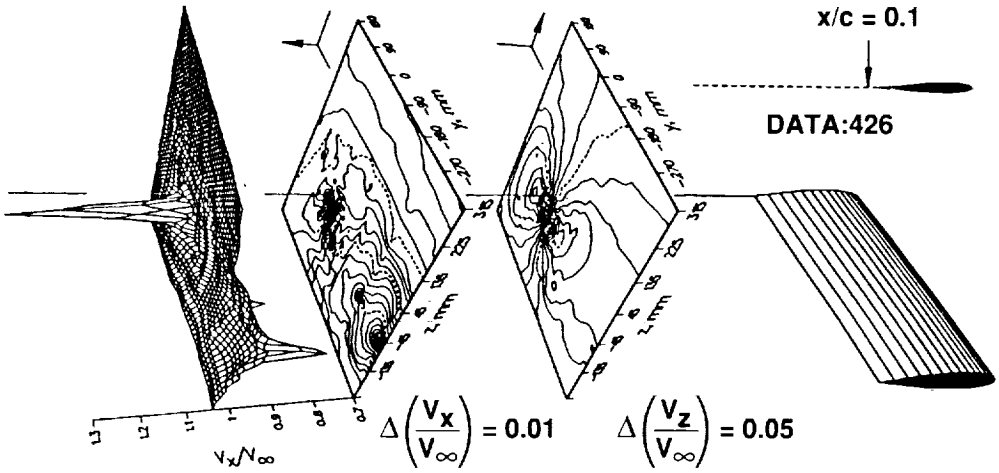

(a) Square-lateral edge

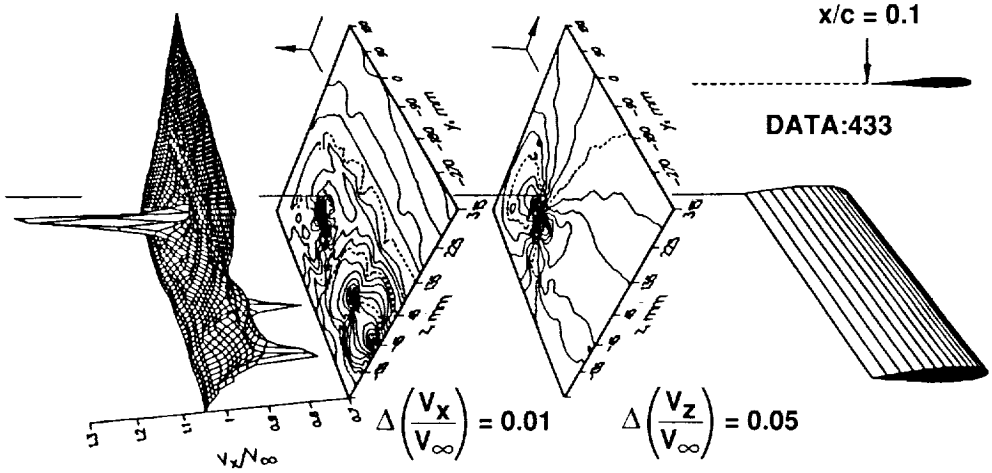

(b) Round-lateral edge

Figure 69. Vertical and streamwise velocity contours around trailing vortex from $c = 52$ cm wing ($AR = 6.6$) at $Re = 2.0 \times 10^6$ and $\alpha = 12°$ for square- and round-lateral edges.

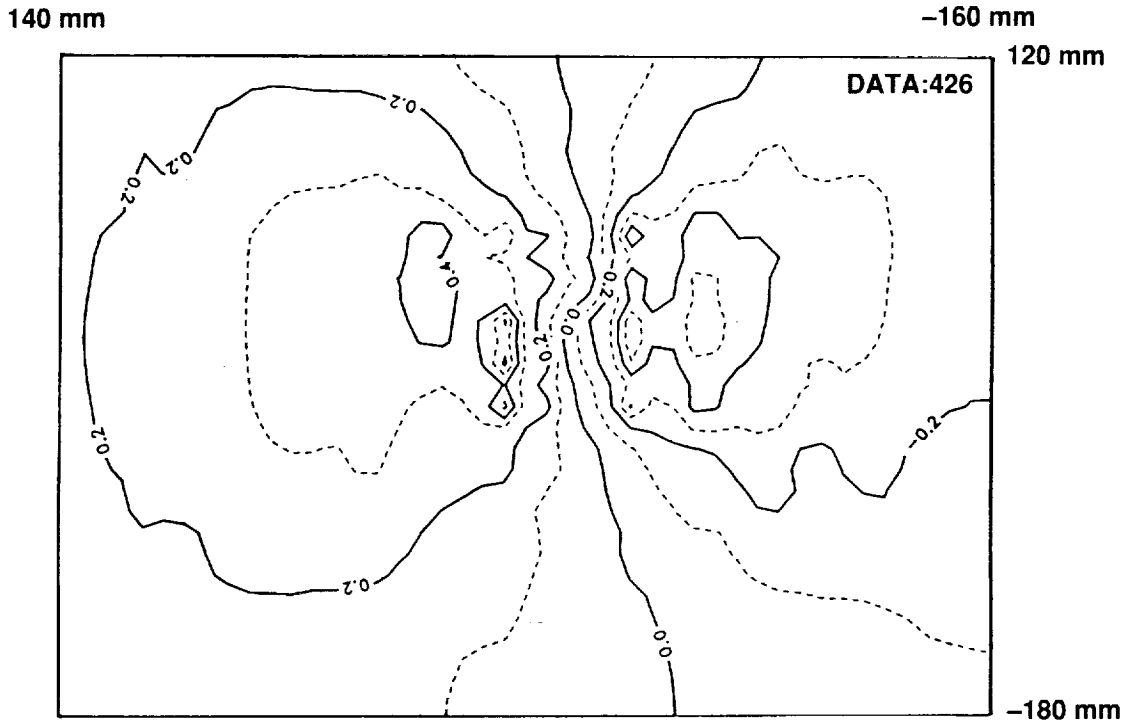

(a) Square-lateral edge

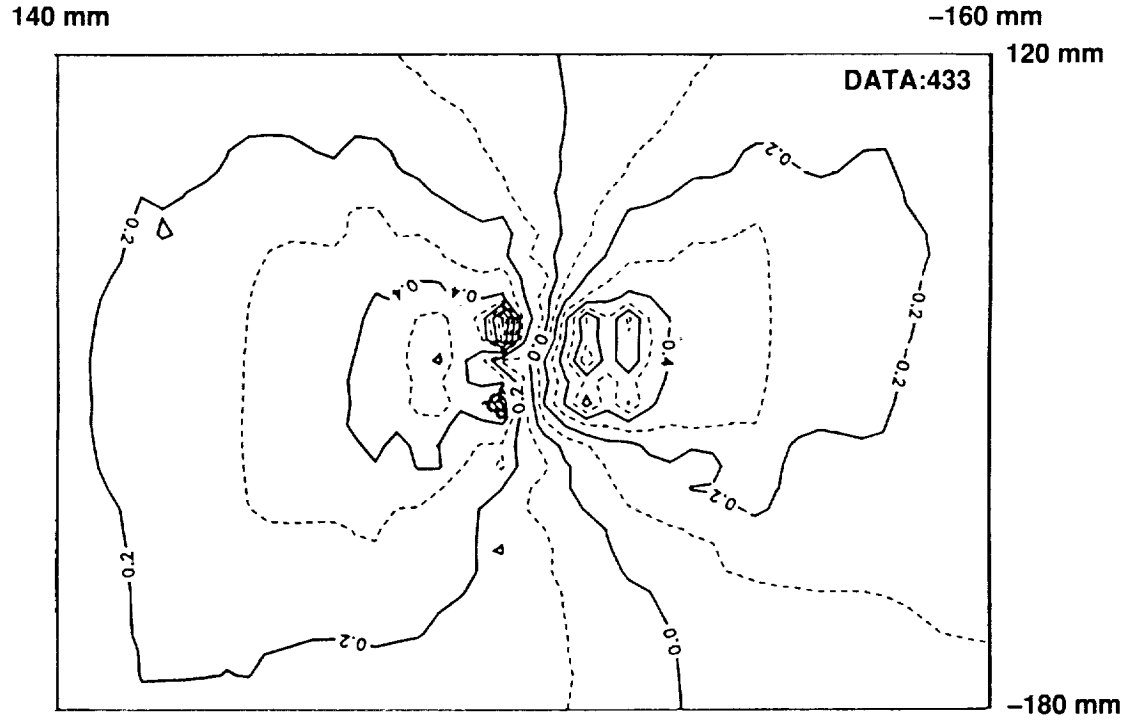

(b) Round-lateral edge

Figure 70. Detailed vertical velocity contours around trailing vortex from $c = 52$ cm wing ($AR = 6.6$) at $x/c = 0.1$ with $Re = 2.0 \times 10^6$ and $\alpha = 12°$ for square- and round-lateral edges.

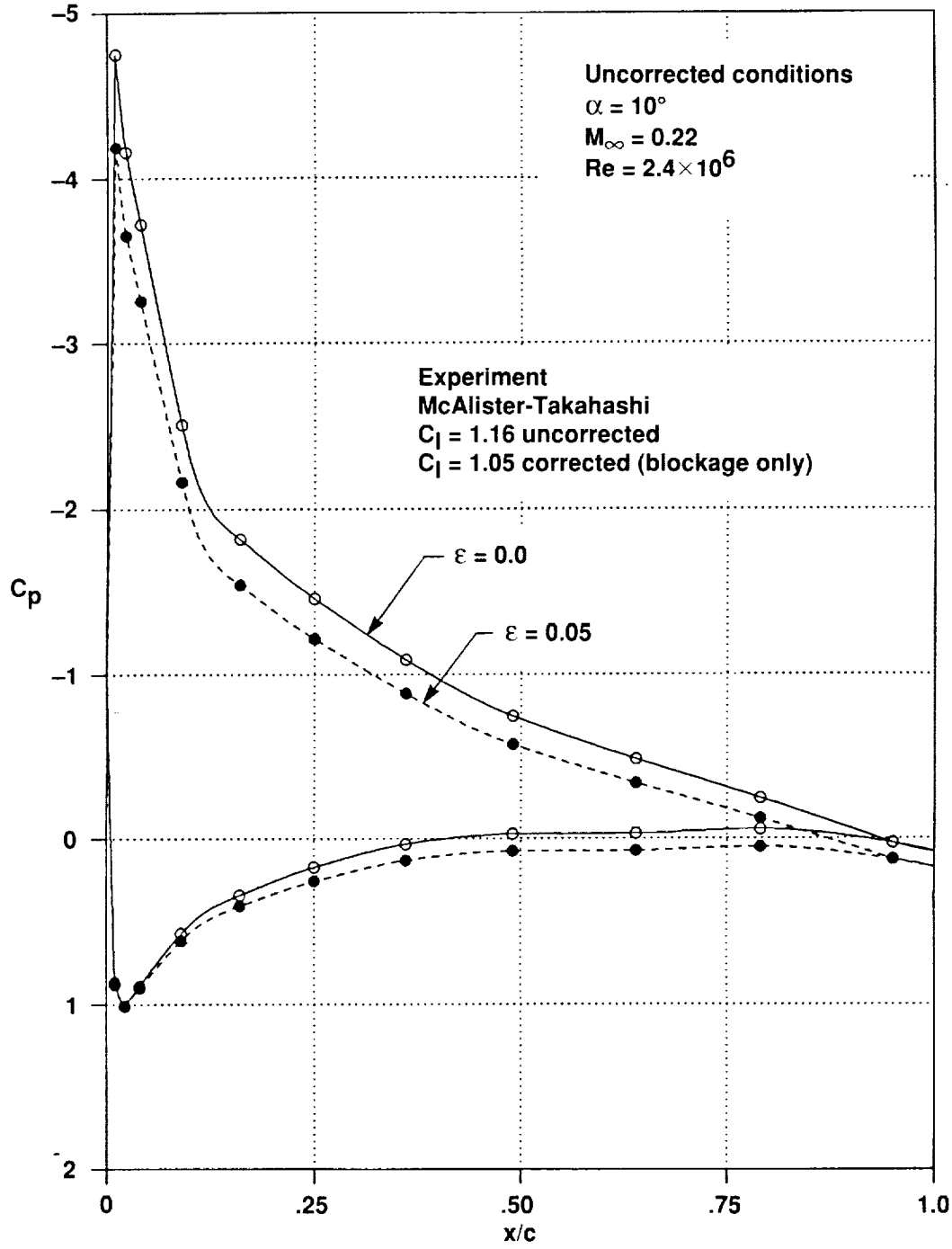

Figure 71. Example of solid-body and wake-blockage effects on 2D pressure distribution.

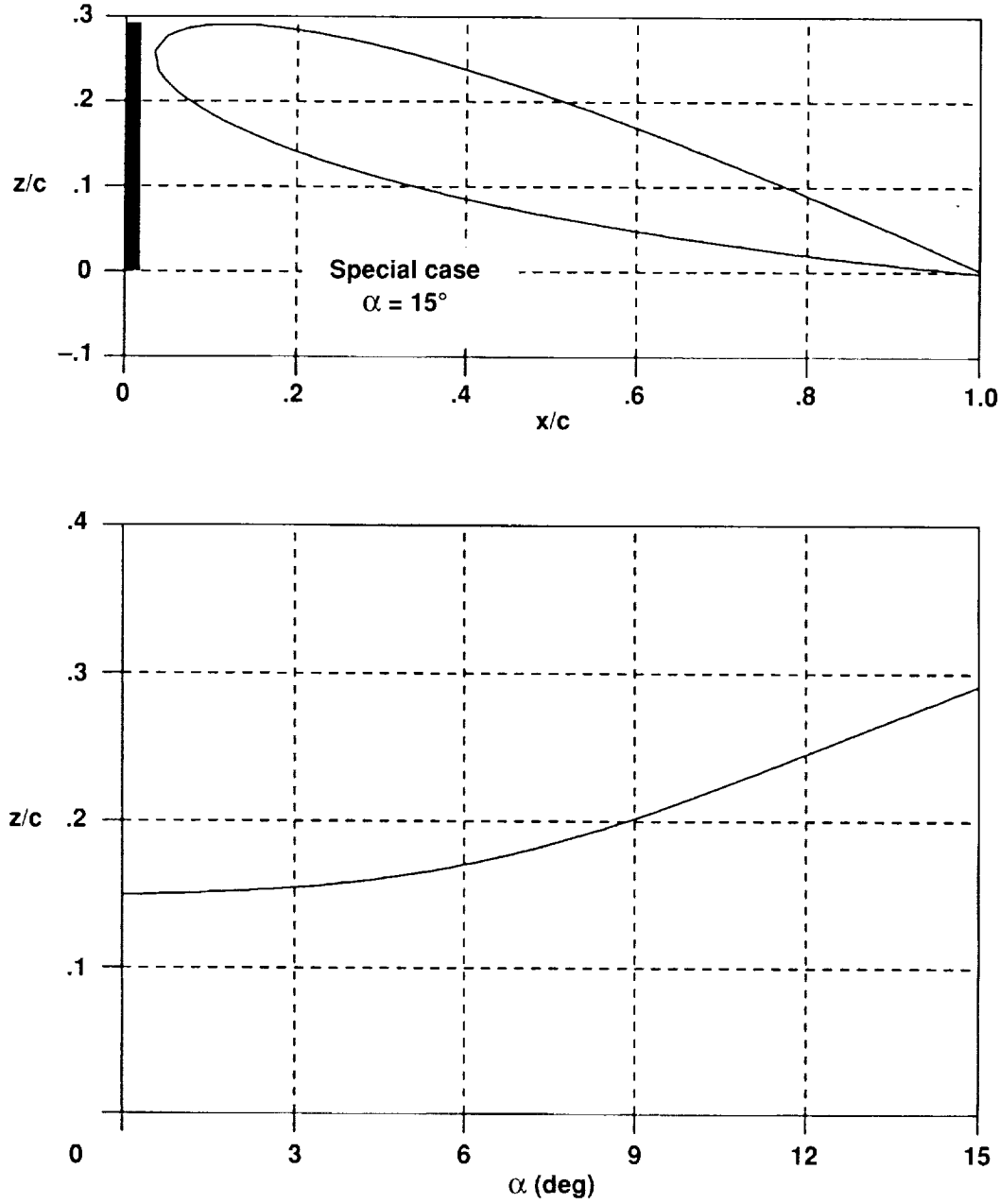

Figure 72. Frontal projection of NACA 0015 airfoil for a range of incidence angles.

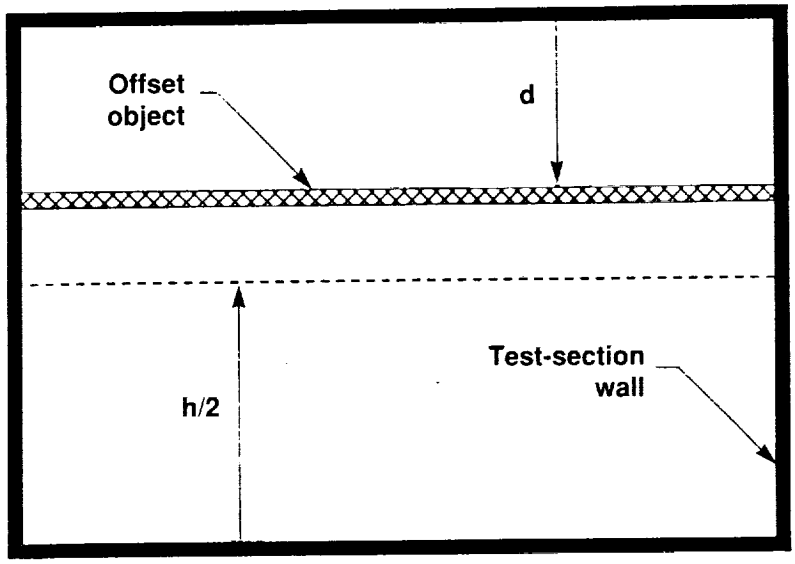

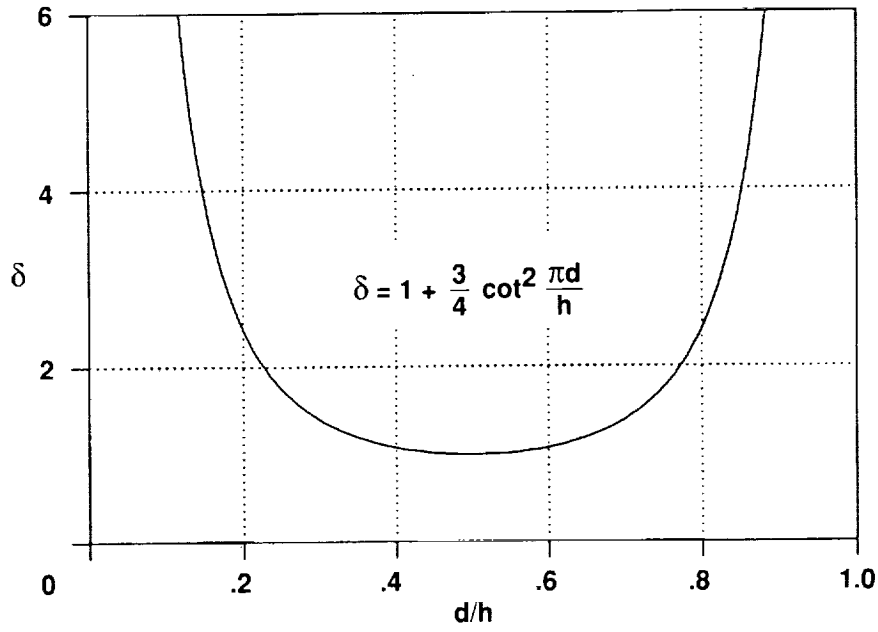

Figure 73. Effect of object offset on solid-blockage factor.

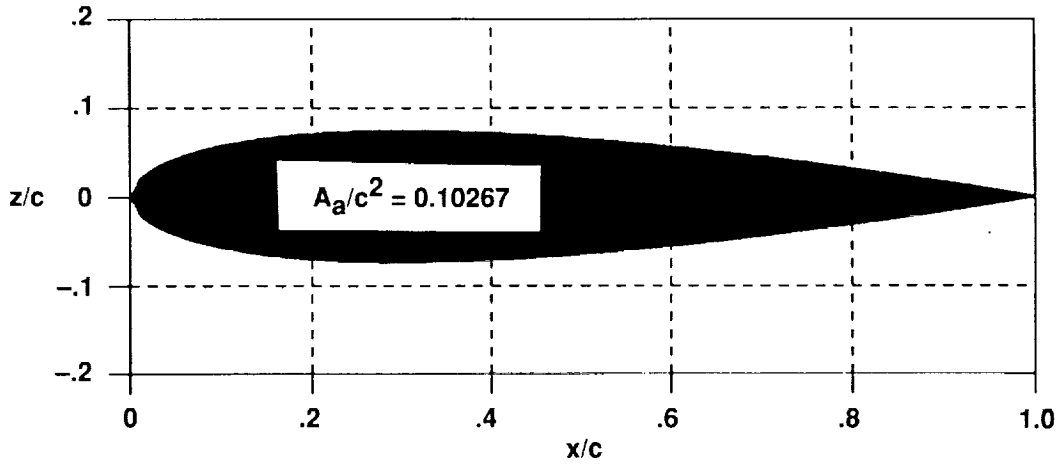

Figure 74. Cross-sectional area of NACA 0015 airfoil.

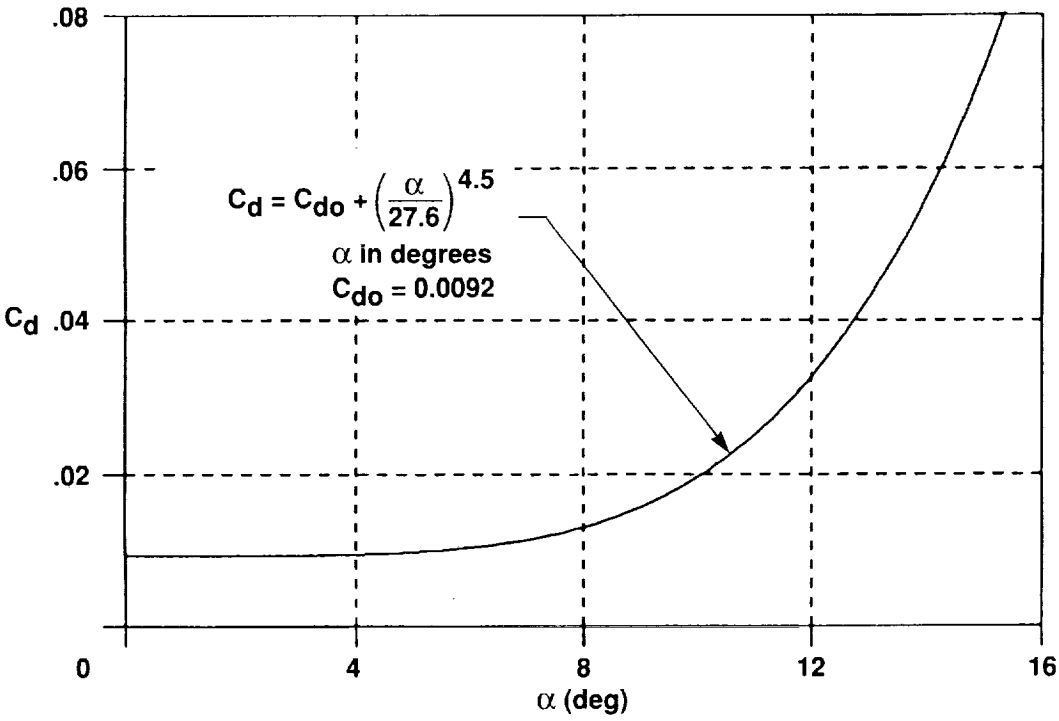

Figure 75. Drag coefficient for NACA 0015 at $Re = 1.2 \times 10^6$ and $M_\infty = 0.1$ (ref. 48).

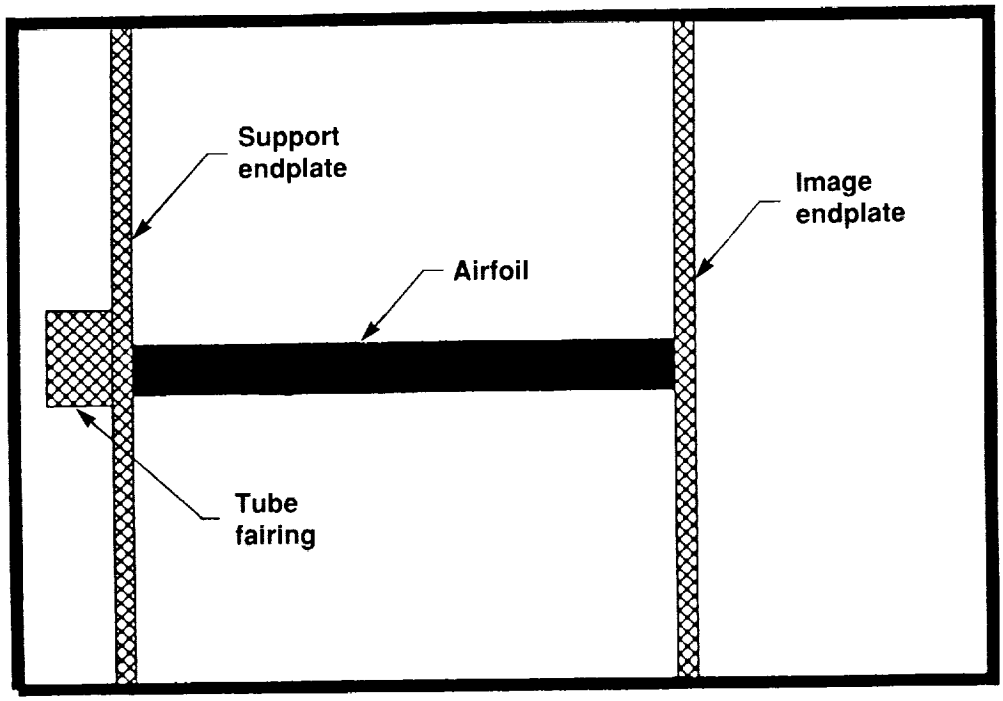

Figure 76. Airfoil at $\alpha = 10°$ between splitter plates in 7- by 10-foot wind tunnel.

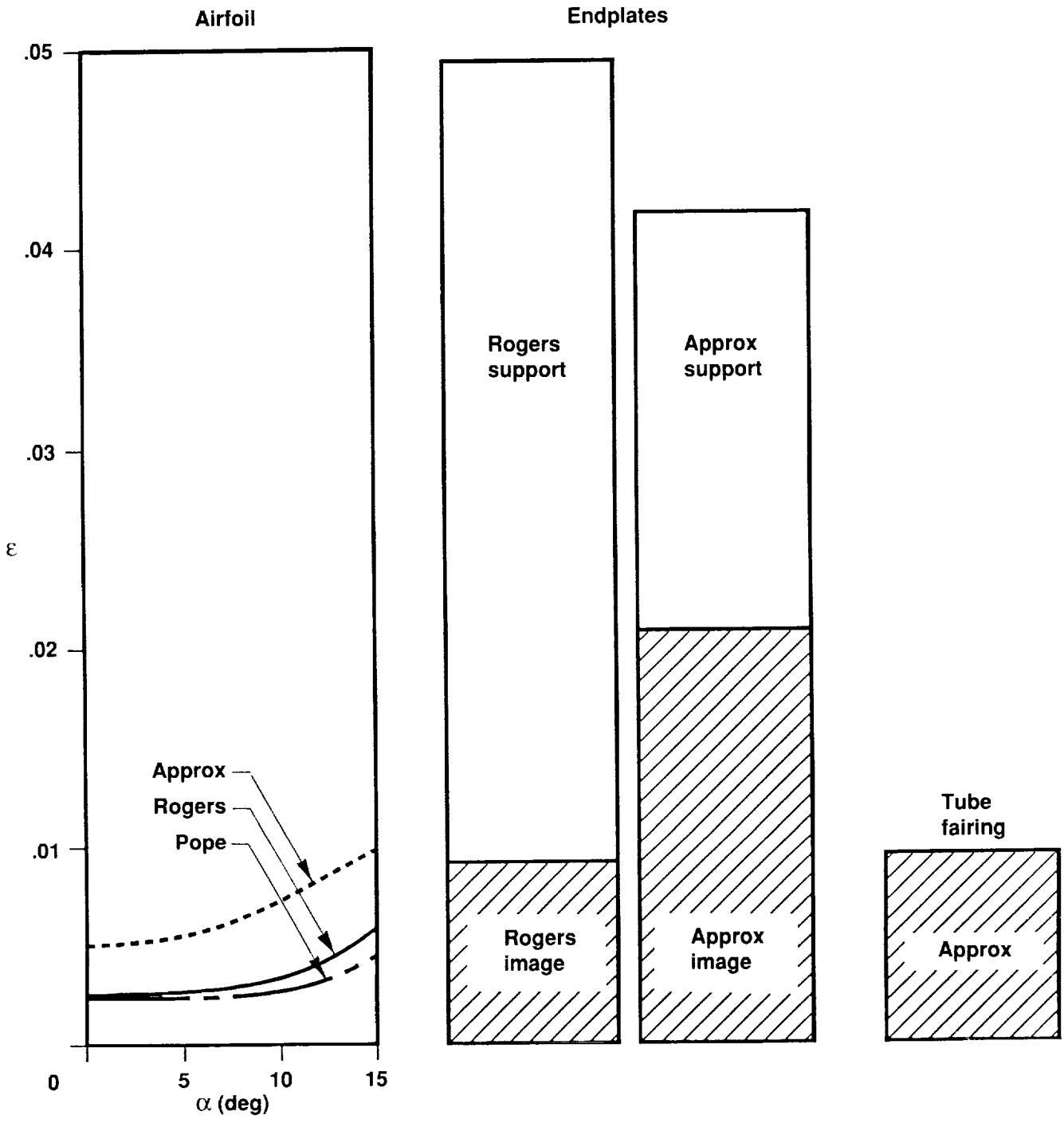

Figure 77. 2D solid-and wake-blockage contributions at $M_\infty = 0.2$.

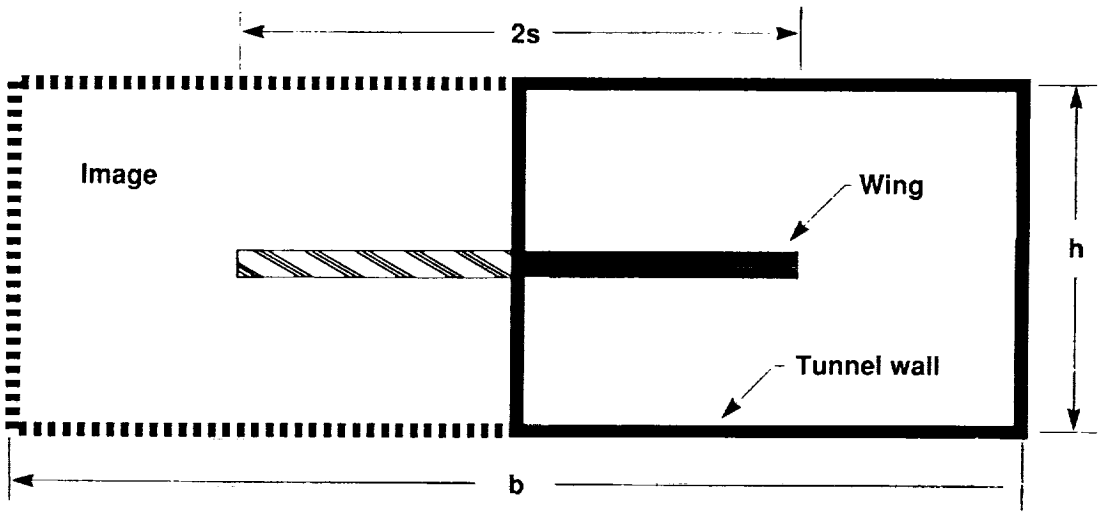

Figure 78. Assumed interference geometry with side-wall reflection.

REPORT DOCUMENTATION PAGE

Form Approved
OMB No. 0704-0188

1. AGENCY USE ONLY *(Leave blank)*	2. REPORT DATE	3. REPORT TYPE AND DATES COVERED
	November 1991	Technical Paper

4. TITLE AND SUBTITLE

NACA 0015 Wing Pressure and Trailing Vortex Measurements

5. FUNDING NUMBERS

WU-505-61-51

6. AUTHOR(S)

K. W. McAlister and R. K. Takahashi

7. PERFORMING ORGANIZATION NAME(S) AND ADDRESS(ES)

Ames Research Center, Moffett Field, CA 94035-1000 and
Aeroflightdynamics Directorate, U.S. Army Aviation Systems Command, Ames Research Center, Moffett Field, CA 94035-1099

8. PERFORMING ORGANIZATION REPORT NUMBER

A-91056

9. SPONSORING/MONITORING AGENCY NAME(S) AND ADDRESS(ES)

National Aeronautics and Space Administration, Washington, D. C. 20546-0001 and U.S. Army Aviation Systems Command, St. Louis, MO 63120-1798

10. SPONSORING/MONITORING AGENCY REPORT NUMBER

NASA TP-3151
AVSCOM TR-91-A-003

11. SUPPLEMENTARY NOTES

Point of Contact: K. W. McAlister, Ames Research Center, MS 215-1, Moffett Field, CA 94035-1000
(415) 604-5892 or FTS 464-5892

12a. DISTRIBUTION/AVAILABILITY STATEMENT

Unclassified-Unlimited
Subject Category – 02

12b. DISTRIBUTION CODE

13. ABSTRACT ***(Maximum 200 words)***

A NACA 0015 semispan wing was placed in a low-speed wind tunnel, and measurements were made of the pressure on the upper and lower surface of the wing and of the velocity across the vortex trailing downstream from the tip of the wing. Pressure data were obtained for both 2D and 3D configurations. These data feature a detailed comparison between wing tips with square and round lateral edges. A two-component laser velocimeter was used to measure velocity profiles across the vortex at numerous stations behind the wing and for various combinations of conditions. These conditions include three aspect ratios, three chord lengths, a square- and a round-lateral tip, presence or absence of a boundary-layer trip, and three image plane positions located opposite the wing tip. Both pressure and velocity measurements were made for angles of attack of $4° \le \alpha \le 12°$ and for Reynolds numbers of $1 \times 10^6 \le Re \le 3 \times 10^6$.

The addition of a round-lateral edge to the wing tip was found to eliminate the secondary vortex near the wing tip, but had little effect on the downstream characteristics of the trailing vortex. The increase in wing lift near the tip because of the presence of the trailing vortex was evident in the surface pressure, but was not captured by circulation-box measurements. The circumferential velocity within the vortex was found to reach free-stream values and produce core rotational speeds as high as 44,000 rpm. The streamwise velocity within the viscous wake that is shed from the wing was observed to form islands of peak velocity in the spiraling sheet that feeds into the trailing vortex. Near the wing, the trailing vortex is asymmetric and contains definite zones where the streamwise velocity both exceeds and falls behind the free-stream value. When referenced to the free-stream velocity, the maximum vertical velocity of the vortex is directly dependent on α and is independent of Re.

14. SUBJECT TERMS	15. NUMBER OF PAGES
NACA 0015 wing, Wing surface pressure, Trailing vortex	144
	16. PRICE CODE A07

17. SECURITY CLASSIFICATION OF REPORT	18. SECURITY CLASSIFICATION OF THIS PAGE	19. SECURITY CLASSIFICATION OF ABSTRACT	20. LIMITATION OF ABSTRACT
Unclassified	Unclassified		

NSN 7540-01-280-5500

Standard Form 298 (Rev. 2-89)
Prescribed by ANSI Std. Z39-18
298-102

NASA-Langley, 1991